Imperial College London
UK Research Centre in Non-Destructive Evaluation, Department of Mechanical Engineering

# MODELLING THE ULTRASONIC RESPONSE FROM ROUGH DEFECTS USING EFFICIENT FINITE ELEMENT MODELLING TECHNIQUES

James Richard Pettit

January 2015

Submitted in part fulfilment of the requirements for the degree of
Engineering Doctorate in Non-Destructive Evaluation of Imperial College London

# Declaration

I herewith certify that all material in this dissertation which is not my own work has been properly acknowledged.

James Richard Pettit

# Copyright Statement

# Abstract

The work of this Engineering Doctorate addresses the research and development of efficient Finite Element (FE) modelling techniques for calculating the ultrasonic response from rough defects for Non-Destructive Evaluation (NDE) applications specific to the nuclear power generation industry. The project has been carried out in collaboration with Imperial College London and Rolls-Royce allowing for the transfer of novel academic research into an applied industrial context.

Within the UK nuclear power generation industry, one of the fundamental principles of regulation and operation is a robust safety culture where the highest levels of quality assurance are applied to safety critical components. This principle places a requirement on NDE to deploy reliable and accurate inspections to ensure the structural integrity of the plant and its components.

To achieve this goal, modelling techniques can be used to aid in the design and justification of ultrasonic NDE inspections. For smooth, relatively large defects, analytical methods can provide an accurate scattering solution; however, for more realistic rough defects, the limitations of these methods are only applicable for specialised cases of roughness.

Defects which possess rough surfaces greatly affect ultrasonic wave scattering behaviour. Ultrasonic NDE inspections of safety-critical components rely upon this response for detecting and sizing flaws. Reliable characterisation is crucial, so it is essential to find an accurate means to predict any reductions in signal amplitude. An extension of Kirchhoff theory has formed the basis for many practical applications; however, it is widely recognised that these predictions are pessimistic owing to analytical approximations. As a result, NDE inspections can be overly sensitive, meaning that small and insignificant indications are incorrectly classed as being potentially hazardous defects. This increases the likelihood of making false-calls and incurring unnecessary expenditure to the programme.

A numerical full field modelling approach does not fall victim to such limitations, and therefore, FE modelling techniques have been developed to deliver a non-conservative methodology for the prediction of expected back-scattering from rough defects. This has been achieved in two parts: improved performance of absorbing boundary methods for use with commercial FE codes, and application of domain linking algorithms to NDE inspection problems. This thesis presents the development of these methods and their application to industrial NDE inspections. Ultimately, the findings of this work will aid in establishing more reliable, less conservative, reporting thresholds for the inspection of power plant components, reducing false call rates and therefore any unnecessary expenditure.

# Acknowledgments

I would firstly like to extend my thanks to Prof. Michael Lowe and Dr. Anthony Walker for their supervision throughout this doctorate. Without their continued support and guidance the completion of this thesis would not have been possible.

I would also like to acknowledgment the contributions made by researchers at Imperial College London, Rolls-Royce, EDF R&D and AMEC. The useful discussions and expertise that they have provided throughout all aspects of this project has been greatly appreciated. Thanks must also be extended to the Research Centre in Non-Destructive Evaluation (RCNDE), and the Engineering and Physical Sciences Research Council (EPSRC) for their financial contributions to this work.

Finally, I would like to thank my friends and family whose continuous help and advice has been the source of motivation for completing this work. The support that you have given me during this project has been invaluable, and for this I am very grateful.

# Contents

**1 Introduction** **24**
1.1 Industrial motivation . . . 24
1.2 Ultrasonic inspections . . . 25
1.3 The role and value of modelling . . . 26
1.4 Outline of thesis . . . 27

**2 Theoretical Background** **29**
2.1 Theory of bulk wave propagation in elastic media . . . 29
2.2 Analytical modelling . . . 32
2.2.1 Method of mathematical similarity . . . 32
2.2.2 Kirchhoff theory . . . 33
2.2.3 Geometrical Theory of Diffraction . . . 36
2.2.4 The Born approximation . . . 41
2.3 Numerical modelling . . . 43
2.3.1 Boundary Element Method . . . 44
2.3.2 Finite Difference method . . . 46
2.3.3 Finite Volume Method . . . 48
2.3.4 Finite Element method . . . 50
2.3.5 Implicit and explicit schemes . . . 53
2.3.6 Comparison of methods . . . 54
2.4 Rough surfaces and geometry definition . . . 55
2.5 Approaches for modelling scattering from rough surfaces . . . 57
2.5.1 Perturbation approach . . . 58
2.5.2 Kirchhoff theory . . . 59
2.5.3 Rayleigh method . . . 63
2.5.4 Finite Elements . . . 63
2.5.5 Discrete Point Source Method . . . 64
2.6 Conclusions . . . 65

**3 Absorbing Boundary Methods** **67**
3.1 Review of methods . . . 68
3.1.1 Infinite Elements . . . 69
3.1.2 Non-Reflecting Boundary Conditions . . . 71
3.1.3 Absorbing layer techniques . . . 72
3.2 Stiffness Reduction Method . . . 77
3.2.1 Stiffness Reduction Method theory . . . 78
3.2.2 One-dimensional Finite Element simulations . . . 79
3.2.3 Two-dimensional Finite Element simulations . . . 82
3.2.4 Results . . . 87
3.2.5 Comparison of absorbing layer methods . . . 89
3.2.6 Applied case . . . 93
3.3 Optimising absorbing regions . . . 97
3.3.1 Generic rules . . . 98
3.3.2 Total Performance Metric . . . 99
3.3.3 The optimisation function . . . 101
3.3.4 Absorbing boundary thickness . . . 102
3.4 Stiffness Reduction Method and Infinite Elements . . . 105
3.4.1 Analytical model . . . 105
3.4.2 Numerical model . . . 110
3.4.3 Performance . . . 114
3.5 Conclusions . . . 115

**4 Efficient Finite Element Techniques** **117**
4.1 Discretisation . . . 118
4.1.1 Two-dimensional meshing . . . 120
4.1.2 Three-dimensional meshing . . . 124
4.2 Domain linking algorithms . . . 127
4.3 Experimental validation . . . 133
4.3.1 Side Drilled Holes . . . 134
4.3.2 Flat Bottomed Holes . . . 141
4.3.3 Beam computation model . . . 146
4.4 Conclusions . . . 148

**5 Ultrasonic Response from Rough Defects** **151**
5.1 Attenuation due to defect roughness . . . 153
5.1.1 Rough surfaces and scattering signals . . . 153
5.1.2 Results . . . 157
5.1.3 Finite sized defects . . . 163
5.1.4 Experimental validation . . . 165
5.2 Oblique incidence backscatter . . . 170
5.2.1 Infinite defect extent . . . 171
5.2.2 Finite defect extent . . . 173
5.3 Influence of roughness on tip diffraction . . . 176
5.3.1 Comparison between Geometrical Theory of Diffraction and Finite Elements . . . 177
5.3.2 FE model for rough tip scattering . . . 183
5.3.3 Influence of roughness on Time of Flight Diffraction . . . 189
5.4 Three-dimensional rough surfaces . . . 191
5.5 Conclusions . . . 195

**6 Conclusions** **197**
6.1 Summary of thesis . . . 197
6.2 Future work . . . 200
6.3 Concluding remarks . . . 201

**7 Bibliography** **203**

**8 List of Publications** **213**

**9 Appendices** **214**
9.1 Appendix 1: Permission documents . . . 214

# List of Figures


Figure 1.2.1 Ultrasonic NDE inspection configuration. . . . . 25

Figure 2.1.1 An infinitesimally small cubic element with density $\rho$, and length $\partial x$. . . . . 30

Figure 2.2.1 Method of mathematical similarity used to estimate the signal amplitude from SDHs with increasing depth for a normal incidence pulse-echo inspection. . . . . 33

Figure 2.2.2 The definition of incident and scattering angles for a) an incident compression wave and b) an incident shear wave interacting with a surface. . . . . 34

Figure 2.2.3 The definition of incident and diffracted rays according to GTD from a defect tip. . . . . 37

Figure 2.2.4 Figure to show the directivity pattern for a) an incident and scattered compression wave $|D_p^p|$ for $\theta_{inc} = 30^o$ and b) an incident and scattered shear wave $|D_s^s|$ for $\theta_{inc} = 140^o$. . . . . 40

Figure 2.2.5 Illustration of ToFD configuration showing a transmitting transducer sending ultrasound towards a defect tip which is then scattered and detected by a transducer in reception for a) top tip diffraction and b) bottom tip diffraction, where the magnitude of the incident and scattering angles are equal and defined by $\alpha$. . . . . 41

Figure 2.2.6 Scattering of a normal incident wave due to scatterer $R$ embedded in three-dimensional elastic space. . . . . 42

Figure 2.3.1 Propagation of wave potentials $\phi$ and $\boldsymbol{\psi}$ in elastic space $\Omega$, across boundary $S$ with surface normal $\hat{\mathbf{n}}$. . . . . 45

Figure 2.3.2 The derivatives of a function $u(x)$, are approximated at points along a one-dimensional grid with spacing $\Lambda$. . . . . 46

Figure 2.3.3 Spatial domain $\Omega$, is discretised into elements with volume $v$, boundary $S$, and surface normal $\mathbf{n}$, where the quantity $\mathbf{q}(\mathbf{r}, t)$ is conserved across each element boundary. . . . . 49

Figure 2.3.4 A discretised FE spatial domain. . . . . 51

Figure 2.4.1 The definition of rough crack geometry for a) incident and scattered waves and b) cross section through a rough surface. . . . . 56

Figure 2.4.2 Figure to show the generation of coherent and diffuse scattered signals from a rough surface. . . . . 57

Figure 2.5.1 Figure to show the closure of a rough surface to allow for a surface integration of the scattered field for a) a bound finite volume and b) a back-wall. . . . . 60

Figure 2.5.2 Coherent and diffuse signal amplitudes predicted by Kirchhoff theory for compression and shear wave modes. . . . . 62

Figure 3.1.1 Figure to show the application of normal and tangential components of stress tensor for a row of Infinite Elements for a) an incident compression wave and b) an incident shear wave. . . . . 69

Figure 3.1.2 Figure to show an a) incident compression wave and b) an incident shear wave into a PML. . . . . 73

Figure 3.2.1 Illustration of an explicit one-dimensional FE model used to investigate absorbing layer performance. . . . . 79

Figure 3.2.2 Reflected signals from absorbing layer regions for a) ALID and SRM, full time record b) zoom of ALID and SRM and c) zoom of CALM and SRM. . . . . 80

Figure 3.2.3 Increase of real and imaginary components of the wavenumber with distance. . . . . 82

Figure 3.2.4 Figure to show application of the Global Matrix method to SRM absorbing

boundary. . . . . 83

Figure 3.2.5 FE model used to assess performance of SRM in bulk elastic wave propagation. . . . . 87

Figure 3.2.6 Analytical reflection coefficients from Global matrix method (GMM) and numerical reflection coefficients for a non-dimensional SRM for a) incident compression and b) incident shear waves. . . . . 88

Figure 3.2.7 Reduction in CFL number due to increase in critical time step across successive layers. . . . . 89

Figure 3.2.8 Reflection coefficients for SRM, ALID and PML for incident compression wave: a) compression analytical reflection coefficients and b) shear analytical reflection coefficients. . . . . 91

Figure 3.2.9 Reflection coefficients for SRM, ALID and PML for incident shear wave: a) compression analytical reflection coefficients and b) shear analytical reflection coefficients. . . . . 92

Figure 3.2.10 FE model used to test performance of SRM and ALID as a function of region thickness. . . . . 93

Figure 3.2.11 Comparison of time history from a single node for SRM with a) $0.2\lambda$ SRM thickness and b) $4\lambda$ SRM thickness. The $0.2\lambda$ SRM shows pollutants to time series from unwanted absorbing layer reflections. . . . . 95

Figure 3.2.12 Correlation function for a) average displacement over a monitoring line and b) at an arbitrary chosen node, for performance of SRM and ALID as a function of region thickness. . . . . 96

Figure 3.3.1 Rectangular FE model of length $a$, height $b$, and absorbing layer thickness $n\lambda$. . . . . 102

Figure 3.3.2 Figure showing a) the frequency response from the incident and reflected signals for increasing layer thickness and b) the reflection coefficient as a function of frequency for each layer. . . . . 104

Figure 3.4.1 Analytical and numerical reflection coefficients for an absorbing boundary

composed of Infinite Elements for an incident compression wave. . . . . 106

Figure 3.4.2 Numerical reflection from Infinite Element boundary for increasingly refined mesh. . . . . 107

Figure 3.4.3 Analytical and numerical reflection coefficients for an absorbing boundary composed of Infinite Elements for an incident compression wave with numerical mesh scattering correction. . . . . 108

Figure 3.4.4 Performance of SRM and Infinite Elements absorbing boundary for an incident compression wave for a) reflected compression wave modes and b)reflected shear wave modes. . . . . 111

Figure 3.4.5 Performance of SRM and Infinite Elements absorbing boundary for an incident shear wave for a) reflected compression wave modes and b)reflected shear wave modes. . . . . 112

Figure 3.4.6 Performance of SRM and Infinite Elements absorbing boundary for an incident compression wave for a) reflected compression wave modes and b)reflected shear wave modes. . . . . 113

Figure 3.4.7 Figure to show the absolute amplitude of the incident wave as it passes through the absorbing layers for a one-dimensional model. . . . . 115

Figure 4.1.1 Figure to show a) a square element b) a triangular element c) a cubic element and d) a tetrahedral element. . . . . 119

Figure 4.1.2 Figure to show a combination of structured and unstructured triangular elements using a partitioning function. . . . . 121

Figure 4.1.3 Figure to show two-dimensional Unit Cell model of a transition between structured and unstructured triangular elements using a partitioning function, where U1 and U2 represent nodal displacements in the x and y directions respectively. . . . . 121

Figure 4.1.4 Figure to show time histories for incident compression wave reflecting from a back-wall after propagating through structured and unstructured triangular meshes. The results from the structured and unstructured meshes are

overlaid, and no difference can be observed between them. . . . . 123

Figure 4.1.5 Figure to show the difference (structured-unstructured) between the time histories from a back-wall after propagating through structured and unstructured triangular meshes. . . . . 123

Figure 4.1.6 Three-dimensional spatial domain containing a complex defect and area immediately surrounding it defining the unstructured meshing using tetrahedral elements. . . . . 124

Figure 4.1.7 Cross-section through a three-dimensional FE model showing a transition between structured and unstructured tetrahedral elements. . . . . 125

Figure 4.1.8 Figure to show three-dimensional Unit Cell model of a transition between structured and unstructured tetrahedral elements using a partitioning function. . . . . 125

Figure 4.1.9 Figure to show time histories for incident compression wave reflecting from a back-wall after propagating through structured and unstructured tetrahedral meshes, where U1, U2 and U3 represent nodal displacements in the x, y and z directions. . . . . 126

Figure 4.1.10 Figure to show the difference (structured-unstructured) between the time histories from a back-wall after propagating through structured and unstructured tetrahedral meshes. The results from the structured and unstructured meshes are overlaid, and no difference can be observed between them. . . . . 126

Figure 4.2.1 Figure to show a) a full numerical model of an ultrasonic inspection and b) a spatially reduced model achieved through the use of a domain linking algorithm. . . . . 128

Figure 4.2.2 Figure to show Hybrid model with a spatially reduced FE model coupled with a domain linking algorithm. . . . . 130

Figure 4.2.3 Figure to show a) a Full FE simulation and b) a Hybrid model for the scattering from an embedded rough defect for the two-dimensional case. . . . . 131

Figure 4.2.4 Absolute amplitude of the scattered field from an embedded, finite, rough

defect, around a circular arc for a) Full FE simulation, b) a reduced spatial domain Hybrid Model, c) the difference between the Full FE simulation and Hybrid model for the two-dimensional case. . . . . 132

Figure 4.3.1 Experimental setup for normal incidence compression wave scattering from SDH with radius $r$, and depth $D$. The incident wave is generated by a transducer with diameter $a$, on a test block with thickness $T$. . . . . 135

Figure 4.3.2 Two-dimensional Hybrid model to calculate the response from SDHs with radius, $r$, at a range of depths, $D$. . . . . 135

Figure 4.3.3 Comparison between two-dimensional Hybrid simulation and experimental data for the ultrasonic response from SDHs with increasing depth. . . . . 137

Figure 4.3.4 Comparison between three-dimensional Hybrid simulation and experimental data for the ultrasonic response from SDHs with increasing depth. . . . . 137

Figure 4.3.5 Experimental setup for normal incidence compression wave scattering at angle $\theta_{sc}$, from a SDH with radius $r$, depth $D$. The incident wave is generated from the first element of a 128 element array, on a test block with thickness $T$. . . . . 138

Figure 4.3.6 Three-dimensional Hybrid model to calculate the response from SDH with radius $r$, and depth $D$, at scattering angle $\theta_{sc}$. . . . . 139

Figure 4.3.7 Absolute amplitude of the scattered field from a SDH as a function of the scattering angle for a) experimental measurement, b) reflected compression wave and c) a mode converted reflected shear wave. . . . . 140

Figure 4.3.8 Experimental setup for $45^o$ shear waves scattering from a FBH with radius $r$, depth $D$. The incident wave is generated by a transducer with diameter $a$, on a test block with thickness $T$. . . . . 142

Figure 4.3.9 Two-dimensional Hybrid model to calculate the response from FBHs with radius $r$, at a range of depths $D$. . . . . 142

Figure 4.3.10 Comparison between two-dimensional Hybrid simulation and experimental data for a $45^o$, 2.25 MHz, incident and reflected shear wave from tilted FBHs with increasing depth. . . . . 143

Figure 4.3.11 Comparison between three-dimensional Hybrid simulation and experimental data for a $45^o$, 2.25 MHz, incident and reflected shear wave from tilted FBHs with increasing depth. . . . . 144

Figure 4.3.12 Comparison between two-dimensional Hybrid simulation and experimental data for a $45^o$, 3.50 MHz, incident and reflected shear wave from tilted FBHs with increasing depth. . . . . 145

Figure 4.3.13 Comparison between three-dimensional Hybrid simulation and experimental data for a $45^o$, 3.50 MHz, incident and reflected shear wave from tilted FBHs with increasing depth. . . . . 145

Figure 4.3.14 Comparison between two-dimensional Hybrid simulation including a simple beam model and experimental data for the ultrasonic response from SDHs with increasing depth. . . . . 147

Figure 4.3.15 Comparison between three-dimensional Hybrid simulation including a simple beam model and experimental data for the ultrasonic response from SDHs with increasing depth. . . . . 148

Figure 5.1.1 Figure to show the coherent and diffuse scattered signals resulting from a normally incident wave. . . . . 154

Figure 5.1.2 Unit Cell FE model with symmetric boundaries to simulate an infinite periodic surface, used to calculate the elastic wave scattering of a normally incident compression wave. The model is repeated for multiple realisations of defects defined by the same statistical class of roughness. The signal is monitored parallel to the plane of the incident wave along a monitoring line. . . . . 156

Figure 5.1.3 Reduction of amplitude of wave reflecting from a rough surface, with respect to a perfectly smooth surface. Results shown for coherent component, comparing Kirchhoff theory and Finite Element simulations. Results are for a normal incident compression wave with wavelength $\lambda_{inc}$, scattering from a defect with surface roughness, $\sigma$. . . . . 158

Figure 5.1.4 The variation in the function $k_{inc}a_{min}\cos^3\theta_{inc}$ with increasing roughness for a normally incident compression wave, which must be significantly greater

than 1 for a valid application of Kirchhoff theory. . . . . 159

Figure 5.1.5 Variation in coherent signal amplitude with increasing number of surface realisations for three classes of surface roughness to show the number of realisations required to tend towards a convergent signal. . . . . 160

Figure 5.1.6 Comparison between the reduction in signal amplitude for the mean total reflected signal (calculated using FE) and the coherent signal (predicted from Kirchhoff theory). The total reflected signal is plotted with the 95.4% spread (or $2\sigma$ confidence) about the mean value. . . . . 162

Figure 5.1.7 Revised FE model to consider the effects of a finite sized defect including scattering from crack tips. . . . . 163

Figure 5.1.8 Comparison between the reduction in signal amplitude from a finite sized defect for the mean total reflected signal (calculated using FE) and the coherent signal (predicted from Kirchhoff theory). The total reflected signal is plotted with the 95.4% spread (or $2\sigma$ confidence) about the mean value. . . . . 164

Figure 5.1.9 Sinusoidal test piece used to validate elastic scattering from rough surface. This sample is scanned from the front face with a 5 MHz, 0.25″ diameter compression wave transducer at normal incidence; this scan is then replicated in FE. . . . . 165

Figure 5.1.10 Figure to show a) experimental scan and b) FE scan of sinusoidal test piece showing (grey scale) reduction in signal amplitude due to roughness; scans are normalised against the response from the smooth back-wall at 0 mm and 37 mm. The response from the sinusoidal section has an arrival time of 3.9 µs and is followed by the response from the smooth section at 4.1 µs. . . . . 166

Figure 5.1.11 Reflection coefficient from a scan over sinusoidal surface, showing comparison between experimental measurements and FE simulations. . . . . 167

Figure 5.1.12 Dimensions of test blocks and the position of the rough back-wall relative to the scanning surface. . . . . 168

Figure 5.1.13 Comparison between the reduction in reflection coefficients for the mean total reflected signal (calculated using FE) and the total reflected signal

measured experimentally. The mean total reflected signal is plotted with the 95.4% spread (or $2\sigma$ confidence) about the mean value. . . . . 169

Figure 5.2.1 Figure to show oblique incidence wave scattering from a rough surface. The scattered signal consists of diffuse and coherent fields. The back-scattered signal lies back along the path of propagation. . . . . 170

Figure 5.2.2 FE model with significantly reduced spatial domain for an incident shear wave interacting with a rough defect at oblique incidence where the extent of the defect is greater than the incident beam. . . . . 172

Figure 5.2.3 The mean total reflected signal amplitude as a function of defect misorientation for an incident shear wave. The scattered response for two classes of defect roughness ($\sigma = 0.063\lambda_{inc}$ and $\sigma = 0.200\lambda_{inc}$) is plotted and normalised against the normal incidence case for a smooth defect. . . . . 173

Figure 5.2.4 FE model with significantly reduced spatial domain for an incident shear wave interacting with a rough defect at oblique incidence where the beam spread is greater than the extent of the defect. . . . . 174

Figure 5.2.5 Magnitude of the total back-reflected signal for an incident shear wave interacting with a rough defect at oblique incidence where the beam spread is greater than the extent of the defect; the magnitude is expressed as attenuation with respect to the reflection from a smooth crack at normal incidence. . . . . 174

Figure 5.2.6 Figure to show superposition of top and bottom tip diffracted signals. . . . . 175

Figure 5.3.1 Incident compression wave on a crack tip across angular range, $\theta_{inc}$, where the compression and shear wave modes are monitored across scattering angle $\theta_{sc}$. . . . . 178

Figure 5.3.2 Scattering matrices showing the magnitude of the scattered compression wave from a smooth defect tip due to an incident compression wave for a) GTD and b) FE simulations. . . . . 179

Figure 5.3.3 Scattering matrices showing the magnitude of the scattered shear wave from a smooth defect tip due to an incident compression wave for a) GTD and b) FE simulations. . . . . 180

Figure 5.3.4 Figure to show the special case where the magnitude of the incident angle equals the magnitude of the scattered angle, $\alpha$ for a) top tip diffraction and b) bottom tip diffraction. . . . . 181

Figure 5.3.5 Comparison between GTD and FE for the magnitude of scattered signal from a smooth defect tip due to an incident compression wave at incident and scattered angle $\alpha$ for a) scattered compression wave and b) mode converted scattered shear wave. . . . . 182

Figure 5.3.6 Incident compression wave on a rough crack tip across angular range $\theta_{inc}$, where the compression and shear wave modes are monitored across scattering angle $\theta_{sc}$. . . . . 183

Figure 5.3.7 Polar plots showing the mean scattered compression wave from five hundred realisations from a rough defect tip along with the 95.4% confidence spread, compared to the scattered compression wave obtained from GTD for a smooth defect tip, due to an incident compression wave at angles $39^o$ to $179^o$ in $10^o$ increments shown in a) to o). . . . . 185

Figure 5.3.8 Polar plots showing the mean scattered shear wave from five hundred realisations from a rough defect tip along with the 95.4% confidence spread, compared to the scattered shear wave obtained from GTD for a smooth defect tip, due to an incident compression wave at angles $39^o$ to $179^o$ in $10^o$ increments shown in a) to o). . . . . 186

Figure 5.3.9 Scattering matrices showing the mean total scattered signal of the a) scattered compression wave and b) scattered shear wave, from a defect tip with roughness $\sigma = 0.100\lambda_{inc}$ due to an incident compression wave. . . . . 188

Figure 5.3.10 FE simulations to calculate the magnitude of the mean scattered signal and confidence bands from a defect tip with roughness $\sigma = 0.100\lambda_{inc}$, due to an incident compression wave at incident and scattered angle $\alpha$ for a) scattered compression wave and b) scattered shear wave. . . . . 190

Figure 5.4.1 Embedded three-dimensional planar rough defect used to calculate the attention in ultrasonic response. . . . . 192

Figure 5.4.2 Reduction in signal amplitude for the mean total reflected signal from three-

dimensional rough defects with increasing roughness expressed as a function of the incident wavelength. The total reflected signal is plotted with the 95.4% spread (or $2\sigma$ confidence) about the mean value. . . . . 193

# Preface

This Engineering Doctorate has been conducted by the Research Centre for Non-Destructive Evaluation (RCNDE) in collaboration with Imperial College London and Rolls-Royce. Under the RCNDE, these two institutions have had a long standing and successful relationship, having invested in a series of research tasks, including four Engineering Doctorate projects within the last decade alone.

Rolls-Royce is responsible for the manufacture and maintenance of Nuclear Steam Raising Plants (NSRP). This industry is heavily reliant upon a stringent safety culture where confidence in the performance of the NSRP is paramount. As a result, the challenge given to Non-Destructive Evaluation (NDE) is to confirm the structural integrity of the plant in a cost effective and timely manner without any compromise made to safety. The need to deliver this capability has resulted in a significant investment from Rolls-Royce in technologies that are advancing new and innovative approaches to solving NDE inspection problems.

The department of UK Research Centre in NDE at Imperial College London has proven to be a world leading academic institution, capable of providing solutions to this challenge. This introduces the role of the Engineering Doctorate; as a means to transfer novel academic research into industry, to support large scale, bespoke, engineering projects.

During this doctorate, the author's primary role has been to ensure the delivery of this thesis. This has meant providing a novel contribution to academia, whilst still establishing a capability that can be directly integrated into industry. To achieve this, the first year of research was carried out at Imperial College London in order to establish a foundation in key scientific principles that would form the basis of this work. Following this, the remaining three years of the project have been spent as a member of the NDE research team at Roll-Royce, where research is conducted within an industrial environment, forcing the project to focus on achieving outputs that are of direct benefit to the business.

Inevitably, studying in an industrial environment has resulted in additional responsibilities within the company. Of greatest interest has been aiding in the design and justification of NDE inspections for deployment on NSRP components. This has been accompanied by excursions to UK naval bases and manufacturing facilities, to either implement these inspections or obtain a greater appreciation of the business as a whole. The opportunity to see the final output of these large scale engineering challenges has been an incredibly motivating and beneficial experience, helping to ensure that the outputs from this doctorate are of direct benefit to the industry.

# 1 Introduction

This thesis discusses the development of efficient Finite Element (FE) modelling techniques to calculate the ultrasonic response from rough defect types that have the potential to form within nuclear power plant components.

The following sections outline the context of this project, focusing on the industrial motivation for developing ultrasonic Non-Destructive Evaluation (NDE) techniques and highlight how numerical modelling methods can be used to aid in the design, justification and deployment of ultrasonic NDE inspections.

## 1.1 Industrial motivation

One of the fundamental principles of regulation and operation within the UK nuclear power generation industry is a robust safety culture where the highest levels of quality assurance are applied to safety critical components [1]. A key aspect of this principle is to demonstrate that nuclear reactor plants are free from significant flaws that could threaten the integrity of the pressure boundary. This is achieved through an extensive use of NDE inspection techniques to identify any potential flaws that may arise, either at the start-of-life, or that result from in-service operation [2].

The frequency and the nature of a deployed NDE inspection is heavily dependent upon structural integrity assessments of the component and the subsequent consequences should failure occur [3]. Although the potential for flaws to manifest is highly unlikely, the requirement to provide a robust safety justification means that it is necessary to demonstrate their absence through rigorous NDE inspections.

It is essential that NDE is capable of correctly detecting, sizing and characterising potential flaws within these components. Infrequent or inaccurate inspections can result in an indication being incorrectly characterised or overlooked, resulting in unknown repercussions. Attempting to resolve this issue with overly sensitive inspections to ensure detection of weak echoes is not always possible. In these instances, reflections from the rough defect can fall below the background ultrasonic noise levels; or alternatively, the inspection can be so sensitive as to misinterpret insignificant indications as being from rough defects, increasing the likelihood of making false-calls, causing unnecessary expenditure.

As a result, considerable interest is placed in technologies such as NDE to provide significant im-

provements to inspection performance in a cost effective and timely manner without any compromise made to safety. Practical solutions to many of the significant engineering challenges faced by the nuclear industry can be achieved through novel and innovative research in academic institutions. In recent decades this demand has resulted in NDE becoming a field of research within its own right, where recent advances are helping to support and maintain the continued operation of safety critical components and structures.

The industrial motivation for this project is therefore to provide highly reliable and dependable NDE inspection methods that can accurately assess the structural integrity of safety critical components within the nuclear industry. Achieving this goal will result in increased confidence in the accuracy of deployed NDE inspections, thereby reducing the likelihood of making false-calls and ultimately, reducing overall costs to the programme.

## 1.2 Ultrasonic inspections

A variety of NDE inspection methods can be deployed on power plant components, however, in most instances ultrasonic techniques are primarily used, owed to their relative flexibility. Many of the inspections offer technical challenges to operators involving circumstances such as inhomogeneous materials, complex geometry and hazardous environments. The versatility offered by ultrasonic methods means that they are highly suited to accounting for circumstances such as these.

The conventional setup for most ultrasonic inspections is to apply an ultrasonic transducer to the surface of a component and examine the nature of the scattered field returning from features within the structure, as illustrated in Figure 1.2.1.

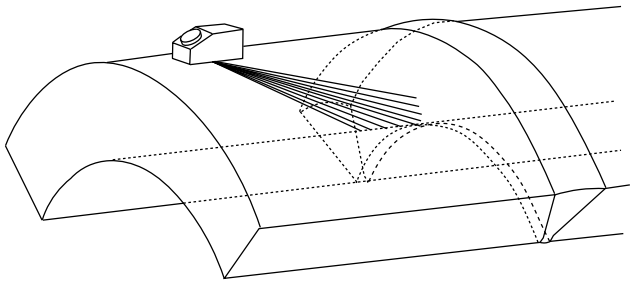

Figure 1.2.1: Ultrasonic NDE inspection configuration.

In this illustration a beam of ultrasound is used to examine a generic weld joining two components. The ultrasound is transmitted from the transducer and upon interacting with a physical change within the structure, a reflected signal will return back along the path of propagation. This scattered signal is then analysed to determine whether or not a defect is present within the component.

There are a number of techniques that can be used to correctly size and characterise any potential flaws that may arise; however, they all rely in some part upon having a relatively high amplitude signal returning back from the defect. The magnitude of this signal is heavily dependent upon the geometry of the defect itself, and often, defects that possess rough surfaces return a severely attenuated scattered signal amplitude in comparison to the smooth equivalent.

This property makes accurately sizing and characterising rough defect types increasingly difficult. Knowing the size of a defect is particularly important, since despite the rigorous safety case for continued and safe operation, not all flaws pose a threat to plant safety. In some cases, it might be advantageous to leave relatively benign flaws within a structure or component, thereby avoiding the need for a lengthy and expensive repair, as well as any unnecessary radiation dose incurred by repair personnel. Therefore a means to accurately predict the nature of ultrasonic signal amplitudes from rough defects is essential.

## 1.3 The role and value of modelling

The ability to tolerate insignificant indications within a component requires the ultrasonic inspection technique to be highly reliable and capable of accurately sizing and characterising potential flaws. This can be achieved through carefully designed ultrasonic inspection systems and procedures that are validated and technically justified through modelling techniques and a detailed understanding of ultrasonic propagation and scattering mechanisms.

For smooth, relatively simple defects, predicting the nature of ultrasonic wave scattering is a well understood problem. Established analytical modelling techniques can be used to aid in the design of an inspection and have formed the basis for technical justifications and procedures. However, for more complex defect geometries with significant surface roughness conventional analytical methods become increasingly inaccurate at calculating the nature of scattered ultrasonic signals. This is attributed to a breakdown of the fundamental assumptions that form the basis of the solution.

To account for this uncertainty a pessimistic approach tends to be taken whereby scattered ultrasonic signal amplitudes from rough defects are assumed to be severely attenuated. This approach ensures that all defects of structural concern are found, however, at the expense of mis-classifying insignificant indications as being potentially hazardous flaws.

An alternative numerical modelling approach does not fall victim to the same fundamental assumptions as analytical methods and can be used to calculate highly accurate solutions to ultrasonic wave scattering problems from complex defect geometries.

The aim of this Engineering Doctorate is to develop and demonstrate the use of efficient FE modelling techniques to calculate the ultrasonic response from defects which possess rough surfaces. Application of these techniques will provide a means to accurately calculate the nature of scattered ultrasonic signals

from rough defects and reduce the conservatism that is currently associated with their detection. This analysis will provide a basis for a less sensitive, yet safe, approach for accounting for defect roughness. This capability will allow for increased accuracy in sizing and characterising potential flaws, reduce the likelihood of mis-classifying defects, and ultimately, reduce the overall expenditure to the programme.

## 1.4 Outline of thesis

This thesis begins by establishing the theoretical background necessary to describe ultrasonic wave propagation and scattering behaviour. A detailed description of conventional analytical modelling techniques is given, with heavy focus placed on applications regarding ultrasonic NDE inspections. Following this, a review of numerical modelling techniques is made where the merits of each technique are assessed against the requirements of an industrial numerical solver. The section concludes with a review of the current advances made in understanding ultrasonic wave scattering from rough surfaces and the application of analytical and numerical methods to solving these scattering problems.

A prerequisite for the application of FE modelling techniques to ultrasonic NDE inspections is the ability to significantly reduce the size of the spatial domain, thereby allowing computational resource to be allocated towards a highly accurate representation of the scatterer. This is achieved in two parts.

Firstly, the need to simulate infinite elastic space through the use of absorbing boundary methods is discussed and a review of the current methods is given. However, despite recent advances in this field it has proven necessary to develop a new absorbing boundary technique which is termed the Stiffness Reduction Method (SRM). The SRM technique meets the bespoke requirements needed for ultrasonic NDE applications as well as those needed for an industrial numerical solver.

The second part is to ensure that highly efficient FE modelling techniques are used. A review of the recent literature is discussed, deducing best practices for spatial and temporal discretisation of rough defect geometries. Following this, the subject of domain linking algorithms is introduced. These allow the spatial domains of FE models to only consider an area immediately surrounding the defect or feature of interest; representing a significant advance in making highly accurate FE models a practical tool for industrial NDE applications. The domain linking algorithm is coupled to a beam computation tool and experimental validation of the model is performed for two and three-dimensional cases.

The penultimate chapter presents practical models that combine the principles of efficient FE techniques and absorbing boundary methods to calculate the ultrasonic response from rough defects. Firstly, a like-for-like comparison is made against the work set out by previous authors which has formed the basis for calculating attenuation due to defect roughness for applications in the UK power generation industry. The FE models make use of a Monte-Carlo approach that allows rough defects to be characterised by a statistical description of surface roughness. Comparisons are made against analytical models and experimental data in order to establish confidence in the new approach.

Following this, FE models are applied to calculating the ultrasonic response from rough defects for oblique incidence cases where the back-scattered signal is measured back along the path of propagation. The investigation then extends to examine the effects of roughness on tip diffracted signals, focusing on the impact this has to Time-of-Flight Diffraction (ToFD) techniques. The chapter concludes with an investigation on the ultrasonic response from embedded, three-dimensional rough surfaces, combining all aspects of the project.

Finally, the conclusions of the project are drawn. The thesis can be categorised into three main areas of research; absorbing boundary methods, efficient FE modelling techniques and calculating the ultrasonic response from rough defects. Each of these can be considered as a self-contained project, applicable to multiple fields of research within their own right. However, in this thesis they combine to form a concise review for modelling the ultrasonic response from rough defects using efficient FE methods for applications specific to industrial ultrasonic NDE inspections.

# 2 Theoretical Background

This chapter presents the theoretical background necessary for completion of this project. The fundamentals of ultrasonic wave propagation are discussed, including the extension of these theories towards ultrasonic NDE.

An extensive library of texts are available detailing ultrasonic wave scattering behaviour. A fundamental description is given by Auld [4], and Achenbach [5], where focus is placed on a mathematical representation of wave propagation from first principles. Krautkramer [6], and more recently Rose [7], also explain the physical principles of wave propagation but more specifically the relationship with ultrasonic NDE inspections. Schmerr [8], gives an understanding of how best to construct ultrasonic models for typical NDE applications by putting the governing equations into a rigorous NDE context. With regards to rough defects, the book by Ogilvy [9] gives an extensive review of the progress made during the last century, including her own contributions to the field. This selection of the literature is referenced throughout this thesis and forms the basis for understanding ultrasonic wave propagation and scattering for the purposes of NDE.

The sections that follow present the theoretical background for bulk wave propagation and scattering in elastic media. Firstly, the derivation of the harmonic wave potentials from first principles is given. This forms the basis for the following discussions on analytical and numerical modelling techniques for ultrasonic NDE inspections. In both cases a qualitative and quantitative description is given. The analytical modelling methods that will be discussed are already well established and have formed the basis for many technical justifications in ultrasonic NDE inspections of safety-critical components in industry. Numerical modelling methods for ultrasonic NDE applications are relatively young in comparison, and although proof-of-concept has been demonstrated in academia, they have yet to be fully incorporated into an industrial environment. The final section reviews the applications of some of these techniques for calculating the elastic wave scattering from rough defects.

## 2.1 Theory of bulk wave propagation in elastic media

Bulk waves (or unbounded waves) are waves that are not contained by their surroundings, assuming that the medium through which they propagate is infinite. Because of this the host medium has no natural modes of vibration, however, waves with particular characteristics may propagate indefinitely

in a steady state.

Figure 2.1.1 shows an infinitesimally small cubic element with density $\rho$, and length $\partial x$, in a Cartesian coordinate system. When acted upon by external force this results in the propagation of stress $\sigma$, through the material.

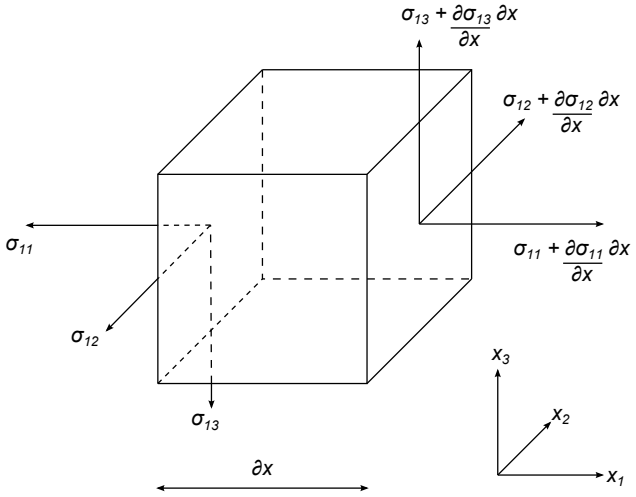


Figure 2.1.1: An infinitesimally small cubic element with density $\rho$, and length $\partial x$.

By applying Newton's II Law to the system a model for the displacement of an individual element, and therefore any neighbouring elements, is obtained. The equation of motion for this system is given by Equation 2.1.1.

$$\rho \frac{\partial^2 u_i}{\partial t^2} = \frac{\partial \sigma_{ij}}{\partial x_j} \tag{2.1.1}$$

This relates the particle displacement, $u$, to the stress field tensor acting on the surface $\sigma$. For an isotropic material the stress $\sigma$, and strain $\epsilon$, are linked by Hooke's law.

$$\sigma_{ij} = \lambda \delta_{ij} \epsilon_{kk} + 2\mu \epsilon_{ij} \tag{2.1.2}$$

where

$$\epsilon_{ij} = \frac{1}{2} \left( \frac{\partial u_i}{\partial x_j} + \frac{\partial u_j}{\partial x_i} \right) \tag{2.1.3}$$

The Lamé constants $\lambda$ and $\mu$, are constant material properties for the propagation medium. From Equation 2.1.1, Equation 2.1.2 and Equation 2.1.3, the Navier governing equation can be derived.

$$\rho\frac{\partial^2 u_i}{\partial t^2} = (\lambda+\mu)\frac{\partial}{\partial x_i}\frac{\partial u_j}{\partial x_j} + \mu\frac{\partial^2 u_i}{\partial x_j^2} \tag{2.1.4}$$

and in vectorial form becomes:

$$\rho\ddot{\mathbf{u}} = (\lambda+\mu)\nabla(\nabla\cdot\mathbf{u}) + \mu\nabla^2\mathbf{u} \tag{2.1.5}$$

From the Helmholtz decomposition the displacement vector $\mathbf{u}$, is linked to the compressional scalar potential $\phi$, and shear vector potential $\boldsymbol{\psi}$.

$$\mathbf{u} = \nabla\phi + \nabla\times\boldsymbol{\psi} \tag{2.1.6}$$

From Equation 2.1.5 and Equation 2.1.6, the Navier governing equation can be expressed in terms of $\phi$ and $\boldsymbol{\psi}$.

$$\nabla\left[(\lambda+2\mu)\nabla^2\phi - \rho\frac{\partial^2\phi}{\partial t^2}\right] + \nabla\times\left[\mu\nabla^2\boldsymbol{\psi} - \rho\frac{\partial^2\boldsymbol{\psi}}{\partial t^2}\right] = 0 \tag{2.1.7}$$

For an elastic solid both the Lamé constants are non-zero. Equation 2.1.7 can be satisfied if both terms are equal to zero and expressed in the form of Helmholtz differential equations.

$$\frac{\partial^2\phi}{\partial t^2} = \frac{(\lambda+2\mu)}{\rho}\nabla^2\phi \tag{2.1.8}$$

$$\frac{\partial^2\boldsymbol{\psi}}{\partial t^2} = \frac{\mu}{\rho}\nabla^2\boldsymbol{\psi} \tag{2.1.9}$$

From dimensional analysis of Equation 2.1.8 and Equation 2.1.9, it can be seen that $\frac{(\lambda+2\mu)}{\rho}$ and $\frac{\mu}{\rho}$ have dimensions of velocity squared. From inspection of these terms it can be seen that they represent the compression wave velocity $C_p$, and shear wave velocity $C_s$, respectively.

$$C_p = \sqrt{\frac{(\lambda+2\mu)}{\rho}} \tag{2.1.10}$$

$$C_s = \sqrt{\frac{\mu}{\rho}} \tag{2.1.11}$$

The Helmholtz differential equations (Equation 2.1.8 and Equation 2.1.9) have harmonic solutions and can be solved using the solutions for the compression and shear wave cases.

$$\phi = \Phi e^{i(\boldsymbol{k}_p\cdot\mathbf{r}-\omega t)} \tag{2.1.12}$$

$$\boldsymbol{\psi} = \Psi e^{i(\boldsymbol{k}_s \cdot \mathbf{r} - \omega t)} \tag{2.1.13}$$

The amplitudes of the compression and shear wave modes are given by the coefficients $\Phi$ and $\Psi$. The harmonic solutions are described by the vector notations for the compression and shear wavevectors $\boldsymbol{k}_p$ and $\boldsymbol{k}_s$, and the angular frequency $\omega$. These describe the variation of the solutions with respect to the displacement vector $\mathbf{r}$ and time $t$.

## 2.2 Analytical modelling

Analytical modelling techniques offer a means to describe ultrasonic wave propagation and scattering problems with relatively little computational expense. The complexity of the solution can often be simplified by making valid assumptions about the system, dependent upon the scenario in question.

The following section reviews four analytical mdoelling techniques that have commonly been used in the field of NDE. These include; the method of mathematical similarity, Geometrical Theory of Diffraction (GTD), Kirchhoff theory and the Born approximation.

### 2.2.1 Method of mathematical similarity

The method of mathematical similarity is specifically derived for the practical scenarios where the reflected ultrasonic amplitudes from two different defects can be directly compared. The technique is described by Ermolov [10], and Krautkramer [6], and has been used within the UK nuclear power generation industry prior to the implementation of more rigorous techniques.

The concept is to calculate the reflection coefficient from standard calibration targets used in NDE such as Side Drilled Holes (SDHs) and Flat Bottom Holes (FBHs), by determining the ratio of the target dimensions to the ultrasonic wavelength. The variation in the reflection coefficient can then be calculated as a function of target depth or size, acting as a baseline response against which the signal amplitude from a known defect or feature can then be compared. The predicted signal amplitude from a scattering target is given by Equation 2.2.1 [10].

$$\frac{V}{V_0} = K \frac{\lambda^2}{S} I e^{-2\delta r} \tag{2.2.1}$$

The amplitude of a reflected signal $V$, is expressed as the ratio with respect to the maximum possible signal amplitude obtained if all the incident energy is returned to the receiver, $V_0$. The magnitude of the response is expressed as a function of a transducer that has surface area $S$, and a material attenuation coefficient $\delta$. The form factor of the defect is given by $K$, and is specific to the defect geometry. The defect depth and the incident wavelength are given by $r$ and $\lambda$ respectively.

The variation in the signal amplitude of the incident wave as it propagates away from the transducer is given by $I$. In the near-field $I = 1$, while in the far-field $I$ is defined by Equation 2.2.2.

$$I = \left(\frac{2S}{\lambda r}\right)^2 \tag{2.2.2}$$

Despite being a simple approach, this does provide a useable estimate for relative signal amplitude from varying defect types as a function of size and position. Figure 2.2.1 shows the variation in signal amplitude from a 3 mm diameter SDH as a function of increasing depth, calculated using Equation 2.2.1. The depth of the SDH is varied from 10 mm to 60 mm in 5 mm increments for a normal incidence inspection. The simulated transducer used has an inspection frequency of 2.25 MHz and 0.5" diameter. The results are normalised against the response from a SDH deemed to be in the far-field of the transducer at 25 mm.

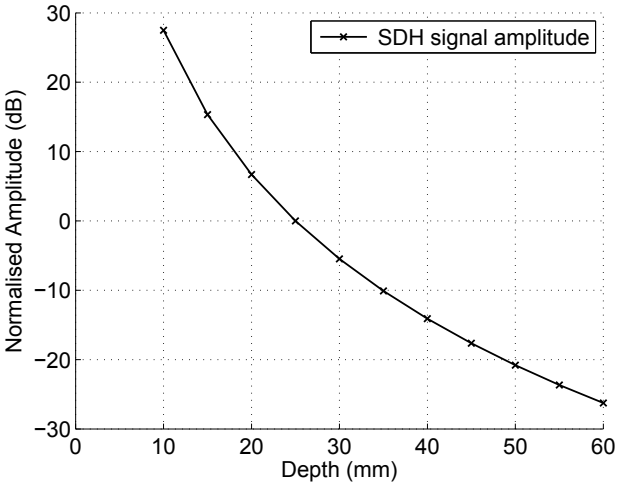


Figure 2.2.1: Method of mathematical similarity used to estimate the signal amplitude from SDHs with increasing depth for a normal incidence pulse-echo inspection.

This provides an estimate as to the predicted signal amplitude that may be obtained from a defect with a similar form factor and can therefore be used to aid in inspection design.

### 2.2.2 Kirchhoff theory

Kirchhoff theory is perhaps the most robust analytical technique and has been the tool of choice for modelling elastodynamic scattering problems for both simple geometrical scatterers [8, 11, 12, 13, 14], and complex geometrical scatterers [15, 16, 17, 18].

Kirchhoff theory provides an approximation for the scattered field on a defect surface in terms

of the incident field and plane wave reflection coefficients. Any point on the defect surface can be assumed to be a smooth reflector with a tangent equal to that of the local surface. The incident wave at that point is reflected in the specular direction with a reflection coefficient equal to that of the plane boundary. Physically this can be understood by assuming that the surface behaves like a mirror, reflecting ultrasound in a direction that is dictated by the local surface gradient as illustrated in Figure 2.2.2.

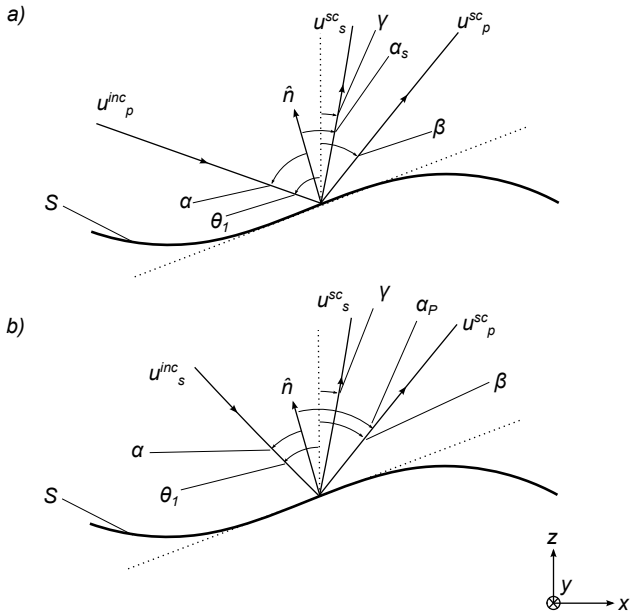


Figure 2.2.2: The definition of incident and scattering angles for a) an incident compression wave and b) an incident shear wave interacting with a surface.

By treating points on the surface as the superposition of a series of secondary sources, the scattered displacement in the far-field can be calculated using the frequency domain Green's theorem as given by Equation 2.2.3. The solution presented here is as discussed by Ogilvy [16].

$$u_k^{sc}(\mathbf{r}) = \int_S \left[\Sigma_{ijk}(\mathbf{r'} - \mathbf{r})u_i^{sc}(\mathbf{r'}) - G_{ik}(\mathbf{r'} - \mathbf{r})\sigma_{ij}^{sc}(\mathbf{r'})\right] \times n_j(\mathbf{r'})dS(\mathbf{r'}) \tag{2.2.3}$$

The $k^{th}$ component of the displacement field scattered from a defect $u_k^{sc}$, can be expressed in terms of an integral over the defect surface $S$, where $\Sigma_{ijk}$ and $G_{ik}$ are the stress and displacement fields respectively at $\mathbf{r'}$ due to a point source at $\mathbf{r}$, where $\mathbf{r'}$ and $\mathbf{r}$ are position vectors. Using Kirchhoff theory the scattered displacements $u_i^{sc}(\mathbf{r'})$, and stresses $\sigma_{ij}^{sc}(\mathbf{r'})$, on the defect surface can be approximated enabling the displacement field to be calculated.

For the two-dimensional case, with a compression wave incident on the defect surface, the components

of the displacement field in the $x$ and $y$ directions at the defect surface are given by Equation 2.2.4, Equation 2.2.5 and Equation 2.2.6.

$$u_x^{sc} = (R_{pp}\sin\beta + R_{ps}\cos\gamma)\, e^{ik_p(x'\sin\theta_1 - z'\cos\theta_1)} \tag{2.2.4}$$

$$u_y^{sc} = 0 \tag{2.2.5}$$

$$u_z^{sc} = (R_{pp}\cos\beta - R_{ps}\sin\gamma)\, e^{ik_p(x'\sin\theta_1 - z'\cos\theta_1)} \tag{2.2.6}$$

For an incident shear wave then these expressions are given by Equation 2.2.7, Equation 2.2.8 and Equation 2.2.9.

$$u_x^{sc} = (R_{ss}\cos\gamma + R_{sp}\sin\beta)\, e^{ik_s(x'\sin\theta_1 - z'\cos\theta_1)} \tag{2.2.7}$$

$$u_y^{sc} = 0 \tag{2.2.8}$$

$$u_z^{sc} = (-R_{ss}\sin\gamma + R_{sp}\cos\beta)\, e^{ik_s(x'\sin\theta_1 - z'\cos\theta_1)} \tag{2.2.9}$$

The scattering angles are dependent upon the normal to the local mean plane as defined in Figure 2.2.2. The plane boundary reflection coefficients are given by $R$, where the subscripts indicate either incident or reflected compression and shear wave modes.

$$R_{pp} = \frac{\sin(2\alpha)\sin(2\alpha_s) - \left(\frac{k_s}{k_p}\right)^2 \cos^2(2\alpha_s)}{\sin(2\alpha)\sin(2\alpha_s) + \left(\frac{k_s}{k_p}\right)^2 \cos^2(2\alpha_s)} \tag{2.2.10}$$

$$R_{ps} = \frac{2\frac{k_s}{k_p}\sin(2\alpha)\cos(2\alpha_s)}{\sin(2\alpha)\sin(2\alpha_s) + \left(\frac{k_s}{k_p}\right)^2 \cos^2(2\alpha_s)} \tag{2.2.11}$$

$$R_{ss} = \frac{\sin(2\alpha)\sin(2\alpha_p) - \left(\frac{k_s}{k_p}\right)^2 \cos^2(2\alpha)}{\sin(2\alpha)\sin(2\alpha_p) + \left(\frac{k_s}{k_p}\right)^2 \cos^2(2\alpha)} \tag{2.2.12}$$

$$R_{sp} = \frac{-\frac{k_s}{k_p}\sin(4\alpha)}{\sin(2\alpha)\sin(2\alpha_p) + \left(\frac{k_s}{k_p}\right)^2 \cos^2(2\alpha)} \tag{2.2.13}$$

The stress field at the defect surface for all instances is given by Equation 2.2.14.

$$\sigma^{sc}(\mathbf{r'}) = -\sigma^{inc}(\mathbf{r'}) \tag{2.2.14}$$

Due to the application of stress-free boundary conditions at the surface, the stress field due to an incident wave can be found by relating the stress and displacements using Hooke's law (Equation 2.1.2). Expressions for $u_i^{sc}(\mathbf{r'})$ and $\sigma_{ij}^{sc}(\mathbf{r'})$ can then be substituted into Equation 2.2.3 to provide a solution for the scattered field.

Bass and Fuks [19], derived the limitations of this approach stating that the deviation of the surface from flat (over a distance comparable to the incoming wavelength) must be small when compared to the wavelength of the incoming wave. This is quantitatively expressed by Equation 2.2.15.

$$ka\cos^3\theta_1 >> 1 \tag{2.2.15}$$

Qualitatively, a restriction is placed on the radius of curvature of the surface $a$, relative to the wavenumber of the incident wave $k$. Physically this means that the approximation becomes invalid at points where the surface profile rapidly changes, for instance at defect tips. There are no explicit restrictions on the height or gradient itself, although the height profile must be without rapid changes in gradient.

An example of the application of Kirchhoff theory in the UK nuclear power generation industry is given by Chapman [13]. This paper describes a model for the ultrasonic inspection of smooth planar cracks for a pulse-echo inspection. Kirchhoff theory is used to make predictions for the reflected signal amplitude from these defect types and results are given as a function of position and depth.

The response from smooth planar defects is of great interest to the nuclear power generation industry. Being able to identify their presence is vital in support of the nuclear safety case. Structural integrity assessments that are based on planar defect types must be supported with a method for reliable defect detection should they arise. Kirchhoff theory provides a reliable means to calculate the ultrasonic response from these defect types and is supported by a thorough history of validation.

### 2.2.3 Geometrical Theory of Diffraction

GTD is a well established technique that was originally developed for a wide range of applications in wave physics and optics [20, 21]. Diffracted rays that result from the interaction of an incident wave with an edge or corner have different properties to reflected or refracted waves that are generated at a change of medium or smooth boundary. To describe this scattering, diffracted wave fronts can be defined as a series of Huygens wavelets reconstructed with appropriate phase variation from the point of interaction.

Qualitatively, a beam incident on the edge of a defect will give rise to cones of diffracted wave modes emanating from the point where the incident wave strikes the surface. For instances where the incident beam strikes the edge at right angles, these cones become disks, whose axis is coincident with the local direction of the edge itself.

The technique was extended to ultrasonics for surface waves by Keller and Karal [22], and then towards elastic wave scattering by Achenbach *et al* [11, 23]. Figure 2.2.3 shows the definition of incident and diffracted rays according to GTD from a defect tip.

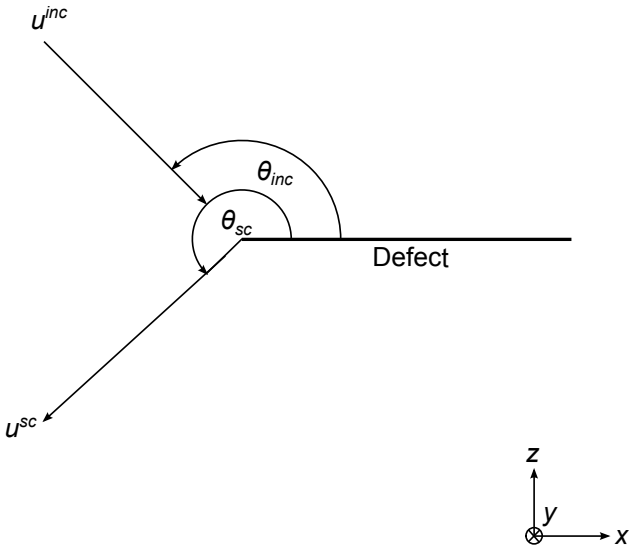


Figure 2.2.3: The definition of incident and diffracted rays according to GTD from a defect tip.

For the far filed amplitude of an incident wave $u^{inc}$, the far filed amplitude of the diffracted field $u^{sc}$ is expressed by Equation 2.2.16. The solution presented here is as discussed by Ogilvy and Temple [24], for ToFD applications.

$$u^{sc} = Du^{inc} r^{-\frac{1}{2}} e^{ikr} \tag{2.2.16}$$

The amplitude of the diffracted field is given in terms of the diffraction coefficient $D$, the distance from the source of the diffracted wave to the point of observation $r$, and the wavenumber $k$.

In these methods the Elastic Green's Theorem, is used to express the displacement due to the elastic wave at a point in the far-field. The wave potentials for the diffracted compression and shear wave modes are given by Equation 2.2.17 and Equation 2.2.18.

$$\begin{bmatrix} \phi_p \\ \phi_s \end{bmatrix} = \begin{bmatrix} D_p^p \\ D_s^p \end{bmatrix} \left( \frac{\lambda_p}{r} \right)^{\frac{1}{2}} e^{ik_p r} \tag{2.2.17}$$

$$\begin{bmatrix} \boldsymbol{\psi}_s \\ \boldsymbol{\psi}_p \end{bmatrix} = \begin{bmatrix} D_s^s \\ D_p^s \end{bmatrix} \left(\frac{\lambda_s}{r}\right)^{\frac{1}{2}} e^{ik_s r} \tag{2.2.18}$$

The diffracted compression waves from incident compression and shear wave modes are given by $\phi_p$ and $\phi_s$ respectively, and the diffracted shear waves from incident compression and shear wave modes are given by $\boldsymbol{\psi}_p$ and $\boldsymbol{\psi}_s$ respectively. The diffraction coefficients $D_p^p$, $D_s^p$, $D_s^s$ and $D_p^s$, corresponding to incident and scattered compression and shear waves, are given by Equation 2.2.19, Equation 2.2.20, Equation 2.2.21 and Equation 2.2.22.

$$D_p^p = e^{\frac{i\pi}{4}} \sin\frac{\theta_{inc}}{2} \left[\frac{A_{pp}^1 + A_{pp}^2}{2\pi B_{pp}^1 K^+(-k_p\cos\theta_{sc})K^+(-k_p\cos\theta_{inc})}\right] \tag{2.2.19}$$

where

$$A_{pp}^1 = \sin\frac{\theta_{sc}}{2}(2k_p^2\cos^2\theta_{inc} - k_s^2)(2k_p^2\cos^2\theta_{sc} - k_s^2)$$

$$A_{pp}^2 = 2k_p^3\cos\frac{\theta_{inc}}{2}\cos\theta_{inc}\sin 2\theta_{sc}(k_s - k_p\cos\theta_{sc})^{\frac{1}{2}}(k_s - k_p\cos\theta_{inc})^{\frac{1}{2}}$$

$$B_{pp}^1 = (k_s^2 - k_p^2)(\cos\theta_{sc} + \cos\theta_{inc})(k_0 - k_p\cos\theta_{sc})(k_0 - k_p\cos\theta_{inc})$$

$$D_s^p = e^{\frac{i\pi}{4}}\left(\frac{k_p}{k_s}\right)^{\frac{1}{2}} k_s^2 \sin\frac{\theta_{inc}}{2}\left[\frac{A_{ps}^1 - A_{ps}^2}{4\pi B_{ps}^1 K^+(-k_s\cos\theta_{sc})K^+(-k_p\cos\theta_{inc})}\right] \tag{2.2.20}$$

where

$$A_{ps}^1 = (2k_p)^{\frac{1}{2}}\sin 2\theta_{sc}(2k_p^2\cos^2\theta_{inc} - k_s^2)(k_p - k_s\cos\theta_{sc})^{\frac{1}{2}}$$

$$A_{ps}^2 = 4k_p^2(2k_s)^{\frac{1}{2}}\cos\frac{\theta_{inc}}{2}\cos\theta_{inc}\sin\frac{\theta_{sc}}{2}\cos 2\theta_{sc}(k_s - k_p\cos\theta_{inc})^{\frac{1}{2}}$$

$$B_{ps}^1 = (k_s^2 - k_p^2)(k_s\cos\theta_{sc} + k_p\cos\theta_{inc})(k_0 - k_s\cos\theta_{sc})(k_0 - k_p\cos\theta_{inc})$$

$$D_s^s = e^{\frac{i\pi}{4}} k_s^3 \sin\frac{\theta_{inc}}{2}\left[\frac{A_{ss}^1 + A_{ss}^2}{2\pi B_{ss}^1 K^+(-k_s\cos\theta_{sc})K^+(-k_s\cos\theta_{inc})}\right] \tag{2.2.21}$$

where

$$A^1_{ss} = k_s \cos 2\theta_{inc} \cos 2\theta_{sc} \sin \frac{\theta_{sc}}{2}$$

$$A^2_{ss} = 2 \cos \frac{\theta_{inc}}{2} \cos \theta_{inc} \sin 2\theta_{sc} (k_p - k_s \cos \theta_{sc})^{\frac{1}{2}} (k_p - k_s \cos \theta_{inc})^{\frac{1}{2}}$$

$$B^1_{ss} = (k_s^2 - k_p^2)(\cos \theta_{sc} + \cos \theta_{inc})(k_0 - k_s \cos \theta_{sc})(k_0 - k_s \cos \theta_{inc})$$

$$D^s_p = e^{\frac{i\pi}{4}} \left( \frac{k_s}{k_p} \right)^{\frac{1}{2}} k_s^2 \sin \frac{\theta_{inc}}{2} \left[ \frac{-A^1_{sp} + A^2_{sp}}{4\pi B^1_{sp} K^+(-k_p \cos \theta_{sc}) K^+(-k_s \cos \theta_{inc})} \right] \tag{2.2.22}$$

where

$$A^1_{sp} = (2k_s)^{\frac{1}{2}} k_p^2 \cos 2\beta_{inc} \sin 2\theta_{sc} (k_s - k_p \cos \theta_{sc})^{\frac{1}{2}}$$

$$A^2_{sp} = 4(2k_p)^{\frac{1}{2}} \cos \frac{\theta_{inc}}{2} \cos \theta_{inc} \sin \frac{\theta_{sc}}{2} (2k_p^2 \cos^2 \theta_{sc} - k_s^2)(k_p - k_s \cos \theta_{inc})^{\frac{1}{2}}$$

$$B^1_{sp} = (k_s^2 - k_p^2)(k_p \cos \theta_{sc} + k_s \cos \theta_{inc})(k_0 - k_p \cos \theta_{inc})(k_0 - k_s \cos \theta_{inc})$$

Equation 2.2.19, Equation 2.2.20, Equation 2.2.21 and Equation 2.2.22 are valid for the far-field limit. The wavenumber for the Rayleigh wave within the medium is given by $k_0$, and the function $K^+(\alpha)$ is given by Equation 2.2.23.

$$K^+(\alpha) = \exp \left[ \frac{-1}{\pi} \int_{k_p}^{k_s} \tan^{-1} \left( \frac{4x^2 (x^2 - k_p^2)^{\frac{1}{2}} (k_s^2 - x^2)^{\frac{1}{2}}}{(2x^2 - k_s^2)^2} \right) \frac{dx}{x \pm \alpha} \right] \tag{2.2.23}$$

Equation 2.2.23 can be evaluated numerically by setting $x$ equal to values within the range $k_p$ to $k_s$, and solved, for example using the Simpson's rule.

As an example, Figure 2.2.4 shows polar plots of the directivity pattern of the diffracted field obtained using the absolute values of the diffraction coefficients. The significance of displaying the directivity pattern is to provide an indication as to the relative magnitude of the scattered field across all scattering angles. Figure 2.2.4a) corresponds to $|D^p_p|$ for $\theta_{inc} = 30^o$ and Figure 2.2.4b) corresponds to $|D^s_s|$ for $\theta_{inc} = 140^o$.

a)

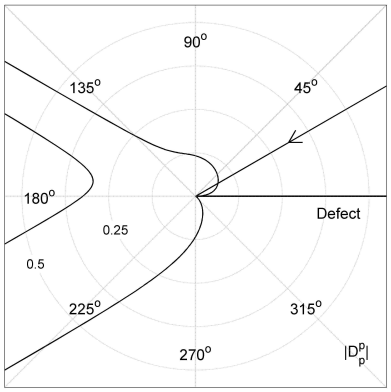


b)

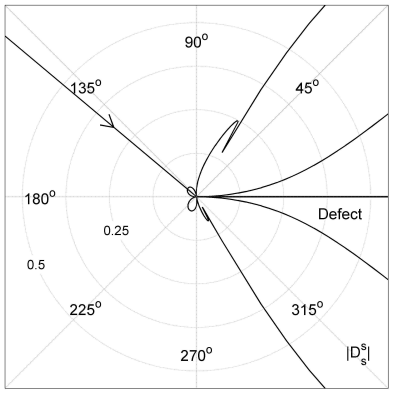


Figure 2.2.4: Figure to show the directivity pattern for a) an incident and scattered compression wave $|D_p^p|$ for $\theta_{inc} = 30^o$ and b) an incident and scattered shear wave $|D_s^s|$ for $\theta_{inc} = 140^o$.

This concept was extended and applied to the field of NDE by Chapman [25], who developed an integrated model capable of combining scattering predictions with local geometry. Ogilvy and Temple [24], have used these solutions for ToFD applications for the inspection of crack tips with reference made to the inspection of large forgings. The ToFD configuration is shown in Figure 2.2.5, where the magnitude of the incident and scattering angles are equal and defined by $\alpha$.

Using the diffraction coefficients along with the known inspection geometry the scattered field for a given type of defect can be calculated. This approach allows for the optimised design of NDE inspections. The same concept can be applied to optimising pulse-echo inspections where a single

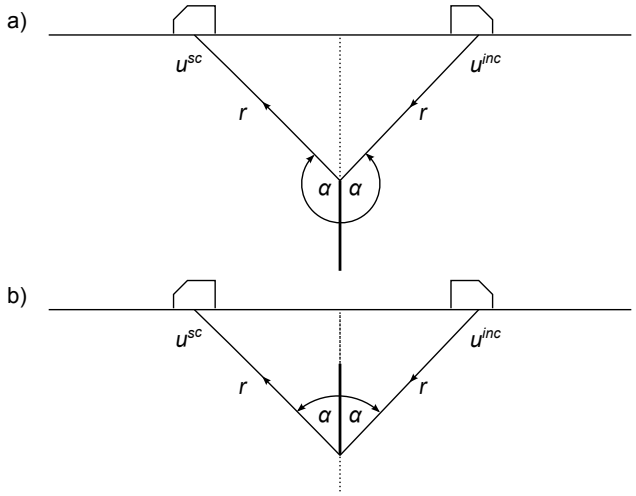


Figure 2.2.5: Illustration of ToFD configuration showing a transmitting transducer sending ultrasound towards a defect tip which is then scattered and detected by a transducer in reception for a) top tip diffraction and b) bottom tip diffraction, where the magnitude of the incident and scattering angles are equal and defined by $\alpha$.

transducer is used in transmission and reception.

The accuracy of the GTD solution has provided industry with the confidence to apply this technique throughout the UK nuclear power generation industry. However, the simplification of GTD to Equation 2.2.17 and Equation 2.2.18, has been derived for the smooth defect case. As a result, discrepancies may arise when this technique is applied to more complex defect geometry.

### 2.2.4 The Born approximation

Defects such as pores or small inclusions can sometimes manifest within power plant components, and from an ultrasonic perspective, their scattering behaviour is very different from that of a planar defect. For this reason a different approach is required to calculate the nature of ultrasonic scattered signals. In these instances the Born approximation can be used where the scattering can be considered to be a small perturbation to a much larger normal incident field.

The Born approximation was first developed for the field of quantum mechanics by Born and Wolf [26], but was later extended to elastodynamic scattering problems by Gubernatis *et al* [27, 28]. The technique is based on a boundary integral method where solutions to differential equations inside the elastic medium are converted into integral formulations of functions which are known at the boundary.

Figure 2.2.6 shows an incident wave $\mathbf{u}^{inc}$, propagating through an elastic medium with elastic stiffness constants $C_{ijkl}$, and density $\rho$. The incident wave then scatters from a finite inclusion of volume $R$ with

boundary $S$, within which the elastic stiffness constant is $C_{ijkl} + \delta C_{ijkl}$ and the density is $\rho + \delta\rho$, where $\delta C_{ijkl}$ and $\delta\rho$ are small so that the parent and inclusion have closely matching material properties.

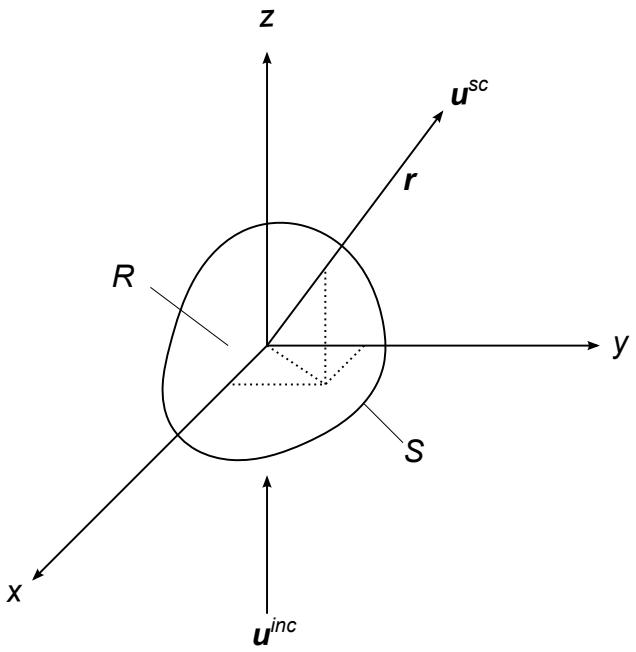


Figure 2.2.6: Scattering of a normal incident wave due to scatterer $R$ embedded in three-dimensional elastic space.

The total elastic field in the domain is given by the sum of the incident field and the scattered field combined.

$$\mathbf{u}^{tot} = \mathbf{u}^{inc} + \mathbf{u}^{sc} \tag{2.2.24}$$

The application of the Born approximation allows the scattered field to be expressed in the form of an integral equation and Equation 2.2.24 becomes:

$$\mathbf{u}^{tot}(\mathbf{r}) = \mathbf{u}^{inc}(\mathbf{r}) + \delta\rho\omega^2 \int_R g_{ij}(\mathbf{r} - \mathbf{r'}) u_j(\mathbf{r}) d\mathbf{r'} + \delta C_{ijkl} \int_R g_{ij,k}(\mathbf{r} - \mathbf{r'}) u_{l,m'}(\mathbf{r'}) d\mathbf{r'} \tag{2.2.25}$$

where the function $g_{ij}$ is the Green's function with spatial derivative $g_{ij,k}$ and $\mathbf{r'}$ is the position vector of points on surface $S$ and $\mathbf{r}$ is the position vector of a location in the far-field of the scatterer.

The scattered field is the sum of two terms involving the density and stiffness of the inclusion. However, to calculate the exact solution for the total field the displacement field inside the scattered

region must be known, which for an arbitrary shaped scatterer remains an unknown. The scattered fields are therefore replaced by an approximation such that Equation 2.2.25 becomes:

$$\mathbf{u}^{tot}(\mathbf{r}) = \mathbf{u}^{inc}(\mathbf{r}) + \frac{A_i e^{i\alpha \mathbf{r}}}{\mathbf{r}} + \frac{B_i e^{i\beta \mathbf{r}}}{\mathbf{r}} \tag{2.2.26}$$

where

$$\alpha^2 = \frac{\rho\omega^2}{\lambda + 2\mu}$$

$$\beta^2 = \frac{\rho\omega^2}{\mu}$$

and $A_i$ and $B_i$ are functions which are dependent upon approximate shape functions determined by the nature of the inclusion. This approximation replaces the exact solution of the field inside the sphere with the known incident field.

This approach is used extensively in NDE, with the derivation given by Gubernatis *et al* [27, 28], being specifically designed for this application. A review of ultrasonic NDE methods given by Thompson [29], introduces the use of analytical modelling techniques for nuclear power applications, of which the Born approximation is one. A more recent application of the Born approximation (although not specific towards the nuclear industry) is to understand grain scattering behaviour, as described by Yalda *et al* [30]. More recent work carried out by Nowers *et al* [31], considers the use of the Born approximation to calculate the scattering response from ellipsoidal grains in anisotropic austenitic stainless steel welds, with specific application towards use on primary circuit pipework.

## 2.3 Numerical modelling

This section discusses the mainstream methods that are commonly used in wavefield modelling. The objective of any numerical method is to present a means to solve a set of differential or integral equations that are either impractical or impossible to solve using an analytical approach. By creating a series of algebraic equations involving a finite number of unknowns a solution to the original problem can be approximated numerically.

A numerical solution to the wave equation for ultrasonic interactions provides a great deal of information about how stress waves propagate through a medium, offering solutions that extend beyond those possible in the analytical domain. For this reason numerical methods have become increasingly popular, especially within NDE since they provide a means to solve the propagation of stress waves for an infinitely variable range of complex cases.

Regarding ultrasonics, the scheme employed must transform the partial differential equations which

describe motion into a set of coupled ordinary differential equations for the equation of equilibrium [32].

$$[M]\,\ddot{\boldsymbol{u}} + [C]\,\dot{\boldsymbol{u}} + [K]\,\boldsymbol{u} = \mathbf{F} \tag{2.3.1}$$

The equation of equilibrium relates an external force vector $\mathbf{F}$, with a mass matrix $[M]$, a damping matrix $[C]$, and a stiffness matrix $[K]$. The acceleration $\ddot{\boldsymbol{u}}$, velocity $\dot{\boldsymbol{u}}$, and displacement $\boldsymbol{u}$, are determined by the Navier governing equation and the Helmholtz decomposition which expresses $\boldsymbol{u}$, in terms of compressional scalar potential $\phi$, and shear vector potential $\boldsymbol{\psi}$ (Equation 2.1.6).

There are four main schemes at the disposal of a numerical modeller, these are; the Boundary Element Method (BEM) [33], Finite Difference (FD) [34], Finite Volume Method (FVM) [35], and FE [32]. The tool of choice is primarily down to the field of application. The fundamental approach taken by each technique means that some assumptions are more suited to certain applications than others. But ultimately, the only practical requirement is that the solution should converge to an adequate level of accuracy.

Of interest for ultrasonic wave propagation is the introduction of time dependence to these systems. Implicit and explicit schemes will be discussed in more detail later in the section, but for the case of the explicit method the central difference operators will be referenced to describe the propagation of information, linking displacement $\boldsymbol{u}^t$, velocity $\dot{\boldsymbol{u}}^t$, and acceleration $\ddot{\boldsymbol{u}}^t$, at time $t$, for successive time increments $\Delta t$.

$$\dot{\boldsymbol{u}}^t = \frac{\boldsymbol{u}^{t+\Delta t} - \boldsymbol{u}^{t-\Delta t}}{2\Delta t} \tag{2.3.2}$$

$$\ddot{\boldsymbol{u}}^t = \frac{\boldsymbol{u}^{t+2\Delta t} - 2\boldsymbol{u}^t + \boldsymbol{u}^{t-2\Delta t}}{4\Delta t^2} \tag{2.3.3}$$

The following sections review each method for the general case and then look to draw relevance to ultrasonic NDE inspections of complex defect geometry. Finally the schemes are compared deducing the most suitable method for this project. Following the discussion of the main numerical methods, applications specific to rough surfaces are discussed in Section 2.5.

### 2.3.1 Boundary Element Method

The BEM solves a system using a surface integral approach; where FE, FD and FVM are domain methods, BEM is a boundary method. To build an understanding of how best to use BEM extensive descriptions of the theory are given by Achenbach [36], Brebbia [33], and Rose [7].

BEM is applicable to multiple disciplines and can be easily extended to ultrasonic NDE problems in the time and frequency domain [37]. BEM has been used to solve bulk and guided wave scattering

problems and is primarily used for instances where large propagation distances are involved [38].

The approach offers a means to solve the problem at a reduced number of spatial dimensions; for example a bound volume in three dimensions is discretised on its surface in two spatial dimensions. Elements are placed over the surface of the domain and over defects within the structure; the boundaries are therefore interfaces between regions of differing material properties. On each surface element the unknown variable is approximated by a Taylor expansion forming a basis function. Conceptually this means that the mesh is constructed over the modelled surface. Computation is therefore more efficient for systems with a small surface-volume ratio, offering a distinct advantage over other numerical domain methods.

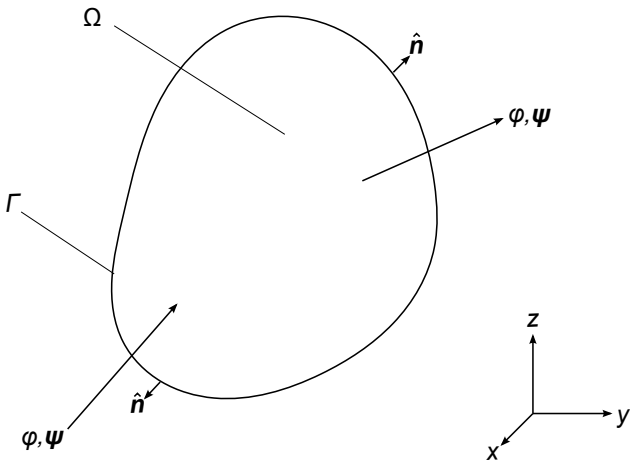


Figure 2.3.1: Propagation of wave potentials $\phi$ and $\boldsymbol{\psi}$ in elastic space $\Omega$, across boundary $S$ with surface normal $\hat{\mathbf{n}}$.

The BEM is applicable to problems for which Green's functions can be calculated in linear homogeneous media. Consider the reduction in spatial dimensions of domain $\Omega$ with volume integral $dV$, to boundary $\Gamma$ with surface integral $dS$, for a potential wave problem with harmonic wave solutions $\phi$ and $\boldsymbol{\psi}$, as shown in Figure 2.3.1.

Green presented three identities derived from the divergence theorem providing a solution to a boundary integral method [39, 40]. The first identity relates the volume and surface integrals for flux (in this instance wave potentials) passing though the domain.

$$\int\int\int_{\Omega}(\phi\nabla^2\boldsymbol{\psi}+\nabla\phi\cdot\nabla\boldsymbol{\psi})dV=\int\int_{\Gamma}\phi\frac{\partial\boldsymbol{\psi}}{\partial n}dS \tag{2.3.4}$$

It can then be shown that:

$$\int\int\int_{\Omega}(\phi\nabla^2\boldsymbol{\psi} - \boldsymbol{\psi}\nabla^2\phi)dV = \int\int_{\Gamma}(\phi\frac{\partial\boldsymbol{\psi}}{\partial n} - \boldsymbol{\psi}\frac{\partial\phi}{\partial n})dS \tag{2.3.5}$$

Using the fundamental solution of Laplace equation $\frac{1}{r}$, the final identity can be defined.

$$\phi = \frac{1}{4\pi}\int\int_{\Gamma}(\frac{1}{r}\frac{\partial\phi}{\partial n} - \phi\frac{\partial\frac{1}{r}}{\partial n})dS \tag{2.3.6}$$

Equation 2.3.6 is of a form which is used in current BEM for potential wave problems. This illustrates the restriction to a linear homogeneous medium, since a solution is only calculated for a medium which is completely uniform in all spatial dimensions. A trade-off for this limitation is that when considering an unbound domain the BEM automatically models the behaviour at infinity and therefore does not require specialised meshes to simulate these effects. Because of this, the surfaces must be closed and must separate regions where there is a change in material properties.

The choice of basis functions used to solve the system is limited to either a constant or linear function of triangular elements. Constant basis functions introduce approximately twice as many unknowns as the linear method, although it has not been demonstrated that this gives a solution that is twice as accurate [41]. A higher element density provides a more accurate representation of the shape, although this is at the expense of increased computation.

### 2.3.2 Finite Difference method

The FD method reduces the differential form of the wave equations into a discrete set of algebraic equations in which the displacements are defined at points on an intersecting grid. The partial derivatives within the wave equations are approximated by a Taylor expansion defined over the intersecting grid where the accuracy of the function depends upon the number of expansion terms taken.

For ultrasonic NDE applications the discrete set of algebraic equations used are often derived from the Navier governing equation in its second order form, as shown by Bond [42], and Harker [43].

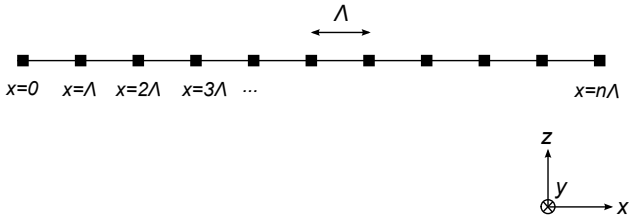


Figure 2.3.2: The derivatives of a function $u(x)$, are approximated at points along a one-dimensional grid with spacing $\Lambda$.

Figure 2.3.2 shows how a given function $u(x)$, can be defined along points of a one-dimensional grid

where displacement is confined to the $x$ direction. The points are separated by constant spacing $\Lambda$, and the displacement $u(x)$, at each point can be approximated using the Taylor expansion.

$$u(x+\Lambda) = u(x) + u'(x)\Lambda + O(\Lambda^2) \tag{2.3.7}$$

Rearranged, this gives the spatial derivative $u'(x)$, in terms of the function $u(x)$, and higher order terms which are deemed to be negligible $O(\Lambda^2)$.

$$u'(x) = \frac{u(x+\Lambda) - u(x)}{\Lambda} - O(\Lambda^2) \tag{2.3.8}$$

The term $O(\Lambda^2)$ represents a truncation error which is of the order of the grid spacing squared. These terms can be removed from the function to give the central difference quotient for the partial derivative $u'(x)$.

$$u'(x) \approx \frac{u(x+\Lambda) - u(x)}{\Lambda} \tag{2.3.9}$$

By applying the same logic to higher order differentials, the central difference quotients replace partial differential equations in the Navier governing equation to give a body node formulation that represents an approximate solution for $u(x)$ at discrete nodal points. This is then applied to the equation of equilibrium (Equation 2.3.1) presenting it in a means that can now be solved.

Reducing the mesh spacing will allow the FD method to converge to the correct solution. However, in the time dependent case, the time step must also be reduced in the same instance to avoid numerical instability. This ultimately will result in an increase in the computational cost of the model. Physically the restriction is that no energy may propagate to adjacent points on the grid faster than the critical time step.

Harumi *et al* [44], was the first to apply numerical modelling methods to NDE wave propagation problems. Following this, applications were made towards understanding impedance changes in materials and composites [42, 43, 45, 46]. In all of these cases FD was the tool of choice. This work begins to make the first steps in differentiating between theoretical predictions and experimental measurements, highlighting the fact that computer simulations can reveal wave properties within a solid which were previously unobtainable.

Perhaps the greatest limitation to the FD method is the difficulty in modelling stress-free boundaries. In order to achieve this a row of pseudo-nodes must be created and placed just outside the free boundary. The displacements of these nodes are altered to represent a solution that achieves a stress-free boundary [47]. This requires special surface node formulations to be developed which extend beyond the capabilities of generic commercial packages.

Despite the limited use of FD in ultrasonic NDE inspections, the method is much more suited to

applications involving geomechanics. An example of this is given by Lombard and Piraux [48], where a FD approach is used simulate the propagation of elastic waves in fractured rock. The success of the FD method to this field is attributed to the increased validity of FD assumptions for large wavelength, seismic, elastic wave propagation.

For greater understanding of the processes required to construct reliable FD models Smith [34], is an often referenced text providing detailed theoretical descriptions of the available methods.

### 2.3.3 Finite Volume Method

The FVM is a numerical modelling tool which uses discretisation to model a system where equations are written in their conservative form. The technique can be applied to complex geometries taking advantage of structured and unstructured meshing algorithms which split the domain into small discretised volumes. The algebraic equations under consideration are then integrated over each volume to obtain a set of equations in the form of surface integrals. The surface integrals are approximated at points on the surface and the unknowns are calculated. A complete set of algebraic equations are obtained by imposing continuity requirements for the surface integrals for every face separating adjacent elements.

The FVM technique is relatively young, and as a result, lacks the extensive literature that is available with other numerical methods. Eymard *et al* [35], provides a history of the major developments towards engineering problems from the early sixties to the latter part of the last century, including derivations for more generic applications.

Although FVM offers similar capabilities to other numerical methods it is perhaps more specialised in its application. Use in NDE is more suited to magnetic inspections [49], eddy-current inspections [50], and Thermography [51]. The FVM has been used for ultrasonic studies by Bolborici *et al* [52], however, its use is more suited to fluid media as demonstrated by Hsiao *et al* [53], and Vanhille *et al* [54].

A specific ultrasonic NDE application is given by Lhémery *et al* [55]. Here the FVM is used to model the ultrasonic field radiated by a transducer which is coupled to an irregular surface profile by a fluid medium such as water or couplant. This is of particular interest to the nuclear power generation industry where conformable membranes could be used to compensate for inspections over weld caps with irregular surface profiles.

FVM is based upon conservation whereby the method is locally conservative. A balance condition is written for each cell and a divergence term is used to obtain integral formulation of fluxes over the boundary. This feature makes the FVM attractive for modelling scenarios where the conservation of flux is a fundamental property of the system such as problems involving heat transfer, fluid mechanics and chemical reactions. This concept is illustrated in Figure 2.3.3.

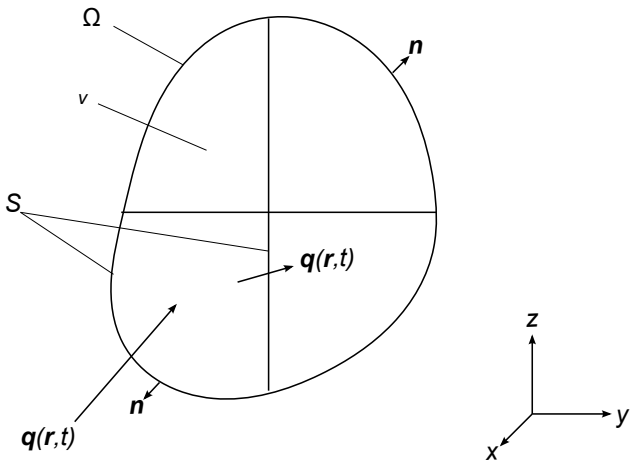


Figure 2.3.3: Spatial domain $\Omega$, is discretised into elements with volume $v$, boundary $S$, and surface normal $\mathbf{n}$, where the quantity $\mathbf{q}(\mathbf{r}, t)$ is conserved across each element boundary.

The FVM discretises conservation laws in space and time. A conserved quantity entering a cell must be accountable as it leaves the cell over a specified time step. These properties, alongside adequate stability approximations, give convergence to the FVM. The solution presented here is as discussed by Baumann and Oden [56].

In the general case, the local conservation of quantity $\mathbf{q}$ can be expressed by:

$$\frac{\partial \mathbf{q}}{\partial t} + \nabla \cdot \boldsymbol{F}\left(\mathbf{q}\right) = 0 \tag{2.3.10}$$

where vector $\mathbf{q}$ is a function of space and time $\mathbf{q}(\mathbf{r}, t)$, and is calculated for each position vector $\mathbf{r}$, and each time $t$. The space divergence operator $\nabla \cdot \boldsymbol{F}(\mathbf{q})$, represents the flux transport mechanism of $\mathbf{q}$ expressed as a possible volumetric change.

Space discretisation is achieved by introducing a mesh to the domain $\Omega$, consisting of elements with volume $v$, for which conservation laws are to be applied. The conservation law for the system is achieved by integrating Equation 2.3.10 over each element in the mesh.

$$\int_v \frac{\partial \mathbf{q}}{\partial t} dv + \int_v \nabla \cdot \boldsymbol{F}\left(\mathbf{q}\right) dv = 0 \tag{2.3.11}$$

Integration of the first term gives the volume average and the application of the divergence theorem to the second term gives:

$$v\frac{d\mathbf{q}}{dt} + \int_S \mathbf{F}(\mathbf{q}) \cdot \mathbf{n} dS = 0 \tag{2.3.12}$$

where $\mathbf{n}$ is the normal vector to the element at surface $S$.

The time discretisation of Equation 2.3.12 is performed by initiating a sequence beginning at $t = 0$ at increments $\Delta t$. The time step does not have to be constant although solving is more straightforward if it is. The system can be discretised by two means. Either a space-time finite volume discretisation where the conservation law is integrated over a time interval and a space control volume, or, a space finite volume discretisation with a time finite difference scheme which is only integrated in space and the time derivative is approximated by a finite difference scheme. Implicit and higher order schemes may also be employed.

The main limitation of the FVM is that it is often difficult to design systems that can give accurate precision, especially when higher order polynomials are required. The domain integrals given by Equation 2.3.12 can be shown to be of second order accuracy using the Taylor series expansion for any point on the surface $\alpha$, for a given function $f$.

$$\int f(x)dx = \int (f(\alpha) + (x-\alpha)f'(\alpha) + \frac{(x-\alpha)^2}{2!}f''(\alpha))dx \tag{2.3.13}$$

This can be simplified to give:

$$\int f(x)dx = f(\alpha)\int dx + f'(\alpha)\int (x-\alpha)dx + O \tag{2.3.14}$$

where $O$ denotes diminishing higher order terms. Equation 2.3.14 can then be simplified further giving:

$$\int f(x)dx = f(\alpha)\Delta x + O((\Delta x)^2) \tag{2.3.15}$$

It is the neglected higher order terms in the Taylor series that give rise to a truncation error which is of the order of the grid spacing squared. This is similar to FD, where both methods use a similar approach. The accuracy of the technique can be controlled by increasing the order of the numerical integration, effectively increasing the number of computation points on each face. However, this results in a trade-off with the stability of the solution. As the number of points is increased this can give rise to the lack of precision that is often associated with the FVM for ultrasonic NDE applications [35].

### 2.3.4 Finite Element method

The FE method reduces a problem with an infinite number of unknowns to one with a finite number of unknowns. This is achieved by dividing the system into elements and expressing each unknown field variable in terms of an assumed interpolation function within each element. Discrete nodal values are then used to express the continuous behaviour of each element.

Figure 2.3.4 shows a FE model of a body that is divided into elements of finite size connected to one another at nodal points situated at the boundary of each element. An external load is applied to one of

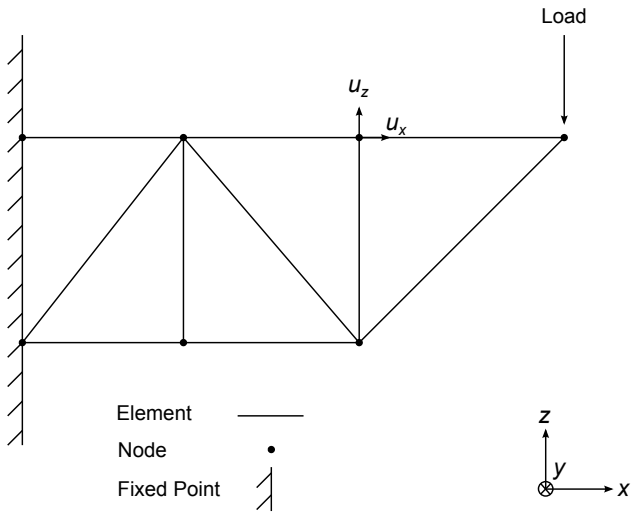


Figure 2.3.4: A discretised FE spatial domain.

the elements and the kinetic and potential strain energies are calculated for nodal point displacements, predicting the distribution of stress through the system. Energy is summed through all elements and generalised forces are calculated using virtual work. Lagrange's equations are then applied allowing differential equations of motion of the assembly to be obtained [57]. An overview of the method is given by Smith and Griffiths [58], MacDonald [59], and Fish and Belytschko [60], which give detailed introductions to the methodology behind the technique.

Of interest in this study is the ability to calculate the displacements of nodes within the system as a function of time using an explicit method. The central difference method can be applied to the equation of equilibrium (Equation 2.3.1), and the central difference operators linking displacement, velocity and acceleration (Equation 2.3.2 and Equation 2.3.3), to give an explicit solution to the FE method [32].

$$\left(\frac{[M]}{\Delta t^2} + \frac{[C]}{2\Delta t}\right)\mathbf{u}^{t+\Delta t} = \mathbf{F}^t - \left([K] - \frac{2[M]}{\Delta t^2}\right)\mathbf{u}^t - \left(\frac{[M]}{\Delta t^2} - \frac{[C]}{2\Delta t}\right)\mathbf{u}^{t-\Delta t} \tag{2.3.16}$$

Using Equation 2.3.16, it is possible to solve for $\mathbf{u}^{t+\Delta t}$, provided that $\mathbf{u}^t$ and $\mathbf{u}^{t-\Delta t}$ are known. If a diagonal mass matrix is employed and $[C]$ is set to zero, then the solution can be expressed as:

$$\left(\frac{[M]}{\Delta t^2}\right)\mathbf{u}^{t+\Delta t} = [R]^t \tag{2.3.17}$$

where

$$[R]^t = \mathbf{F}^t - \left([K] - \frac{2[M]}{\Delta t^2}\right)\mathbf{u}^t - \left(\frac{[M]}{\Delta t^2}\right)\mathbf{u}^{t-\Delta t} \tag{2.3.18}$$

Subsequent time steps can therefore be calculated using only matrix multiplications, as governed by Equation 2.3.19.

$$\mathbf{u}^{t+\Delta t} = [R]^t \left(\frac{\Delta t^2}{[M]}\right) \tag{2.3.19}$$

An assembly is created which represents the complete structure and all its constituent elements. This results in a global matrix equation which relates the forces and displacements of the whole structure. The solution to this equation for applied loads is used to calculate displacements at nodal points giving rise to the stresses and strains within each element. Other significant errors which arise from the approximation of the method can be reduced by refining the mesh. In BEM, FVM and FD this reduces the stability of the solution, which is not the case for FE, however, it does result in an increase in the number of degrees of freedom to be solved.

For ultrasonic scattering problems the refinement of the mesh can be defined in terms of nodes per wavelength $N$, of a propagating ultrasonic signal with wavelength $\lambda$, and mesh spacing $d$.

$$N = \frac{\lambda}{d} \tag{2.3.20}$$

FE offers various algorithms for analysis. The performance of these methods has been considered by Rebelo *et al* [61], for non-linear problems and by Sun *et al* [62], for quasi-static non-linear problems. The earliest bodies of work investigating the use of FE techniques for NDE applications (for example Smith [63]), consider the scattering effects that evolve from wave propagation problems. As with the other methods considered FE can be applied across a variety of fields, however, its success mainly lies in structural analysis.

FE capabilities can surpass those of analytical models, as demonstrated by Ludwig and Lord [64]. This work demonstrates the numerical modelling of ultrasonic wave propagation in elastic solids, applicable to NDE applications. It is apparent that interactions with boundaries of realistic defect shapes and geometries can be calculated with relative ease in comparison to analytical solutions based on the Cagniard-de Hoop formulation (an analytical method for solving seismic pulse problems). The two-dimensional codes developed clearly validated the analytical comparisons and provide proof-of-concept against which future numerical codes can be evaluated.

Modelling of this nature was the first to highlight to others the advantages that FE could offer. Following this some workers who previously used FD methods switched to FE techniques. Although FD schemes are faster and require less storage, FE schemes are more flexible, highly accurate and can model stress-free boundaries with ease.

### 2.3.5 Implicit and explicit schemes

Implicit and explicit schemes are used for numerical solutions to time dependent ordinary or partial differential equations which have been discretised in the time domain. This is achieved by using information at a given time period to calculate the solution for the next.

Implicit schemes assume that equilibrium will be achieved at a given time in the future. Subsequent displacements are obtained by solving simultaneous equations governing the system, to which there is no critical time step. Because of this the time step can be much larger than the explicit equivalent, however, the greatest limitation to this approach is that a matrix which is of the order of the number of displacements in the system must be inverted at each time step, which is computationally demanding.

Explicit schemes assume that the system is in equilibrium at the present time. This information, and the information at the previous time step, is then used to calculate the next. The major disadvantage of this method is that the process is only conditionally stable, where stability is defined as the requirement that the growth of an initial disturbance be bound. The restriction is that no energy may propagate through the mesh spacing in under the critical time step $t_c$, as detailed in Lax's equivalence theorem [34]. Explicit systems are governed by the central difference operator (Equation 2.3.2 and Equation 2.3.3), which describes the propagation of information, linking displacement, velocity and acceleration.

Simply put, the expressions are explicit because the process advances using known values from the previous time step. They enable numerical integration to be performed using the minimum of information and do not require a large matrix inversion provided that a diagonal mass matrix is employed. The limitation of only being able to use a diagonal mass matrix is not of importance since the accuracy of the solution can be improved for increasingly refined meshes; which for ultrasonic NDE problems is almost always the case.

Since the stability limit for an explicit operator is such that the maximum time increment $\Delta t$, must be less than a critical value $t_c$; the CFL condition is introduced, where the Courant number (or $CFL$) is given by Equation 2.3.21 [65].

$$CFL = \frac{\Delta t}{t_c} \tag{2.3.21}$$

Therefore, the time step $\Delta t$, is calculated using Equation 2.3.22, where $CFL$ is a number between 0 and 1.

$$\Delta t = CFL \times t_c \tag{2.3.22}$$

The CFL condition is necessary for convergence while solving certain partial differential equations numerically. The requirement of the condition is that the scheme must be able to access the information from the previous time step, in order to solve the next.

If a procedure requires an increasingly large number of time steps, implicit schemes are advantageous over explicit methods since they do not require as many time increments. However, the implicit method can require large matrix inversions, especially with three-dimensional models, which can drastically increases computational cost. Explicit techniques should be used for short transient problems that can overcome the disadvantages of implicit methods. The computational cost is approximately proportional to the size of the model and does not change dramatically unlike those for similar implicit approaches. The advantage of incrementing the solution temporally is that the computations are carried out using an incremental approach. This is still more efficient than using global mass and stiffness matrices (especially with a larger number of degrees of freedom) and removes the need to perform large matrix inversion.

### 2.3.6 Comparison of methods

For solving ultrasonic NDE wave propagation and scattering problems an approach is required that has the capability of modelling mode conversion and stress-free boundaries for complex geometries, whilst still being highly accurate and computationally efficient.

For the high accuracy required in ultrasonic NDE applications with complex defects the FE method is the most suitable technique. FVM and FD are limited by the Taylor expansion that is used to derive the solver and BEM results in a dramatic increase in computational cost as a trade-off for increased accuracy. The inaccuracies present in FE techniques are often a result of a lack of knowledge about the system itself, as opposed to approximations made in the governing equations.

The ease with which stress-free boundaries can be modelled is an important feature. All techniques are capable of achieving this but with varying degrees of difficulty. FE is the only technique that can model stress-free boundaries and mode conversion without the need for implementation of specialised algorithms. In FE, elastic mode conversion is also possible from complex geometries, which again is more difficult to implement with BEM, FVM and FD.

The computational demand of each solver varies and is dependent upon the technique and system being modelled. BEM is perhaps the most efficient if it is applied to scenarios where the surface-area to volume ratio is small, and also provides a solution for infinite space at no extra computational expense. Because FVM and FD share a similar approach in their derivation, the approximations require that both solvers are efficient in their use of computation memory. In comparison, FE can be considered to be relatively slow. Large amounts of memory are required and the computation time is proportional to the number of time steps to be solved. Parallel processing is therefore required to reach acceptable computation times, especially when using three-dimensional models.

The BEM, FVM and FD are the least suitable candidates for this project due to their relative lack of flexibility, accuracy and precision. Despite having some clear advantages, such as BEM being able to

model infinite elastic medium or FD and FVM faster computation time, this is ultimately outweighed by the flexibility of FE.

Detailed comparisons between the differences in FE and FD schemes are given by Blake [47], for wave propagation problems. The conclusions state that errors in wave displacement are less in FE schemes than in the equivalent FD scheme. However, the critical time step for two-dimensional elements is greater in FD schemes, allowing the system to advance more rapidly and thus require less computation. Similarly, Frehner *et al* [66], states the ability of FE to handle an unstructured mesh is more suitable for arbitrary scatterer geometry, which is required for modelling complex defects.

Many commercial FE codes are available with user friendly interfaces for pre and post-processing. The choice of software tools used for modelling is dependent on a variety of parameters. These are not only dependent on the system being modelled, but also the practicality and logistics of introducing solutions into an industrial context.

Within industry, significant importance is placed on the use of commercially available software packages to calculate numerical solutions as opposed to highly specialised algorithms. Commercial packages offer a thorough history of validation, technical support and their common place across multiple disciplines allows for the distribution of compatible data. There is therefore a strong case for the use of commercial FE codes to model ultrasonic wave scattering and propagation problems. As part of this project, delivering a solution that can be implemented using commercial software packages is therefore highly desirable, and forms a key aspect of ensuring successful technology transfer into industry.

## 2.4 Rough surfaces and geometry definition

The nature of rough surfaces mandates that a local coordinate system must be established that describes the surface profile of the defects and ultrasonic waves. The geometry definition outlined in Figure 2.4.1 has been chosen to remain consistent with the work of previous authors [9, 67].

A rough surface that extends in the $x$ and $y$ directions with a varying surface profile in $z$, can be described by Equation 2.4.1.

$$z = h(x, y) = h(\mathbf{r}) \tag{2.4.1}$$

where $\mathbf{r}$ is the position vector on the surface. The rough surface has a mean plane which is set at $z = 0$. The deviation of the surface from the mean plane is described by $h(\mathbf{r})$. The incident wave is defined by angle $\theta_1$, from the $z$ axis. The scattered wave is defined by angles $\theta_2$ and $\theta_3$.

The nature of a rough defect implies that no two are ever the same. Therefore, it is necessary to characterise defects by a set of common surface statistical parameters such that any rough defect

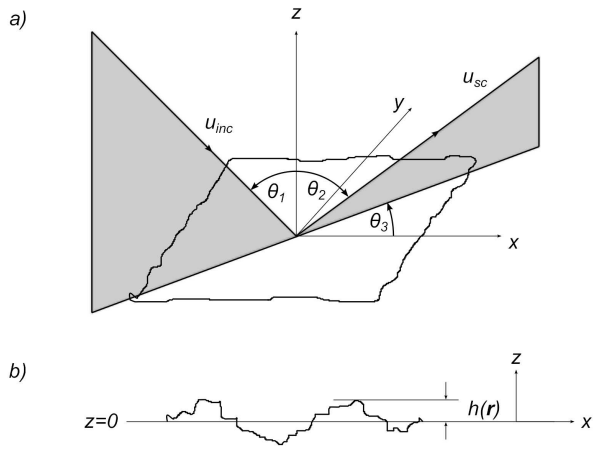


Figure 2.4.1: The definition of rough crack geometry for a) incident and scattered waves and b) cross section through a rough surface.

can be assigned to a statistical class of roughness. It is noted from experimental measurements that the variation in height of real rough surfaces typically follow a distribution that is close to Gaussian [68, 69], where the root-mean-square (rms) height of defect roughness $\sigma$, represents the variation in the surface profile from its mean plane.

The mean plane passing through the rough surface is defined by:

$$< h(\mathbf{r}) >= 0 \tag{2.4.2}$$

where the rms height $\sigma$, is defined by:

$$\sigma^2 =< h^2(\mathbf{r}) > \tag{2.4.3}$$

Because of Gaussian surface statistics, the surface height profile can be characterised by Equation 2.4.4.

$$p(h)dh = \frac{1}{\sigma\sqrt{2\pi}} \exp\left[-\frac{h^2}{2\sigma^2}\right] dh \tag{2.4.4}$$

This states that the probability of the surface being at a height between $h$ and $h + dh$ for a given surface rms is given by $p(h)dh$. A second parameter is required to describe the rate at which the surface height varies with distance along the crack. This can be characterised by use of a correlation function $C(\mathbf{R})$, as given by Equation 2.4.5.

$$C(\mathbf{R}) = \frac{< h(\mathbf{r})h(\mathbf{r}+\mathbf{R}) >}{\sigma^2} \tag{2.4.5}$$

The distance over which the correlation function falls by $\frac{1}{e}$ is called the correlation length $\lambda_0$. It is the correlation length that describes the variation in defect roughness along its length and can be considered to be acting in a perpendicular direction to $\sigma$.

As well as the rough surface geometry it is also necessary to define the nature of ultrasonic signals that scatter from a rough surface. When an incident wave scatters from the rough surface, two scattered signals are produced; the coherent signal and the diffuse signal. The coherent signal lies in the specular (or mirror like) direction whilst the diffuse field is scattered in multiple scattering directions and is the random aspect of the ultrasonic signal which is introduced by the random nature of the rough surface as shown in Figure 2.4.2.

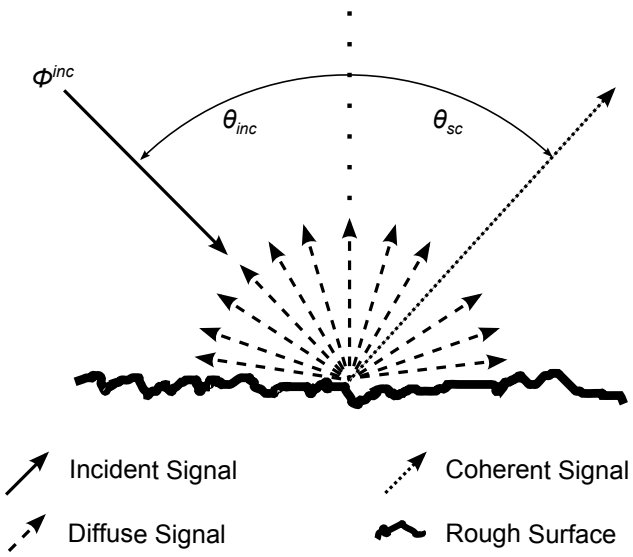


Figure 2.4.2: Figure to show the generation of coherent and diffuse scattered signals from a rough surface.

At this point, it is important to note that the total field that is measured in the specular direction will therefore contain contributions from both the coherent and diffuse fields combined.

## 2.5 Approaches for modelling scattering from rough surfaces

Defects which possess rough surfaces can greatly affect ultrasonic wave scattering behaviour and this is therefore an area of significant interest for a wide range of fields across physics and engineering.

Regarding NDE, the inspection of safety-critical components requires reliable defect detection and characterisation. Therefore, it is essential to understand and accurately calculate the influence of roughness on ultrasonic signal amplitudes.

Currently, predictions for rough defect response are generally made using an extension of analytical theories which have been applied to ultrasonic scattering problems for the purposes of NDE. Ogilvy [9, 67], provides an extensive literature review of the leading analytical techniques developed over the last century (pre 1987). Focus is primarily on ultrasonic applications for elastic and acoustic cases, although there are some discussions regarding solutions to electromagnetic problems. The following sub-sections will review the leading methods for calculating ultrasonic response from rough defects, using both analytical and numerical approaches.

### 2.5.1 Perturbation approach

The perturbation approach regards the rough surface as a perturbation to a smooth plane; whereby the change in scattering coefficient due to the presence of roughness can be expressed as an $n^{th}$ order infinite series [70].

$$\psi(\mathbf{r}) = \psi^{inc}(\mathbf{r}) + \sum_{n=0}^{\infty} \psi_n^{sc}(\mathbf{r}) \tag{2.5.1}$$

The measured field $\psi(\mathbf{r})$, is expressed as the sum of the incident wave $\psi^{inc}(\mathbf{r})$, and the $n^{th}$ order approximation to the scattered field $\psi_n^{sc}(\mathbf{r})$, where the $n = 0$ case describes a smooth plane. It is also assumed that the boundary conditions obeyed on the rough surface may be expanded in a Taylor series about the mean plane, $z = 0$. Because the scattered field is expressed in this manner, the technique carries limitations relating to the surface gradient. Firstly, the deviation of the surface from the smooth plane is small compared to the wavelength of the incident wave (Equation 2.5.2) and secondly, the gradient of the surface must be small in comparison to unity (Equation 2.5.3).

$$k|h| << 1 \tag{2.5.2}$$

$$|\nabla h| << 1 \tag{2.5.3}$$

Physically, these two limitations state that the surface profile is slowly varying without discontinuities, placing restrictions on the height and the surface gradient.

The validation of this technique has been provided by Gilbert and Knopoff [70], and Hudson *et al* [71]. The perturbation approach is applied to the scattering of seismic waves on two-dimensional triangular facets with a known profile. Reasonable agreement was found for cases with small height

variation and gradient, whilst increasing either variable caused a deviation from theoretical predictions. These findings are in-line with the limitations set by the perturbation approach.

The above case illustrates instances for which the profile of the scattering surface is known. Bass and Fuks [19], applied the perturbation approach to random surfaces where the explicit profile is not known, but rather, certain statistical properties describing the surface are. Due to the randomness of the surface the associated scattered field will also be random; as a result the governing equations are modified to include properties such as average field intensity for successive orders of a Taylor series.

Applications of this theory do not extend beyond the 2nd order expansion since higher order terms contribute little to the final result. Perturbation methods give an adequate level of approximation for surfaces for which they are valid, although they remain severely limited by surface height and gradient restrictions.

### 2.5.2 Kirchhoff theory

The application of Kirchhoff theory to defect scattering has already been discussed in Section 2.2.2. The theory provides an approximation for the scattered field on the defect surface which can then be passed into a Green's function to calculate the field displacement at a location in the far-field.

The flexibility of Kirchhoff theory has meant that it is easily extended towards more complex geometries, including the scattering from rough surfaces. Due to the difficulties associated with mode conversion, applications using acoustic waves have been more extensive [72, 73, 74]. However, application of Kirchhoff theory to ultrasonic scattering problems for the purposes of NDE have resulted in the development of the elastic solutions [15, 16, 17].

Unlike the Perturbation approach, Kirchhoff theory does not place restrictions on the height or on the gradient of the surface. Instead, the solution is only valid for situations where the deviation of the surface away from the mean plane is small over a distance comparable to the wavelength of the incident wave. A restriction is therefore placed on the rate of change of the surface gradient, there is no explicit restriction on the magnitude of the height or gradient itself. This limitation has already been discussed in Section 2.2.2 and is described by Equation 2.2.15 [19].

For rough defects, the limitations of Kirchhoff theory results in scattering phenomena that are not considered in the final solution. Despite being able to include elastic scattering, the generation of surface waves along the defect surface is not considered. This results in inaccuracies in the magnitude of the predicted signal amplitudes; however, these discrepancies are normally expected to be small. Surface shadowing effects (where part of the defect is obscured behind an adjacent section) are not considered. This will become more pronounced for instances where the incident angle relative to the local normal of the defect is increased. Finally, it is assumed that once the incident field has scattered from the defect surface, it will propagate through infinite elastic space. This means that multiple

scattering events, whereby a scattered signal interacts with the defect multiple times, are also not considered.

The use of a surface integral in Kirchhoff theory sets a requirement that the scattering surface $S$, must be closed. If the scattering surface does not bound a finite volume, such as a rough back-wall, then the surface must be closed with the aid of a closing boundary positioned at infinity. It is therefore necessary to split the bounding surface into the scattering surface $S_R$, and the closing surface $S_C$, as shown in Figure 2.5.1.

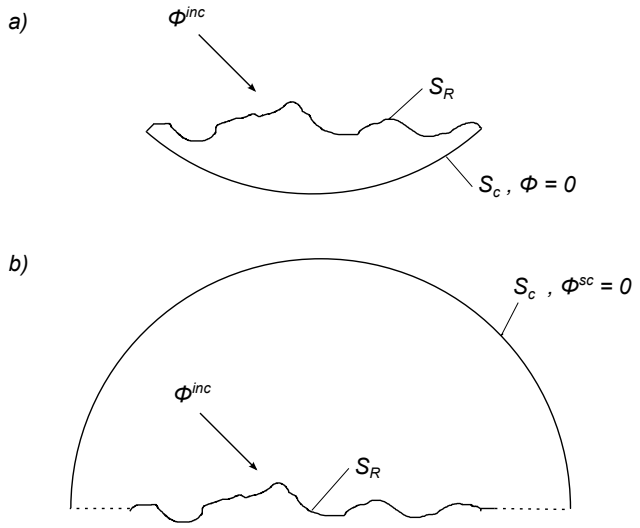


Figure 2.5.1: Figure to show the closure of a rough surface to allow for a surface integration of the scattered field for a) a bound finite volume and b) a back-wall.

Closing the path for the surface integral will result in a mathematical remnant that is responsible for the scattering at defect edges. For the case where a bound finite volume is used, this remnant of the scattered signal can be likened to the scattering from defect tips. Despite this being represented mathematically in this expression, the scattered field obtained at this location is not representative of tip diffracted signals. This places a limit on the use of Kirchhoff theory for cases where the size of the scattering surface $S_R$, approaches the size of the incident wavelength.

Ogilvy quantified inaccuracies in Kirchhoff theory by comparing the scattering coefficients for smooth surfaces to those obtained using the variational approach for the acoustic case [15]. The results indicate that general angular variations are consistent with one another, with the greatest amplitude found in the specular direction. For a smooth defect, Kirchhoff theory gives identical scattering amplitude for the specular direction (Equation 2.5.4) and the back-scattered direction (Equation 2.5.5).

$$\theta_1 = \theta_2 \tag{2.5.4}$$

$$\theta_1 = -\theta_2 \tag{2.5.5}$$

Away from these directions Kirchhoff theory generally underestimates the scattered response when the scattering angle is between the back-scattering and specular directions (Equation 2.5.6).

$$-|\theta_1| < \theta_2 < |\theta_1| \tag{2.5.6}$$

For scattering angles outside of this range, Kirchhoff theory will generally overestimate the response. For rough defects, the accuracy of Kirchhoff theory decreases as roughness is increased. Although these findings are applied to the acoustic case there is no inherent reason why the same method cannot be applied to the treatment of elastic wave scattering.

The application of Kirchhoff theory to this problem by Ogilvy [16], has resulted in the derivation of a single expression for the reduction in coherent ultrasonic signal amplitude due to increasing defect roughness.

$$\frac{|\phi^{\sigma}_{coh}|}{|\phi^{\sigma=0}_{coh}|} = \exp\left[-\left(k_{inc}\cos\theta_{inc} + k_{sc}\cos\theta_{sc}\right)^2 \frac{\sigma^2}{2}\right] \tag{2.5.7}$$

The magnitude of coherent signal $|\phi^{\sigma}_{coh}|$, is a function of $\sigma$, and the wavenumbers of the incident and scattered signals $k_{inc}$ and $k_{sc}$ in directions $\theta_{inc}$ and $\theta_{sc}$ respectively. The coherent signal is normalised against $|\phi^{\sigma=0}_{coh}|$, the magnitude of the reflected signal from a smooth surface. Equation 2.5.7 does not include an expression for tip diffracted signals and applies to cases where the beam spread is less than the extent of the defect.

The expression given by Equation 2.5.7 represents the coherent signal only and has formed the basis for calculating attenuation in ultrasonic scattered signals due to roughness in the UK nuclear power generation industry. It is not possible to calculate an exact expression for the diffuse field due to its incoherent nature. However, an approximate calculation that takes the average field intensity into account is used to give an order of magnitude estimate [16].

For a normally incident wave, Figure 2.5.2 shows the predicted amplitudes of the coherent and diffuse signals due to increasing roughness expressed as a function of the incident wavelength $\lambda_{inc}$ as calculated by Ogilvy [16].

The amplitude of the reflected field given by Equation 2.5.7 is not sensitive to the correlation length $\lambda_0$. Equation 2.5.7 is applicable to scenarios where the correlation length is such that the profile of the rough surface remains ergodic, and must therefore be small in comparison to the extent of the

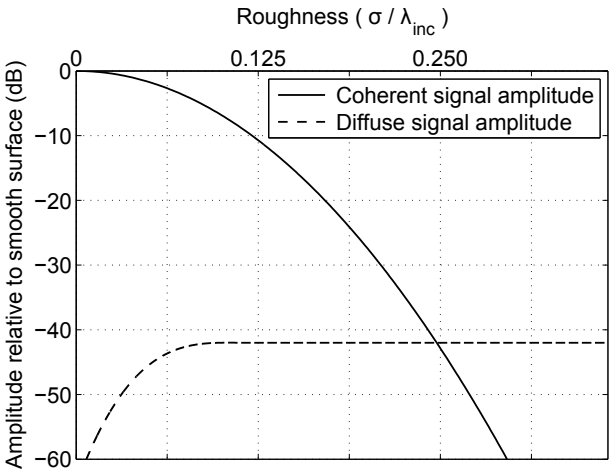


Figure 2.5.2: Coherent and diffuse signal amplitudes predicted by Kirchhoff theory for compression and shear wave modes.

surface. The analysis presented in Figure 2.5.2 assumes an infinite rough surface making the results independent of the correlation length. For the purpose of NDE, finite sized defects with rough surfaces by their very nature will be ergodic, making the independence of correlation length a valid assumption for this application.

The software package TRANGLE, based upon Kirchhoff theory, provides an estimate for the elastic wave scattering from rough surfaces for the purposes of NDE, and has had successful application in the power generation industry [75]. The model represents a specific known rough surface by a series of triangular facets and then predicts the scattered field for a particular inspection geometry.

The model is validated against experimental data for which there is good agreement, although it is noted that predictions tend to be higher amplitude than experimental measurements. The model is most accurate for normal incidence and has been validated for furrowed surfaces and embedded defects. At increased angles of incidence the predictions diverge from experimental measurements since the model fails to account for finer scales of roughness. Fine-scale roughness can be approximated by the use of an attenuation factor $\alpha$, potentially accounting for the discrepancies [75].

$$\alpha = e^{-2\sigma^2 k^2 \cos^2 \theta_1} \tag{2.5.8}$$

The application of this attenuation factor does account for the discrepancies observed; however, this only applies to the coherent component of the reflected signal and the value of $\sigma$ must be estimated. Although this approach can be seen to give good agreement, it is fair to assess that application is limited by the approximation of the Kirchhoff theory. Deviations away from regions where the approximations

are valid results in unquantifiable discrepancies between predicted and measured results.

### 2.5.3 Rayleigh method

The Rayleigh method states that for a normally incident wave, the scattered field can be written as the sum of plane waves traveling away from the rough surface [76]. The theory was initially developed for the interaction of a plane wave with wavevector $\mathbf{k}$, incident at angle $\theta_1$ to the surface normal, scattering from a sinusoidal surface defined:

$$h(x) = \sigma \cos(Kx) \tag{2.5.9}$$

where the surface profile variation is defined by $K$.

The sinusoidal surface behaves in a similar manner to a diffraction grating with the scattered field prominent at a series of lobes $m$, at specific scattering angles $\theta_m$.

$$\sin(\theta_m) = \sin(\theta_1) - \frac{mK}{k} \tag{2.5.10}$$

The scattered field $\psi^{sc}$, can therefore be defined as the sum of plane waves leaving the surface as given by Equation 2.5.11.

$$\psi^{sc}(\mathbf{r}) = \psi^{inc}(\mathbf{r}) + \sum_{m=-\infty}^{\infty} A_m e^{i\mathbf{k}_m \cdot \mathbf{r}} \tag{2.5.11}$$

The Rayleigh method has one main advantage over Kirchhoff theory: there is no restriction on the radius of curvature of the surface being analysed. The main assumption made by the Rayleigh method is that the scattered field is composed of waves travelling away from the surface, therefore multiple scattering events are not considered. Surfaces defined by rapid changes in surface profile that are not suitable for Kirchhoff theory, can therefore be analysed using the Rayleigh approach.

### 2.5.4 Finite Elements

Within recent years FE codes have been used increasingly to simulate elastic wave propagation and scattering problems. Analytical solutions to these interactions are often impossible or impractical to solve, whereas numerical techniques offer solutions that extend to any desired level of complexity. Two advances have led to the success of the numerical approach. Firstly, low cost computing capability is now readily available and secondly, the FE approach is well established in commercial packages that are able to model the ultrasonic response from simple scatterers such as SDHs, FBHs and smooth cracks [63, 64, 77, 78].

The efficiency of FE modelling techniques can be improved by making use of domain linking algorithms. These allow modellers to only consider a small area immediately surrounding a defect or feature of interest [79, 80, 81, 82]. By using this method, computational resource can be focused on a highly accurate representation of the scatterer, as opposed to solving wave propagation problems. This is particularly advantageous when considering three-dimensional problems where even a significantly reduced spatial domain can consist of tens of millions of degrees of freedom to be solved.

Based on the success of these methods extensions to complex defect geometries have been made by Zhang *et al* [18] and Velichko *et al* [81]. The scattered field from a rough defect is calculated using a frequency domain FE model with a spatial domain that immediately surrounds the defect. The scattered field is then presented in the form of a scattering matrix $S(f, \theta_{inc}, \theta_{sc})$, describing the far-field scattering coefficient for all possible combinations of frequency, incident and scattering directions.

$$u^{sc}(r, f, \theta_{inc}, \theta_{sc}) = S(f, \theta_{inc}, \theta_{sc}) u^{inc} \frac{\lambda}{r} e^{ikr} \tag{2.5.12}$$

The far-field scattered signal $u^{sc}$, is a function of the distance from the centre of the scatterer $r$, the excitation frequency $f$, and the incident and scattering angles $\theta_{inc}$ and $\theta_{sc}$.

The results of that study show good agreement between the scattering amplitudes obtained using FE and those calculated using Kirchhoff theory. The study concludes that the surface roughness and correlation length of the defect will have an influence over the nature of the scattering matrix, confirming the findings of current analytical approaches.

The findings of this work have helped to confirm a valid range of defect roughness for which Kirchhoff theory methods can be applied. This is an important finding since the savings in computational time associated with a Kirchhoff theory solution far outweight a FE based approach (despite the advances in efficiency). Furthermore, this helps to validate the use of FE methods to solve scattering problems of this nature, increasing the confidence in the use of these techniques.

### 2.5.5 Discrete Point Source Method

The Discrete Point Source Method (DPSM) is a semi-analytical technique based upon Huygens' principle [83]. The field intensity from a source on a given target can be expressed by taking into account attenuation and geometric spreading.

$$p_m(r) = A_m \frac{e^{ik_f r_m}}{\sqrt{r_m}} \tag{2.5.13}$$

DPSM calculates the pressure $p$, at point $m$, where $r_m$ is the distance between point source and target, $A_m$ is the point source amplitude for a wave at frequency $f$ and wavenumber $k_f$. Point and target sources are placed immediately outside boundaries and interfaces, thereby removing the need

for a complete mesh of the spatial domain. This provides a great deal of flexibility over conventional numerical techniques, and as a result, reduces computation times.

This technique has been adopted for purposes in NDE by Cegla *et al* [84, 85]. The model predicts the scatter from inner surface breaking defects and rough back-walls for the acoustic case; showing good agreement with experimental and numerical models. This is achieved by applying targets to the crack surface with stress-free boundary conditions and approximating them as passive sources with zero pressure. Equation 2.5.13 is extended to include a series of point sources simulating the transducer $N$, interacting with a series of targets defining the crack and back-wall $M$.

$$P_T = Q_{TS}A_S + Q_{TI}A_I \tag{2.5.14}$$

The pressure at a target $P_T$, is expressed as the sum of the incident field from the source and the reflected field from the defect. This is achieved through a propagation matrix going from source $S$, to target $T$, $Q_{TS}$ (and vice versa), multiplied by the amplitudes at the source $A_S$, and defect $A_I$.

To date, the application of this technique to defect roughness has considered acoustic normal incidence cases in two and three-dimensions. Good agreement has been obtained with FE modelling techniques with drastic improvements in computational run times. The flexibility of the method means that it can be easily adapted to scenarios of increasing complexity, however to maintain good agreement with numerical methods, the solution may need to be adapted to include mechanisms such as elastic mode conversion.

## 2.6 Conclusions

This chapter has provided the theoretical background required for this thesis. The derivation of ultrasonic wave propagation from first principles has been discussed, with focus on the propagation of bulk waves in elastic space. The relationships between displacement, stress and wave potentials are derived and expressed as functions of known material constants.

A literature review of analytical modelling techniques specific to ultrasonic NDE propagation and scattering problems has been provided. The techniques discussed are used to understand the scattering behaviour from smooth simple targets to aid in the design of NDE inspections. Due to the assumptions made with analytical methods, different techniques have to be applied to different inspection scenarios. The techniques considered are qualitatively described with the governing equations given for generic cases. The limitations of each technique are discussed, along with evidence to support their use in the field of NDE.

Numerical modelling techniques which have been applied to ultrasonic propagation and scattering problems are discussed. Four numerical techniques are discussed along with the differences between

implicit and explicit solvers, specifically focusing on computational requirements and stability. The section concludes with a comparison between the solvers.

A discussion of ultrasonic scattering from rough surfaces is given. This section reviews the work of previous authors and the use of numerical and analytical modelling techniques to solve the scattering problem. An important definition of the local geometry is made for incident and scattering waves interacting with rough surfaces. A detailed description of how modelling techniques are specialised to calculating the scattering from rough surfaces is given.

For ultrasonic NDE applications in the nuclear industry Kirchhoff theory has often been the tool of choice for both smooth and rough defects. GTD is also widely used, but this is more applicable to tip diffraction scattering. The introduction of numerical methods, particularly FE, has shown how the limitations that exist with these analytical methods can be overcome, providing the focus and motivation for this thesis.

# 3 Absorbing Boundary Methods

Commercial FE codes have been identified as an accurate and viable means to calculate the ultrasonic response from rough defect types for NDE applications in the nuclear power generation industry. However, the accuracy of the FE solution comes at the expense of two undesirable qualities.

Firstly, FE methods result in increased computational cost compared to current calculation methods used in industry, both in the form of compilation time and accessible memory. If ultrasonic NDE FE methods are to become a viable tool for use in industry, it is vital that the computational burden be reduced to an acceptable level. Secondly, FE models do not offer an embedded means to simulate infinite elastic space. This is an essential requirement since it is often the case that the scattered response from a defect needs to be considered in isolation, without the influence of any other scattering boundaries.

Absorbing boundary methods go part way to solving both of these problems. Boundary conditions are applied to the FE models that simulate unbound isotropic media and therefore simulate infinite elastic space within a significantly reduced finite sized domain. However, the addition of an absorbing boundary will inevitably result in some form of increase to the computational expense of the model, and furthermore, the boundary conditions applied are not always perfect. The greatest limitation when using absorbing boundary methods is the generation of unwanted reflections that are produced by the absorbing boundary itself. These reflections manifest themselves as additional remnants in ultrasonic signals.

The removal of unwanted reflections has proven to be a challenging problem, becoming a research topic within its own right. This has lead to the development of techniques such as Infinite Elements, Non-Reflecting Boundary Conditions (NRBC) and absorbing layer techniques. This chapter therefore addresses the role of absorbing boundary methods and their importance towards making commercial FE codes a viable tool for use in industrial NDE applications.

There is no single text that reviews the subject in its entirety; there is however literature on specific subject areas. For details on Infinite Elements an extensive review is given by Bettess [86], covering derivation and implementation of the method. The description of NRBC varies with many different methods being developed specific to their respective fields. However, the first example of a successful implementation is provided by Givoli *et al* [87], where a frequency domain solution for a perfect non-reflecting boundary is given. For elastodynamic wave problems there are four successful absorbing layer

techniques; Perfectly Matched Layers (PML) [88], Absorbing Layers by Increasing Damping (ALID) [89], Caughey Absorbing Layer Method (CALM) [90], and Stiffness Reduction Method (SRM) [91]. A comparisons of ALID and PML is given by Rajagopal *et al* [92], which also includes discussion of the other methods identified here.

The SRM is a new technique specifically developed by the author for the requirements of this project which provides a substantially improved performance over previous methods of this kind. This chapter includes the derivation, implementation and validation of this method and relates its applicability towards the requirement of an industrially viable solver.

Following this, generic rules are established to produce a good performing absorbing boundary for almost all FE models considered. However, for instances where it is desirable to significantly reduce the size of the spatial domain (such as three-dimensional models), a highly specialised absorbing boundary is required. This can be achieved through the use of optimisation functions, which can find the optimum input variables, that meet a given condition for a specific FE model. Finally, the chapter discusses a hybrid absorbing layer, where the SRM and Infinite Elements techniques are combined.

From this chapter, the author's own contributions to the field of absorbing boundary research are primarily focused upon the development and implementation of the SRM [91, 93]. This work identifies the need for a new absorbing boundary method and makes comparisons with the more conventional ALID approach. Following the development of the SRM, a methodology for implementing a highly specialised absorbing boundary was established [94]. This method makes use of optimisation algorithms that calculate specific values for the absorbing layer properties, achieving exceptional levels of performance, but this is only realised for a very specific application. This approach helps to make three-dimensional numerical models a viable and accessible tool for use in industry.

## 3.1 Review of methods

When using absorbing boundary methods, there is a requirement that the propagation and interaction of an ultrasonic wave with a scatterer be completely isolated from all unwanted geometrical features that do not represent the system being modelled.

The removal of unwanted reflections has proven to be a challenging problem, becoming a research topic within its own right. The simplest technique has been to increase the geometric size of models, isolating unwanted reflections in time from those of the desired response. This approach has unrealistic implications requiring unnecessarily large simulations and reducing computational efficiency. More innovative techniques have been developed which can be collated into the three categories: Infinite Elements, NRBC and absorbing layer methods.

### 3.1.1 Infinite Elements

Infinite Element methods use a type of element with properties that simulate infinite space [86]. The Infinite Element operates within a single row of elements positioned outside the Area of Study (AoS), meaning that they contribute the minimum in computational expense. Furthermore, Infinite Elements are common in commercial FE packages and do not limit the flexibility of the solver.

For a boundary that contains only Infinite Elements, instead of the stress-free boundary conditions, Lysmer *et al* [95, 96] states that the normal and tangential components of the stress at the model boundaries are given by:

$$\sigma_{xx} = a\rho C_p \frac{\partial u_x}{\partial t} \tag{3.1.1}$$

$$\sigma_{xy} = b\rho C_s \frac{\partial u_y}{\partial t} \tag{3.1.2}$$

where $a$ and $b$ are dimensionless parameters which when varied alter the performance of the boundary. The proposed boundary conditions correspond to a situation where the boundary is supported on infinitesimal dash-pots oriented normal and tangential to the boundary, as shown in Figure 3.1.1. Here, the definition of the incident and scattering angles are relative to the surface, not the surface normal. This has been done to remain consistent with the work of previous authors [95, 96].

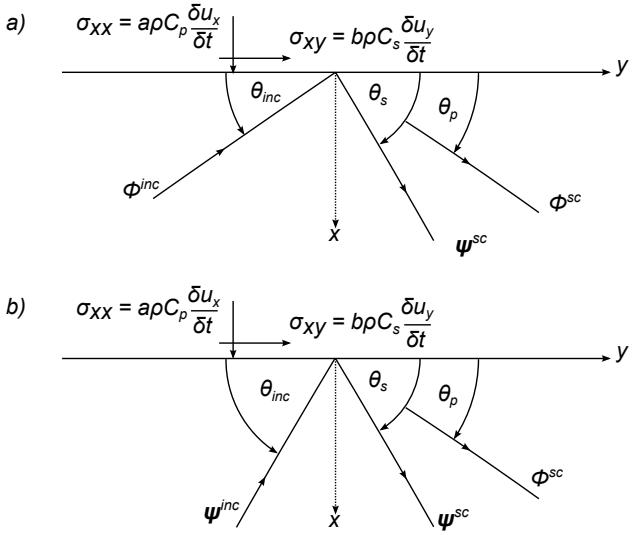


Figure 3.1.1: Figure to show the application of normal and tangential components of stress tensor for a row of Infinite Elements for a) an incident compression wave and b) an incident shear wave.

By applying these conditions to the wave equation and using standard harmonic solutions from the Helmholtz decomposition, the amplitudes of the reflected compression and shear wave modes $A$ and $B$, can be calculated.

$$A = a_3/a_2 - (a/a_2)B \tag{3.1.3}$$

$$B = \frac{b_3/b_2 - a_3/a_2}{s(b_1/b_2 - a_1/a_2)} \tag{3.1.4}$$

where

$$a_1 = \sin 2\theta_s + a\cos\theta_p \tag{3.1.5}$$

$$a_2 = 1 - 2\beta\cos\theta_p\cos\theta_p + a\sin\theta_p \tag{3.1.6}$$

$$a_3 = 2\beta\cos\theta_p\cos\theta_p + a\sin\theta_p - 1 \tag{3.1.7}$$

$$b_1 = \cos 2\theta_s - b\sin\theta_s \tag{3.1.8}$$

$$b_2 = \beta\sin 2\theta_p + b\cos\theta_s \tag{3.1.9}$$

$$b_3 = \beta\sin 2\theta_p - b\cos\theta_s \tag{3.1.10}$$

For an incident shear wave the amplitudes of the reflected compression wave mode, $A$, and shear wave mode, $B$, are given by Equation 3.1.11 and Equation 3.1.12.

$$A = (a_3/a_1 - (a_2/a_1)B)\, s \tag{3.1.11}$$

$$B = \frac{b_3a_1 - b_1a_3}{b_2a_1 - b_1a_2} \tag{3.1.12}$$

where

$$a_1 = s^2\sin 2\theta_p + b\cos\theta_s \tag{3.1.13}$$

$$a_2 = \cos 2\theta_s - b \sin \theta_s \tag{3.1.14}$$

$$a_3 = -\cos 2\theta_s - b \sin \theta_s \tag{3.1.15}$$

$$b_1 = -\cos 2\theta_s + a \sin \theta_p \tag{3.1.16}$$

$$b_2 = \sin 2\theta_s + a \cos \theta_p \tag{3.1.17}$$

$$b_3 = \sin 2\theta_s - a \cos \theta_p \tag{3.1.18}$$

where

$$\beta = \left( \frac{C_s}{C_p} \right)^2 \tag{3.1.19}$$

$$s = \left( \frac{1 - 2\nu}{2(1 - \nu)} \right)^{\frac{1}{2}} \tag{3.1.20}$$

and $\nu$ is Poisson's ratio.

Although this method dramatically reduces the geometric size of the absorbing boundary and is available in some commercial packages, application is focused towards single-mode electromagnetic and acoustic problems. The greatest limitation for ultrasonic applications is that discrepancies arise at the Infinite Element boundaries due to there being insufficient degrees of freedom for complete absorption, resulting in a poor performance. Thus, is not suitable for the high accuracy removal of unwanted signals. This is consistent with observations made when applied to elastic scattering, with both the compression and shear wave modes present [92, 97].

### 3.1.2 Non-Reflecting Boundary Conditions

NRBC simulate an unbound medium within the same geometric size since they possess no area or volume. To simulate infinite material surrounding the system, the boundary conditions introduce extra variables into the governing equations that aim to prevent reflections occurring. Many different methods have been developed specific to their respective fields [87, 98, 99, 100, 101, 81], where the first example of a successful implementation is provided by Givoli *et al* [87]. This provides a frequency domain solution for a perfect non-reflecting boundary.

This approach has recently been extended by Velichko *et al* [81], for NDE applications where a frequency domain FE model is used to calculate the complete scattering behaviour of the defect using boundaries that are perfectly non-reflecting. The use of these perfect NRBC allows for only a single layer of elements surrounding the defect to be used, making the model computationally efficient. However, these methods require modification of the standard solving procedures using non-sparse matrices solved only in the frequency domain.

### 3.1.3 Absorbing layer techniques

Absorbing layer techniques append a number of finite sized layers to the boundary of the spatial domain. The layers are made of the same elements as the model but with gradually varying properties that absorb incident waves. This technique generates a larger increase in geometric size than the preceding methods, however, it can be directly implemented into commercial FE packages. Layer properties are optimised such that reflected waves are of a magnitude that can be considered negligible. The ease of implementation makes this approach appealing to modellers, provided the additional size of the spatial domain can be minimised.

For modelling elastodynamic wave problems there are four successful absorbing layer techniques; PML [88], ALID [89], CALM [90], and SRM [91]. All techniques append layers to the model boundary with absorbing properties that gradually increase, thereby attenuating incident waves.

#### 3.1.3.1 Perfectly Matched Layers

The PML technique was first developed for use in electromagnetism by Berenger [88], but has since been developed for ultrasonic studies for both the acoustic [102, 103, 104], and elastic cases [105, 106, 107, 108, 109]. A layer of absorbing material is added to the AoS, having an impedance that perfectly matches the parent material. This property allows incident waves to enter the region without reflection and then decay exponentially as described by an attenuation term as given by Equation 3.1.21.

$$u_x = u_0 e^{i(kx-\omega t)} e^{-\alpha(x)kx} \tag{3.1.21}$$

Inside the AoS, $\alpha(x)$ is zero and $u_x$ is not attenuated. However, outside the AoS $\alpha(x)$ gradually increases and therefore causes decay of incident waves.

$$\alpha(x) = A_x \left(\frac{x}{L}\right)^p \tag{3.1.22}$$

Here, $A_x$ is a coefficient describing the maximum amplitude of attenuation, $x$ defines the position within the PML (of thickness $L$), where $x = 0$ at the PML-AoS boundary and $x = L$ at the end of the PML. The increase must vary following a power law, $p$, and defined such that the wave re-

entering the AoS has negligible amplitude. This argument can then be extended for both the two and three-dimensional cases.

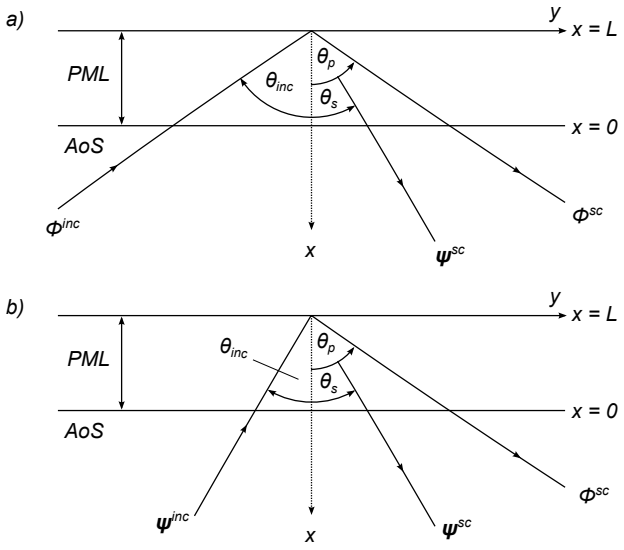


Figure 3.1.2: Figure to show an a) incident compression wave and b) an incident shear wave into a PML.

Figure 3.1.2 shows an incident wave entering the PML without any reflection due to impedance mismatch. Once inside the layer, the incident wave will begin to decay. From Equation 3.1.21 and Equation 3.1.22, the amplitude of the incident wave at a given point $x$, heading into the PML can be calculated using Equation 3.1.23.

$$\frac{u_x}{u_0} = \exp\left[\frac{(-A_x k_x x \cos(\theta_{inc})}{(p+1)}\right] \tag{3.1.23}$$

The total performance of the PML can now be assessed. An incident wave will attenuate as it propagates through the PML until it reaches the model boundary. For elastic waves, this is a stress-free boundary, therefore, elastic mode conversion will occur. The equations for the reflection coefficients at a stress-free boundary have already been given in Section 2.2.2, in relation to Kirchhoff theory (Equation 2.2.10, Equation 2.2.11, Equation 2.2.12 and Equation 2.2.13 with the change in notation such that $\alpha$, $\alpha_p$ and $\alpha_s$ are replaced by $\theta_{inc}$, $\theta_p$ and $\theta_s$).

After scattering at the stress-free boundary, the reflected compression and shear wave modes propagate back towards the AoS. Whilst returning, they are further attenuated by the PML before finally manifesting as unwanted reflections in the parent material.

The reflection coefficients for an incident wave entering the PML are calculated using Equation

3.1.24 and Equation 3.1.25 for incident compression waves, and Equation 3.1.26 and Equation 3.1.27 for incident shear waves.

$$\frac{\phi^{sc}}{\phi^{inc}} = R_{pp} \exp\left[\frac{(-Ak_pL\cos(\theta_{inc})}{(p+1)}\right] \exp\left[\frac{(-Ak_pL\cos(\theta_p)}{(p+1)}\right] \tag{3.1.24}$$

$$\frac{\psi^{sc}}{\phi^{inc}} = R_{ps} \exp\left[\frac{(-Ak_pL\cos(\theta_{inc})}{(p+1)}\right] \exp\left[\frac{(-Ak_sL\cos(\theta_s)}{(p+1)}\right] \tag{3.1.25}$$

$$\frac{\psi^{sc}}{\psi^{inc}} = R_{ss} \exp\left[\frac{(-Ak_sL\cos(\theta_{inc})}{(p+1)}\right] \exp\left[\frac{(-Ak_sL\cos(\theta_s)}{(p+1)}\right] \tag{3.1.26}$$

$$\frac{\phi^{sc}}{\psi^{inc}} = R_{sp} \exp\left[\frac{(-Ak_sL\cos(\theta_{inc})}{(p+1)}\right] \exp\left[\frac{(-Ak_pL\cos(\theta_p)}{(p+1)}\right] \tag{3.1.27}$$

The technique has had great success for electromagnetic and acoustic cases. Applications towards elastic waves have been considered; however the technique is more suited to frequency domain applications. Time domain solutions are possible, but this requires specific programming and functionality, which is currently only available in a minority of commercial FE packages.

From inspection of Equation 3.1.22, it can be observed the increasing the value of $A_x$ will result in absorption of an incident wave within a vanishingly small thickness, $L$. However implementation of the PML into the FE method does not produce this result. Due to the approximations of the FE method, element-to-element scattering occurs within the PML, therefore a significant absorbing region is still required. This phenomenon was identified by Rajagopal *et al* [92] and is discussed further in Section 3.2.5.

#### 3.1.3.2 Absorbing Layers by Increasing Damping

The ALID technique changes the physical properties of the elements within successive layers such that they absorb incident wave energy. Work by Castaings *et al* [110, 111, 112], shows the application of the ALID method in FE codes.

The physical properties must be changed gradually, but at an optimum rate because of two competing mechanisms. The first is that reflections are caused by impedance mismatches between successive absorbing layers. Thus, alterations in the physical properties of adjacent elements cause reflections that return energy back into the AoS at each interface. The second is that the incident wave may not be fully absorbed within the total thickness of the absorbing region and so may reflect from the model boundary back into the AoS. An efficient ALID allows for compensation between these two mechanisms by minimising impedance mismatches between successive layers in a minimal thickness to produce a net reflection below a pre-defined threshold.

The equation of dynamic equilibrium (Equation 2.3.1) that forms the basis of the FE discretisation of the wave propagation problem has already been introduced in Section 2.3. This has a harmonic solution expressed in the form $u(x,t) = e^{i(kx-\omega t)}$ for the one-dimensional case where $k$ is the wavenumber and $\omega$ is the angular frequency. By expressing acceleration, $\ddot{u}$, and velocity, $\dot{u}$, in terms of displacement, $u$, Equation 2.3.1 becomes:

$$-[M]\,\omega^2 u - [C]\,i\omega u + [K]\,u = F \tag{3.1.28}$$

The damping matrix can be expressed most simply as two separate components proportional to the mass and stiffness matrices, consistent with options available in most commercial FE packages:

$$[C] = C_M\,[M] + C_K\,[K] \tag{3.1.29}$$

Combining Equation 3.1.28 and Equation 3.1.29 produces a new equation for dynamic equilibrium where damping is expressed solely as a function of coefficients $C_M$, mass proportional damping and $C_K$, stiffness proportional damping:

$$-[M]\left(1 + i\frac{C_M}{\omega}\right)\omega^2 u + [K]\,(1 - i\omega C_K)\,u = F \tag{3.1.30}$$

From the inspection of the coefficients of Equation 3.1.30 it can be shown that damping terms can be replaced with complex values of the density $\rho$, and Young's modulus $E$:

$$\rho \to \rho\left(1 + i\frac{C_M}{\omega}\right) \tag{3.1.31}$$

and

$$E \to E\,(1 - i\omega C_K) \tag{3.1.32}$$

Inside the AoS where damping is normally zero ($C_M = 0$ and $C_K = 0$), Equation 3.1.31 and Equation 3.1.32 default to their real form. Inside the absorbing region, damping is non-zero, meaning that incident wave energy is absorbed by the imaginary parts of the complex terms introduced into the solution via $\rho$ and $E$. This can be illustrated by noticing that the wavenumber is related to the density and stiffness such that:

$$k \propto \sqrt{\frac{\rho}{E}} \tag{3.1.33}$$

Inside the absorbing layers $k = k_{real} + ik_{imag}$. Substituting this back into the original harmonic solution of the one-dimensional problem gives:

$$u(x,t) = e^{i(k_{real}x - \omega t)} e^{-k_{imag}x} \tag{3.1.34}$$

It is the term $e^{-k_{imag}x}$ which induces the decay of the waves inside the absorbing region and therefore that must be exploited. Commercial FE packages do not offer a means to alter the wavenumber directly. This must be achieved indirectly, by altering values of the stiffness, damping and mass matrices, to increase the value of $k_{imag}$ inside the absorbing region. Consequently, this will also increase the value of $k_{real}$ which must be managed carefully in order to minimise the reflection between adjacent elements.

From Equation 3.1.31 and Equation 3.1.33 it can be shown that the complex wavenumber can be expressed as:

$$k(k_{real}, k_{imag}) \propto \sqrt{\frac{\rho(1 + \frac{iC_M}{\omega})}{E}} \tag{3.1.35}$$

The optimal outcome would be a means of increasing the value of $k_{imag}$ without increasing $k_{real}$. To date such capability for time domain commercial FE packages has not been established, therefore layer properties must be carefully selected such that successive values of $k_{real}$ result in impedance mismatches that generate reflections which can be considered negligible.

To define an effective absorbing region it is necessary to optimise variables that the user has control over. Progress made in ALID by Rajagopal *et al* [92], gives a good indication of how best to optimise initial parameters. Firstly, it is noted that introducing damping into the model can decrease the value of the stable time increment within explicit schemes, thereby reducing computational efficiency. However, a high value of $C_M$ causes only a small decrease in the stable increment as compared to that of $C_K$ [92]. It is therefore preferable to avoid using $C_K$ to define an absorbing boundary within an explicit scheme. Setting $C_K$ to zero eliminates this issue and allows damping to be controlled solely by $C_M$, in which case it is found that the stability is not compromised.

Secondly, damping is defined as an increasing power law set by the power $p$, to gradually alter the value across successive layers.

$$C_M(x) = C_{Mmax} X(x)^p \tag{3.1.36}$$

$C_{Mmax}$ is a positive real number, $X(x)$ ranges from 0 at the AoS-ALID boundary to 1 at the end of the absorbing region with layer thickness equal to the element width. Therefore, for a spatial discretised FE model, $x$ takes discrete values corresponding to an integer number of element widths that increases while moving away from the AoS-ALID boundary.

There is no established method for directly calculating the ideal values for the variables in Equation 3.1.36, however there is literature that suggests how best to begin optimising the technique [92]. The value of $C_{Mmax}$ is found using a trial and error method until the acceptability criterion of reflection

for all modes in the model is validated. In those studies, the thickness of the absorbing region was set to be three times the size of the largest wavelength travelling through the system.

#### 3.1.3.3 Caughey Absorbing Layer Method

A recent development to the ALID approach has been made by Semblat *et al* [90], based on a Rayleigh/Caughey damping formulation. Rayleigh/Caughey damping is available in most commercial FE packages and the technique developed is thus called Caughey Absorbing Layer Method or CALM. Spatial variation of damping is controlled by varying the mass and stiffness proportional damping coefficients to give a diagonal damping matrix.

The damping matrix is expressed by two separate components proportional to the mass and stiffness matrices. Unlike ALID, $C_K$ is now non-zero. Following the same derivation as ALID, it can be shown that the complex wavenumber can be expressed as:

$$k(k_{real}, k_{imag}) \propto \sqrt{\frac{\rho(1 + \frac{iC_M}{\omega})}{E\,(1 - i\omega C_K)}} \tag{3.1.37}$$

The CALM can outperform conventional ALID when applied to the same application case whilst still offering the same ease of implementation as mass proportional damping. However, the increase in performance has come at the expense of a decrease in the stable time increment that is associated with having a non-zero $C_K$ term.

## 3.2 Stiffness Reduction Method

The SRM is a new absorbing boundary technique that has been specifically developed to meet the requirements of this project, although it can be applied to any commercially available FE package.

For time domain explicit solvers, ALID has proven successful because it offers flexibility to modellers and, unlike the PML approach, can be readily implemented into most commercial FE software packages without requiring access to the source code. However, despite good overall performance, ALID requires the spatial model to extend significantly outside the domain of interest, often requiring absorbing region thickness of three incident wavelengths.

The SRM has been developed to operate within a significantly reduced spatial domain. The technique is applied by altering the damping and stiffness matrices of the system, inducing decay of any incident wave. Absorbing region variables are expressed as a function of known model constants, helping to apply the technique to generic elastodynamic problems. This section is also discussed in work presented by Pettit *et al* [91].

### 3.2.1 Stiffness Reduction Method theory

As discussed in Section 3.1.3.2, it is the imaginary component of the wavenumber within the absorbing region $k_{imag}$, which induces the decay of the incident waves. This must be achieved indirectly by altering values of the stiffness, damping and mass matrices, to increase the value of $k_{imag}$ inside the absorbing region.

$$k(k_{real}, k_{imag}) \propto \sqrt{\frac{\rho(1 + \frac{iC_M}{\omega})}{E}} \tag{3.2.1}$$

The development made with SRM is to notice that under these conditions, the wavenumber can be incrementally increased by using $C_M(x)$ but also by decreasing the value of the Young's modulus $E$. Therefore, within the absorbing region $E$ becomes a function of $x$, decreasing gradually across the absorbing region to avoid any dramatic changes in material properties. The Young's modulus is reduced using an exponential decay function containing an attenuation factor $\alpha$, as given by Equation 3.2.2.

$$E(x) = E_0 e^{-\alpha(x) k_{inc} x} \tag{3.2.2}$$

where $E_0$ is the Young's modulus inside the AoS and $k_{inc}$ is the incident wavenumber.

To avoid excessive mismatches in impedance between adjacent layers the attenuation factor $\alpha(x)$, does not remain constant. It is necessary to gradually increase this value across the absorbing region as given in Equation 3.2.3.

$$\alpha(x) = \alpha_{max} X(x)^p \tag{3.2.3}$$

The SRM still maintains the mass proportional damping $C_M(x)$, which is varied in the same manner as ALID, but now includes the additional reductions made to the stiffness matrix. The combination of these two effects allows for the attenuation of incident waves within a significantly reduced spatial domain.

Having established that reducing the stiffness and increasing the damping will absorb incident waves, it is now necessary to optimise the performance. A one-dimensional explicit FE model has been used to optimise and compare model variables. Following this, the concept is applied to test models set up using the commercial FE package ABAQUS/Explicit [113], in order to obtain quantitative values for the reflection coefficients as a function of the incident angle for two-dimensional analysis. Numerical results from these simulations are then compared to an analytical model using the Global Matrix method, reported in detail by Lowe [114].

### 3.2.2 One-dimensional Finite Element simulations

To understand the behaviour of the system, an explicit one-dimensional FE model has been created that is governed by Equation 2.3.19. The system is composed of a string of 2-node rod or Truss elements each with a single degree of freedom being the displacement parallel to the direction of propagation. A length of undamped elements forming the AoS is terminated by an absorbing region. An illustration of this system is given in Figure 3.2.1.

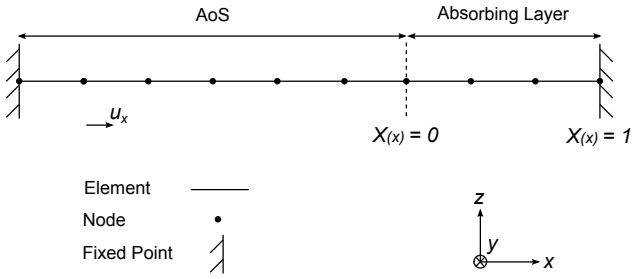


Figure 3.2.1: Illustration of an explicit one-dimensional FE model used to investigate absorbing layer performance.

A short pulse is generated in the AoS and is incident at the absorbing region. The performance of the absorbing region is assessed by examining the unwanted reflection returning from it. The FE model is non-dimensional with material properties that produce a propagation wavelength of 1 unit. The total length of the absorbing region is 1.5 units ($1.5\lambda_{inc}$ of the system) and the model is discretised using 20 nodes per wavelength with a Courant or CFL number of 1 [65].

SRM variables that need to be optimised are the maximum Rayleigh damping $C_{Mmax}$, the power to which successive layer properties are raised $p$, and the maximum attenuation factor in the final absorbing layer $\alpha_{max}$. To achieve this an optimisation function is used which calculates the optimal values for input variables that will render the lowest possible reflection coefficient for the absorbing boundary (see Section 3.3.3 for an explanation of the optimisation function).

The SRM and ALID are directly compared for the one-dimensional case, with their respective layer properties optimised for maximum absorption. All variables between the two models remain constant except for the Young's modulus in the absorbing region of the SRM. Figure 3.2.2a) and Figure 3.2.2b) show the performance of the two techniques. The time history of a single excited node is recorded showing the incident 5 cycle tone burst and the observed reflection from the absorbing region later in time.

Figures 3.2.2a) and Figure 3.2.2b) show that for the example under consideration, the SRM behaves significantly better than ALID. The maximum amplitude of the reflected signal for the ALID is -35.2 dB whereas the SRM gives -45.0 dB.

a)

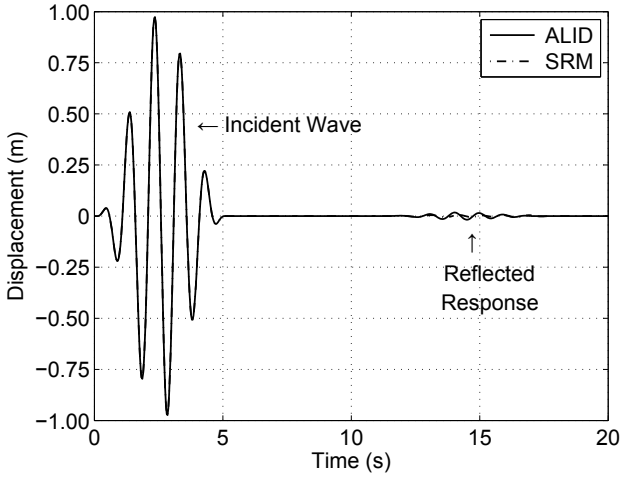


b)

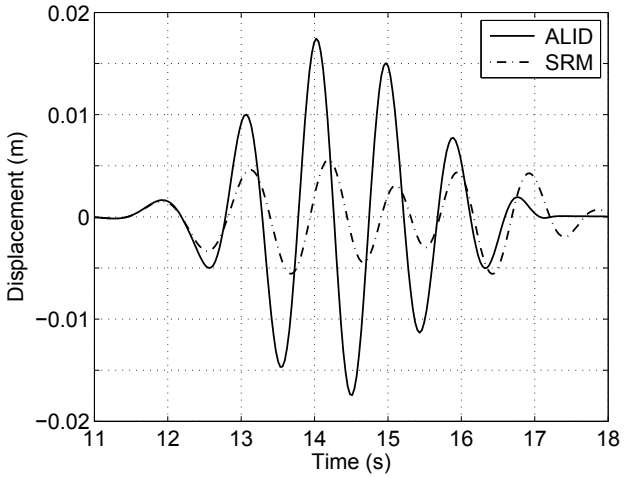


c)

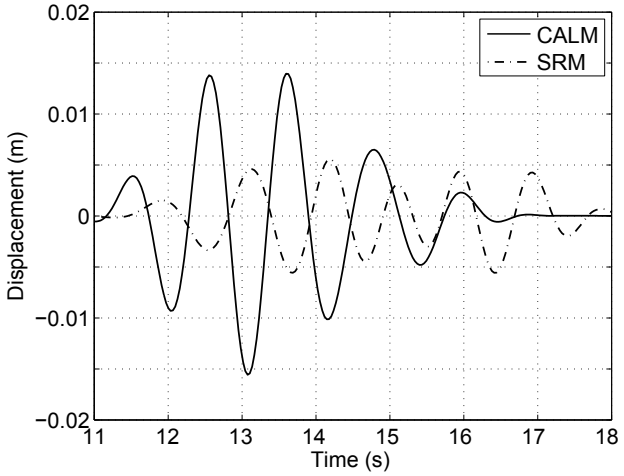


Figure 3.2.2: Reflected signals from absorbing layer regions for a) ALID and SRM, full time record b) zoom of ALID and SRM and c) zoom of CALM and SRM.

Due to the likened approach to a Rayleigh/Caughey damping formulation proposed by Semblat *et al* [90], a further comparison is made between SRM and CALM. To incorporate Rayleigh/Caughey damping, the damping matrix is defined by Equation 3.1.29, where $C_M$ and $C_K$ are non-zero. Again $C_M$ and $C_K$ are varied gradually across the absorbing layer, as in Equation 3.1.36, but with the introduction of an additional variable $C_{Kmax}$, the maximum stiffness proportional damping coefficient. The definition of SRM remains unchanged.

For a fair comparison to be made with SRM, an optimisation function (see Section 3.3.3) is used which calculates the optimal values for $C_{Mmax}$ and $C_{Kmax}$ that will render the lowest possible reflection coefficient for the CALM absorbing boundary. The SRM and CALM are directly compared for the one-dimensional case, with their respective layer properties optimised for maximum absorption. All variables between the two models remain constant except for the Young's modulus in the absorbing region of the SRM. Like the comparison made with ALID and SRM in Figure 3.2.2b), Figure 3.2.2c) shows the time history of the observed reflection from the absorbing regions.

CALM absorbing boundaries have marginally outperformed the ALID in this example, with a maximum amplitude of the reflected signal being -36.2 dB. This increase in performance over conventional ALID has been achieved by the inclusion of stiffness proportional damping to the damping matrix, with the same ease of implementation as mass proportional damping. However, the increase in performance has come at the expense of a significant decrease in the stable time increment that is associated with having a non-zero $C_K$ term. Despite this improvement Rayleigh/Caughey damping does not offer the same performance that has been achieved with SRM.

Figure 3.2.3 shows how the change of matrix variables changes the value of the wavenumber. Both the real and imaginary components have been plotted. The first observation is that within the SRM, $k_{imag}$ increases dramatically in comparison to the ALID. This is as expected and is in agreement with the predictions made using Equation 3.1.35. It is the increase in this value that produces such successful decay of any incident waves whilst inside each layer. The desired increase in $k_{imag}$ is also accompanied by the undesired increase in $k_{real}$. Again the increase observed inside the SRM is considerably greater than that in the ALID, which should suggest sizable reflections at successive layer boundaries. However, dramatic changes only occur once the wave has propagated a significant distance into the absorbing region.

Here, the thickness of each layer remains constant and is fixed to a value of one-element-thickness. Work carried out by Rajagopal *et al* [92], has stated that it is preferable to minimise the change in any material properties between adjacent layers so that impedance changes are gradual and thus the thinner each layer is the better. However, for one-dimensional FE models, increasing element thickness could potentially offset impedance mismatches. The stiffness of a single Truss element is the product of the Young's modulus multiplied by the element thickness, thereby allowing for another parameter by which to control material properties. This is not however suitable for two and three-dimensional FE

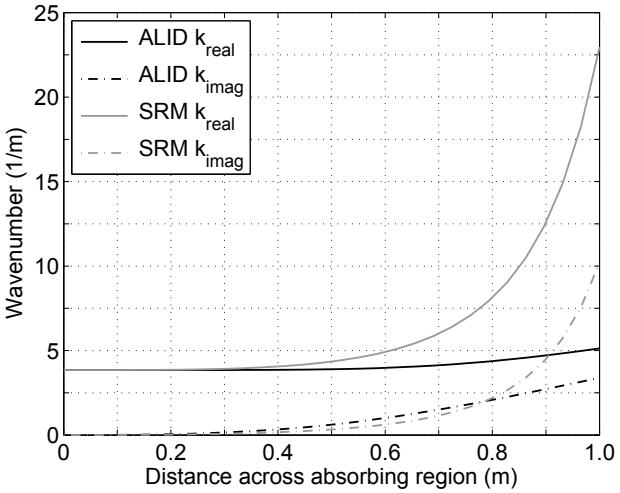


Figure 3.2.3: Increase of real and imaginary components of the wavenumber with distance.

models so has not been pursued. In this instance a variation in element size must be performed across a rectangular or quadrilateral element, greatly distorting the structured arrangement of the mesh. Furthermore, variation of the mesh density will result in scattering from the mesh itself, producing an additional mechanism whereby unwanted reflections are radiated back into the AoS.

### 3.2.3 Two-dimensional Finite Element simulations

Having established a mechanism to generate a successful absorbing region, it is now necessary to assess behaviour for the two-dimensional case in a commercial FE package. The package ABAQUS/Explicit [113], has been chosen for the study, as it is widely available, developed and supported for wave propagation simulations. To assess the validity of the numerical model, results are compared to an analytical approach based upon the Global Matrix method [114].

#### 3.2.3.1 Analytical model

The Global Matrix method establishes a matrix relationship which describes plane wave propagation across all the layers of a multi-layered body as illustrated by Figure 3.2.4. Each layer contains a local description of the wave, where adjacent layers are coupled by applying Snell's law for continuity of stress and displacement. Rajagopal *et al* [92], successfully applied this technique to analyse the performance of the ALID by gradually implementing damping using the complex expression for density (Equation 3.1.31). The extension made here is to include the reduction in Young's modulus, as well as the complex density used by ALID.

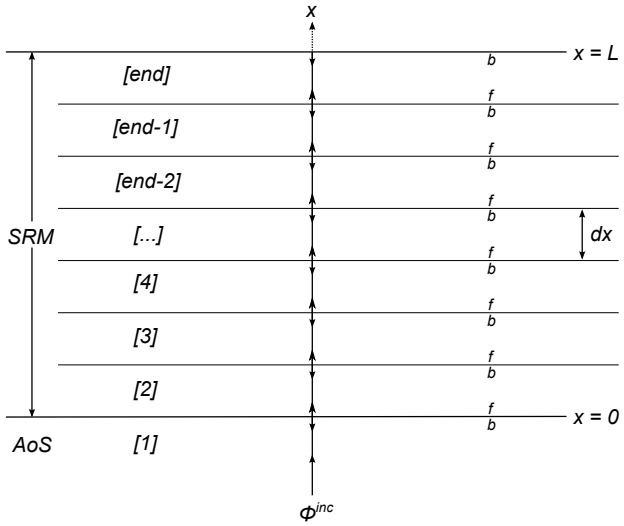


Figure 3.2.4: Figure to show application of the Global Matrix method to SRM absorbing boundary.

At the front boundary, $f$, of any layer in the absorbing region the displacements and stresses are linked by Equation 3.2.4.

$$\begin{bmatrix} u^f_{x[n]} \\ u^f_{y[n]} \\ \sigma^f_{xx[n]} \\ \sigma^f_{xy[n]} \end{bmatrix} = M^f_{[n]} \begin{bmatrix} \phi_{P[n]} \\ \psi_{P[n]} \\ \phi_{N[n]} \\ \psi_{N[n]} \end{bmatrix} \tag{3.2.4}$$

where

$$M^f_{[n]} = \begin{bmatrix} ik_{px} & -ik_{sy} & -ik_{px}e^{-ik_{px}x} & -ik_{sy}e^{-ik_{sx}x} \\ ik_{py} & ik_{sx} & ik_{py}e^{-ik_{px}x} & -ik_{sx}e^{-ik_{sx}x} \\ -(\lambda k^2_{px} + 2\mu k^2_{py}) & 2\mu k_{sx}k_{sy} & -(\lambda k^2_{px} + 2\mu k^2_{py})e^{-ik_{px}x} & -2\mu k_{sx}k_{sy}e^{-ik_{sx}x} \\ -2\mu k_{px}k_{py} & -2\mu(k^2_{sx} - k^2_{sy}) & 2\mu k_{px}k_{py}e^{-ik_{px}x} & -2\mu(k^2_{sx} - k^2_{sy})e^{-ik_{sx}x} \end{bmatrix}$$

Waves entering and leaving the layer are travelling in the positive, $P$, and negative, $N$, directions respectively, with $k_{px}$, $k_{py}$, $k_{sx}$ and $k_{sy}$ being the projections of the wavenumbers of the compression and shear waves on the x and y axes.

Similarly at the back boundary, $b$, the displacements and stresses are linked by Equation 3.2.5.

$$\begin{bmatrix} u^b_{x[n]} \\ u^b_{y[n]} \\ \sigma^b_{xx[n]} \\ \sigma^b_{xy[n]} \end{bmatrix} = M^b_{[n]} \begin{bmatrix} \phi_{P[n]} \\ \boldsymbol{\psi}_{P[n]} \\ \phi_{N[n]} \\ \boldsymbol{\psi}_{N[n]} \end{bmatrix} \tag{3.2.5}$$

where

$$M^b_{[n]} = \begin{bmatrix} ik_{px}e^{ik_{px}x} & -ik_{sy}e^{ik_{sx}x} & -ik_{px} & -ik_{sy} \\ ik_{py}e^{ik_{px}x} & ik_{sx}e^{ik_{sx}x} & ik_{py} & -ik_{sx} \\ -(\lambda k^2_{px} + 2\mu k^2_{py})e^{ik_{px}x} & 2\mu k_{sx}k_{sy}e^{ik_{sx}x} & -(\lambda k^2_{px} + 2\mu k^2_{py}) & -2\mu k_{sx}k_{sy} \\ 2\mu k_{px}k_{py}e^{ik_{px}x} & -2\mu(k^2_{sx} - k^2_{sy})e^{ik_{sx}x} & 2\mu k_{px}k_{py} & -2\mu(k^2_{sx} - k^2_{sy}) \end{bmatrix}$$

Following the Global Matrix arguments given by Lowe [114] and allowing the displacements and stresses to be equal at each interface, the relationship between any adjacent layers can be defined, as given by Equation 3.2.6.

$$M^b_{[n]} \begin{bmatrix} \phi_{P[n]} \\ \boldsymbol{\psi}_{P[n]} \\ \phi_{N[n]} \\ \boldsymbol{\psi}_{N[n]} \end{bmatrix} = M^f_{[n+1]} \begin{bmatrix} \phi_{P[n+1]} \\ \boldsymbol{\psi}_{P[n+1]} \\ \phi_{N[n+1]} \\ \boldsymbol{\psi}_{N[n+1]} \end{bmatrix} \tag{3.2.6}$$

It is important to consider the special case at the back of final layer, where the wave changes direction and returns back through the absorbing region. This stress free boundary condition is given by Equation 3.2.7.

$$L^b_{[end]} \begin{bmatrix} \phi_{P[end]} \\ \boldsymbol{\psi}_{P[end]} \\ \phi_{N[end]} \\ \boldsymbol{\psi}_{N[end]} \end{bmatrix} = 0 \tag{3.2.7}$$

where

$$L^b_{[end]} = \begin{bmatrix} -(\lambda k^2_{px} + 2\mu k^2_{py})e^{ik_{px}x} & 2\mu k_{sx}k_{sy}e^{ik_{sx}x} & -(\lambda k^2_{px} + 2\mu k^2_{py}) & -2\mu k_{sx}k_{sy} \\ 2\mu k_{px}k_{py}e^{ik_{px}x} & -2\mu(k^2_{sx} - k^2_{sy})e^{ik_{sx}x} & 2\mu k_{px}k_{py} & -2\mu(k^2_{sx} - k^2_{sy}) \end{bmatrix}$$

Finally, for a given incident wave entering the absorbing region the boundary conditions are known and are given by Equation 3.2.9.

$$M^b_{[1]} \begin{bmatrix} \phi_{P[1]} \\ \boldsymbol{\psi}_{P[1]} \\ \phi_{N[1]} \\ \boldsymbol{\psi}_{N[1]} \end{bmatrix} = M^f_{[2]} \begin{bmatrix} \phi_{P[2]} \\ \boldsymbol{\psi}_{P[2]} \\ \phi_{N[2]} \\ \boldsymbol{\psi}_{N[2]} \end{bmatrix} \tag{3.2.8}$$

which becomes:

$$M^b_{LHS[1]} \begin{bmatrix} \phi_{N[1]} \\ \boldsymbol{\psi}_{N[1]} \end{bmatrix} - M^f_{[2]} \begin{bmatrix} \phi_{P[2]} \\ \boldsymbol{\psi}_{P[2]} \\ \phi_{N[2]} \\ \boldsymbol{\psi}_{N[2]} \end{bmatrix} = -M^b_{RHS[1]} \begin{bmatrix} \phi_{P[1]} \\ \boldsymbol{\psi}_{P[1]} \end{bmatrix} \tag{3.2.9}$$

where

$$M^b_{LHS[1]} = \begin{bmatrix} ik_{px}e^{ik_{px}x} & -ik_{sy}e^{ik_{sx}x} \\ ik_{py}e^{ik_{px}x} & ik_{sx}e^{ik_{sx}x} \\ -(\lambda k^2_{px} + 2\mu k^2_{py})e^{ik_{px}x} & 2\mu k_{sx}k_{sy}e^{ik_{sx}x} \\ 2\mu k_{px}k_{py}e^{ik_{px}x} & -2\mu(k^2_{sx} - k^2_{sy})e^{ik_{sx}x} \end{bmatrix}$$

$$M^b_{RHS[1]} = \begin{bmatrix} -ik_{px} & -ik_{sy} \\ ik_{py} & -ik_{sx} \\ -(\lambda k^2_{px} + 2\mu k^2_{py}) & -2\mu k_{sx}k_{sy} \\ 2\mu k_{px}k_{py} & -2\mu(k^2_{sx} - k^2_{sy}) \end{bmatrix}$$

The complete global matrix for waves propagating in the absorbing region is defined by Equation 3.2.10.

$$\begin{bmatrix} [M^b_{LHS[1]}] & -[M^f_{[2]}] & 0 & ... & 0 \\ 0 & [M^b_{[2]}] & -[M^f_{[3]}] & ... & 0 \\ ... & ... & ... & ... & 0 \\ 0 & 0 & 0 & [M^b_{[end-1]}] & -[M^f_{[end]}] \\ 0 & 0 & 0 & 0 & [L^b_{[end]}] \end{bmatrix} \begin{bmatrix} \begin{bmatrix} \phi_{N[1]} \\ \boldsymbol{\psi}_{N[1]} \end{bmatrix} \\ \begin{bmatrix} \phi_{P[2]} \\ \boldsymbol{\psi}_{P[2]} \end{bmatrix} \\ \begin{bmatrix} \phi_{N[2]} \\ \boldsymbol{\psi}_{N[2]} \end{bmatrix} \\ ... \\ ... \\ \begin{bmatrix} \phi_{P[end]} \\ \boldsymbol{\psi}_{P[end]} \end{bmatrix} \\ \begin{bmatrix} \phi_{N[end]} \\ \boldsymbol{\psi}_{N[end]} \end{bmatrix} \end{bmatrix} = \begin{bmatrix} -\left[M^b_{RHS[1]}\right] \begin{bmatrix} \phi_{P[1]} \\ \boldsymbol{\psi}_{P[1]} \end{bmatrix} \\ 0 \\ ... \\ 0 \\ 0 \end{bmatrix} \tag{3.2.10}$$

For a given model of known material properties the left hand matrix is known. Similarly, for a specified incident wave, the initial amplitude propagating into the absorbing region $\begin{bmatrix} \phi_{P[1]} \\ \boldsymbol{\psi}_{P[1]} \end{bmatrix}$ is also known. Matrix inversion is used to calculate the value of the wave amplitudes within each layer, thereby deducing the amplitude of the wave returning into the AoS, $\begin{bmatrix} \phi_{N[1]} \\ \boldsymbol{\psi}_{N[1]} \end{bmatrix}$. Since the amplitude of the incident wave mode is known, this gives the reflection coefficient of both reflected wave modes for angles of incidence within the range $0^o$ to $90^o$.

#### 3.2.3.2 Numerical model

A harmonic bulk wave is incident on the absorbing region across a range of angles $\theta_{inc}$, as shown in Figure 3.2.5. For each incident angle, the model is re-run by adjusting the inclination of the excitation plane. The amplitudes of the incident and reflected wave modes are monitored along their predicted lines of propagation and the reflection coefficient deduced.

The FE models are non-dimensional and the material properties are defined such that the compression and shear wavelengths are 1 and 2 units respectively; each incident wave mode is considered separately. The length of the absorbing region is equal to 1.5 times the incident wavelength. The attenuation parameters are defined such that the Young's modulus in the final absorbing layer is 1% of the value in the AoS, $C_{Mmax} = \omega$ and $p = 3$.

Since the requirement is only to assess the performance of the SRM, reflections from the other model boundaries must be removed. This is achieved by the use of an 'ultra ALID' which has thickness that is sufficiently large as to only generate reflections that can be considered extremely low (-120 dB) as

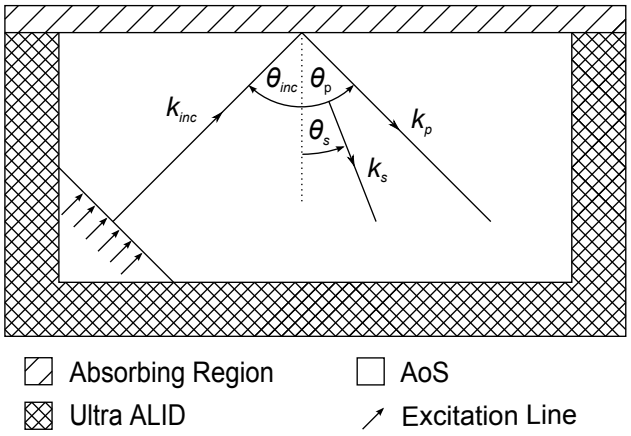


Figure 3.2.5: FE model used to assess performance of SRM in bulk elastic wave propagation.

demonstrated by Rajagopal *et al* [92], and Drozdz [115]. The figure illustrates the mode conversion of the incident waves whereby the angles are calculated using Equation 3.2.11:

$$\sin\theta_s = \gamma \sin\theta_p \tag{3.2.11}$$

where $\gamma = \frac{k_p}{k_s}$.

### 3.2.4 Results

Results for the analytical and numerical models are shown in Figure 3.2.6a) for an incident compression wave and in Figure 3.2.6b) for an incident shear wave.

There is excellent agreement between the numerical and analytical solutions, confirming the reliability of the analysis. Performance at low angles of incidence is significantly better than at higher glancing angles; consistent with other absorbing layer techniques. This confirms that the angle of incidence plays a critical role in the selection of SRM variables. Performance at high angles will always render a less acceptable solution (however it is often the case that these angles are not of concern in simulations).

The presence of critical angles generates evanescent waves propagating parallel to the back boundary of the SRM. The angle at which this occurs is not necessarily obvious since it is due to a net effect from all the layers combined. This is illustrated in Figure 3.2.6b), whereby after the critical angle for an incident shear wave, the reflected compression wave component is not radiated back into the AoS. Finally, for time domain simulations, the incident wave packet is composed of waves with energy over a range of frequencies. The performance of the absorbing region is a function of the frequency, meaning that individual frequency components of the incident wave packet will all perform differently.

a)

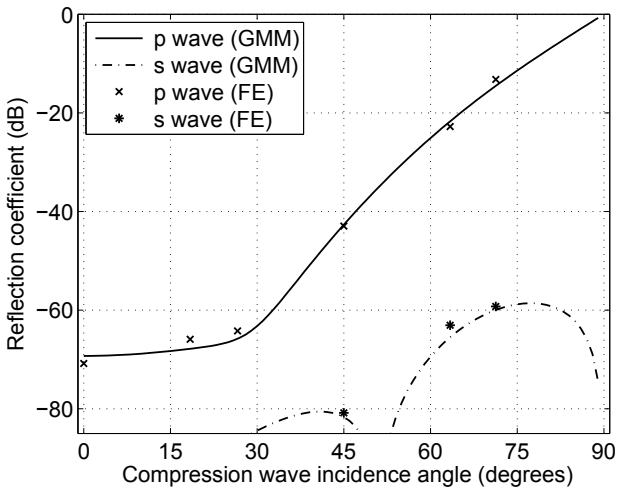


b)

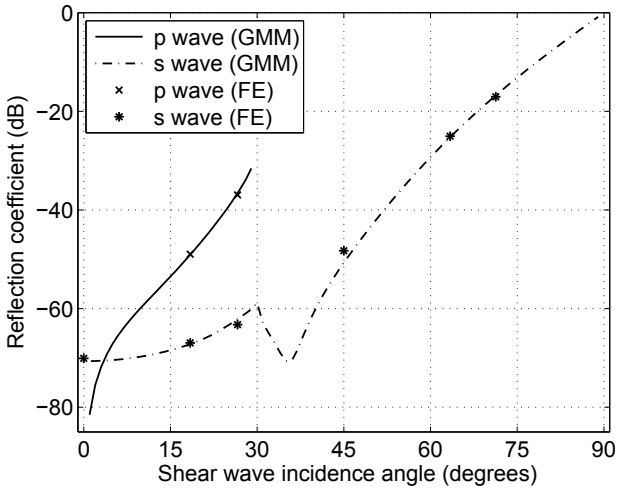


Figure 3.2.6: Analytical reflection coefficients from Global matrix method (GMM) and numerical reflection coefficients for a non-dimensional SRM for a) incident compression and b) incident shear waves.

A noticeable trade-off for reduction in the spatial domain is the increase in the critical time step. Optimising the material properties of the absorbing region results in the desired increase in wavenumber coinciding with a reduction in wave speed. If element size remains constant this must result in an increase in the critical time step across successive layers. Since the time step must be constant for the entire model and must be stable across all elements within the model, the CFL number is reduced, see Figure 3.2.7.

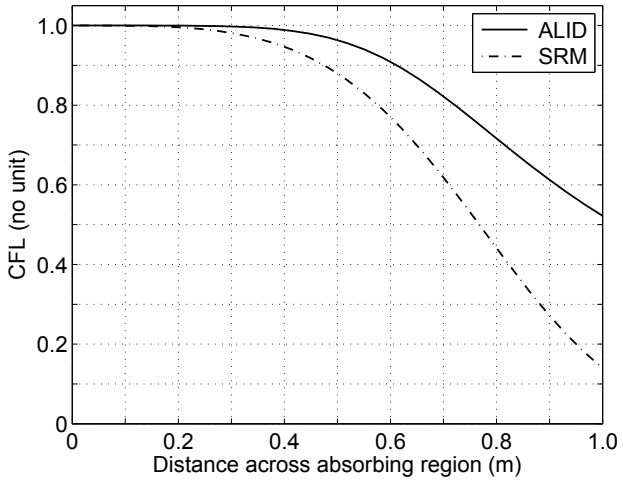


Figure 3.2.7: Reduction in CFL number due to increase in critical time step across successive layers.

The effect of having a low CFL number has been studied by Drozdz [115]. The findings show that a low CFL number causes an increase in the error of propagation velocity. However this effect can be nullified by using a high mesh density to define the system. For this reason such effects are not of concern, as accurate modelling of elastic wave scattering problems requires mesh refinement, for example to use a minimum of 15 nodes per wavelength, for which errors in propagation velocity are low (less than 1%). Furthermore, inaccuracies with propagation velocity within the SRM are not of concern. This is only an issue if spurious reflections return into the AoS, which has not been observed.

### 3.2.5 Comparison of absorbing layer methods

Comparison of SRM, ALID and PML absorbing layer techniques can be made by examining results published by Rajagopal *et al* [92], with those in this study. Reflection coefficients for the three methods are calculated using analytical models applied to the same non-dimensional case. The layer thickness for all three cases is the same as the wavelength of the incident wave, and the optimisation function (see Section 3.3.3) is used to select the optimum model variables.

The results for the incident compression wave are shown in Figure 3.2.8a) and Figure 3.2.8b) and for an incident shear wave in Figure 3.2.9a) and Figure 3.2.9b).

The results show that PML generally outperforms both ALID and SRM for almost all angles of incidence across both modes. However, SRM shows a significant improvement over the ALID. The presence of critical angles is also evident, maintaining that the same underlying mechanisms are present with all three techniques. SRM maintains an advantage since its accessibility is equal to that of ALID and does not require specific programming of functionality. Furthermore, like ALID, SRM is defined using standard material properties that do not limit it to isotropic media. The application of PML to anisotropic material would again require further specific implementation.

Figure 3.2.8b) shows a reduction in the reflection coefficient of a mode converted shear wave with SRM when using an incident compression wave approaching $40^o$. This relative reduction in reflection coefficient is not observed with ALID or PML. The relationship between variables that contribute to the wave attenuation is complex, however a possible explanation can be provided.

The partial success of SRM results from a dramatic reduction in wave speed as the wave propagates through successive absorbing layers. A similar effect is observed with ALID but to less of an extent. For PML this effect is not observed due to impedance matching between absorbing layers, meaning that the wave speed remains constant. A reduction in the wave speed increases the total time taken for the wave to propagate through the absorbing boundary, ultimately aiding in attenuation. As the angle of incidence increases, the path length through the absorbing region also increases. This increase in path length and reduction in wave speed results in an increase in the wave attenuation. The fact that the signal in question is a mode converted shear wave enhances the effect further, since the wave speed reduction is even more pronounced.

The reducing wave speed and increasing path length effect is not apparent across all incident angles. As is consistent with all other absorbing boundary methods, high incident angles produce high reflection coefficients due to glancing effects. As a result, a trade-off is observed between the two. For incident angles approaching $40^o$ the increase in path length and reduction in wave speed is dominating wave attenuation since the incident angle is not so large as to introduce reflections from the higher glancing angles.

It is important to note that the PML analytical solution can achieve a further improved performance. PML variables have been capped to give a -60 dB reflection coefficient at $0^o$ since it is observed that beyond this point the analytical model breaks down and does not coincide with what is observed in numerical models. Work by Rajagopal *et al* [92], discusses the effects of numerical reflections caused by element boundaries as a cause for this disagreement. As a result it is recommended that optimal values of $3\lambda_{inc}$ and $\lambda_{inc}$ be used for ALID and PML thickness respectively. From the observations made thus far and the discussions that follow, proposed optimal SRM thickness is $1.5\lambda_{inc}$.

a)

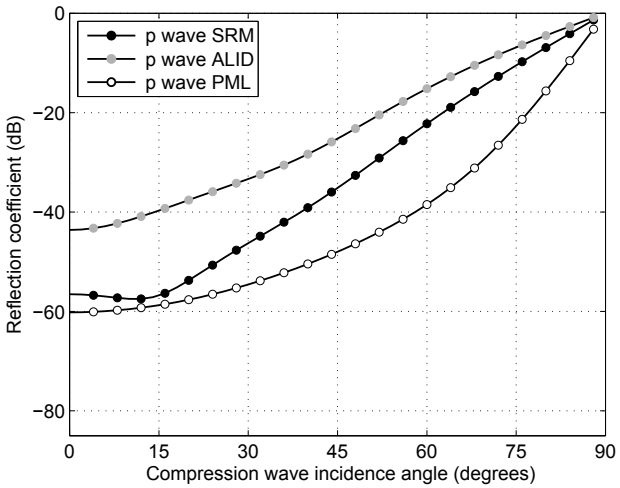


b)

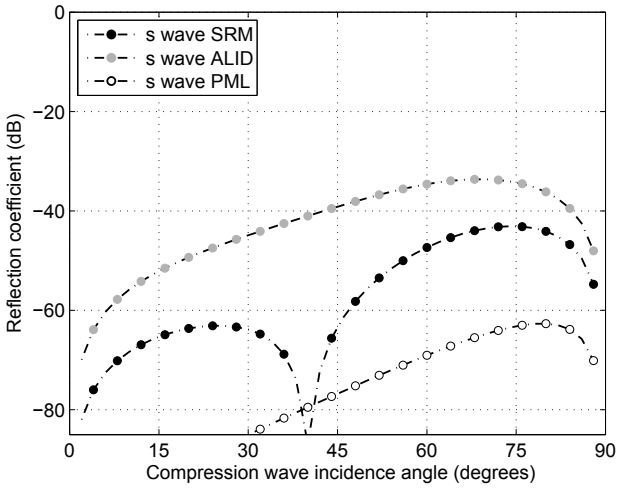


Figure 3.2.8: Reflection coefficients for SRM, ALID and PML for incident compression wave: a) compression analytical reflection coefficients and b) shear analytical reflection coefficients.

a)

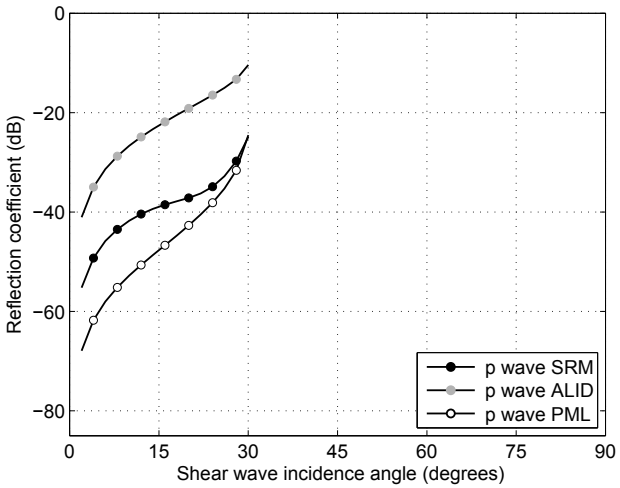


b)

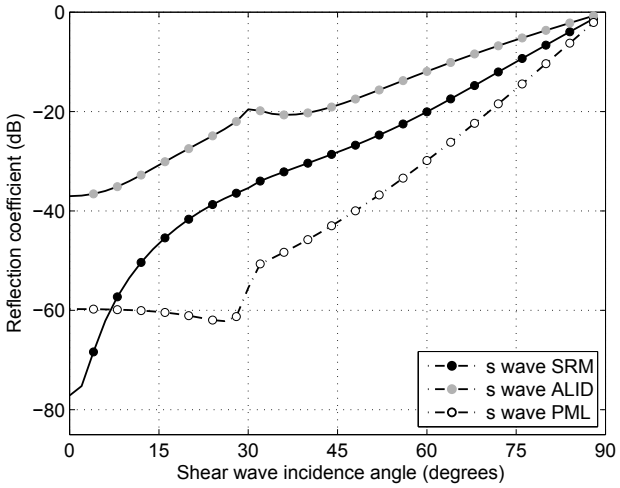


Figure 3.2.9: Reflection coefficients for SRM, ALID and PML for incident shear wave: a) compression analytical reflection coefficients and b) shear analytical reflection coefficients.

### 3.2.6 Applied case

To illustrate the performance of the SRM, the absorbing layer technique is applied to an example realistic simulation. An embedded rough defect is acting as a scatterer of incident ultrasonic waves. The system is surrounded by infinite elastic space and the scattered signal is monitored. Both the SRM and ALID absorbing boundary methods are compared for increasing thickness of absorbing region, as shown in Figure 3.2.10.

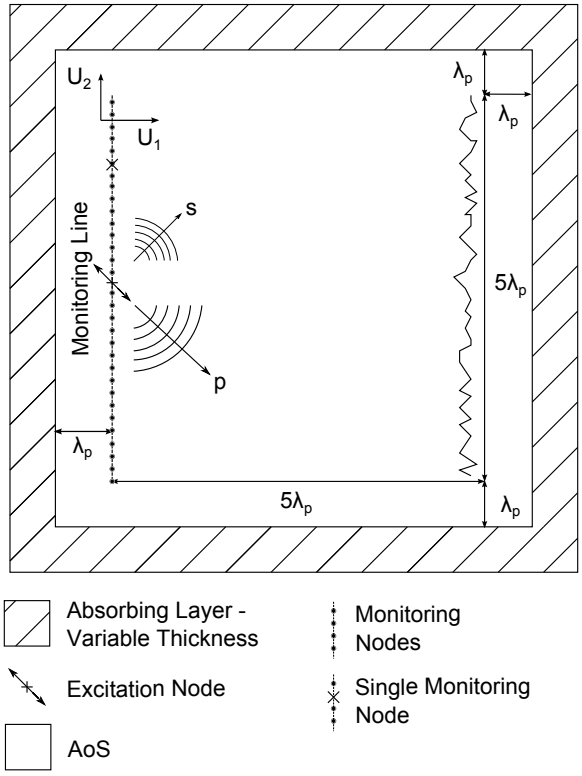


Figure 3.2.10: FE model used to test performance of SRM and ALID as a function of region thickness.

The material is defined by a Young's modulus of 70 GPa, Poisson's ratio of 0.31 and density of 2700 $\text{kgm}^{-3}$. The compression wavelength of the incident wave, $\lambda_p$, is 3.00 mm and the system is spatially discretised at 30 nodes per compression wavelength. A 2 MHz, 5 cycle incident wave is applied to a single excitation node which is excited in a direction that is inclined at $45^o$ to the U1 axis. Exciting the node in this manner generates a spherically propagating compression wave and a perpendicular spherically propagating shear wave. This excitation ensures that both wave modes interact with the complex multifaceted scatterer, fully testing the performance of the absorbing layers.

The defect of choice is a two-dimensional rough surface with a rms $\sigma = 0.100\lambda_p$, away from the

mean plane. The rough surface is generated using a moving average process as described by Ogilvy, [116]. The method represents a rough surface by a set of discrete heights at discretised points along the defect surface. Initially the heights are uncorrelated, having a normal distribution governed by the rms height. To correlate the heights, a moving average is taken, effectively smoothing out the height profile, thereby correlating the surface.

The depth and width of the defect is $5\lambda_p$ and the distance separating the excitation node/defect from the absorbing region boundary is $\lambda_p$. Again this ensures a complex scattering pattern that thoroughly tests the performance of the layers, see Figure 3.2.10.

The scattering pattern is monitored along a line parallel to the rough surface at the same separating distance as the excitation node/defect of $5\lambda_p$. Again the extremities of the monitoring line are separated from the absorbing layer by $\lambda_p$. The line consists of a series of nodes that monitor displacements in the U1 and U2 directions. The response is monitored using two techniques. Firstly displacement in the U1 direction is averaged along the monitoring line for all time producing a single time history response from the defect. The second method measures displacement at a single, arbitrarily selected, node (denoted by a cross) within the monitoring line to ensure that averaging time histories has not eliminated any scattering behaviour.

The performance of the SRM and ALID are assessed. $C_{Mmax}$ is set to $\omega$ for both cases and the Young's modulus within the final layer for the SRM is 1% of the AoS. Layer thickness is varied in increments of $0.2\lambda_p$ to a value of $4.0\lambda_p$.

Figure 3.2.11a) and Figure 3.2.11b) compare two of the time histories directly for the case where the SRM thickness is set to $0.2\lambda_p$ and $4.0\lambda_p$ respectively at a single node within the motoring line. Four signals can be identified corresponding to the incident and reflected waves for each mode.

From the results it can be seen that an insufficiently thick absorbing region of $0.2\lambda_p$ performs very poorly in comparison to the $4\lambda_p$ case. Reflections from the smaller absorbing region pollute the time signal almost immediately, with artifacts continuing to reverberate within the model for the duration. The characteristic features of the incident shear wave have been completely lost and both reflected wave modes have been heavily distorted.

The contribution of the absorbing layers pollutants to the time history can be quantified by calculating the convergence of the time history to that obtained from the case where the model boundaries have no contribution to the scattered signal. This time history is obtained by compiling a model with a significantly larger spatial domain, such that the model boundaries have no interaction with the incident or scattered fields. The convergence of the time histories is calculated using a correlation function given by Equation 3.2.12.

a)

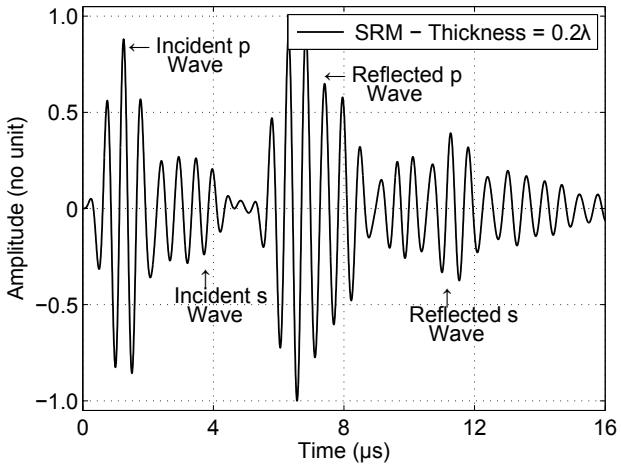


b)

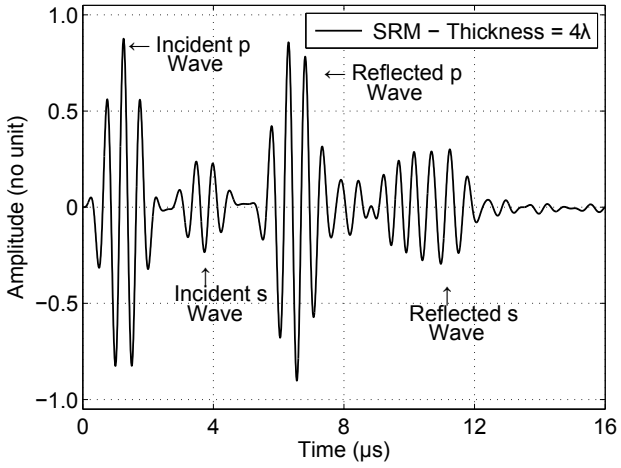


Figure 3.2.11: Comparison of time history from a single node for SRM with a) 0.2$\lambda$ SRM thickness and b) 4$\lambda$ SRM thickness. The 0.2$\lambda$ SRM shows pollutants to time series from unwanted absorbing layer reflections.

a)

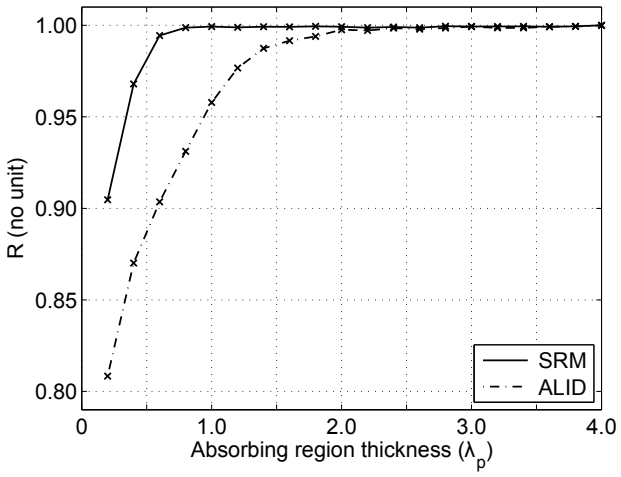


b)

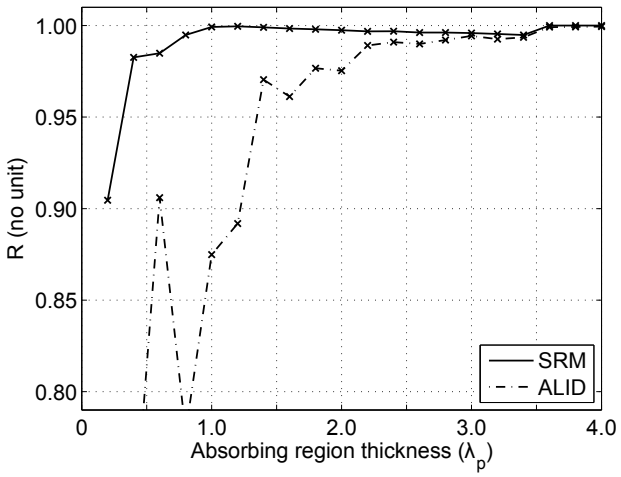


Figure 3.2.12: Correlation function for a) average displacement over a monitoring line and b) at an arbitrary chosen node, for performance of SRM and ALID as a function of region thickness.

$$R = \frac{\sum_{i=1}^{N}(x_i - \overline{x})(y_i - \overline{y})}{\left[\sum_{i=1}^{N}(x_i - \overline{x})^2 \sum_{i=1}^{N}(y_i - \overline{y})^2\right]^{\frac{1}{2}}} \tag{3.2.12}$$

where R is the correlation function ranging between 0 and 1, $i$ is an increment in the discretised time series of length $N$, $x$ is the response from the classic case with mean value $\overline{x}$ and $y$ is the response for each simulation with mean value $\overline{y}$. The value $R = 1$ corresponds to a case of perfect correlation between two compared time histories; the significance being that there is no influence of the absorbing layers on the scattered response. The results are shown in Figure 3.2.12.

It can be seen that the SRM tends to a value of $R = 1$ for an absorbing layer thickness of $\lambda_p$, after which there are diminishing returns in performance. The more varied response observed at a single node can be explained by the lack of averaging, which would filter out any spurious reflections detected. Comparing time series suggests that there is little to gain by having an excessively large SRM since any pollutants that add to the desired time series are of negligible value. In comparison the ALID performance is less effective in reduced spatial domains. Again there are diminishing returns for excessively large thicknesses, however this trend does not begin until thicknesses of $2.5\lambda_p$.

These results show that a proposed SRM thickness of $1.5\lambda$ would be sensible. This is suitably larger that the thickness $\lambda$ at which reasonable convergence has occurred giving a suitable margin of safety, but not so large as to unnecessarily increase the spatial domain.

## 3.3 Optimising absorbing regions

When building any absorbing region, there are a number of variables at the disposal of the user. Generic rules can be applied to absorbing region techniques that will ensure good performance. However, through the use of optimisation functions, highly specialised absorbing regions can be designed that will meet a bespoke set of requirements [94].

This section will discuss methods to optimise the SRM absorbing layer. Here, the optimisation function 'fminsearch' provided by Matlab is used [117]. To do this, the requirements of the layer must first be defined and generic rules must be established to act as a starting point for the optimisation function to operate.

For the purposes of this project, the requirement is that the SRM absorbing layer will be optimised such that any unwanted reflections are of a pre-determined 'tolerable' magnitude across all incident angles. This must be achieved within the smallest thickness of absorbing material possible. The procedure outlined here is transferable to other absorbing boundary methods.

### 3.3.1 Generic rules

For the algorithm to work successfully initial values for the input variables must be specified. From inspection of Equation 3.1.31, it can be seen that $C_M(x)$ is intrinsically linked to the angular frequency of the incident wavelength, $\omega$. From trial and error methods carried out by Rajagopal *et al* [92], it has been observed that the optimal value selected for $C_{Mmax}$ is of the same order as $\omega$. This makes the application of the absorbing regions to different inspection scenarios more straightforward, since now variables can be expressed as a function of frequency rather than resulting to a trial and error method. Ultimately, this enables another variable of the system to be expressed in terms of the single fundamental unit of the model, $\lambda_{inc}$.

For the generic case, the power to which successive layers are raised $p$, is best expressed as a cubic function so that the interface between layers is continuous to the 1st and 2nd order. This is consistent with findings from Rajagopal *et al* [92], who stated that this is sufficient to minimise impedance mismatches between successive layers. The larger impedance mismatches that do occur happen deep within the absorbing region where the incident wave has already been diminished.

When designing an absorbing boundary the user can vary:

1. The total thickness of the layer, $L$.
2. The maximum damping term, $C_{Mmax}$.
3. The maximum attenuation of the stiffness matrix, $\alpha_{max}$.
4. The variation of attenuation across the layer, $p$.

The influence these variables will have on an incident wave is also dependent upon:

1. The inspection angular frequency, $\omega$.
2. The bandwidth of the incident signal.
3. The mesh density, $N$.
4. The amplitude of incident waves as a function of incident angle.

Because of the complex interaction of the incident wave across a multi-layered system, the total performance of the layer is calculated using the Global Matrix method [114]. Despite this, it has been observed that a good overall performance can be achieved for any system, if the following conditions are applied.

1. The total thickness of the layer, $L = 1.5\lambda_{inc}$.

2. The maximum damping term, $C_{Mmax} = \omega$, such that

$$C_M(x) = C_{Mmax} X(x)^p \tag{3.3.1}$$

where

$$X(x) = \frac{x}{L} \tag{3.3.2}$$

producing a number between 0 and 1.

3. The attenuation of the stiffness matrix is given by,

$$E(x) = E_0 e^{-\alpha(x) k_{inc} x} \tag{3.3.3}$$

where

$$\alpha(x) = \alpha_{max} X(x)^p \tag{3.3.4}$$

The maximum attenuation of the stiffness matrix term, $\alpha_{max}$, is such that,

$$\alpha_{max} = \frac{\ln(\alpha_{SRM})}{k_{inc} L} \tag{3.3.5}$$

where,

$$\alpha_{SRM} = \frac{E(L)}{E_0} = 0.01 \tag{3.3.6}$$

4. The variation of attenuation across the layer, $p = 3$.

Generally speaking, performance can always be improved by increasing the total thickness of the absorbing boundary.

### 3.3.2 Total Performance Metric

To design an optimised absorbing boundary it is necessary to calculate the reflection coefficients of incident wave modes and combine these results into a single value that relates to the total performance of the absorbing layer.

Here, the Total Performance Metric (TPM) is defined, which characterises the total performance of the absorbing layer for a given setup.

$$TPM = \frac{R_E}{I_E} \tag{3.3.7}$$

where $R_E$ is the reflected energy from the absorbing boundary and $I_E$ is the incident energy into the absorbing boundary.

$R_E$ can be expressed as a sum over all incident angles for both the compression, $R_E^p$ and shear, $R_E^s$, reflected wave modes.

$$R_E = \int_0^{\frac{\pi}{2}} R_E^p(\theta)d\theta + \int_0^{\frac{\pi}{2}} R_E^s(\theta)d\theta \tag{3.3.8}$$

where $R_E^p(\theta)$ and $R_E^s(\theta)$ are proportional to the amplitudes of the measured mode displacements squared, such that

$$R_E^p(\theta) \propto |A^p(\theta)|^2 \tag{3.3.9}$$

$$R_E^s(\theta) \propto |A^s(\theta)|^2 \tag{3.3.10}$$

By substituting Equation 3.3.9 and Equation 3.3.10 into Equation 3.3.8 and replacing the proportionality with a normalising factor $\frac{2K}{\pi}$, where $K$ is a constant, Equation 3.3.8 becomes

$$R_E = \frac{2K}{\pi}\left(\int_0^{\frac{\pi}{2}} |A^p(\theta)|^2 d\theta + \int_0^{\frac{\pi}{2}} |A^s(\theta)|^2 d\theta\right) \tag{3.3.11}$$

The introduction of the constant $K$ for both wave modes, removes the relationship with energy, and instead produces a convenient metric for assessing the performance of the absorbing boundaries.

The integration is performed from 0 to $\pi/2$ and $A(\theta)$ is calculated using the Global Matrix method. Due to the discretisation of the numerical model, this is not a continuous function, so instead the integration is replaced by a summation in the limit of $d\theta \to 0$, where $d\theta$ becomes the increment.

$$R_E = \frac{2K}{\pi}\left(\sum_{i=1,d\theta}^{\frac{\pi}{2}} |A_i^p|^2 d\theta + \sum_{i=1,d\theta}^{\frac{\pi}{2}} |A_i^s|^2 d\theta\right) \tag{3.3.12}$$

$I_E$ can also be calculated using Equation 3.3.8 by setting the incident amplitude of the displacements to be 1 across all angles and using the same normalisation constant to give $I_E = K$.

A quantitative assessment of the absorbing layers can now be performed across all angles of incidence. The TPM value of the layer will range from 0 - 1 with 0 being complete absorption and 1 being complete

reflection.

### 3.3.3 The optimisation function

Optimisation functions can be used to find the optimum input variables, that meet a given condition, for a given function. Here, the optimisation function 'fminsearch' provided by Matlab is used [117]. The function looks to find the minimum TPM possible for a given scenario. This is achieved by varying all input values until the minimum TPM has been found.

For the SRM, the input variables that can affect the TPM are: total thickness of the layer $L$, maximum damping term $C_{Mmax}$, attenuation of the stiffness matrix $\alpha_{max}$ (or $\alpha_{_{SRM}}$) and the variation of attenuation across the layer $p$.

The first point to amend is the variation of attenuation across the layer $p$ (as referred to in Equation 3.1.36 and Equation 3.2.3). Currently, the literature suggests that a cubic variation is required to minimise impedance mis-matches between successive layers [92]. Since performance is now quantified by the TPM, which is a function of $p$, this assumption can now been lifted.

Furthermore, it has been assumed that the variation in $\alpha(x)$ and $C_M(x)$ are both characterised by $p$. These functions can vary independently of one another and are instead expressed by Equation 3.3.13 and Equation 3.3.14.

$$C_M(x) = C_{Mmax} X(x)^{p_{C_M}} \tag{3.3.13}$$

$$\alpha(x) = \alpha_{max} X(x)^{p_\alpha} \tag{3.3.14}$$

where $p_{_{C_M}}$ and $p_{_\alpha}$ represent the variation of attenuation across the layer for the damping and stiffness functions respectively.

Having made this distinction, the TPM for a given absorbing layer can be expressed by the function:

$$TPM = f\left(\omega, N, C_{Mmax}, \alpha_{_{SRM}}, L, p_{_{C_M}}, p_{_\alpha}\right) \tag{3.3.15}$$

The optimisation function can now be run until the TPM reaches a pre-determined level that is deemed acceptable. If an absorbing layer is being built for a specific case, it may be necessary to put restrictions in place. This is achieved by fixing one or more of the variables within the TPM function, for example, $\omega$, $N$ and $L$, which will be constants of the FE model.

In other instances, it may be a requirement that the absorbing layer need only be optimised for a specific incident angle or wave mode. To achieve this, instead of optimising the layer for the TPM, the function will instead optimise for $A(\theta_{inc})$, the reflected amplitude of a given mode at a given angle.

To use the optimisation function correctly, it is important to avoid being trapped by local minima

when looking for the global minimum. To achieve this, the optimisation function requires starting values for the inputs, before finding the optimal input values themselves. These should be equal to those given for the generic case. This will help to avoid finding the local minima over the global values.

### 3.3.4 Absorbing boundary thickness

Performance of absorbing layer techniques will always improve with increasing thickness. This is due to there being a greater amount of attenuative material within which the wave can decay. Here the goal is to achieve a tolerable level of reflection from the layer within a minimal thickness, thereby offering the maximum efficiency possible to the FE solver.

The addition of absorbing layers will inevitably increase the number of degrees of freedom of the system. A generic expression for the percentage increase in this value can be expressed for rectangular domains containing structured quadrilateral elements. Figure 3.3.1 shows such a system with length $a$, height $b$, absorbing layer thickness, $n\lambda$, containing structured rectangular elements of size $d$.

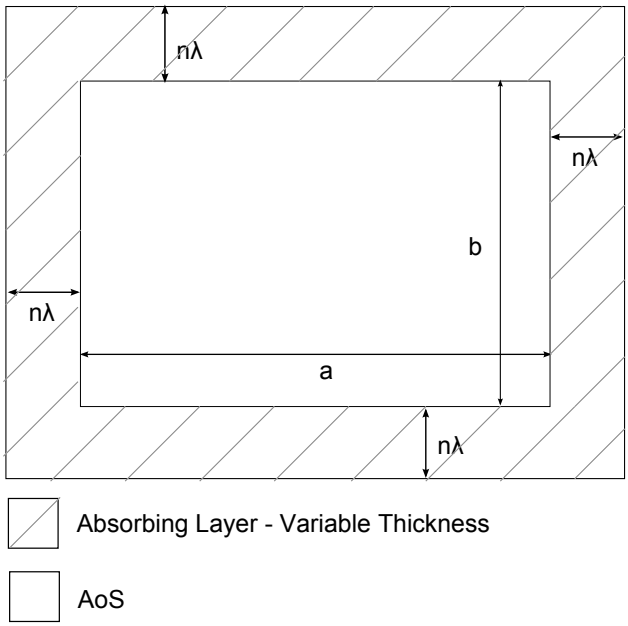


Figure 3.3.1: Rectangular FE model of length $a$, height $b$, and absorbing layer thickness $n\lambda$.

Equation 3.3.16 provides an expression for the number of degrees of freedom that are to be solved inside the AoS, $DoF^{2D}_{AoS}$.

$$DoF^{2D}_{AoS} = \frac{ab}{d^2} \tag{3.3.16}$$

The addition of absorbing layers with thickness $n\lambda$ increases the number of degrees of freedom, $DoF^{2D}_{total}$, as given by Equation 3.3.17.

$$DoF^{2D}_{total} = \frac{ab + 2n\lambda(a+b) + (2n\lambda)^2}{d^2} \tag{3.3.17}$$

From Equation 3.3.16 and Equation 3.3.17, the percentage increase in degrees of freedom, $DoF^{2D}_{\%}$, due to the addition of absorbing layers can be calculated, Equation 3.3.18.

$$DoF^{2D}_{\%} = \frac{DoF^{2D}_{total} - DoF^{2D}_{AoS}}{DoF^{2D}_{AoS}} \times 100 \tag{3.3.18}$$

which gives

$$DoF^{2D}_{\%} = \frac{2n\lambda\left[(a+b) + 2n\lambda\right]}{ab} \times 100 \tag{3.3.19}$$

Equation 3.3.19 can be readily extended to a three-dimensional problem by the inclusion of breadth c, containing structured quadrilateral elements. In this case the percentage increase in degrees of freedom, $DoF^{3D}_{\%}$, is given by Equation 3.3.20.

$$DoF^{3D}_{\%} = \frac{2n\lambda\left[(2n\lambda)(a+b+c) + (ab+ac+bc) + (2n\lambda)^2\right]}{abc} \times 100 \tag{3.3.20}$$

For absorbing regions operating within significantly reduced spatial domains, performance is more susceptible to changes in the frequency of the incident wave. This point is illustrated in Figure 3.3.2a) and Figure 3.3.2b). Here, the one-dimensional model described in Section 3.2.2 is used to evaluate the performance of the SRM in the frequency domain for increasing layer thickness expressed as a function of the wavelength of the incident wave. The frequency spectrum of the incident 5 cycle tone burst is compared with the frequency spectrum of the reflected signals.

Figure 3.3.2a) and Figure 3.3.2b) show that thicker absorbing layers are less susceptible to wider bandwidth signals. If the optimisation function is used to minimise layer thickness, it should be done with care, since the high performance of the absorbing region may only be achievable within a narrow frequency range. For this reason, sources with wider bandwidths would need to consider the performance of the SRM across a frequency range rather than a central maximum. This property partly explains the good performance of PML, since it is normally used in the frequency domain and therefore only has to be optimised for the single frequency of excitation.

From the observations made in this study, a suitable SRM thickness of $1.5\lambda_{inc}$ is capable of achieving the tolerable levels of reflections required for all possible incident angles across a sufficiently broad frequency spectrum.

a)

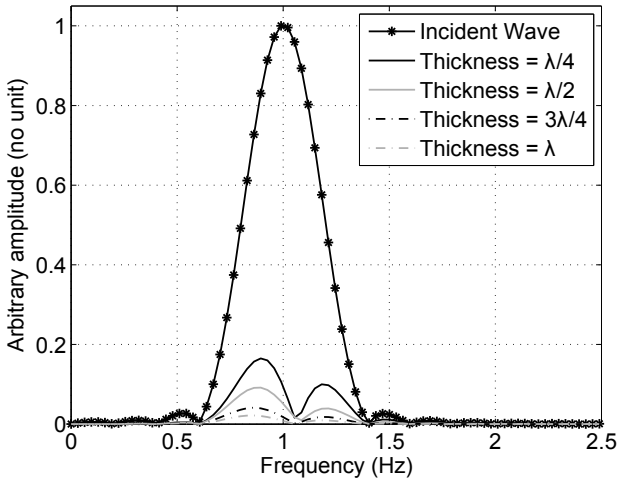


b)

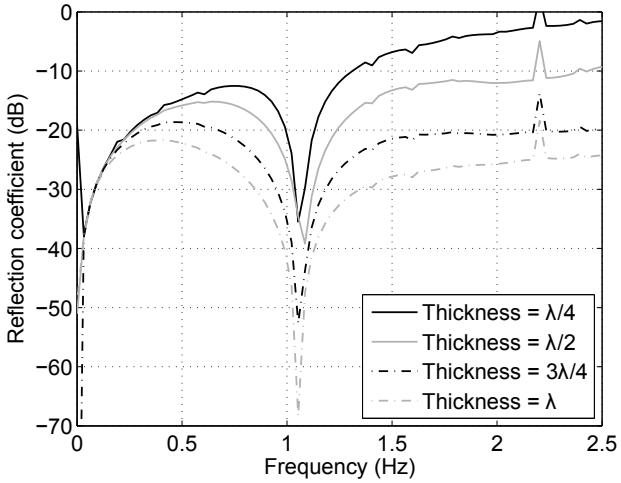


Figure 3.3.2: Figure showing a) the frequency response from the incident and reflected signals for increasing layer thickness and b) the reflection coefficient as a function of frequency for each layer.

## 3.4 Stiffness Reduction Method and Infinite Elements

To date, it is widely thought that Infinite Elements offer a reasonable means to replicate infinite elastic media. Boundary conditions are applied at the edge of the spatial domain that absorb incident waves with minimal reflection [86]. The Infinite Element operates within a single row of elements meaning that they contribute the minimum in computational expense. Furthermore, Infinite Elements are common in commercial FE packages and do not limit the flexibility of the solver. However, despite operating in virtually zero space, they do not offer the high level of performance required for elastodynamic scattering [92, 97].

As a result, absorbing layer methods have been developed, and have been discussed here for use in explicit time domain commercial FE codes. Despite their success, it has been noticed that for three-dimensional models, the additional contribution of the absorbing layer to the spatial domain is relatively large. Recent advances in absorbing layer methods have seen the development of the Stiffness Reduction Matrix (SRM), which partly overcomes this issue by reducing the size of the spatial contribution from $3\lambda$ to $1.5\lambda$.

With the size of the spatial domain having such a direct effect on three-dimensional model sizes, it is difficult to ignore the attraction of improved performance that Infinite Elements may offer. Therefore, a further extension can be made by placing a layer of Infinite Elements at the end of absorbing layers. The combination of the two should offer a spatial domain that is further reduced in size, with no compromise to performance.

### 3.4.1 Analytical model

Before this approach can be implemented, an analytical solution must be established such that the performance of the layers can be quantified. Firstly, this is done for a boundary that contains only Infinite Elements as discussed by Lysmer *et al* [95, 96]. Instead of the stress-free boundary conditions, the normal and tangential components of the stress at the model boundary are modified to include dimensionless parameters which when varied, alter the performance of the boundary (Equation 3.1.1 and Equation 3.1.2).

The proposed boundary conditions corresponds to a situation where the boundary is supported on infinitesimal dash-pots oriented normal and tangential to the boundary. By applying these conditions to the wave equation and using standard harmonic solutions from the Helmholtz decomposition, the amplitudes of the reflected wave modes from the boundary can be calculated (Equation 3.1.3, Equation 3.1.4, Equation 3.1.11 and Equation 3.1.12).

Figure 3.4.1 shows results of this analytical solution compared against results from a numerical simulation (using ABAQUS/Explicit [113]) for an incident compression wave across a range of incident angles.

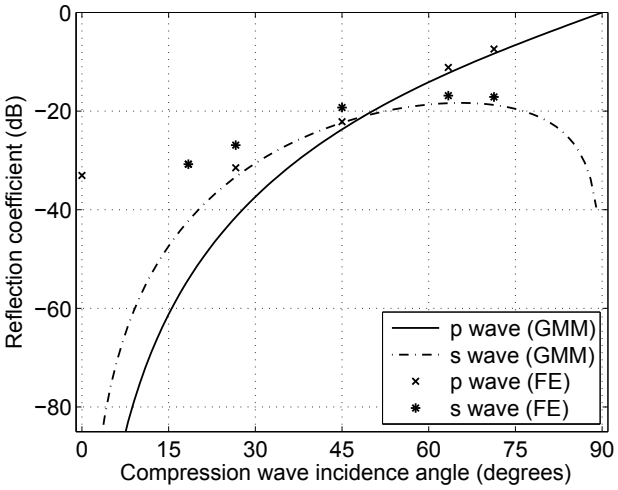


Figure 3.4.1: Analytical and numerical reflection coefficients for an absorbing boundary composed of Infinite Elements for an incident compression wave.

Figure 3.4.1 shows some disagreement between the two methods. The same trends are observed; whereby increasing the angle of incidence results in an increase in the magnitude of the reflection coefficient. However, the predictions made using an analytical approach are far more optimistic that what has been measured numerically. This discrepancy can however be explained and accounted for.

From inspection of Equation 3.1.3, Equations 3.1.4, Equations 3.1.11 and Equations 3.1.12, it can be seen that the performance of Infinite Elements is independent of inspection frequency. The only material constant that determines the magnitude of the reflection coefficients is the ratio of the compression and shear wavenumbers. For homogeneous, isotropic, elastic media this is almost always equal to $\frac{1}{2}$, or small deviations away from this value.

The performance of the Infinite Elements is however dependent upon the mesh density of the FE model. So far, the analytical solution does not account for any numerical reflections that result from the spatial discretisation of the mesh itself. This is unavoidable and is the dominant scattering mechanism associated with the application of Infinite Elements to FE problems.

To understand this behaviour, the reflections caused by mesh scattering at the Infinite Element boundary are quantified. This is done by calculating the reflection coefficient from a row of Infinite Elements for a normal incidence compression wave. This case has been chosen because from Figure 3.4.1 it can be seen that the analytical model reflection coefficient is approaching zero, i.e. perfect performance at $\theta_{inc} = 0^o$. Therefore, any reflections that are observed for this case in a numerical model, must be a result of numerical mesh scattering. The reflection coefficient for this case is recorded for increasingly finer meshes, see Figure 3.4.2.

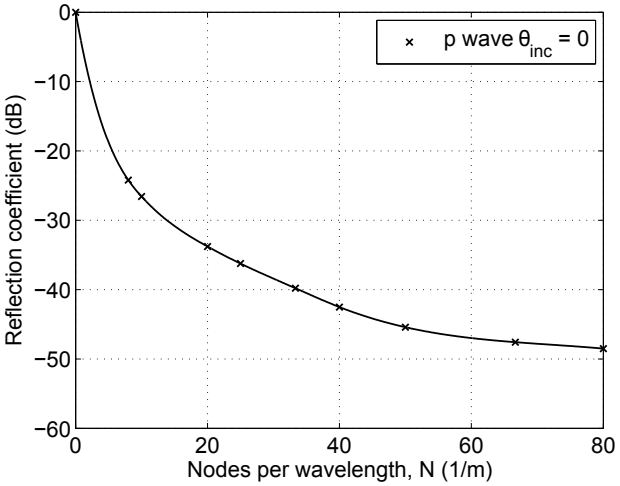


Figure 3.4.2: Numerical reflection from Infinite Element boundary for increasingly refined mesh.

From Figure 3.4.2 it can be seen that increasing the refinement of the mesh will decrease the magnitude the numerical mesh scattering. This however is not a linear relationship; to completely remove the component of the numerical reflection the mesh spacing between elements must tend to 0.

The introduction of mesh scattering is not so dissimilar to a phenomenon as reported by Rajagopal *et al* when investigating the performance of PML [92]. In theory, no reflection should occur at the interface with the PML, nor inside it. However, numerical results do not confirm this. Reflections from the PML are observed for normally incident compression waves. Again the magnitude of the numerical reflection is a function of mesh density, and therefore attributed to a mesh scattering phenomenon.

The numerical reflection caused by mesh scattering can be found by taking the reflection coefficient from a row of Infinite Elements for a normal incidence compression wave. This component is then added to the prediction made using the analytical model, Figure 3.4.3.

By making this correction, there is now very good agreement between the two models. The behaviour of the Infinite Elements can be predicted confidently and the performance assessed. The performance of the layers is affected by the variables $a$ and $b$, with optimal performance achieved when $a$ and $b$ are equal to 1 [95].

Having established a means to predict the performance of a set of Infinite Elements, a fully functional analytical model is required the can combine the performance of SRM containing a row of Infinite Elements. This will allow for a means to validate the performance of the boundary and provide a quick method for calculating optimal model variables. To achieve this the Global Matrix method will be used [114]. Previously it has been used to calculate the reflection coefficient from a multi-layered system.

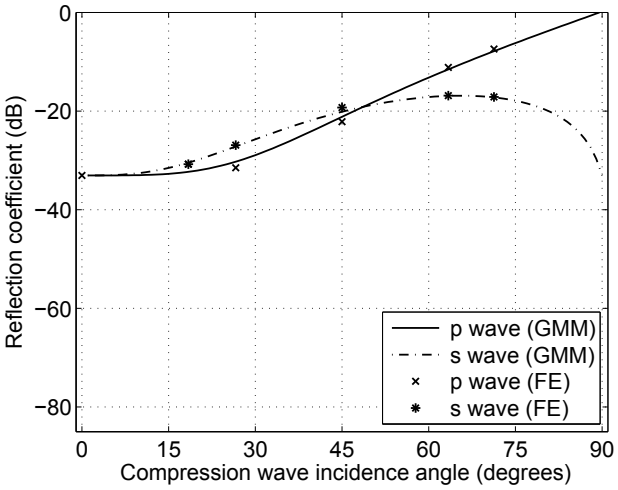


Figure 3.4.3: Analytical and numerical reflection coefficients for an absorbing boundary composed of Infinite Elements for an incident compression wave with numerical mesh scattering correction.

The Global Matrix method establishes equilibrium for the displacements and stresses at each layer interface in both the forward and backward propagating directions. By generating an equation for each layer interface and inserting known model variables at the incident boundary, the system can be solved simultaneously. At the end of the final layer, stress-free boundary conditions are applied.

$$\sigma_{xx} = 0 \tag{3.4.1}$$

$$\sigma_{xy} = 0 \tag{3.4.2}$$

Integration of Infinite Elements in the Global Matrix method for this system (Equation 3.2.10), will require these boundary conditions to be changed to those given in Equation 3.1.1 and Equation 3.1.2.

The difficulty with implementing the two techniques is caused by the fact that the Infinite Element boundary conditions are non-zero and unknown. Referring to Equation 3.2.10, the layer properties and the RHS are all known, allowing for a matrix inversion techniques to be used to obtain the wave potentials traveling out of the layer, $\phi_{N[1]}$ and $\boldsymbol{\psi}_{N[1]}$.

To correct for this, the stress-free boundary conditions given by Equation 3.2.7 need to be moved to the LHS of the equation. This allows for the RHS to remain 0 and the Infinite Element boundary conditions to be expressed as a function of wave potentials, which can then be solved using matrix inversion.

The equation within the final layer of an absorbing boundary with Infinite Elements becomes,

$$L^b_{[end]} \begin{bmatrix} \phi_{P[end]} \\ \boldsymbol{\psi}_{P[end]} \\ \phi_{N[end]} \\ \boldsymbol{\psi}_{N[end]} \end{bmatrix} = \begin{bmatrix} \sigma_{xx} \\ \sigma_{xy} \end{bmatrix} \tag{3.4.3}$$

From Equation 3.1.1 and Equations 3.1.2 this becomes

$$L^b_{[end]} \begin{bmatrix} \phi_{P[end]} \\ \boldsymbol{\psi}_{P[end]} \\ \phi_{N[end]} \\ \boldsymbol{\psi}_{N[end]} \end{bmatrix} = \begin{bmatrix} a\rho C_p \frac{\partial u_x}{\partial t} \\ b\rho C_s \frac{\partial u_y}{\partial t} \end{bmatrix} \tag{3.4.4}$$

To solve the matrix all the variables are brought over to the LHS, giving

$$L^b_{[end]} \begin{bmatrix} \phi_{P[end]} \\ \boldsymbol{\psi}_{P[end]} \\ \phi_{N[end]} \\ \boldsymbol{\psi}_{N[end]} \end{bmatrix} - \begin{bmatrix} a\rho C_p \frac{\partial u_x}{\partial t} \\ b\rho C_s \frac{\partial u_y}{\partial t} \end{bmatrix} = \begin{bmatrix} 0 \\ 0 \end{bmatrix} \tag{3.4.5}$$

The term $\frac{\partial u}{\partial t}$ can now be expressed in terms of the wave potentials and becomes

$$L^b_{[end]} \begin{bmatrix} \phi_{P[end]} \\ \boldsymbol{\psi}_{P[end]} \\ \phi_{N[end]} \\ \boldsymbol{\psi}_{N[end]} \end{bmatrix} - \begin{bmatrix} -i\omega a\rho C_p M^f_{1[end]} \\ -i\omega b\rho C_s M^f_{2[end]} \end{bmatrix} \begin{bmatrix} \phi_{P[end]} \\ \boldsymbol{\psi}_{P[end]} \\ \phi_{N[end]} \\ \boldsymbol{\psi}_{N[end]} \end{bmatrix} = \begin{bmatrix} 0 \\ 0 \end{bmatrix} \tag{3.4.6}$$

where $M^f_{1[end]}$ and $M^f_{2[end]}$ are the first and second rows respectively of $M^f_{[end]}$ given by Equation 3.2.4. Finally, the common wave potentials can be factorised leaving

$$\left( \left[ L^b_{[end]} \right] - \begin{bmatrix} -i\omega a\rho C_p M^f_{1[end]} \\ -i\omega b\rho C_s M^f_{2[end]} \end{bmatrix} \right) \begin{bmatrix} \phi_{P[end]} \\ \boldsymbol{\psi}_{P[end]} \\ \phi_{N[end]} \\ \boldsymbol{\psi}_{N[end]} \end{bmatrix} = \begin{bmatrix} 0 \\ 0 \end{bmatrix} \tag{3.4.7}$$

From inspection, in the instance where $a$ and $b$ are zero the Infinite Elements are removed and the stress-free boundary conditions resumed.

### 3.4.2 Numerical model

Despite the Infinite Element boundary conditions being successfully implemented into the Global Matrix method, this derivation does not include the addition of the numerical mesh scattering reflection. This cannot be directly implemented into the Global Matrix method. This is because the numerical calculation of mesh scattering, given in Figure 3.4.2, only reveals the absolute value of the reflected signals. Implementation of this into the Global Matrix method would require these amplitudes to be expressed as a function of wave potentials, which is an unknown.

Two approaches are now possible, both of which allow for an approximation to be made for the SRM and Infinite Element combination. These involve the establishment of a performance range, within which the expected reflection for the layers is obtained; or adjustment of the Infinite Element constants, $a$ and $b$, to operate less than perfectly.

For both instances the same FE model is used. A $1Hz$ wave is incident on the absorbing boundary across all incident angles for both compression and shear wave modes. The model has 40 nodes per wavelength for the incident compression wave case, and the SRM thickness is $0.75\lambda_{inc}$. The SRM input variables have been selected using an optimisation function.

#### 3.4.2.1 Establishing a performance range

To establish a performance range the Global Matrix method is used to calculate the reflection coefficients from a set of absorbing regions for two instances; the SRM on its own and the SRM and Infinite Elements combined. This will establish an upper and lower band, within which the measured numerical value will lie. Figure 3.4.4 and Figure 3.4.5 show the results for incident compression and shear wave modes respectively.

The results show that for all instances, the measured numerical reflections fall within the expected range. The performance of the absorbing layers will not be as good as the predictions made using the analytical model due to the fact that numerical mesh scattering is not included in the solution. Although, as incident angle increases, the discrepancy between the two predictions diminishes, showing better agreement between the numerical and analytical results.

#### 3.4.2.2 Adjustment of the Infinite Element constants

The performance of the Infinite Elements is dependent upon the values of $a$ and $b$, with optimal performance observed when $a = b = 1$. Here, these values are altered to operate outside of the optimal values to account for mesh scattering that is not included in the analytical solution. Figure 3.4.6 shows the results for an incident compression wave, where the values $a = b = \frac{2}{3}$ is used, to indirectly account for the mesh scattering.

a)

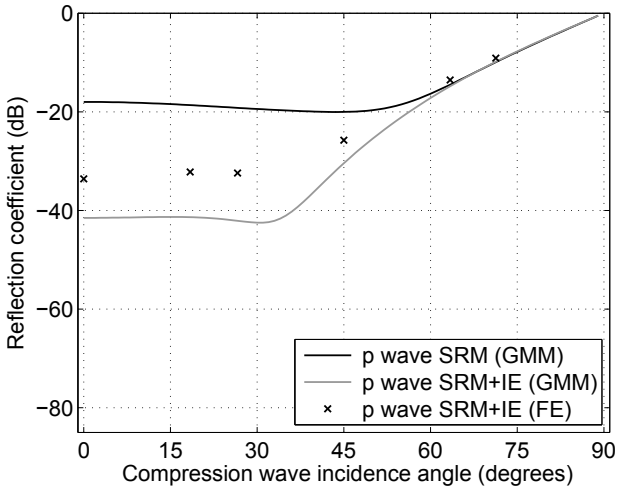


b)

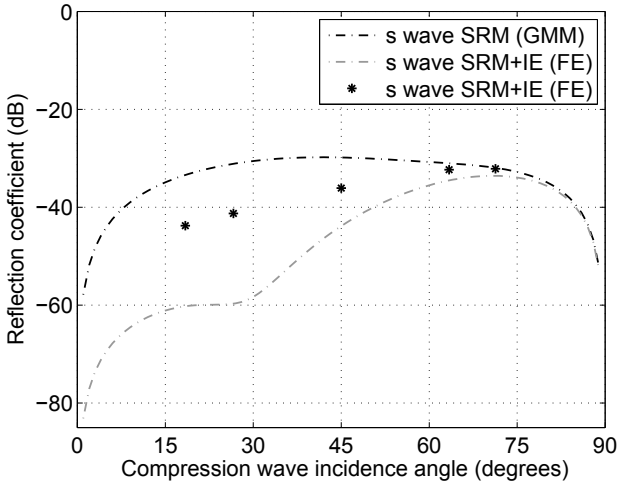


Figure 3.4.4: Performance of SRM and Infinite Elements absorbing boundary for an incident compression wave for a) reflected compression wave modes and b)reflected shear wave modes.

a)

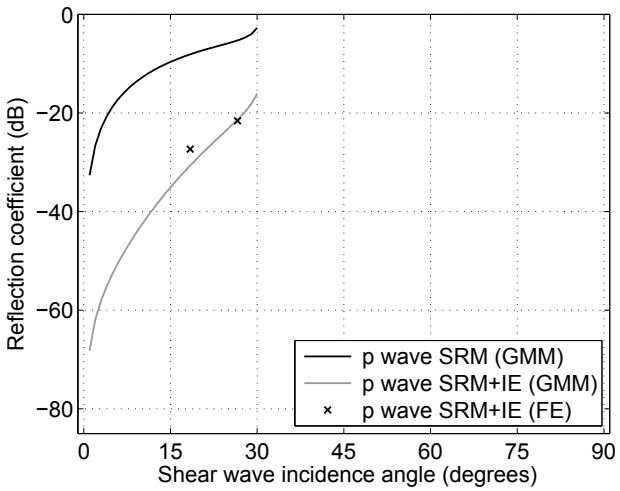


b)

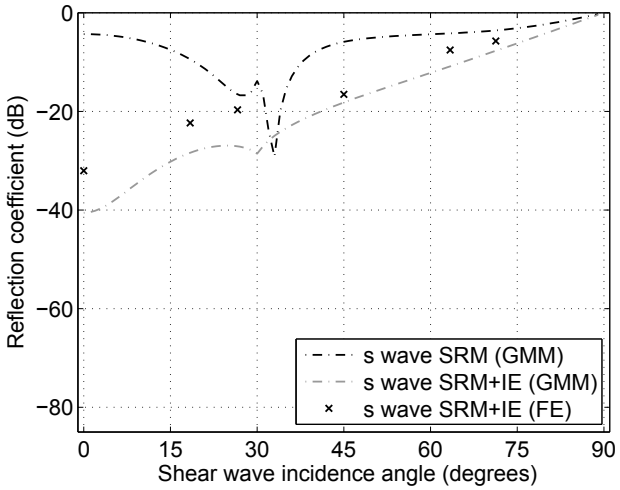


Figure 3.4.5: Performance of SRM and Infinite Elements absorbing boundary for an incident shear wave for a) reflected compression wave modes and b)reflected shear wave modes.

a)

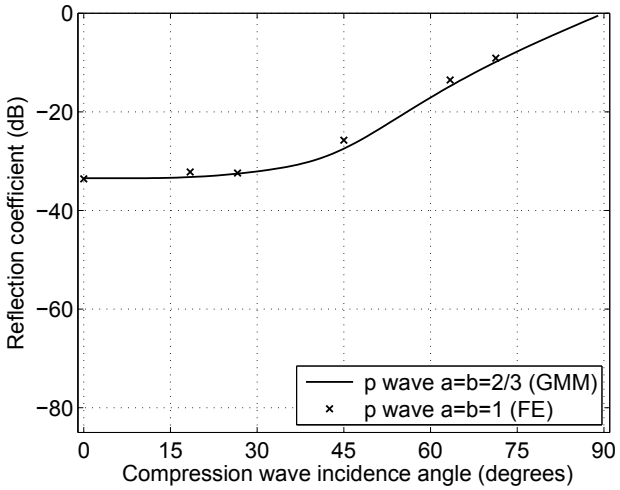


b)

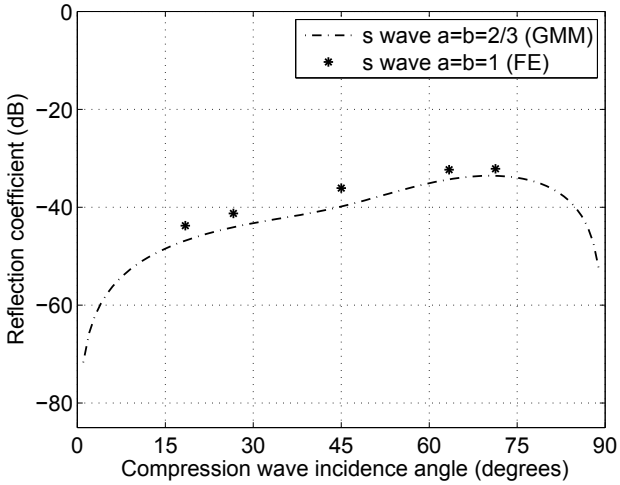


Figure 3.4.6: Performance of SRM and Infinite Elements absorbing boundary for an incident compression wave for a) reflected compression wave modes and b)reflected shear wave modes.

Although this method for compensating for mesh scattering can provide the correct answer, it is unclear what the values of $a$ and $b$ must be. Here, $a$ and $b$ have been found using a trial and error method. This is not an appropriate solution since the requirement is to confidently predict the performance of the absorbing region by solely using an analytical model. For this reasons, this approach will no longer be investigated.

### 3.4.3 Performance

Unfortunately, the performance that was thought to be possible with a combination of SRM and Infinite Elements has not been realised. It was originally expected that appending a layer of Infinite Elements at the end of absorbing layers would allow for increased absorption of incident waves; where the process of attenuation is shared. This in turn would result in an absorbing region that could offer the same level of performance as SRM alone, but within a significantly reduced spatial domain.

When using absorbing layer methods, it is thought that two phenomena are responsible for unwanted reflections returning from the boundary; reflections from successive layers due to impedance mismatching and reflections from the stress-free boundary at the end of the absorbing region. By introducing Infinite Elements to absorbing layers, the latter could ideally be considered negligible.

With conventional absorbing regions, multiple layers with gradually increasing damping properties are used to attenuate the wave. To avoid impedance mismatches between successive layers, the material properties of the layers close to the AoS are similar to those of the parent material. As a result these layers are responsible for very little damping in comparison to those situated at the end of the layer. These layers are best thought of as transition layers; a region that allows for a wave to propagate from the AoS to a region of heavy damping. It is only the final few layers at the end of the absorbing region that are responsible for the vast majority of wave attenuation.

This can be demonstrated through the use of a one-dimensional FE model. A compression wave with frequency 1 Hz is incident on a SRM absorbing region. The absorbing layer has $C_{Mmax} = \omega$, $\alpha_{SRM} = 0.01$ and a thickness of $1.5\lambda_{inc}$. Figure 3.4.7 shows the absolute amplitude of the incident wave as it passes through the absorbing layers.

From Figure 3.4.7 it can be seen that the wave attenuates very slowly as it enters the layer; with the final third providing the majority of the attenuation.

When combining SRM with Infinite Elements, the heavily damped elements are replaced. By doing this, the main attenuation mechanism offered by absorbing layers is lost. The transition layers remain, but they provide insufficient absorption of the incident wave, and instead provide semi-impedance matching to the Infinite Elements. What remains is a row of Infinite Elements that are connected to the AoS by transition elements. This provides insufficient absorption of incident waves. If the final few layers of heavily damped elements remain, then appending a row of Infinite Elements is of little benefit.

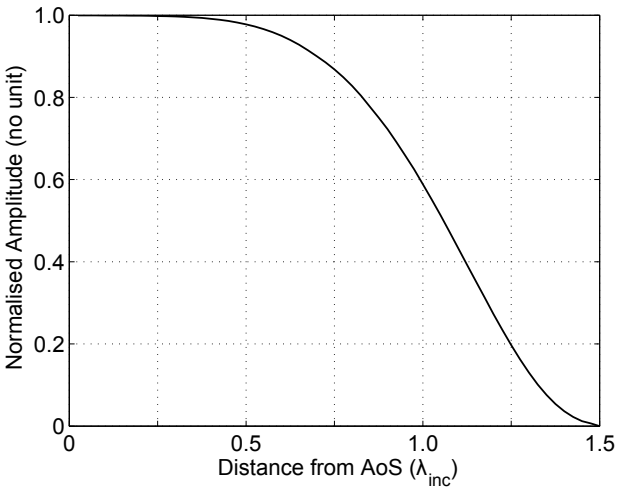


Figure 3.4.7: Figure to show the absolute amplitude of the incident wave as it passes through the absorbing layers for a one-dimensional model.

The vast majority of incident wave energy has already been absorbed by the absorbing layers making the addition of Infinite Elements redundant. It has also been noticed that the source of unwanted reflections from absorbing layers is more due to the impedance mis-matching between successive layers, than it is from reflections from the stress-free boundary. Therefore, unwanted reflections back into the AoS have already occurred before the Infinite Elements absorb the incident wave.

This results in a paradox. The addition of Infinite Elements to a set of absorbing layers will improve their performance. However, this improvement in performance cannot be converted into a reduction in the size of the spatial domain of the absorbing region. The performance increase observed has diminishing returns; for a set of absorbing layers that are already performing well, the addition of Infinite Elements will result in a negligible contribution to the net absorption offered by the region.

For the reasons outlined here, and owed to the fact that a successful means to integrate mesh scattering into an analytical model could not be found, the addition of Infinite Elements to absorbing layers will no longer be considered in this study.

## 3.5 Conclusions

This chapter reviewed absorbing boundary methods that are applicable for the absorption of ultrasonic waves in FE codes. The techniques were assessed according to their applicability in solving ultrasonic NDE inspection problems using commercially available, explicit, time domain, FE codes. This resulted in the development of a new absorbing boundary method, the SRM.

Previously, ALID had been the tool of choice for these applications over the more spatially efficient PML. This was due to the flexibility offered to modellers for applications in commercial codes without the need for specific programming. Extensions to absorbing boundary techniques, such as CALM, have shown improvements over conventional ALID. However, despite this, increasing demand placed on computational resource means that further improvements were required.

The SRM, which has been developed by the author specifically for this project, has been shown to outperform ALID across all angles of incidence within a significantly reduced spatial domain, whilst still maintaining the requirement for there to be no implementation of specific programming or functionality, so that it can be deployed in commercial FE codes. All absorbing layer variables can be controlled from the easily accessible stiffness and damping matrices. The reduction in stiffness is defined as a function of the known physical properties of the model, maximum damping values are a function of the inspection frequency and the thickness of the absorbing region is of the order of $1.5\lambda_{inc}$. A two-dimensional analytical model based upon the Global Matrix method was shown to achieve excellent agreement with numerical simulations and can be used to further optimise SRM variables if required.

The trade-off observed is a noticeable reduction in the Courant or CFL number in successive absorbing layers, resulting in an increase in propagation velocity errors in the absorbing region. However, this is of little concern since sufficient decay of incident waves has already occurred before the wave reaches these layers, the effects are minimised for increasingly refined meshes and these waves are not radiated back into the AoS.

A set of generic rules have been established to allow for the development of a well-performing absorbing region. Performance of absorbing regions can however be developed further through the use of optimisation functions. This is done using the TPM, a single parameter the characterises the performance of an absorbing region across an angular range. The optimisation function looks to reduce the TPM for a given scenario, thereby allowing for a high performing absorbing region to be built within a significantly reduced spatial domain.

Finally, the concept of appending a row of Infinite Elements onto the end of an absorbing region is discussed. Due to the difficulties associated with calculating mesh scattering, a fully inclusive analytical model could not be derived. Furthermore, the expected performance was not realised, owed to the fact that absorbing layer methods are composed of transition elements which contribute very little to the total attenuation. For these reasons, the combination of an absorbing layer and Infinite Elements is no longer considered.

# 4 Efficient Finite Element Techniques

Within recent years commercial FE packages have been used increasingly to simulate elastic wave propagation and scattering problems [63, 64]. Analytical solutions to these interactions are often impossible or impractical to solve, whereas numerical techniques offer solutions that extend to any desired level of complexity.

The greatest limitation when using FE codes is the computational resource that can be allocated to solving the problem. To maintain a highly accurate solution, novel techniques have been developed that allow for the use of reduced spatial domains that do not compromise on having an accurate representation of the system.

Such methods include the simulation of infinite elastic space, as discussed in Chapter 3, and the use of domain linking algorithms [79, 80, 82, 118]. These methods allow modellers to only consider a small area immediately surrounding a scatterer or feature of interest. Computational resource can therefore be focused on a highly accurate representation of the AoS. This is particularly advantageous when considering three-dimensional problems where even a significantly reduced spatial domain can consist of tens of millions of degrees of freedom to be solved.

This chapter will discuss efficient spatial and temporal discretisation methods for the assembly of FE models specific to ultrasonic NDE inspection problems using commercial FE codes. Generic rules are established from a review of the recent literature and findings from investigations carried out in this project.

The chapter also discusses the application of domain linking algorithms to ultrasonic NDE inspection simulations. The foundation for this approach is based upon developments made by researchers at Imperial College London [82, 118], where the domain linking concept is derived for the generic case and applied to the commercial software package ABAQUS/Explicit [113].

The focus here is on the development of this particular domain linking concept and ensuring that the deployed methods are viable for industrial practices. Where previous authors have demonstrated a proof-of-concept in an academic environment, here validation is achieved through thorough experimental validation using standard calibration targets that are often referred to for industrial applications.

Finally, the domain linking algorithm is coupled to a beam computation tool, allowing the transducer response to be considered in the scattering problem. The validation of FE models is achieved by making comparisons with experimental data for both two and three-dimensional cases.

The author's contributions to the field of efficient FE modelling techniques have been to identify a methodology that allows FE methods to become an industrially viable solution for modelling ultrasonic NDE inspections. Specifically, the approach taken by Rajagopal *et al* [82] has formed the basis for satisfying this requirement. The extension made here has focused on reducing the total computational demand of FE models, allowing them to run within an acceptable time-frame as outlined by industrial standards. Following the development of a robust methodology, extensive experimental validation for both the two and three-dimensional cases has been performed. The author's own contributions to this field, especially towards the three-dimensional case, are discussed by Choi *et al* [118].

## 4.1 Discretisation

One of the main advantages when using the FE method for elastic wave scattering problems is the ability to automatically calculate the response from complex, stress-free, boundaries that can be defined by structured or unstructured meshes. This feature requires no additional programming or functionality in the FE method and is only dependent upon having an accurate representation of the system.

When meshing a spatial domain a key parameter that determines computation time is the number of degrees of freedom to be solved. In general, the number of degrees of freedom associated with a FE model is proportional to the number of nodes defining the system.

Nodal density is an important property for defining the accuracy of a FE model. Because the FE model is a discretised system, errors arise in the propagation velocities of incident waves. Work by Drozdz [115], calculated the variation in propagation velocity as a function of mesh density. These errors are calculated numerically, but have been approximated by an analytical expression.

$$E_c = \frac{180}{N^2} \tag{4.1.1}$$

where $N$ is the nodes per wavelength as defined in Equation 2.3.20 and $E_c$ denotes the percentage error in propagation velocity.

The mesh density has a considerable impact on computation time. From inspection of Equation 4.1.1, it can be seen that $E_c$ is inversely proportional to $N^2$. Therefore, the benefits of increasing mesh density have diminishing returns on the accuracy of the solution. Drozdz [115], states that it is difficult to apply a generic rule for acceptable mesh density. However, it can be stated that a mesh density of 10 nodes per wavelength achieves good qualitative results and that a mesh density of 30 nodes per wavelength achieves excellent results. Ultimately the decision lies at the discretion of the modeller.

Temporal discretisation can also affect the accuracy of a FE model. In order to obtain a stable solution, the time step of the model must not be greater than the critical time step as characterised by the CFL number (see Section 2.3.5). If the nodal separation is not constant, or if there are varying

material properties, it may be necessary to have a CFL number that is less than 1 in many parts of the model to maintain a stable solution. As with varying the mesh density, a CFL number less that 1 will introduce errors in the propagation velocity.

Drozdz [115], has quantified these effects by numerical studies. As the CFL number decreases the error in the propagation velocity will increase. However, the variation in the error is still a function of nodal density. The analytical expression given in Equation 4.1.1 must therefore be modified to include the CFL term.

$$E_c = \frac{180(1 - CFL^2)}{N^2} \tag{4.1.2}$$

As the CFL number tends to 0, Equation 4.1.2 tends to Equation 4.1.1. Drozdz explains that although decreasing the CFL number increases errors in propagation velocity, these errors can be offset by having a high nodal density. However, modellers should consider that reducing the CFL number will result in an increase in the number of time steps to be solved, and therefore, increase the computation time of the model.

A variety of element types can be selected for representing the spatial domain. The most fundamental of these are square and triangular elements, which when extended into three dimensions become cubic and tetrahedral.

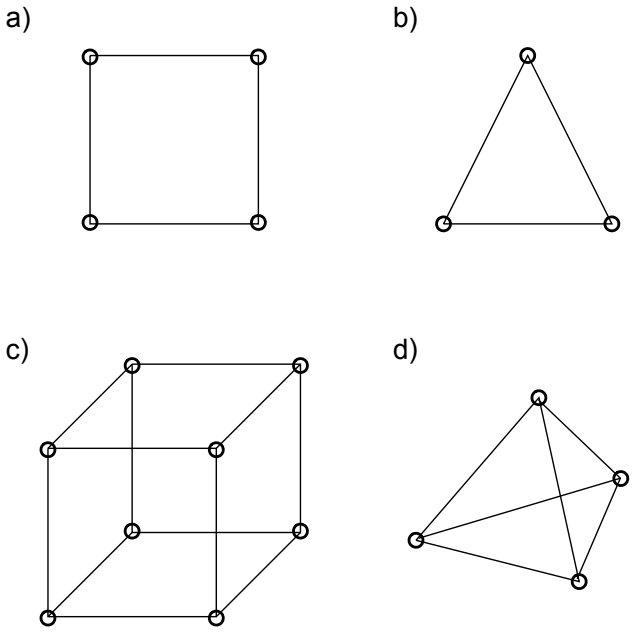


Figure 4.1.1: Figure to show a) a square element b) a triangular element c) a cubic element and d) a tetrahedral element.

Both structured and unstructured meshes can be used, however, unstructured meshes, and particularly those made of triangular and tetrahedral elements, allow for the mesh to conform to complex defect geometry. One concern is that if a poor meshing algorithm is used triangular elements can become deformed. This deformation of elements leads to a local change in the acoustic impedance of the element and consequently unwanted reflections from within the mesh.

One approach has been to consider a refined structured mesh to define complex geometry in a stair case definition. Work by Drozdz [115], has shown this to be an inaccurate representation of the system, regardless of nodal density. Triangular meshes generated by free meshing algorithms are more suited to complex geometry, with any variation in element size causing a negligible deterioration of results. It is recommended that regular square elements should be used for models where features can be aligned to a structured nodal grid and free meshes of triangular elements be used for complex geometry.

In some instances, it may be advantageous to use a combination of coarse and refined meshes by implementing local mesh refinement. In this scenario, a coarse mesh is used to define the majority of the model, but a refined mesh defines a small region immediately surrounding the defect or feature of interest. Again this has been studied by Drozdz [115], where abrupt and gradual mesh density variation is considered. The acoustic impedance of an element is a function of the element size. Any variation in the size of the elements will introduce impedance mismatches between adjacent elements and therefore scattering from the mesh itself. Although a gradual variation in mesh density reduces this phenomenon, both approaches produce an unacceptable level of reflection.

A more acceptable approach uses a combination of structured and unstructured triangular or tetrahedral elements with a partitioning function that allows the modeller to control areas where the mesh can vary. This approach is discussed for the two and three-dimensional cases for modelling complex defect geometries.

### 4.1.1 Two-dimensional meshing

Figure 4.1.2 shows the use of structured and unstructured triangular elements controlled using a partitioning function. The partition is used to define the boundary between the structured and unstructured regions, allowing the unstructured mesh to conform to boundaries that are not aligned with a structured nodal grid.

In this model, all the elements are triangular with the same nodal separation. The majority of the domain is defined by structured elements and a free, unstructured, triangular mesh is used for the more complex geometry of the defect.

Although there is no variation in the type of element, and any variations in element size will be small, it is important to understand whether a transition from a structured mesh to a free mesh causes reflections. To investigate this point, a Unit Cell FE model has been built to examine the reflection

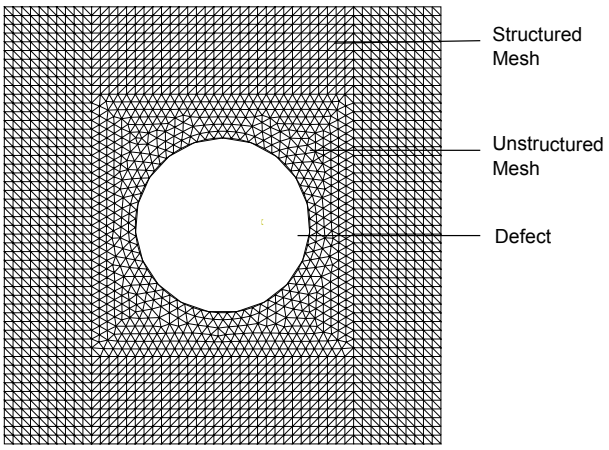


Figure 4.1.2: Figure to show a combination of structured and unstructured triangular elements using a partitioning function.

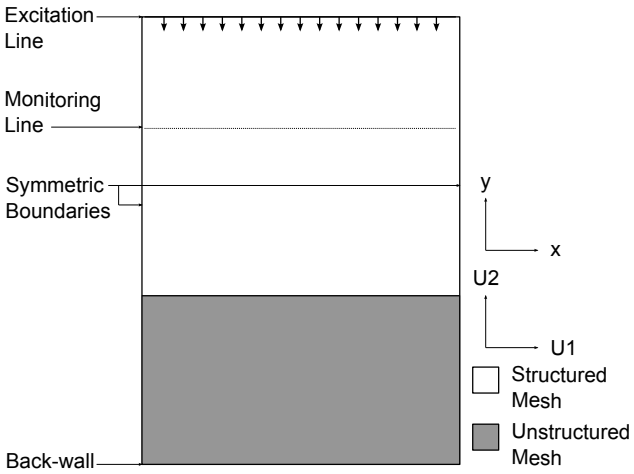


Figure 4.1.3: Figure to show two-dimensional Unit Cell model of a transition between structured and unstructured triangular elements using a partitioning function, where U1 and U2 represent nodal displacements in the x and y directions respectively.

coefficient from the transition in the mesh.

The Unit Cell model [119] has symmetric boundary conditions such that the scattering from a small section of an infinitely long periodic spatial domain can be calculated. The model is non-dimensional such that all scalar quantities can be expressed as a function of the incident wavelength. An excitation frequency of 1 Hz is used in a material that has a velocity of 2 and 1 units for compression and shear waves respectively and is discretised at 30 nodes per incident wavelength. The symmetric boundary conditions allow for the generation of an infinite plane compression wave at normal incidence to the transition in the mesh.

Two models are directly compared. The first consists entirely of structured triangular elements and monitors the propagation of an incident compression wave reflecting from a smooth back-wall. The second model is identical to the first except that the mesh approaching the back-wall consists of unstructured triangular elements, see Figure 4.1.3.

The first simulation acts as a baseline against which the model containing the unstructured mesh can be compared. Because the models are identical, any differences that are observed must be due to the change in the mesh alignment. Figure 4.1.4 shows the time histories from the two models and Figure 4.1.5 shows the difference between them (structured-unstructured).

The initial signal in Figure 4.1.4 shows the incident compression wave propagating past the monitoring line. The signal arriving later in time is the reflected signal from the back-wall. By using a Unit Cell model, it is possible to obtain a perfect incident compression wave at normal incidence, therefore there is no mode conversion at the model boundaries and the reflected signal at the boundary is of the same amplitude as the incident wave. Any scattering that occurs due to the change in the mesh will occur before the arrival of the reflected signal.

In Figure 4.1.4, it is not possible to distinguish between the structured and unstructured mesh results. This confirms that mesh scattering for a partitioned boundary can be considered to be of negligible magnitude. Only by taking the difference (structured-unstructured) and magnifying the scale, can the magnitude of the reflection from the change in mesh be seen, Figure 4.1.5.

Now we can see that there is an initial reflection from the boundary between the two meshed regions, which has a magnitude of -70.0 dB in comparison to the incident wave. The later signal is of higher amplitude, -55.2 dB, since this has propagated further through the free meshed region. These signals are of negligible magnitude confirming that the use of structured and unstructured triangular elements with a partitioning function is a practical means for modelling complex defects types in FE spatial domains.

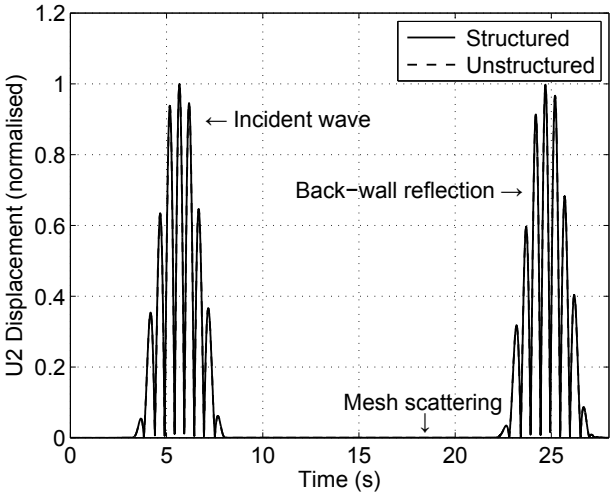


Figure 4.1.4: Figure to show time histories for incident compression wave reflecting from a back-wall after propagating through structured and unstructured triangular meshes. The results from the structured and unstructured meshes are overlaid, and no difference can be observed between them.

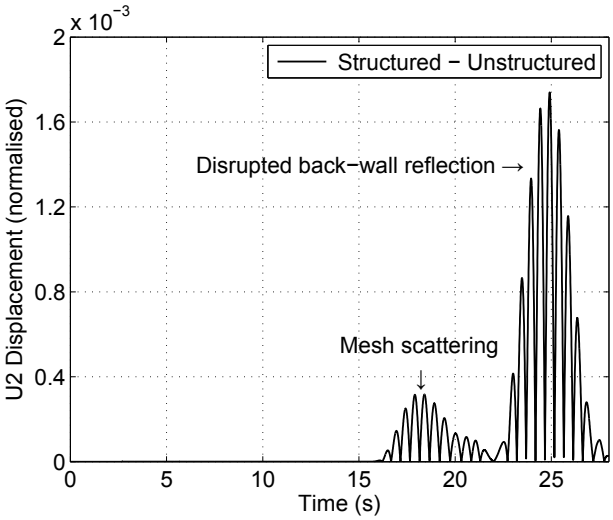


Figure 4.1.5: Figure to show the difference (structured-unstructured) between the time histories from a back-wall after propagating through structured and unstructured triangular meshes.

### 4.1.2 Three-dimensional meshing

Having established a means to implement a transition from structured and unstructured meshing regions in two-dimensions, it is now necessary to achieve this for the three-dimensional case. The same principles apply; except that triangular elements are replaced by tetrahedral elements. A free mesh is used to define the defect and the area immediately surrounding it, whereas the remainder of the model is defined by a structured arrangement.

Figure 4.1.6 shows a three-dimensional rough defect that has been cut from a cubic domain immediately surrounding it. This defines the area of unstructured meshing.

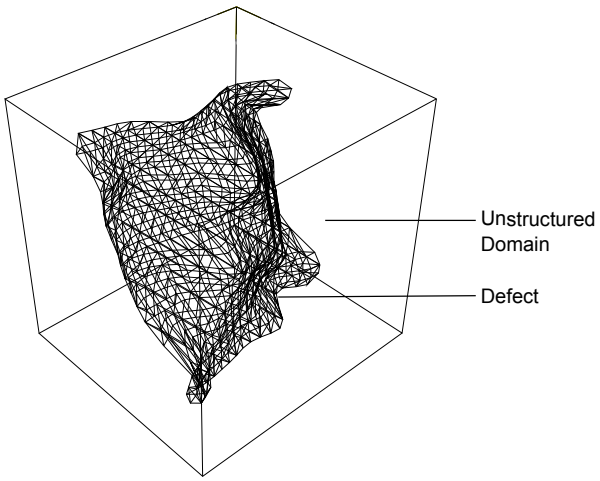


Figure 4.1.6: Three-dimensional spatial domain containing a complex defect and area immediately surrounding it defining the unstructured meshing using tetrahedral elements.

Figure 4.1.7, shows a cross-section through the spatial domain once the structured tetrahedral elements have been added. The unstructured mesh conforms around the defect leaving a void that creates the stress-free boundary of the defect.

The scattering from this transition must also be characterised and is again done using the same Unit Cell [119] approach, with the only difference being an extension into three-dimensional space, Figure 4.1.8.

As with the two-dimensional case, two simulations are compared. The first consists entirely of structured tetrahedral elements and the second contains a partition boundary with a transition into an unstructured region. The first simulation acts as a baseline so as to identify any differences that are due to the change in the mesh alignment. Figure 4.1.9 shows the time histories from the two models and Figure 4.1.10 shows the difference between them (structured-unstructured).

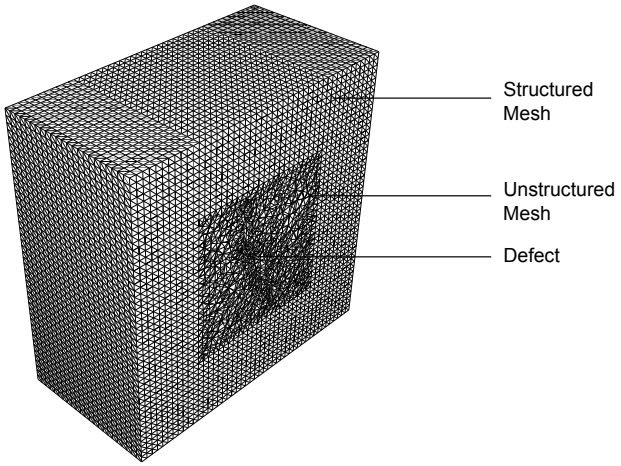


Figure 4.1.7: Cross-section through a three-dimensional FE model showing a transition between structured and unstructured tetrahedral elements.

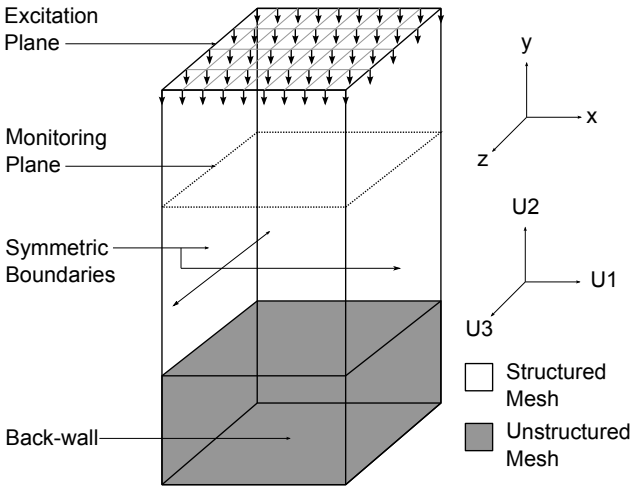


Figure 4.1.8: Figure to show three-dimensional Unit Cell model of a transition between structured and unstructured tetrahedral elements using a partitioning function.

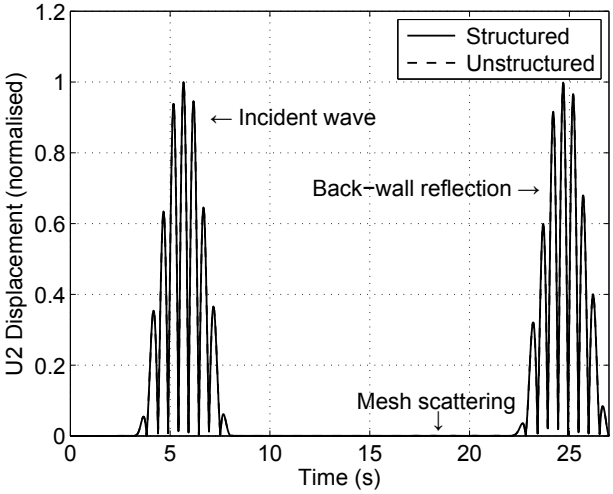


Figure 4.1.9: Figure to show time histories for incident compression wave reflecting from a back-wall after propagating through structured and unstructured tetrahedral meshes, where U1, U2 and U3 represent nodal displacements in the x, y and z directions.

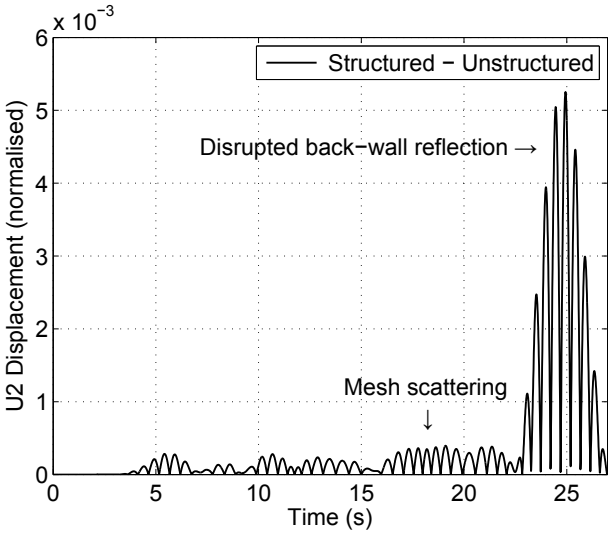


Figure 4.1.10: Figure to show the difference (structured-unstructured) between the time histories from a back-wall after propagating through structured and unstructured tetrahedral meshes. The results from the structured and unstructured meshes are overlaid, and no difference can be observed between them.

The initial signal in Figure 4.1.9 shows the incident compression wave propagating past the monitoring line. The signal arriving later in time is the reflected signal from the back-wall. As in the two-dimensional case, it is not possible to distinguish between the structured and unstructured mesh results. This confirms that mesh scattering due to a change in the alignment of tetrahedral elements can be considered to be negligible. Only by taking the difference (structured-unstructured) and magnifying the scale, can the magnitude of the reflection from the change in mesh be seen, Figure 4.1.10.

There is an initial reflection from the boundary between the two meshed regions, which has a magnitude of -68.1 dB in comparison to the incident wave. The latter signal is of higher amplitude, -45.6 dB, since this has propagated further through the free meshed region. These signals are of negligible magnitude confirming that the use of structured and unstructured tetrahedral elements with a partitioning function is a practical means for modelling complex defects in FE spatial domains.

The unwanted reflections noticed in three-dimensions are greater than those measured for the two-dimensional case. This is due to the fact that there is some variation in the element size within the unstructured region. This variation is small, however due to the nature of tetrahedral elements it is larger for the three-dimensional case. It is also noted that there are small differences in the signals earlier in the time history, these are not observed in the two-dimensional case. This is due to the fact that although both meshes are structured, they are not identical. When transitioning between structured and unstructured tetrahedral meshes, element faces must be aligned at the partition boundary. Although nodal positions in the structured sections are identical for both, the nature of structuring tetrahedral elements does not always guarantee the same alignment of the elements.

The results presented here for both the two and three-dimensional cases are an illustrative representation of what is likely to occur. The performance that has been demonstrated here may diminish if a complex feature causes increased irregularity in the mesh.

## 4.2 Domain linking algorithms

When using FE models, accurately modelling large spatial domains has proven to be a limiting factor. The separation between the source of ultrasound and the feature of interest can often be extensive, and the model is therefore dominated by solving the generation and propagation of ultrasound within the host medium. Although FE can be used to calculate transducer response and wave propagation, this aspect of the problem can be solved using faster analytical methods.

A solution to this problem has been to divide the ultrasonic inspection into three regimes, transducer response, wave propagation and defect response. Transducer response and wave propagation can both be solved using fast analytical methods that calculate that nature of the ultrasonic field at a location surrounding the defect or feature of interest. Computational resource can therefore be focused on a highly accurate representation of the scatterer using FE, from which the response of the defect can be

calculated, as shown in Figure 4.2.1.

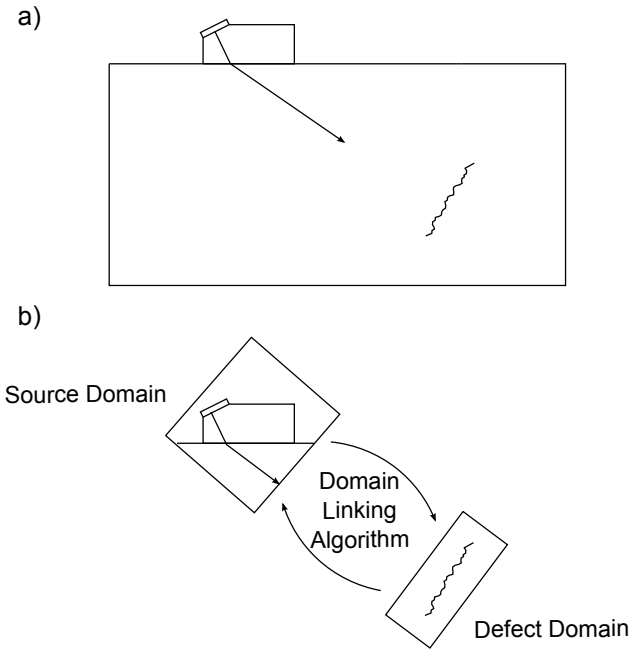


Figure 4.2.1: Figure to show a) a full numerical model of an ultrasonic inspection and b) a spatially reduced model achieved through the use of a domain linking algorithm.

A frequency domain linking algorithm, or Hybrid model, is used to propagate the ultrasound from the source to the defect and vice-versa. This uses the free-space Greens' function, $G(\mathbf{r}_2|\mathbf{r}_1)$, to calculate field potential at $\mathbf{r}_2$, $\phi(\mathbf{r}_2)$, due to a known field potential at $\mathbf{r}_1$, $\phi(\mathbf{r}_1)$, over a surface $S$, where $\mathbf{r}_1$ and $\mathbf{r}_2$ are position vectors, governed by Equation 4.2.1.

$$\phi(\mathbf{r}_2) = \int_s (\phi(\mathbf{r}_1)\nabla G(\mathbf{r}_2|\mathbf{r}_1) - G(\mathbf{r}_2|\mathbf{r}_1)\nabla\phi(\mathbf{r}_1)).\mathbf{n}dS \tag{4.2.1}$$

The potential at $\mathbf{r}_1$, $\phi(\mathbf{r}_1)$, must be the scattered field leaving the domain. This can be calculated by Equation 4.2.2, where the scattered field $\phi^{sc}(\mathbf{r}_1)$, is the incident field $\phi^{inc}(\mathbf{r}_1)$, subtracted from the total field $\phi^{tot}(\mathbf{r}_1)$.

$$\phi^{sc}(\mathbf{r}_1) = \phi^{tot}(\mathbf{r}_1) - \phi^{inc}(\mathbf{r}_1) \tag{4.2.2}$$

To apply this technique to time domain FE models, the known displacements and stresses are measured in the time domain and then used to calculate the frequency spectra of the wave potentials using Fourier synthesis. The field is then propagated using Equation 4.2.1 and Equation 4.2.2 at

discretised steps in the frequency domain. The final solution is then converted back to the time domain using an inverse Fourier transform.

This approach offers flexibility to modellers as to how it is deployed. Wilcox and Velichko [79], have developed a frequency domain approach for commercial FE codes, where a plane wave is incident on a spatial domain that immediately surrounds a scatterer, achieved by applying a specific forcing profile to a set of nodes that surround the defect domain. The scattered field is recorded in the form of a scattering matrix, giving the far-field response from the defect for each scattered wave mode.

Mahaut *et al* [80], demonstrate the coupling of a semi-analytical beam modelling tool (CIVA, developed by the CEA) with a specialist fictitious domain FE code (Athena code, developed by EDF). This allows for a time-domain calculation of the response from an arbitrary complex flaw from within a component. In their paper, comparisons between simulated and experimental scans of EDM notches show good agreement with one another, allowing for simulation tools to optimise the inspection of complex defect configurations.

Rajagopal *et al* [82], had developed a time domain approach for more generic applications. In this instance wave potentials between any two domains can be linked allowing for the propagation and excitation of ultrasound within commercial FE codes. This allows for the use of free-meshing algorithms, offering greater accuracy than fictitious domain methods. Validation for the use of this algorithm is given by Rajagopal *et al* [82], for two-dimensional cases and Choi *et al* [118], for three-dimensional cases. In both instances, the scattering response from a planar reflector and SDHs is compared using a Full FE simulation and Hybrid model. In the two-dimensional and three-dimensional studies, excellent agreement between the time domain and frequency domain scattered signals is observed. Experimental validation is provided for the three-dimensional case, where the ultrasonic response from a 3 mm diameter SDH is calculated at depths of 15 mm and 25 mm. The Hybrid modelled results show good agreement with the experimental measurements, increasing the confidence in the use of two and three-dimensional Hybrid models.

The distinct advantage of all these methods is that they reduce the size of the spatial domain and therefore reduce computational demand. However, a more accurate description is that the computational burden has been shifted from the FE spatial domain, into the analytical domain linking algorithm. The domain linking algorithm still remains to be a faster and more efficient allocation of resource, but this does place an upper limit of the maximum size of the problem that can be solved. In the case where an incident wave is transmitted from the source domain to the defect domain and then the scattered response is returned, the computational demand is determined by: the number of nodes surrounding the source domain, the number of nodes surrounding the defect domain, and the propagation time of ultrasound to return from the defect domain.

For the purposes of this project, significant improvements in computational run time can be achieved without compromising the accuracy of the solution. This is achieved by recognising that a detailed

representation of the transducer is not needed in these studies, so the source domain can be replaced by a plane wave excitation immediately surrounding the defect domain, similar to the approach taken by Wilcox and Velichko [79]. By doing this, the model run time is reduced to the time required for the ultrasonic wave to enter and leave the defect domain. Similarly, the scattered response need only be calculated at a single location, as opposed to the re-excitation of the original source domain, as shown in Figure 4.2.2.

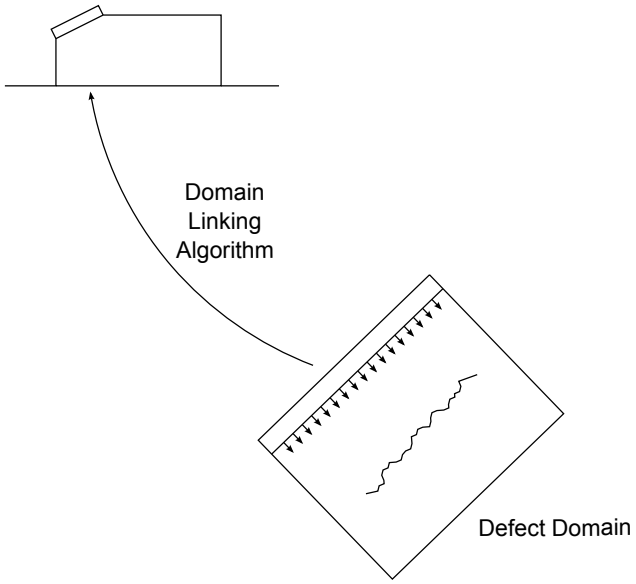


Figure 4.2.2: Figure to show Hybrid model with a spatially reduced FE model coupled with a domain linking algorithm.

Running this simulation alone will produce the total field in the defect domain. To obtain the scattered field, and therefore satisfy Equation 4.2.2, a calculation of the incident field is required. This can be obtained by re-running the model without the defect, allowing for the scattered field to be calculated and passed into the domain linking algorithm.

This approach offers significant improvements in computation time, however it has a distinct disadvantage since the exact profile of the incident ultrasonic wave is unknown, and is instead approximated by plane wave excitation. This approximation is valid in the far-field of the transducer, however, in the near-field a more detailed description is needed.

For three-dimensional modelling, computational run times drastically increase with the size of the spatial domain, therefore any unnecessary addition to the size of model is undesirable. To identify how accurate the simplified model can be when using a small spatial domain, a two-dimensional Hybrid model has been compared to a Full FE simulation, as shown in Figure 4.2.3.

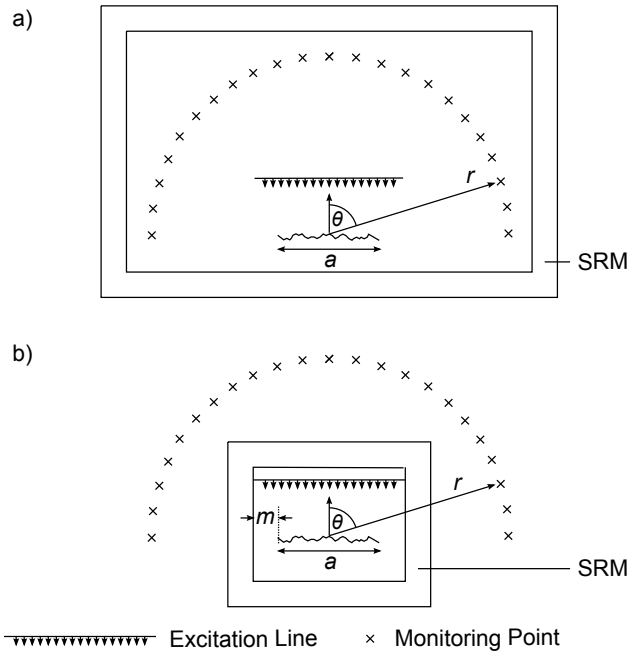


Figure 4.2.3: Figure to show a) a Full FE simulation and b) a Hybrid model for the scattering from an embedded rough defect for the two-dimensional case.

The response from an embedded rough defect of length $a = 4$ mm, roughness $\sigma = 100$ µm and surface correlation length $\lambda_0 = 100$ µm is calculated. The incident wave is a 2.25 MHz, 5 cycle, plane compression wave at normal incidence to the defect and the response is calculated around a circular arc with a separation of $r = 20$ mm from the centre of the defect. A free mesh is used to accurately define the rough defect. A partitioning function is used to define a transition into a structured mesh, which is needed for the absorbing boundaries and to define a definitive location where the scattered wave potentials can be measured.

The two quantities that can significantly reduce the size of Hybrid models are the separation between the extremities of the defect edge to the AoS, $m$, and the thickness of the SRM absorbing boundary that surrounds the model. The separation can be small with the only requirement being to allocate sufficient space to allow for a successful mesh of the defect. The thickness of the absorbing regions can also be significantly reduced through the use of an optimisation function, as discussed in Chapter 3. From this inspection problem the total thickness of the SRM is equal to $\lambda_{inc}/4$.

Figure 4.2.4 shows the amplitude of the scattered field across the radial arc defined by $r$, for the Full FE and Hybrid simulations of this system.

The results from each simulation are normalised against the amplitude of the maximum scattered

a)

b)

c)

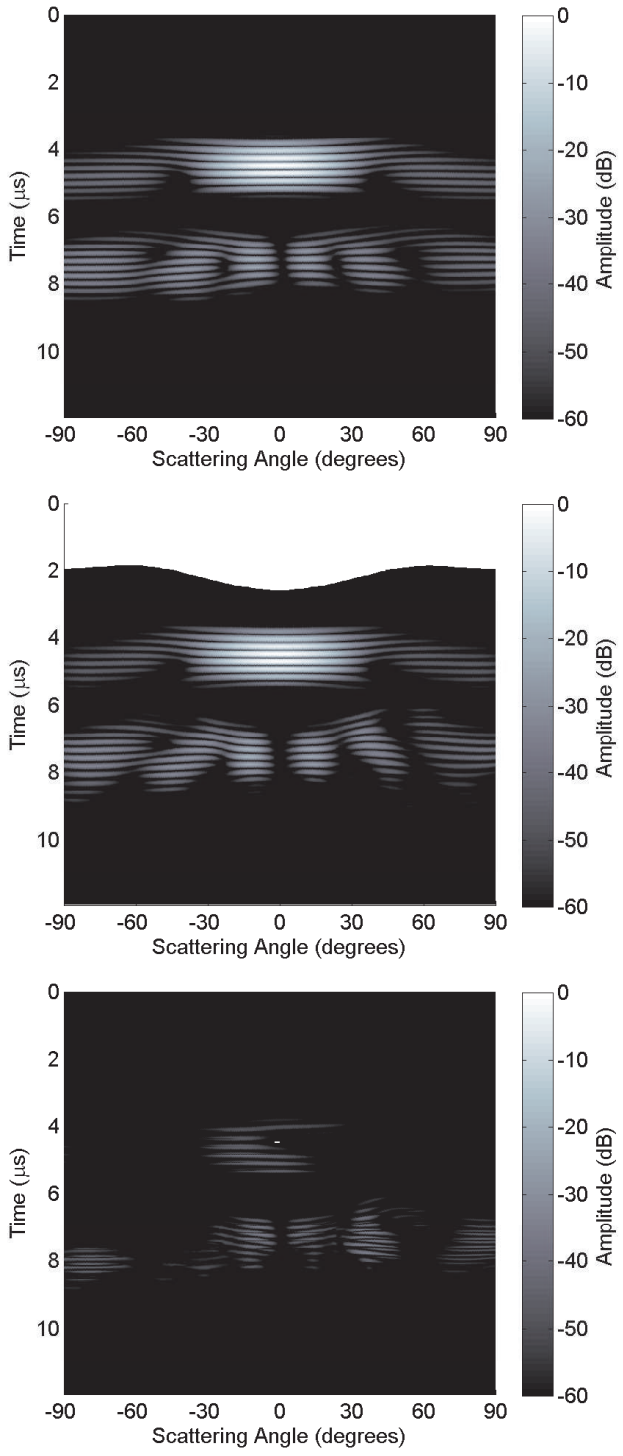


Figure 4.2.4: Absolute amplitude of the scattered field from an embedded, finite, rough defect, around a circular arc for a) Full FE simulation, b) a reduced spatial domain Hybrid Model, c) the difference between the Full FE simulation and Hybrid model for the two-dimensional case.

field. The reflected signal arriving between 4 µs and 6 µs corresponds to a compression wave being reflected back from the surface. The maximum amplitude of this signal lies around $0^o$, which corresponds to the specular direction for normal incident inspections. Due to the complex nature of the scatterer, a mode converted shear wave is also reflected from the surface, with an arrival time between 6 µs and 8 µs.

The lack of information (amplitude shown as white after 0 µs) shown in Figure 4.2.4b), corresponds to the time taken for the domain linking algorithm to propagate the scattered field from the defect domain to the monitoring points at $r$ and therefore has zero amplitude (and not applicable to a dB scale).

There is good agreement between the amplitude and phase of the scattered field from the complex defect between both simulations. Figure 4.2.4c), shows the difference between the two simulations, where any disagreement is of the order of -33.7 dB. This disagreement is small due to the good agreement between the predicted amplitudes of the two models. Variations of this nature are not of concern since they are small in comparison to differences that can be observed experimentally.

The success of this result is partly attributed to the $\lambda_{inc}/4$ SRM absorbing boundary. The SRM has been specifically designed for the bulk material and inspection frequency. Furthermore, the reduced spatial domain of the model ensures that the vast majority of scattered signals enter the SRM at an angle close to $0^o$, therefore the SRM has been optimised to absorb waves at this angle of incidence. For these reasons, a $\lambda_{inc}/4$ SRM absorbing boundary would not be as successful for a Full FE simulation.

The results from this study provide confidence for the use of domain linking algorithms using significantly reduced spatial domains for future simulations. As model complexity increases, along with the use of three-dimensional models, making comparisons with Full FE simulations will no longer be possible due to the significant increase in computational demand. Therefore, confidence in the domain linking algorithms must be established by making comparisons with these smaller two-dimensional results.

## 4.3 Experimental validation

Comparisons of Hybrid simulations with Full FE simulations verify that reduced spatial domains and domain linking algorithms can be used in place of the much larger, fully numerical models. However, to validate these techniques, comparisons with experimental data sets are also required.

Comparisons between Hybrid simulations and experimental data are made by taking a series of ultrasonic scans from a range of test blocks. The test blocks contain standard calibration targets used in NDE, each with a range of depths and sizes. Piezoelectric transducers or arrays are used to generate ultrasound at a given inspection frequency. The ultrasound is coupled to the propagation medium using a combination of couplant and Perspex wedges, dependent upon the required angle of incidence

or wave mode.

Previous authors such as Rajagopal *et al* [82], and Choi *et al* [118], have made comparisons between experimental scans and Hybrid simulations using time and frequency domain responses. In these cases, the exact form of the ultrasonic response from the transducer is measured and used as the excitation for the Hybrid simulation. This allows for an accurate representation of the incident wave and therefore the scattering system.

In this study, comparisons are made in a manner that is consistent with ultrasonic NDE inspections. As is often the case, the exact ultrasonic response of the transducer is unknown, and is instead approximated by a finite pulse with a centre frequency described by a Hanning window. Furthermore, the response from scatterers is quantified by the absolute amplitude of the reflected signal in any given direction, which can be used to size and characterise potential flaws.

### 4.3.1 Side Drilled Holes

The response from SDHs is measured experimentally and compared to Hybrid simulations. Two set-ups are considered, the first is a pulse-echo inspection of SDHs with increasing depth and the second considers scattering from a single SDH across an angular range.

#### 4.3.1.1 Response as function of depth

A 2.25 MHz, 0.5", GE MSWQC circular transducer is used to generate normal incident compression waves which reflect and scatter from SDHs. The response is measured back along the path of propagation for a range of depths between 10 mm and 55 mm. Figure 4.3.1 shows the experimental setup, where $a$ is the transducer diameter, $D$ is the depth of the SDH, and $T$ is the total thickness of the test block.

The range of depths of SDHs is such that a reflected compression wave is isolated in time from any transducer ring-down and the response from the back-wall at depth $T$. The thickness of the block is 60 mm and has compression and shear wave speeds of 5840 $\text{ms}^{-1}$ and 3190 $\text{ms}^{-1}$ respectively. The radius of each SDH is $r = 1.5$ mm at depths $D = 10$ mm, 15 mm, 20 mm, 25 mm, 35 mm, 45 mm and 55 mm. When taking the signal amplitude there is some uncertainty over the exact amplitude and position of the response. This is determined by the difficulty to accurately know the position of the transducer and the signal to noise amplitude of the responses.

A two-dimensional Hybrid model of this system is shown in Figure 4.3.2. The defect domain immediately surrounds the SDH followed by a region of SRM absorbing boundary. The transducer response is estimated to be equivalent to a normal incidence plane wave, illustrated by the excitation line. The response from the SDH is then propagated back towards the centre of the transducer using a domain linking algorithm.

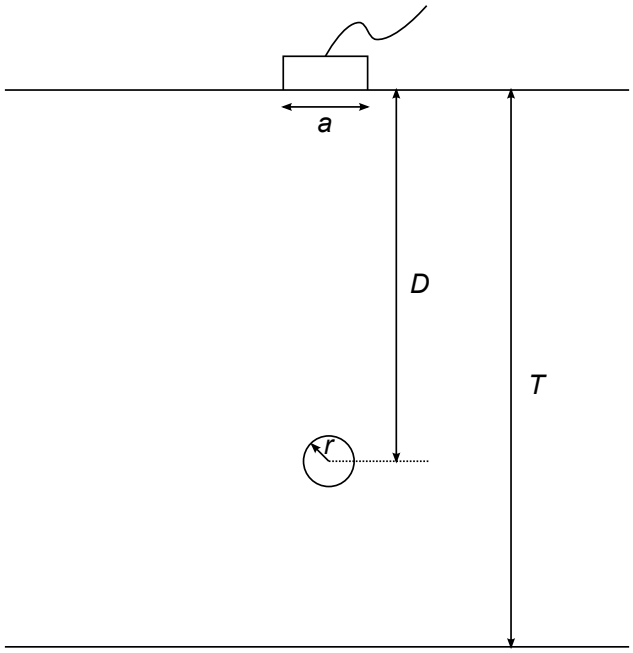


Figure 4.3.1: Experimental setup for normal incidence compression wave scattering from SDH with radius $r$, and depth $D$. The incident wave is generated by a transducer with diameter $a$, on a test block with thickness $T$.

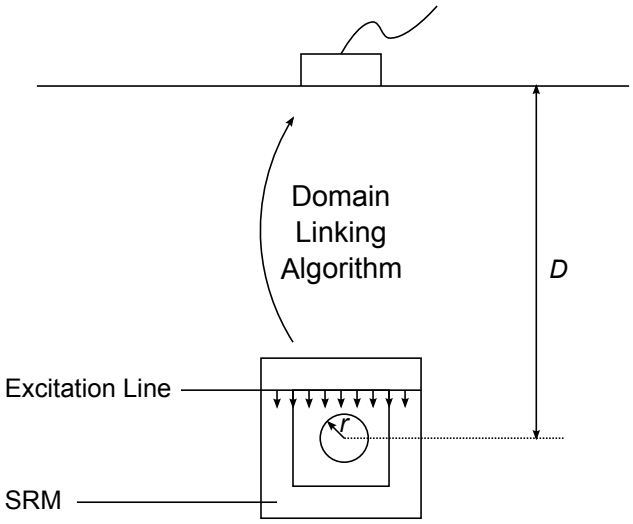


Figure 4.3.2: Two-dimensional Hybrid model to calculate the response from SDHs with radius, $r$, at a range of depths, $D$.

The response of the transducer can be calculated in a number of ways, reliant upon the hybrid model calculating the scattered field at discretised points normal to the face of the transducer. Once this has been achieved, the transducer response can be taken as an average of these values, or a weighted average according to the profile of the transducer. A faster method is to only consider the scattered field at the centre of the transducer, since this reduces the number of points at which to calculate the scattered field. In the scenarios considered here, negligible difference has been observed between either of the approaches, especially when the results are normalised against one-another, therefore, due to the preferred savings in computation time, the response at the centre of the transducer has been taken.

To begin with, the amplitude of the normal incident plane wave remains constant, and is not varied as a function of depth. This does not conform to experimental reality, where the incident amplitude decreases with range from the probe for distances beyond the near-field of the transducer, which can be approximated by Equation 4.3.1.

$$NFE = \frac{a^2}{4\lambda_{inc}} \tag{4.3.1}$$

where $NFE$ represents the Near Field Extent, $a$ is the transducer diameter and $\lambda_{inc}$ is the incident wavelength. Later, in Section 4.3.3, the importance of the providing the correct excitation to the FE domain is discussed.

The results from the two-dimensional Hybrid simulation and experimental data are shown in Figure 4.3.3. The respective amplitudes are shown on a dB scale, and are both normalised against the response from the SDH at $D = 25$ mm. This target has been used to normalise the signals, because it lies sufficiently beyond the NFE , which in this instance is calculated to be 13.9 mm.

The Hybrid simulations illustrate a general trend, where the amplitude of the reflected signal returning from a SDH decreases with increasing depth. For defects which lie beyond the $NFE$, the results from experimental data show the same trend. The amplitudes are consistent with one another, with the greatest difference in amplitude being 3.1 dB at a depth of 55 mm, however, it is noticed that the reduction in signal amplitude measured experimentally is decreasing at a greater rate than the simulated data. This can be attributed to the amplitude variation of the incident wave not being accounted for as the target has increased range away from the transducer.

Within the $NFE$ there is considerable difference between simulated and experimental data. The near-field response is not correctly accounted for and as a result, the simulated data fails to predict the correct trend in signal amplitude. Furthermore, despite a two-dimensional model being a good approximation for calculating the scattering response from a SDH, it is likely that the disagreement observed is due to an incident beam being poorly represented in two-dimensions.

To assess the validity of this finding, the same experimental data can be compared to results from a three-dimensional Hybrid simulation of the same system. Again, the response from both data sets

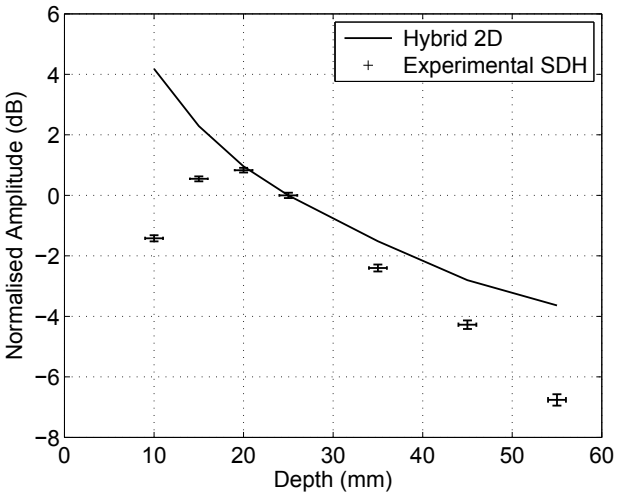


Figure 4.3.3: Comparison between two-dimensional Hybrid simulation and experimental data for the ultrasonic response from SDHs with increasing depth.

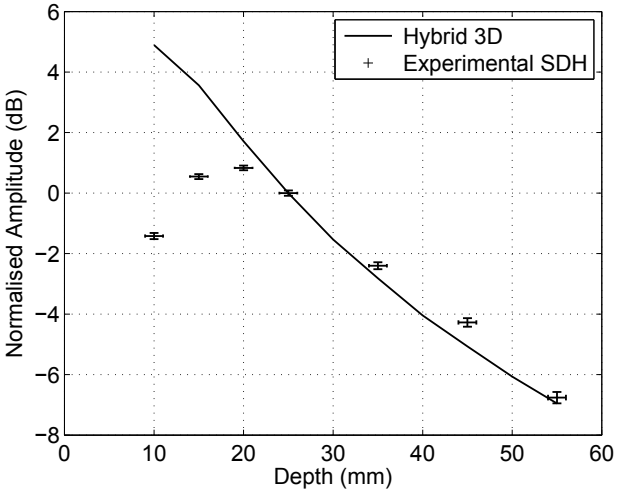


Figure 4.3.4: Comparison between three-dimensional Hybrid simulation and experimental data for the ultrasonic response from SDHs with increasing depth.

are normalised against a defect that lies sufficiently beyond the near-field of the transducer, shown in Figure 4.3.4.

The far-field amplitude response from the SDHs now shows good agreement between experimental and three-dimensional Hybrid simulated data, however, it is important to remember that the variation in the incident signal amplitude as a function of depth is not considered. The greatest disagreement observed in the far-field response is 0.5 dB and both responses are following the same trend in signal attenuation. Disagreement still exists within the $NFE$, suggesting that a plane wave excitation is invalid within this region. This result provides a level of confidence in the ability of Hybrid simulations to accurately predict the response from scatterers beyond the $NFE$, but the uncertainty in the nature of the incident signal must be called into question.

#### 4.3.1.2 Response as function of scattering angle

The response from a SDH is measured experimentally as a function of scattering angle $\theta_{sc}$. In this example a normal incidence 2 MHz compression wave is transmitted from the first element from within a 128 element array. The remaining elements detect the scattered signal, allowing for the response as a function of scattering angle to be measured as shown in Figure 4.3.5.

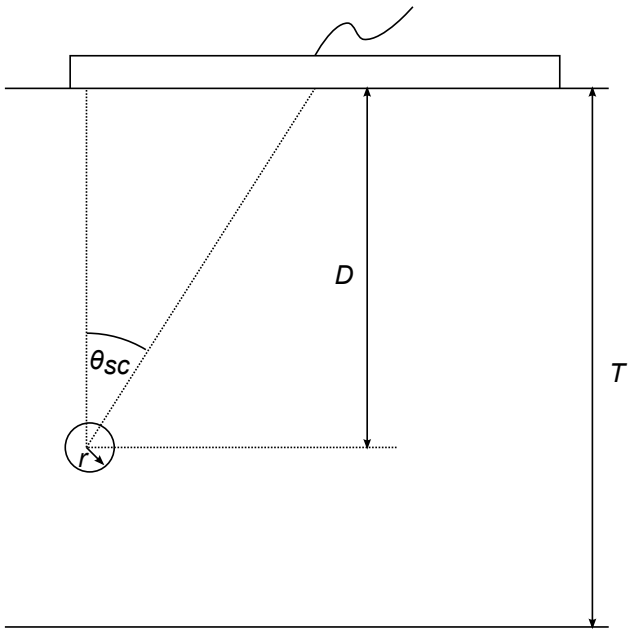


Figure 4.3.5: Experimental setup for normal incidence compression wave scattering at angle $\theta_{sc}$, from a SDH with radius $r$, depth $D$. The incident wave is generated from the first element of a 128 element array, on a test block with thickness $T$.

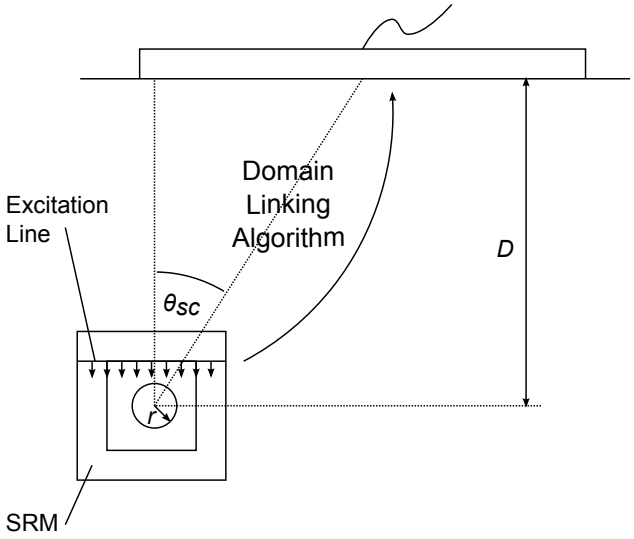


Figure 4.3.6: Three-dimensional Hybrid model to calculate the response from SDH with radius $r$, and depth $D$, at scattering angle $\theta_{sc}$.

A three-dimensional Hybrid simulation is compared to the experimental data, as shown in Figure 4.3.6. The defect domain immediately surrounds the SDH followed by a region of SRM absorbing boundary. The transducer response is estimated to be equivalent to a normal incidence plane wave, illustrated by the excitation line. The response from the SDH is then propagated back towards elements within the array using the domain linking algorithm.

In this case, the range of the target from the transmitting element within the array remains fixed, thereby making the plane wave excitation a good approximation to the incident wave. The reception of scattered response on the receiving elements is calculated using the same method as described in Section 4.3.1.1; the directivity of the elements has not been considered as this is thought to have little influence with this array at this inspection frequency.

The SDH has radius $r = 1.5$ mm at depth $D = 50$ mm and is isolated from any other scatterers. The array consists of 128 elements with a width of 0.55 mm, each separated by 0.20 mm. An in-house, data acquisition software package, is used to control the array and capture the ultrasonic field scattered from the SDH. Figure 4.3.7a) shows the data captured from the array.

From Figure 4.3.7a) three signals can be identified. The first occurs early in time and corresponds to the ring down of the firing element and the propagation of a surface wave along the length of the array. The second is a reflected compression wave from the SDH, which occurs at approximately 18 µs for $\theta_{sc} = 0^o$. The third is a mode converted shear wave reflecting from the SDH. The experimental scan data has isolated the reflected compression and shear wave modes, apart from a point at a scattering

a)

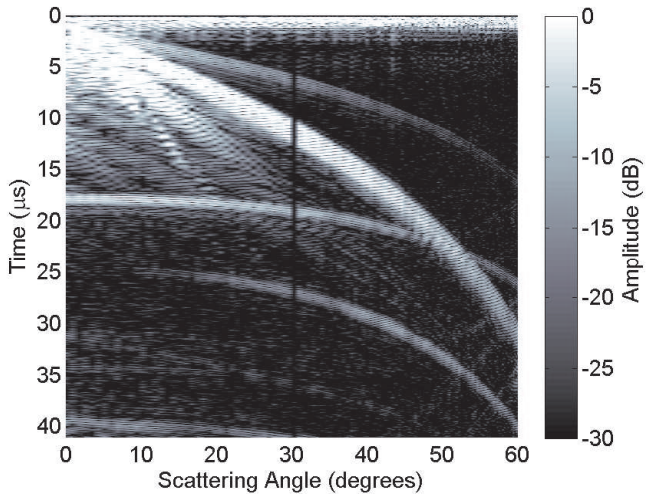


b)

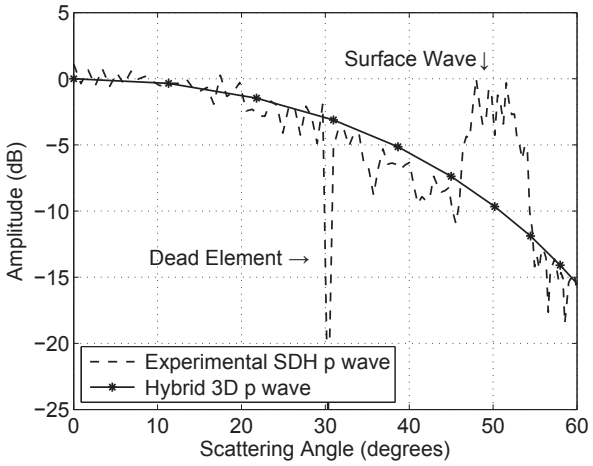


c)

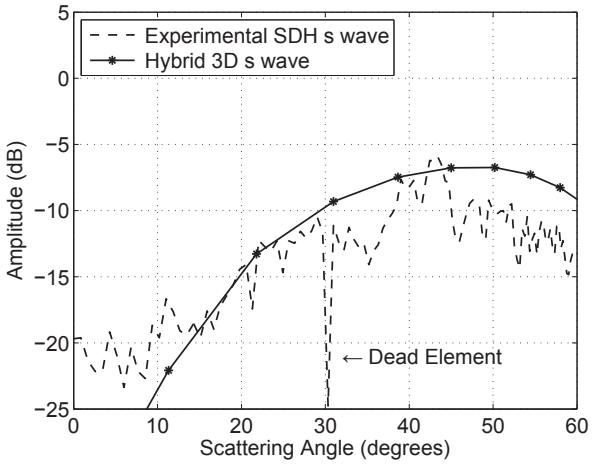


Figure 4.3.7: Absolute amplitude of the scattered field from a SDH as a function of the scattering angle for a) experimental measurement, b) reflected compression wave and c) a mode converted reflected shear wave.

angle of $50^o$ where the surface wave propagating along the array, coincides with the arrival of the reflected compression wave. This is not included in the Hybrid model.

Figure 4.3.7b) and Figure 4.3.7c) show the amplitude of the reflected compression and shear wave modes respectively from the SDH as a function of scattering angle. The results are normalised against the reflected compression wave at $\theta_{sc} = 0^o$ and Hybrid and experimental data sets are directly compared.

Figure 4.3.7b) and Figure 4.3.7c) both show good agreement. The three-dimensional Hybrid simulation is capable of accurately predicting the amplitude of the scattered signal across the angular range considered. There are two areas of disagreement in Figure 4.3.7b) and Figure 4.3.7c) which can easily be explained.

The experiential data shows a significantly reduced amplitude at $\theta_{sc} = 30^o$ and an uncharacteristic increase in amplitude between $45^o - 55^o$. The first corresponds to a dead element within the array that is incapable of collecting the ultrasonic data. The latter is due to a surface wave propagating along the array that interacts with the scattered compression wave at this particular angle. Disagreement is observed between the mode converted shear wave at scattering angles beyond $55^o$, with the Hybrid model over estimating the amplitude of the scattered signal, however this is of the order 2.5 dB, which is an acceptable variation. This difference could be attributed to the element directivity of the receiving elements not being considered.

### 4.3.2 Flat Bottomed Holes

The response from FBHs tilted at $45^o$ with depths ranging between 2.7 mm and 27.0 mm is measured. A comparison is made at two different inspection frequencies in order to assess the performance of the Hybrid simulation for different configurations, one at 2.25 MHz and the other at 3.50 MHz.

In both cases a 0.25", GE MSWQC circular transducer is used to generate $45^o$ shear waves which reflect and scatter from the front face of the FBH. The transducer is coupled to the test block using a Perspex wedge. The response is measured back along the path of propagation. Figure 4.3.8 shows the experimental setup, where $a$ is the transducer diameter, $D$ is the depth of the FBH, and $T$ is the total thickness of the test block.

The range of depths of FBHs is such that a reflected shear wave is isolated in time from any transducer ring-down. The thickness of the block is 35 mm and has compression and shear wave speeds of 5840 $\text{ms}^{-1}$ and 3190 $\text{ms}^{-1}$ respectively. The radius of each FBH is $r = 1.5$ mm at depths $D = 2.7$ mm, 5.4 mm, 8.1 mm, 10.8 mm, 13.5 mm, 16.2 mm, 18.9 mm, 21.6 mm, 24.3 mm and 27.0 mm.

A two-dimensional Hybrid model of this system is shown in Figure 4.3.9. The defect domain immediately surrounds the FBH followed by a region of SRM absorbing boundaries. Because the scatterer must lie within the defect domain the back-wall is not considered. Therefore, in two-dimensions the

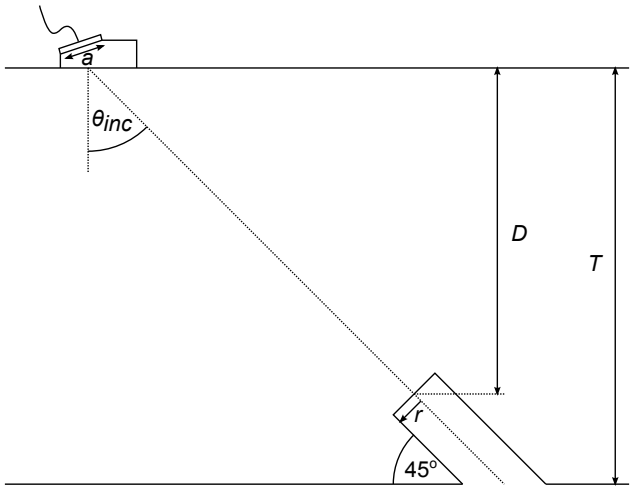


Figure 4.3.8: Experimental setup for $45^o$ shear waves scattering from a FBH with radius $r$, depth $D$. The incident wave is generated by a transducer with diameter $a$, on a test block with thickness $T$.

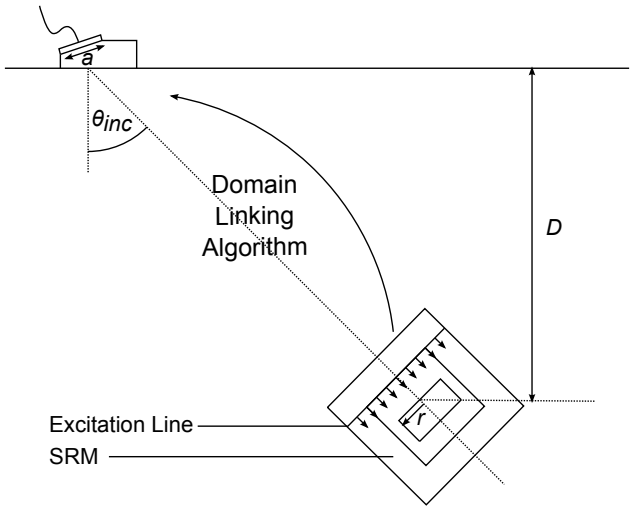


Figure 4.3.9: Two-dimensional Hybrid model to calculate the response from FBHs with radius $r$, at a range of depths $D$.

FBH is consistent with an infinite rectangular slot and in three-dimensions becomes an embedded penny shaped reflector.

As in Section 4.3.1.1, the transducer response is approximated to be equivalent to a normal incidence plane wave, illustrated by the excitation line. To generate a shear wave excitation the displacement of the excitation line is perpendicular to the path of propagation. The response from the FBH is then propagated back towards the centre of the transducer using the domain linking algorithm.

#### 4.3.2.1 Response at 2.25 MHz inspection

The results from the 2.25 MHz frequency inspection are shown in Figure 4.3.10 and Figure 4.3.11 for the two and three-dimensional cases respectively. The respective amplitudes are shown on a dB scale and are both normalised against the response from the FBH at $D = 10.8$ mm, which lies sufficiently beyond the near-field of the transducer.

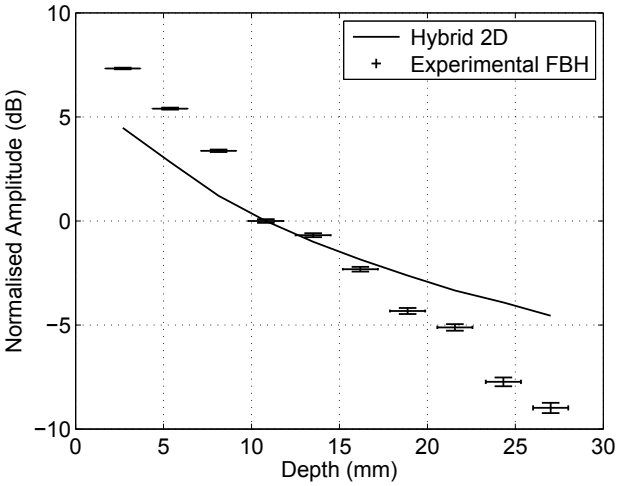


Figure 4.3.10: Comparison between two-dimensional Hybrid simulation and experimental data for a $45^o$, 2.25 MHz, incident and reflected shear wave from tilted FBHs with increasing depth.

Both the two-dimensional Hybrid and experimental data show that increasing the depth of the FBH results in a reduction in the reflected signal amplitude. There is disagreement in the rate of attenuation between the two data sets. The biggest disagreement is observed at a depth of 27.0 mm, where the two-dimensional Hybrid simulation is over estimating the reflected shear wave signal by 4.5 dB. This suggests that the two-dimensional approximation is not correctly considering the full attenuation of the scatterer as a function of depth, which is as expected since the variation in the incident signal amplitude has not been accounted for.

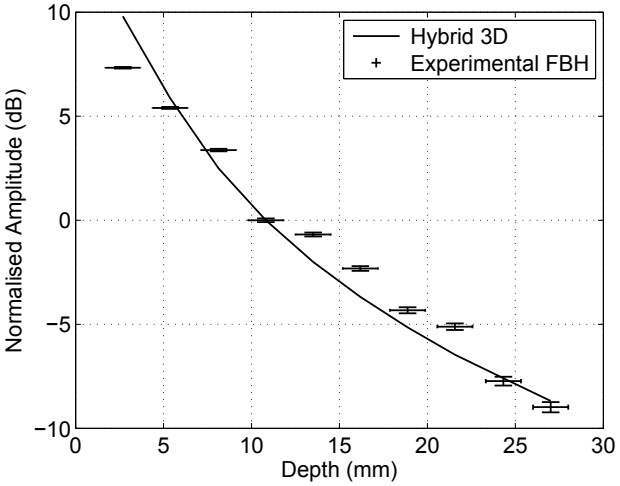


Figure 4.3.11: Comparison between three-dimensional Hybrid simulation and experimental data for a $45^o$, 2.25 MHz, incident and reflected shear wave from tilted FBHs with increasing depth.

A three-dimensional Hybrid simulation, has also been compared to the same experimental data, shown in Figure 4.3.11.

In this instance there is now better agreement between the simulated and experimental data, although consideration must be given to the fixed nature of the incident wave as a function of depth. Both are correctly predicting the same rates of attenuation. The near-field effects of the transducer are not as apparent in this comparison, this can be attributed to the fact that the transducer diameter is smaller and an incident shear wave is used. The biggest difference observed in this comparison is 2.5 dB for the 2.7 mm deep FBH. This level of disagreement is within an acceptable level of tolerance and occurs at a depth that is within the $NFE$, where the exact form of the incident ultrasonic wave is not considered.

When comparing two-dimensional and three-dimensional simulations, it is apparent that a three-dimensional model shows better agreement with experimental data. Generally speaking, two-dimensional approximations will over estimate defect response. The level of disagreement will increase with an increase in the range of the target. This is attributed to the nature of attenuation as a function of depth between two-dimensional and three-dimensional models.

#### 4.3.2.2 Response at 3.50 MHz inspection

The variation in ultrasonic response from FBHs is measured against increasing depth using a 3.50 MHz inspection frequency. The results from the two and three-dimensional simulations are shown in Figure 4.3.12 and Figure 4.3.13 respectively. The respective amplitudes are shown on a dB scale, and are

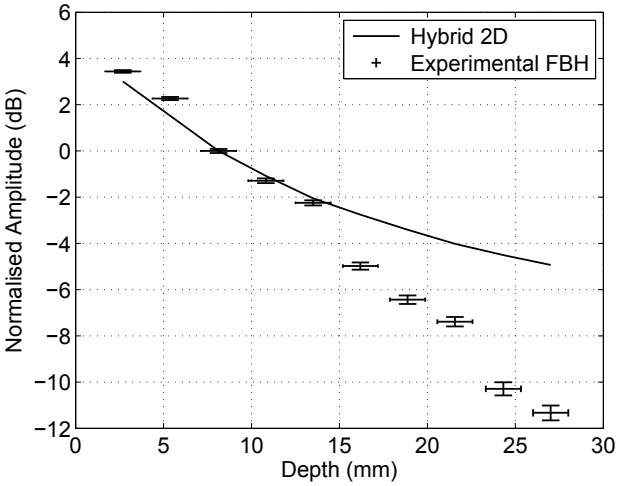


Figure 4.3.12: Comparison between two-dimensional Hybrid simulation and experimental data for a $45^o$, 3.50 MHz, incident and reflected shear wave from tilted FBHs with increasing depth.

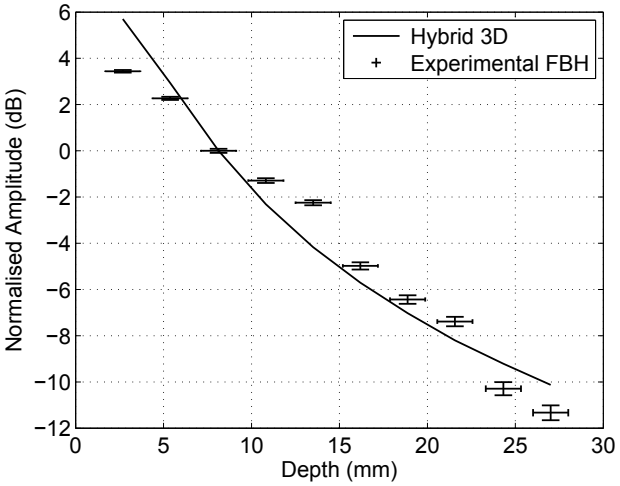


Figure 4.3.13: Comparison between three-dimensional Hybrid simulation and experimental data for a $45^o$, 3.50 MHz, incident and reflected shear wave from tilted FBHs with increasing depth.

both normalised against the response from the FBH at $D = 8.1$ mm, where the target lies sufficiently beyond the near-field of the transducer.

The variation in ultrasonic response at 3.50 MHz remains consistent with that which is observed at

2.25 MHz. Increasing the depth of the FBH results in a reduction in the reflected signal amplitude. For the two-dimensional simulation, there is disagreement in the rate of attenuation between the two data sets. The biggest disagreement is observed at a depth of 27.0 mm, where the two-dimensional Hybrid simulation is over estimating the reflected shear wave signal by 6.4 dB. This suggests that the two-dimensional approximation is not correctly considering the full attenuation of the scatterer as a function of depth. This can be improved by using a three-dimensional Hybrid simulation, which has been compared to the same experimental data, shown in Figure 4.3.13.

The three-dimensional simulation shows better agreement with the experimental data. The rate of attenuation with increasing depth is consistent across experimental and simulated data. The biggest disagreement is observed in the $NFE$ of the transducer at $D = 2.7$ mm, with the Hybrid simulation overestimating the response by 2.3 dB. This can be attributed to the plane wave excitation used in the Hybrid simulation, which does not correctly represent the transducer response.

### 4.3.3 Beam computation model

So far, Hybrid simulations have approximated the transducer response to a plane wave excitation which has resulted in discrepancies with experimental data. The transducer response can be corrected for by introducing a beam computation model. This can be achieved by replacing the plane wave excitation line with an excitation that is more representative of the field produced by a transducer as a function of position. Calculations for wave potentials generated by the transducer can be converted into an excitation within the defect domain.

A computational beam model of this nature can reach any desired level of complexity, therefore, at an initial stage a simplified version of a beam computation tool developed by Coffey and Chapman [13, 120] has been added to the Hybrid simulation.

The beam model is in the form of an approximate analytical expression that calculates the amplitude and phase variation of an ultrasonic field due to a single element transducer with simple geometrical shape (strip, circular or ellipse).

$$\phi(\mathbf{r}) = -i\pi\frac{\sqrt{N_x N_y}}{R}exp^{ikR}\frac{1}{\sqrt{B_x B_y}}\left[\frac{1}{B_x}(0.5 - A_x) + \frac{1}{B_y}(0.5 - A_y)\right]exp^{-(A_x + A_y)} \tag{4.3.2}$$

The field amplitude and phase is given by $\phi(\mathbf{r})$, $\mathbf{r}$ is a position vector at range $R$ from the transducer. The face of the transducer has dimension $2C_x$ and $2C_y$ and $N_x$, $N_y$, $B_x$, $B_y$, $A_x$ and $A_y$ are constants defined by:

$$R = \sqrt{x^2 + y^2 + z^2}, \quad N_{(x,y)} = \frac{C^2_{(x,y)}}{\lambda}, \quad B_{(x,y)} = 1 - i\frac{4\pi N_{(x,y)}}{15R}, \quad A_{(x,y)} = \frac{kC_{(x,y)}(x,y)^2}{15B_{(x,y)}R^2} \tag{4.3.3}$$

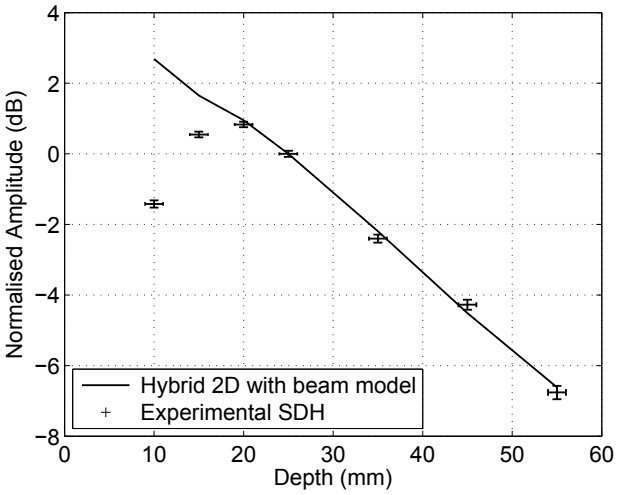


Figure 4.3.14: Comparison between two-dimensional Hybrid simulation including a simple beam model and experimental data for the ultrasonic response from SDHs with increasing depth.

where $x$ and $y$ are the distances from the beam axis at depth $z$.

Equation 4.3.2 and Equation 4.3.3 are used to propagate a time domain excitation from the transducer face, to each excitation node along the excitation line using a Fourier synthesis approach. By doing this, each simulation has a unique time domain excitation profile, as opposed to a plane wave excitation that was previously used. This approach retains the amplitude and phase variation that is generated by a transducer, however the excitation in the defect domain is only derived from the scalar wave potentials. The introduction of shear wave potentials will require an additional level of complexity that is not considered here.

The results of the Hybrid simulation including the beam model are compared against experimental data for the response from SDHs with increasing depth in Figure 4.3.14 and Figure 4.3.15 for the two and three-dimensional cases respectively. This is consistent with the experimental data shown in Figure 4.3.3 and Figure 4.3.4, which compared Hybrid simulations without a beam model.

To remain consistent with the previous simulations, the amplitudes are normalised against the SDH at $D = 25$ mm. The Hybrid simulations now have a means to calculate defect response within the $NFE$. For the two-dimensional case, the rate of attenuation has changed significantly from that shown in Figure 4.3.3. Defects beyond the $NFE$ now have an amplitude that is in excellent agreement with the experimental data. However, the introduction of the beam model to the two-dimensional simulations has not corrected for the amplitude within the $NFE$, with the amplitude being over estimated for targets at depths which are less than $D = 20$ mm. It has been reported by Chapman [13], that the beam model is capable of predicting the total signal amplitude to within $0.8NFE$. This partly explains

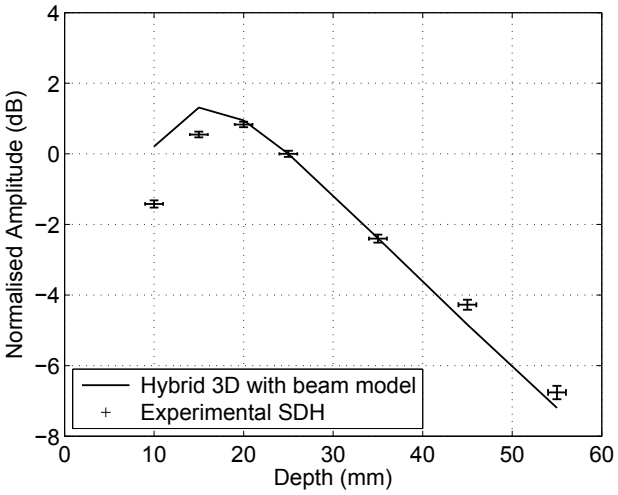


Figure 4.3.15: Comparison between three-dimensional Hybrid simulation including a simple beam model and experimental data for the ultrasonic response from SDHs with increasing depth.

the disagreement observed, however another likely explanation is that the two-dimensional plane strain boundary conditions are artificially increasing the amplitude of the excitation that is incident on the target. Since a circular transducer is being used, the implementation of the beam model into the FE plane-strain boundary conditions is likely to be invalid, especially within the $NFE$ where the relative signal amplitude is expected to be lower.

For the three-dimensional case, the implementation of the beam model provides a very good calculation for attenuation as a function of depth. The near-field response is now correctly accounted for and there is very little disagreement in the magnitude of these signals in both the near and far-field. Within the $NFE$ the simulated data is slightly over estimating the response with the $D = 10$ mm SDH over estimating the response by 1.6 dB. This level of disagreement is within a tolerable level, furthermore, it supports the statement made by Chapman [13], regarding accuracy of the beam model within the $NFE$. This also explains the disagreement observed in the two-dimensional case. The three-dimensional implementation of the beam model does not assume plane-strain boundary conditions and the response from a circular transducer is fully incorporated into the excitation line.

## 4.4 Conclusions

Commercial FE packages can been used to simulate elastic wave propagation and scattering problems, offering solutions that extend beyond the capabilities of analytical solutions. The use of triangular and

tetrahedral meshing algorithms is justified by comparing the performance of these elements against the need for a highly accurate representation of defect geometry. Partitioning functions can be used to control the variation of the mesh between structured and unstructured regions, with minimal mesh scattering. A review of recent literature is used to establish suitable levels of spatial and temporal discretisation. Poor selection of these variables results in an increased error in the wave speed propagation values, however, spatial discretization is by far the more important parameter. A highly refined mesh can offset any uncertainty introduced by poor temporal discretisation due to its inverse-square relationship with velocity error.

A domain linking algorithm, or Hybrid model, has been developed that allows for the use of reduced spatial domains to calculate defect scattering. The application of this model is verified by making comparisons with more conventional Full FE models for the two-dimensional case, along with a review of recent literature.

To validate the use of the Hybrid model comparisons are made with experimental data. The experimental data is consistent with ultrasonic NDE inspections, where a piezoelectric transducer is used to generate ultrasound which subsequently scatters from a target or defect. Previous authors have made time and frequency domain comparisons with experimental data, where the exact transducer response is known.

In this study, two version of the Hybrid model are used. The first approximates the transducer response by a Hanning window, producing a plane wave excitation on the defect domain, and the amplitude response is measured from a range of standard calibration targets at a range of depths and scattering angles. Comparisons are made with different wave modes, frequencies, host media and scattering angles. In all instances good agreement has been observed with experimental data, especially for three-dimensional Hybrid simulated data for defects lying in the far-field of the transducer. Within the near-field the Hybrid model fails to accurately predict the transducer response and results in some discrepancy in this range. This is attributed to the plane wave excitation that had been used, which does not correctly account for any variation in the incident signal amplitude as a function of range. It has also been observed that two-dimensional simulations will over estimate defect response, where the level of disagreement increases with an increase in the range of the target.

The second version of the Hybrid model attempts to account for the variation in the incident amplitude by introducing a beam computation model. The model is capable of correctly predicting variations in amplitude and phase from a transducer to within $0.8NFE$.

Implementation of this model in two-dimensional Hybrid simulations has proven to be partially successful. The far-field amplitude of targets shows excellent agreement between simulated and experimental data, however over estimates the responses within the $NFE$. This has been attributed to the plane-strain boundary conditions that are present in two-dimensional simulations, incorrectly incorporating the response from a circular transducer.

The implementation of a beam computation model to three-dimensional simulations has proven to be very successful. By fully incorporating the response from a single element transducer in a three-dimensional simulation, both the near and far-field response from the scatterers were correctly calculated. The ability to accurately and reliably calculate the ultrasonic response from standard calibration targets, by coupling the beam computation tool with a three-dimensional Hybrid model, is of significant importance to industry. This has demonstrated that FE methods offer a viable means to aid in the design of an industrial ultrasonic NDE inspection.

# 5 Ultrasonic Response from Rough Defects

Defects which possess rough surfaces can greatly affect ultrasonic wave scattering behaviour. A variety of analytical techniques have been developed to understand the effects of roughness on ultrasound, such as the Perturbation approach [19, 70], the Rayleigh method [76], and Kirchhoff theory. Kirchhoff theory is perhaps the most robust analytical technique and has been the tool of choice for modelling elastodynamic scattering problems, for both simple geometrical scatterers [8, 11, 12, 13, 14], and complex geometrical scatterers [15, 16, 17, 18, 75], which is discussed in Section 2.5.

This chapter will firstly make a comparison between FE and a specific extension to the Kirchhoff theory solution provided by Ogilvy [16], which has formed the basis for calculating signal attenuation due to defect roughness in the UK nuclear power generation industry. The FE model is designed to allow for a like-for-like comparison to be made between the two methods specific to the normal incidence case. An important distinction is made between the coherent, diffuse and total scattered signals, and the significance of these signals in a deployed NDE inspection. The FE models used make use of a Monte-Carlo approach to calculate the expected attenuation in total signal amplitude due to a statistical class of defect roughness. The consideration of the total field that results from the combination of coherent and diffuse fields has been previously reported by Ogilvy [9]. The extension made here is to consider a large number of surface realisations with the use of a full numerical simulation approach. The FE models are also compared with results obtained from experimental data, helping to increase the confidence in the results.

Comparisons between FE and Kirchhoff theory have also been made by Zhang *et al* [18]. In their study, a FE scattering matrix is used to identify a valid regime of Kirchhoff theory and concludes that for defects with low levels of roughness Kirchhoff theory provides a very accurate solution where the benefit in computational efficiency out-weighs the increased accuracy offered by FE. The work presented here goes beyond this range of validity, using a time domain commercially available solver to consider defect roughnesses that can not be solved using Kirchhoff theory.

The next section extends the FE model to consider oblique incident inspections for rough surfaces that are invalid for a Kirchhoff theory solution. The FE model is used to calculate back-scattered ultrasonic signals that return back along the path of propagation of the incident wave. This is a common occurrence in NDE inspections where previously the influence of misorientation and roughness had been considered as two separate scattering phenomena. In these simulations, the influence of both

can be considered together. This work is applicable to many ultrasonic inspection scenarios, but here it is of particular interest for the inspection of large pressure vessel forgings.

Following this, investigations are carried out to examine the influence of defect roughness on tip diffracted signals, again using a Monte-Carlo method. Comparisons are made with GTD and the impact of the results are discussed for applications involving ToFD and pulse-echo ultrasonic inspections. To date, the consideration of this problem in the UK nuclear power generation industry has made qualitative extensions of ideas presented in the previously reference literature. To the author's knowledge this is the first attempt at providing a quantitative solution for the influence of roughness on tip diffracted signals.

Finally, the ultrasonic response from a three-dimensional embedded, finite sized defect, is calculated using a FE model. A Monte-Carlo method is used once again, however in this instance the physical roughness of the defect remains fixed and the inspection frequency is changed. This, in effect, changes the defect roughness when expressed in terms of the incident wavelength, and provides an alternative approach to calculating signal attenuation due to roughness. This application case is more representative of the physical geometry associated with a deployed inspection and aims to identify any discrepancies that may arise between the two-dimensional generic approaches previously made and a more physical three-dimensional inspection representation.

This final study draws upon all aspect of the thesis. A time domain, elastic, FE solution is used and implemented into a commercial solver. To model the three-dimensional defect a highly discretised FE mesh is used which is then coupled to a domain linking algorithm. To reduce the overall size of the spatial domain, an optimised, spatially efficient SRM absorbing boundary is applied. This allows the FE simulations to compile using relatively little computational expense, providing an accurate and viable means to calculate ultrasonic response from rough defects for industrial NDE inspection problems in the nuclear power generation industry.

Having established an efficient methodology for using FE in ultrasonic NDE applications, the author has been able to make contributions towards calculating the ultrasonic response from rough defects. The first aspect of this work has been to make like-for-like comparisons with an extension of Kirchhoff theory that has formed the basis for accounting for the influence of defect roughness within the UK nuclear power generation industry [121, 122]. Following this, FE models are extended to investigate oblique incidence inspections, including a publication that makes specific reference to large forging inspections for misorientated, planar rough defect types [123]. Finally an investigation into the influence of roughness on tip diffracted signals is considered. This is believed to be the the first quantitative assessment of this scattering regime, the findings of which are outlined in this thesis.

## 5.1 Attenuation due to defect roughness

Defect roughness can significantly reduce the reflected signal amplitude when compared to that from a smooth defect. Ultrasonic NDE inspections of safety-critical components rely upon knowledge of this response for detecting and sizing flaws. Reliable characterisation is crucial, so it is essential to find an accurate means to predict any reductions in signal amplitude.

Analytical methods such as Kirchhoff theory can be used to calculate the ultrasonic response from rough defect types. However, it has been widely recognised that these approaches are very conservative, often over estimating signal attenuation, especially for high levels of roughness. As a result, this can lead to problems with overly sensitive inspections and consequent false call problems.

A numerical method, such as a FE model, does not have the same limitations as an analytical technique. FE offers the potential to calculate a full and accurate elastic wave solution for the scattering from rough surfaces, with the only limitation being computational resource that can be allocated to solving the problem.

Here, FE models are used to calculate the elastic scattering from multiple realisations of defects within a statistical class of roughness for normal and oblique incidence. Results from FE models are compared with Kirchhoff theory predictions and experimental measurements. An important distinction is made between the total, coherent and diffuse signals and how they relate to scattering responses observed in ultrasonic NDE inspections. This will provide a much more accurate prediction for the attenuation due to defect roughness, aiding in establishing dependable thresholds for inspecting safety-critical components.

### 5.1.1 Rough surfaces and scattering signals

The nature of a rough surface implies that no two are ever the same. It is therefore necessary to characterise defects by a set of common statistical parameters such that any rough defect can be assigned to a statistical class of roughness. It is noted from experimental measurements that the variation in height of the rough surface follows a distribution that is close to Gaussian [68, 69], where the root-mean-square (rms) height, $\sigma$, represents the variation in height of the defect from its mean plane. An approach making use of this observation and the resulting statistical characteristics has been widely adopted in previous studies and will be used here.

The scattered ultrasonic wave can be defined by two components, termed the coherent and diffuse fields [16]. Here, we consider the normal incidence case where the coherent signal is reflected back along the path of propagation as illustrated in Figure 5.1.1.

The coherent field is equal and in constant phase for all rough surfaces from the same statistical class and is located in the specularly reflected direction. The diffuse field is the random component of the ultrasonic signal which is introduced by the random nature of the rough surface and contributes

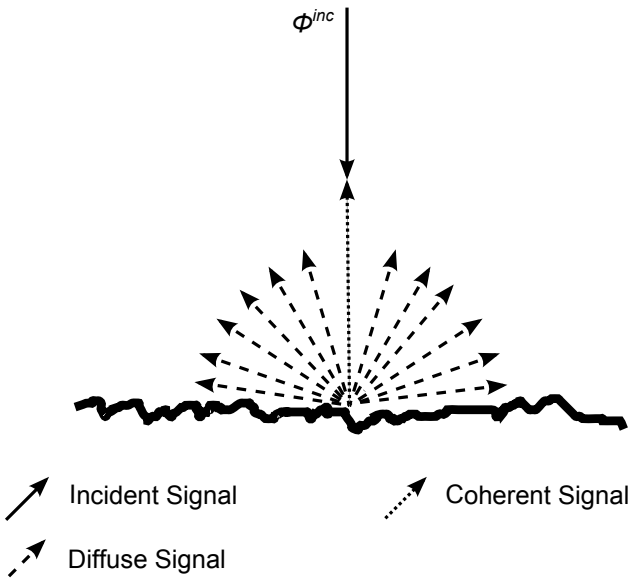


Figure 5.1.1: Figure to show the coherent and diffuse scattered signals resulting from a normally incident wave.

to the field in all scattering directions; this remains incoherent with respect to scattering signals from multiple realisations of surfaces within the same statistical class.

When making measurements of waves scattered from rough defects, the total signal received at any scattering angle, for a specific rough surface, is therefore comprised of a component from the coherent signal (which is common to all rough surfaces with the same surface statistics and lies in the specular direction) and a component of the diffuse field (specific to the surface under consideration and has a component in all scattering directions).

An important distinction must be made between these fields and the, commonly referred to, specular signal. The specular signal is that which is observed in the specular (or mirror-like) direction. For rough surfaces, this is comprised of all of the coherent signal and a contribution from the diffuse field. Since the coherent signal is in-phase for all realisations of the same statistical class, it must lie in the specular direction only. Parts of the wave that scatter away from the specular direction across multiple angles are random and therefore diffuse. These concepts have also been illustrated and discussed in Section 2.4.

Currently, for applications in the power generation industry, predictions of the back-scattered signals from rough defects are generally made through an extension of Kirchhoff theory provided by Ogilvy [16]. For this reason, the numerical models developed here will first be compared directly to findings from Kirchhoff theory. This will be to confirm the equivalent performance of both approaches under

conditions where Kirchhoff theory is known to be accurate, and demonstrate the advantage of using the FE approach when the surface characteristics are out of range for Kirchhoff theory.

#### 5.1.1.1 The Kirchhoff approximation

The application of Kirchhoff theory to this problem by Ogilvy [16], has resulted in the derivation of a single expression for the reduction in coherent ultrasonic signal amplitude due to increasing defect roughness. This is discussed in detail in Section 2.5.2 and shown in Figure 2.5.2.

As defect roughness increases, the magnitude of the coherent signal that is scattered from the rough surface is reduced. It is not possible to calculate an exact expression for the diffuse signal amplitude due to its incoherent nature. However, an approximate calculation that takes the average field intensity is used to give an order of magnitude estimate. This partly explains the reason for highly pessimistic predictions for reduction in signal amplitude made when using this expression, since the total field signal amplitude is not considered.

The amplitude of the reflected field given by Ogilvy [16] (Equation 2.5.7), is not sensitive to the correlation length $\lambda_0$. The expression is applicable to scenarios where $\lambda_0$ is such that the profile of the rough surface remains ergodic, and must therefore be small in comparison to the extent of the surface. The analysis assumes an infinite rough surface making the results independent of the correlation length. For the purpose of NDE, finite sized defects with rough surfaces by their very nature will be ergodic, making the independence of correlation length a valid assumption for this application. Furthermore, the use of transducers in practical NDE inspections means that an ultrasonic field is incident over a significant lateral extent, which further supports this conclusion.

This is of practical importance for industrial applications since now the defect roughness is expressed as a function of a single parameter, $\sigma$. This reduces the overall complexity of the problem and simplifies the concept for rigorous use in an industrial context.

#### 5.1.1.2 Finite Element model

Using a FE model, it is possible to calculate both the coherent signal and the total scattered field, by performing multiple simulations of the scattering from different surface realisations that satisfy the same statistical description. The results for the coherent field can then be compared against predictions for coherent signal amplitude obtained using Kirchhoff theory.

In order for a fair comparison to be made between the FE and Kirchhoff theory solutions it is important that the FE model is defined to represent the same setup that was assumed for the Kirchhoff model results. The expression given by Equation 2.5.7 is limited to a number of fundamental assumptions. These translate to a far-field solution from a plane wave scattering from an infinitely wide rough surface (i.e. no crack tips) described by a Gaussian distribution of roughness, for instances where the

scattering can be assumed to be independent of the correlation length.

This is achieved by using a Unit Cell model [119]. The model has symmetric boundary conditions at the lateral boundaries of its domain (Figure 5.1.2) such that the scattering from a small section of an infinitely long periodic defect can be calculated; provided the width of the cell is significantly larger than the correlation length.

The method for generating the defect surface is the same as that discussed in Section 3.2.6, where the rough surface is generated using a moving average process in order to correlate the heights, as described by Ogilvy, [116].

This model can provide a good representation of the reflection behaviour of the infinitely wide case, hence, the FE model assumptions are essentially the same at those used in Equation 2.5.7, except for the nature of the solver itself.

The model is configured using 30 nodes per incident wavelength and produces non-dimensional results, such that all scalar quantities (including defect roughness, $\sigma$) can be expressed as a function of the incident wavelength. Forcing along the nodes of the excitation line (Figure 5.1.2) represents the generation of an infinitely wide plane wave at normal incidence to the rough surface.

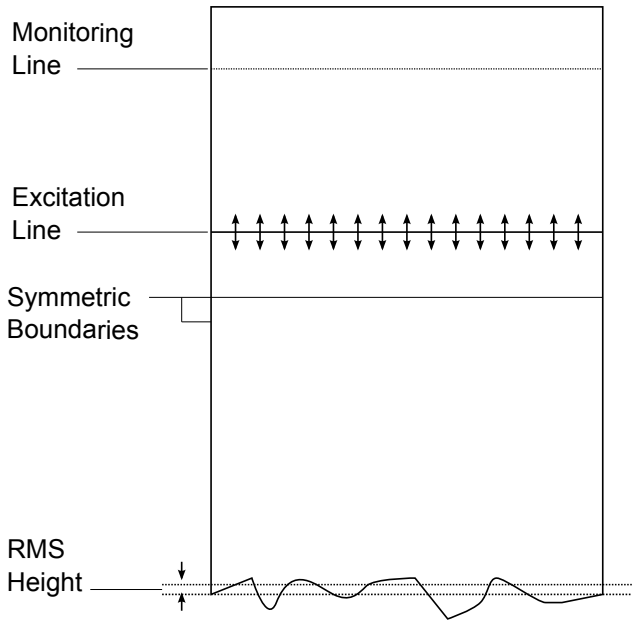


Figure 5.1.2: Unit Cell FE model with symmetric boundaries to simulate an infinite periodic surface, used to calculate the elastic wave scattering of a normally incident compression wave. The model is repeated for multiple realisations of defects defined by the same statistical class of roughness. The signal is monitored parallel to the plane of the incident wave along a monitoring line.

The signal is monitored parallel to the plane of the incident wave at range that is sufficient to distinguish between the reflected compression and shear wave modes. The response is then averaged along the length of the monitoring line to produce a single time history for the response from the rough surface.

### 5.1.2 Results

The FE model considers twenty classes of roughness within a range from $\sigma = 0.017\lambda_{inc}$ up to and including a value of $\sigma = 0.340\lambda_{inc}$. For each class, multiple realisations of defects all defined by the same statistical class are processed using the Unit Cell model. The number of realisations required to calculate the mean signal attenuation is dependent upon the class of defect roughness. When defect roughness is low, the number of realisations required for a convergent solution is less than for higher classes of roughness, therefore surface realisations are considered until a convergent solution has been obtained. Results from the convergence study are discussed and compared to work presented by Zhang *et al* [18], who discuss the convergence of solutions obtained from Kirchhoff theory simulations.

#### 5.1.2.1 Coherent signal amplitude

To extract the coherent signal amplitude the responses from each defect realisation within the statistical class of roughness must be superposed, as governed by Equation 5.1.1.

$$\phi^{\sigma}_{coh} = \frac{\sum_{i=1}^{N} \phi^{\sigma}_{i}}{N} \tag{5.1.1}$$

where $\phi^{\sigma}_{i}$ denotes the scattering response from an individual surface realisation $i$, within the statistical class of defect surface roughness $\sigma$, for the total number of realisations for that class of roughness $N$.

By summing the responses from each defect realisation within the statistical class, the effects of superposition cause any out-of-phase artifacts that are inconsistent across all the surfaces to be cancelled out. What remains is the in-phase coherent signal which is common to all surfaces within that class of roughness. Using Equation 5.1.1, the reduction in coherent signal amplitude for the rough surface with respect to the smooth surface becomes

$$\frac{|\phi^{\sigma}_{coh}|}{|\phi^{\sigma=0}_{inc}|} = \frac{|\frac{\sum_{i=1}^{N} \phi^{\sigma}_{i}}{N}|}{|\phi^{\sigma=0}|} \tag{5.1.2}$$

where $\phi^{\sigma=0}$ is the scattering response from a smooth defect with $\sigma = 0$. Figure 5.1.3 shows the comparison between the analytical solution (Equation 2.5.7) and numerical solution (Equation 5.1.2).

For low levels of roughness there is excellent agreement between the two techniques. This is as expected, since the FE method provides a highly accurate solution to elastic wave scattering and

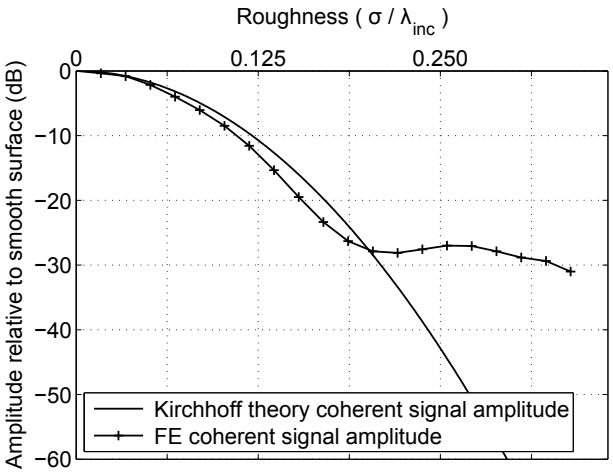


Figure 5.1.3: Reduction of amplitude of wave reflecting from a rough surface, with respect to a perfectly smooth surface. Results shown for coherent component, comparing Kirchhoff theory and Finite Element simulations. Results are for a normal incident compression wave with wavelength $\lambda_{inc}$, scattering from a defect with surface roughness, $\sigma$.

Kirchhoff theory is known to be a good approximation at low levels of roughness [16].

At high levels of roughness disagreement is observed confirming the pessimism of Kirchhoff theory. Due to the limitations of Kirchhoff theory, scenarios where multiple reflections or surface shadowing occur are not accounted for. An accurate scattering solution is only obtained from the scatterer if the deviation of the surface from flat is small in comparison to the wavelength of the incoming wave [19].

This surface property can be expressed quantitatively as a function of the radius of curvature of the defect, $a$. The Gaussian nature of the surface means that this parameter is itself defined by a distribution function. It is important to know the minimum value within this spread $a_{min}$, (defined by the $95^{th}$ percentile), since these smaller surface artifacts are not considered in the analytical solution [9].

$$a_{min} = \frac{0.1\lambda_0^2}{\sigma} \tag{5.1.3}$$

From Equation 5.1.3 it can be seen that $a_{min}$ is inversely proportional to roughness explaining why Kirchhoff theory is no longer valid at high levels of roughness. The accuracy of Kirchhoff theory due to this limitation has already been discussed in Section 2.2.2, and by extension of Equation 2.2.15 it can be quantitatively expressed by the condition:

$$k_{inc} a_{min} \cos^3 \theta_{inc} >> 1. \tag{5.1.4}$$

which relates the physical size of the radius of curvature $a_{min}$, to the incident wavenumber $k_{inc}$, and incident angle $\theta_{inc}$. Combining Equation 5.1.3 and Equation 5.1.4 allows for a single expression that relates the validity of Kirchhoff theory to defect roughness:

$$\frac{0.1 k_{inc} \lambda_0^2 \cos^3 \theta_{inc}}{\sigma} >> 1. \tag{5.1.5}$$

By plotting Equation 5.1.5 as a function of roughness, a valid regime of Kirchhoff theory can be identified, as shown in Figure 5.1.4.

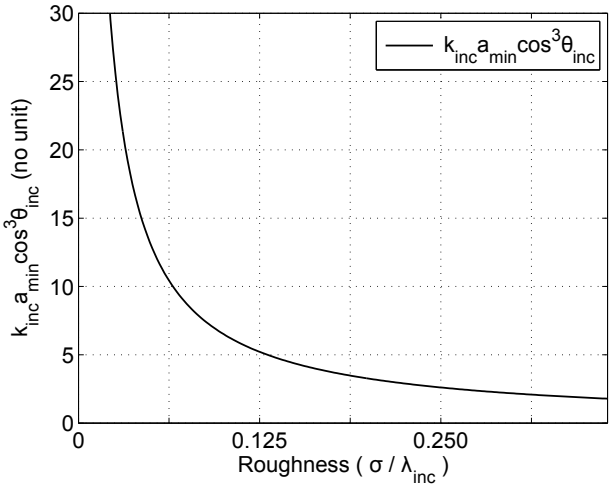


Figure 5.1.4: The variation in the function $k_{inc} a_{min} \cos^3 \theta_{inc}$ with increasing roughness for a normally incident compression wave, which must be significantly greater than 1 for a valid application of Kirchhoff theory.

As roughness increases the function $k_{inc} a_{min} \cos^3 \theta_{inc}$ tends to a value of 1. This denotes scenarios where Kirchhoff theory becomes increasingly inaccurate and explains the observed disagreement at high levels of roughness.

Since multiple realisations of rough surfaces from statistical classes are used to calculate the coherent signal, it is important to understand how many simulations are required to extract the true coherent signal. If too few are considered, not all of the out-of-phase components will have been removed from the scattered signal. However, running an unnecessarily large number of surface realisations, drastically increases computational expense with little benefit to the accuracy of the overall result.

To illustrate this point, the variation in coherent signal amplitude with increasing number of simulations is shown for three classes of roughness, Figure 5.1.5.

The values selected ($\sigma = 0.102\lambda_{inc}$, $\sigma = 0.153\lambda_{inc}$, $\sigma = 0.340\lambda_{inc}$) relate to low, medium and high levels of roughness. It can been seen that for low levels of roughness relatively few realisations

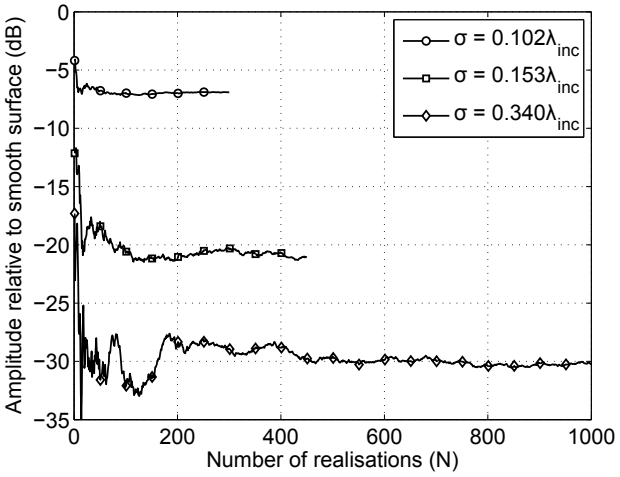


Figure 5.1.5: Variation in coherent signal amplitude with increasing number of surface realisations for three classes of surface roughness to show the number of realisations required to tend towards a convergent signal.

are required, typically of the order of one hundred. Little benefit is gained over the accuracy of the coherent signal amplitude by running further simulations. For rougher surfaces this is no longer the case, where thousands of surface realisations maybe required. This results from the increased variation in the surface profile height that can be expected with surfaces that are defined by much larger rms values.

Studies of simulated reflections from multiple realisations of rough surfaces have previously been considered by Ogilvy [9], using Kirchhoff theory for acoustic wave scattering, and Zhang *et al* [18], using Kirchhoff theory for the elastic case. Zhang also includes the use of a FE model, presenting the scattering from the defect in the form of a scattering matrix. The numerical model is used to identify a valid regime of Kirchhoff theory, concluding that for defects with low levels of roughness, the computational efficiency of the Kirchhoff approach out-weighs the increased accuracy offered by FE. Zhang *et al* [18], also investigate convergence of the total field with increasing numbers of simulations. Although different to the coherent field discussed here, the same principles are observed with increasingly rough surfaces requiring a greater number of surface realisations to tend towards convergence. It is also clear that for low levels of roughness, the difference between Kirchhoff theory and FE is small, however, as defect roughness is increased, Kirchhoff theory becomes increasingly inaccurate and a fully numerical approach is therefore required.

#### 5.1.2.2 Total signal amplitude

The convention in dealing with the ultrasonic NDE of rough defects in the power generation industry has been to quantify the reduction of the reflected signal amplitude by calculating the expected coherent signal. However, of greater practical interest and relevance is the mean of the total signal amplitude, which considers both the coherent and diffuse signal amplitudes combined. Multiple realisations must still be considered, but in this instance, instead of superposing the scattering response to obtain a coherent average, the amplitude of the signal from each simulation is obtained, and then the average of these amplitudes is calculated.

This delivers the value of the amplitude of the reflected signal that we would expect, on average, in an experimental setup. This is the total field, comprising the coherent field and the contribution of the diffuse field in this back-scatter direction. The consideration of the total field that results from the combination of coherent and diffuse fields has been previously reported by Ogilvy using a Kirchhoff theory solution [9]. The extension made here is to consider a larger number of surface realisations with the use of a full numerical simulation approach.

$$\phi^{\sigma}_{tot} = < |\phi^{\sigma}_{i,N}| > \tag{5.1.6}$$

Using Equation 5.1.6, the reduction in total signal amplitude due to increasing roughness becomes:

$$\frac{|\phi^{\sigma}_{tot}|}{|\phi_{inc}|} = \frac{< |\phi^{\sigma}_{i,N}| >}{|\phi^{\sigma=0}|} \tag{5.1.7}$$

Figure 5.1.6 shows the comparison between the analytical solution for the reduction in coherent signal amplitude (Equation 2.5.7) and the numerical solution for the reduction in total signal amplitude (Equation 5.1.7). Usually, these two signals would not be directly compared, however, as stated earlier, in NDE the inspection of safety critical components has often relied upon the coherent signal amplitude only, as a means to calculate attenuation due to defect roughness. Furthermore, an analytical expression for the total signal amplitude can not be deduced.

The significance of identifying this total field for evaluation is that it is consistent with what is observed when performing an NDE inspection. During an inspection there is normally only a single defect under consideration, therefore there is no means to calculate the coherent signal. On the other hand, the calculation of the amplitude of the total field from multiple realisations of defects of the same statistical description provides the best possible estimate of the expected amplitude: the average value of the amplitude of the received signal for different realisations of such a surface.

The results in Figure 5.1.6 show that as defect roughness is increased, the mean maximum amplitude of the total field is reduced, but not nearly to the same extent as for the Kirchhoff predictions for the coherent field, nor for the FE predictions of the coherent field that were shown in Figure 5.1.3. For

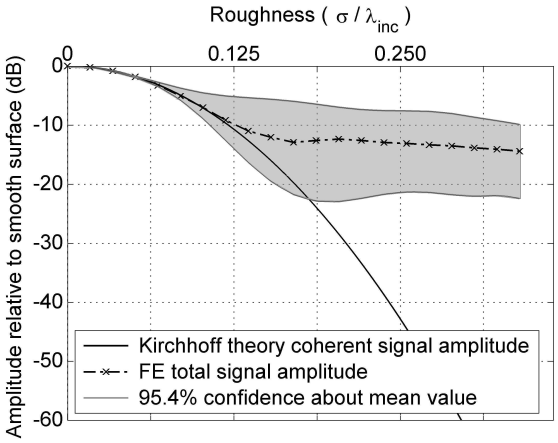


Figure 5.1.6: Comparison between the reduction in signal amplitude for the mean total reflected signal (calculated using FE) and the coherent signal (predicted from Kirchhoff theory). The total reflected signal is plotted with the 95.4% spread (or $2\sigma$ confidence) about the mean value.

defect roughness above $\sigma = 0.125\lambda_{inc}$, the mean reduction in signal amplitude plateaus to a value of approximately -12.0 dB.

Since multiple realisations of defect roughness are considered, the uncertainty about the mean reduction in the total signal amplitude can also be shown. As defect roughness increases, the uncertainty in the mean signal amplitude also increases. The confidence bands in Figure 5.1.6, show the 95.4% spread (or $2\sigma$ confidence) about the mean value. The confidence bands are calculated using an empirical cumulative density function, which makes no assumptions over the nature of the results or their distribution [117].

By making comparisons with the coherent signal amplitude from Equation 2.5.7, it can be seen that for low levels of roughness there is excellent agreement between the two techniques. For low levels of roughness, Kirchhoff theory is a very good approximation for the elastic wave scattering. Furthermore, in this region the majority of the total scattered field consists of the coherent scattered field, with the diffuse field still being of relatively low amplitude. However, beyond roughness values of $\sigma = 0.125\lambda_{inc}$ the total measured field and coherent field begin to deviate. This is due to the fact the total field is now comprised of a diffuse scattering component which is increasing with increasing roughness. This confirms the pessimism of Kirchhoff theory for severely rough surfaces and provides a more accurate estimate as to the attenuation in signal amplitude due to defect roughness.

### 5.1.3 Finite sized defects

The procedure outlined to calculate the total and coherent signals from rough defects has so far considered an infinitely wide rough surface. This limitation had been placed upon the FE model such that direct comparisons could be made with the extension to Kirchhoff theory provided by Ogilvy [16]. However, FE is not confined by this restriction, and if desired, it can be lifted to consider a more specific scenario.

In this instance, the FE model considers the scattering response from a finite sized defect of width 4 mm, to include scattering from crack tips. To generate this defect, both surfaces of the crack have the same morphology, excluding a small separation that defines the opening of the defect. This separation is at its greatest in the centre of the defect, and is gradually reduced until it is zero at the defect tips such that the crack is closed. Both surfaces of the defect are stress free boundaries within the FE models.

The case of a normal incident compression wave of frequency 2 MHz is used to calculate the attenuation in defect roughness. The range of defect roughness considered remains the same as was considered for the infinite defect case. Because this model considers the finite defect case, it is no longer necessary to use the Unit Cell model, instead the symmetric boundaries are replaced by absorbing layers, as shown in Figure 5.1.7.

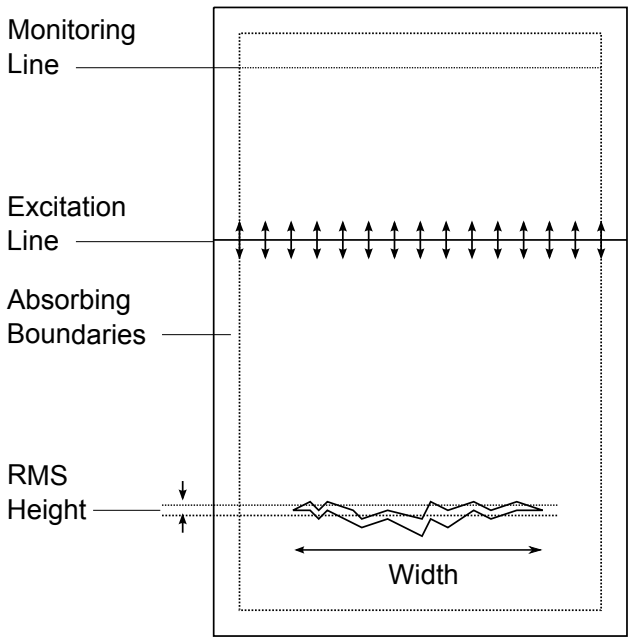


Figure 5.1.7: Revised FE model to consider the effects of a finite sized defect including scattering from crack tips.

The signal is monitored in the same manner as the infinite defect case, parallel to the plane of the incident wave at a range that is sufficient to distinguish between the reflected compression and shear wave modes.

For each class of defect roughness considered, multiple realisations of defects all defined by the same statistical class are processed. As with the infinite defect case, the number of realisations required to calculate the mean signal attenuation is dependent upon the class of defect roughness, therefore surface realisations are considered until a convergent solution has been obtained.

The application of Kirchhoff theory provided by Ogilvy [16] (in the power generation industry), does not account for any difference that may occur due to the finite size of the defect. For this reason, the FE model will be compared directly to findings from Kirchhoff theory. The results from this simulation are shown in Figure 5.1.8.

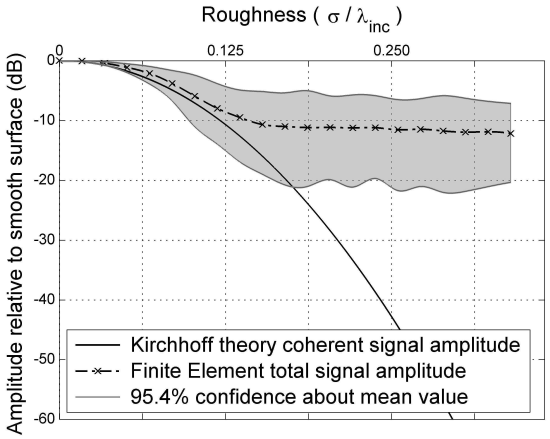


Figure 5.1.8: Comparison between the reduction in signal amplitude from a finite sized defect for the mean total reflected signal (calculated using FE) and the coherent signal (predicted from Kirchhoff theory). The total reflected signal is plotted with the 95.4% spread (or $2\sigma$ confidence) about the mean value.

The results shown in Figure 5.1.8 follow the same trends as observed with the infinite defect (Figure 5.1.6). As defect roughness increases the mean scattered signal is reduced. For defect roughness above $\sigma = 0.125\lambda_{inc}$, the mean reduction in signal amplitude plateaus to a value of approximately -11.0 dB, which lies significantly above the coherent signal component of Kirchhoff theory.

Differences are observed between the infinite and finite cases. Although consistent with one another, the finite defect case predicts the plateau in the mean attenuated signal to be -11.0 dB in comparison to -12.0 dB for the infinite case. When considering finite sized defects, the level of uncertainty appears to be greater than the infinite defect case, especially at lower levels of roughness. This is likely to be

due to the additional diffraction generated by the rough crack tips, which is present across all levels of roughness from finite sized defects.

### 5.1.4 Experimental validation

The methodology is validated by comparisons with two experiments, one involving a simple regular profile that can be studied in a deterministic non-statistical manner, and the other involving a real rough surface that is studied statistically.

#### 5.1.4.1 Simple regular profile

A rectangular test piece of thickness 10 mm with a sinusoidal artificial defect machined into the back face is scanned. The experimental setup is shown in Figure 5.1.9. The sample is scanned from the front face with a 5 MHz, 0.25″ diameter compression wave transducer at normal incidence. The sinusoidal back-wall is corrugated such that the surface profile varies in one direction only with a period of 4 mm, with a value of $\sigma = 0.220\ \lambda_{inc}$. Either side of the sinusoidal defect the back-wall is smooth, this is used to normalise the response from the rough surface to that from a smooth surface, so that the results can be presented in the conventional manner as the reduction of amplitude caused by roughness.

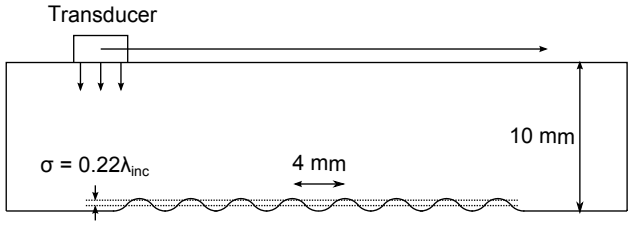


Figure 5.1.9: Sinusoidal test piece used to validate elastic scattering from rough surface. This sample is scanned from the front face with a 5 MHz, 0.25″ diameter compression wave transducer at normal incidence; this scan is then replicated in FE.

The significance of this sample is that it is a well understood scatterer that can be represented by two-dimensional plane-strain models used in both the Kirchhoff theory and FE approaches. Furthermore, because the sample is sinusoidal, the value of $\sigma$ remains constant across the surface of the defect.

A pulse-echo configuration is deployed in both the experiment and the modelling, such that the monitored response is a single time history at a position above the defect. The transducer scans along the sinusoidal sample extracting the pulse-echo time history at 1 mm increments. Signals from the flat back-wall on each side of the defect are used to normalise signals at every rough surface scan position. The experimental approach is replicated in FE by computing individual simulations at every scanning position. The scan results from the experimental and FE simulations are shown in Figure 5.1.10a) and

a)

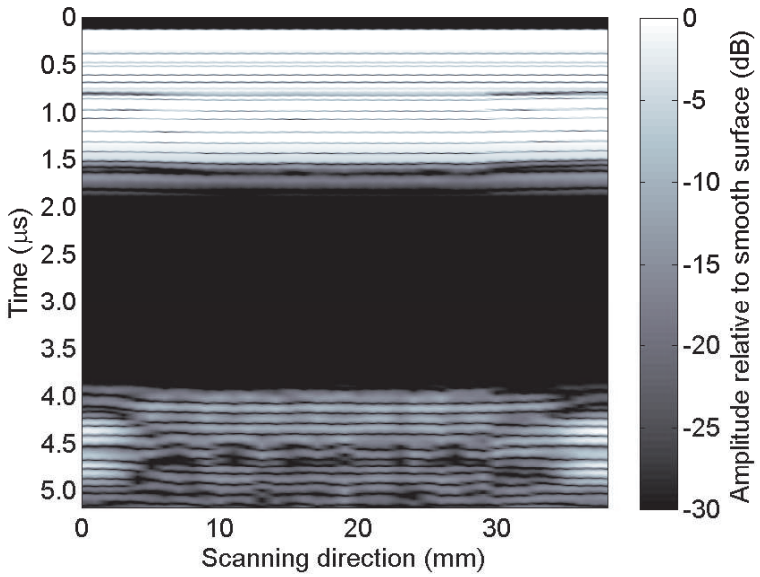


b)

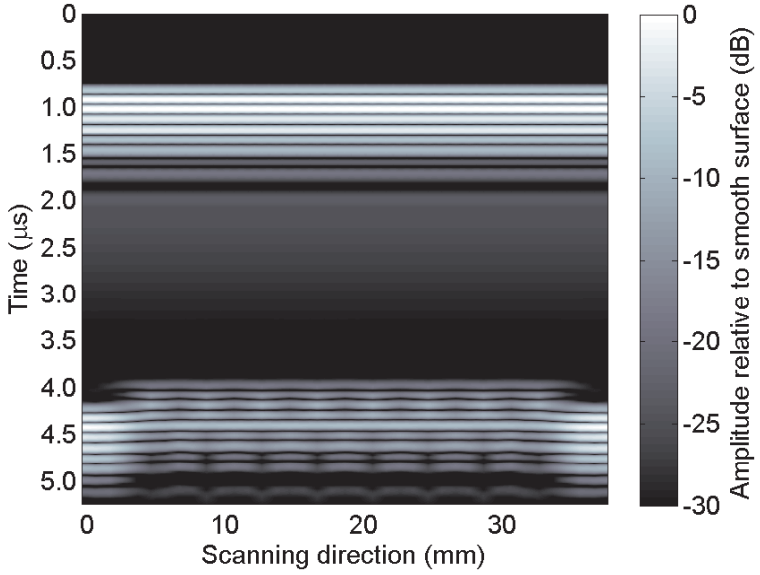


Figure 5.1.10: Figure to show a) experimental scan and b) FE scan of sinusoidal test piece showing (grey scale) reduction in signal amplitude due to roughness; scans are normalised against the response from the smooth back-wall at 0 mm and 37 mm. The response from the sinusoidal section has an arrival time of 3.9 μs and is followed by the response from the smooth section at 4.1 μs.

Figure 5.1.10b) respectively. A time domain window is used to remove transducer ring-down from the experimental results.

Figure 5.1.10a) and Figure 5.1.10b) show good agreement with one another. The times of arrival of the reflected signals are consistent with one another, with both showing similar patterns of reduction of the signal amplitude due to roughness. The response from the smooth back-wall can be seen at scanning positions 0 mm and 37 mm. To better appreciate the reduction in signal amplitude due to roughness, the maximum response within the time window 3.9 µs - 5.0µs is plotted against scanning direction, Figure 5.1.11.

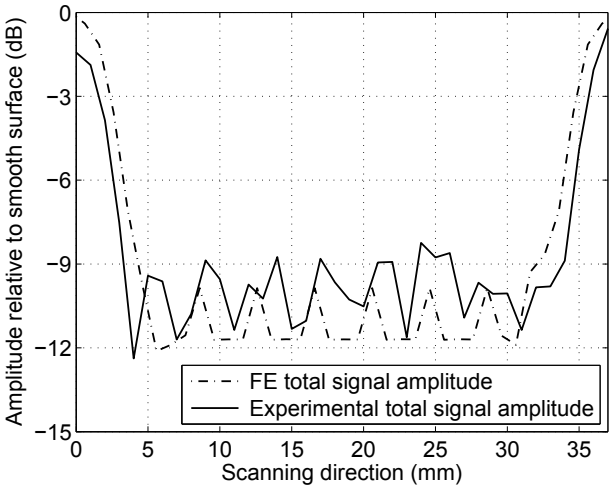


Figure 5.1.11: Reflection coefficient from a scan over sinusoidal surface, showing comparison between experimental measurements and FE simulations.

There is excellent agreement between the experiment and the simulations, with the FE model accurately predicting the reduction in the scattered amplitude due to roughness. The mean measured reduction due to roughness is -9.9 dB, with FE slightly over estimating the reduction (-11.0 dB).

#### 5.1.4.2 Real rough surface

The FE model presented here is a two-dimensional plane-strain representation of elastic scattering from rough surfaces. To check the validity of this approach, the attenuation due to defect roughness shown in Figure 5.1.6, is compared against experimental data.

Four rectangular test blocks of length 60 mm, breadth 40 mm and thickness 40 mm have been produced with back-walls which have roughness varying in both dimensions. In each case, the roughness of the back-wall has been generated by cyclic loading which has resulted in three types of cracking; fatigue, ductile tear and brittle fast fracture. Although each of these three types of cracking is not

necessarily applicable to the power generation industry, the statistical variation of the rough surfaces is, and therefore can be used to provide some form of experimental validation for the FE model. The rough back-walls are scanned using an Alicona microscope to give an accurate measurement of their surface profiles. From these profiles, measurements of surface roughness can be made.

The test blocks are raster scanned from the front face at 1 mm steps with a 4 MHz, 0.5″ diameter, unfocused compression wave transducer at normal incidence. The roughness of the back-wall varies in two directions and as a result contains a distribution of rms values. A small section of the back-wall is smooth which is used to normalise the responses to establish the reduction in signal amplitude due to roughness. The experimental configuration is shown in Figure 5.1.12.

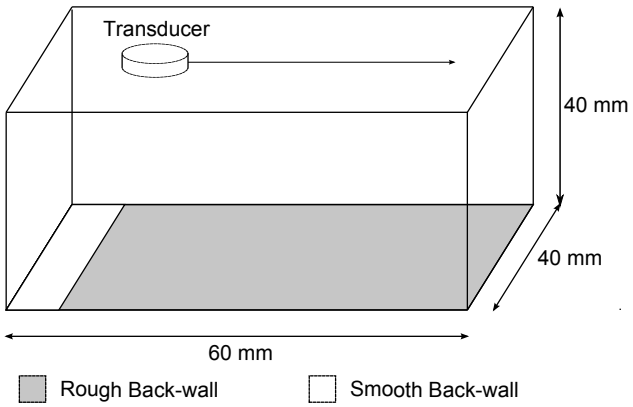


Figure 5.1.12: Dimensions of test blocks and the position of the rough back-wall relative to the scanning surface.

For each increment over the surface a single time history is obtained. Each time history shows the reduction in signal amplitude of the back-wall signal due to roughness. This reduction varies over different scanning positions due to local variations in surface roughness across the sample. From the surface profile data, the local rms of the surface for the area immediately beneath the transducer can be calculated. Combining this local rms value of the surface with the reduction in signal amplitude (compared to a smooth back-wall) gives an experimental measurement of the reduction in signal amplitude due to increasing roughness. Across the four samples, 4396 experimental discrete measurements have been taken. Scan positions that are close to the test block edges have been omitted since the effect of the edge of the test block on the scan data is unknown.

Figure 5.1.13 shows a comparison between predictions made using the FE model and the experimental data points. There is good agreement between the predictions made using the FE model and the experimental data. As predicted with the FE model, rough surfaces with the same level of roughness show a spread in the reduction in signal amplitude, this being due to the unique nature of each surface

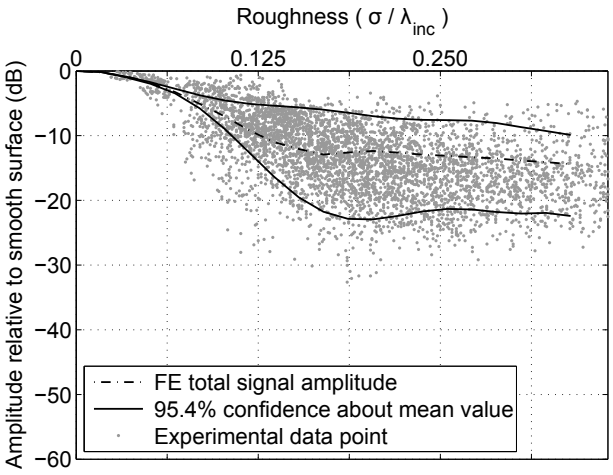


Figure 5.1.13: Comparison between the reduction in reflection coefficients for the mean total reflected signal (calculated using FE) and the total reflected signal measured experimentally. The mean total reflected signal is plotted with the 95.4% spread (or $2\sigma$ confidence) about the mean value.

within the statistical class.

The measurements taken experimentally show a plateau in signal attenuation as roughness is increased. This suggests that increasing the roughness further will have no effect on the mean attenuation or the confidence in the spread of data.

From the 95.4% spread (or $2\sigma$ confidence), by definition it is expected that 2.3% of the experimental data points would lie beneath the lower confidence level. Here, 14.1% of the data points were found to lie below this line. The largest difference between the FE model and the experimental data is at mid-roughness values in the range $\sigma = 0.050\lambda_{inc}$ to $\sigma = 0.167\lambda_{inc}$. The mean attenuation is still applicable, however, experimentally an increase in the spread of values is observed. Therefore, the lower confidence band in this range for the FE model is optimistic. This discrepancy could be attributed to the FE model not considering the response of the transducer or inconsistencies of coupling across the extent of the scanning surface. The use of a two-dimensional model has been justified and remains consistent with approximations imposed on the solution derived from Kirchhoff theory [16], however, the experimental configuration will only truly be represented by a three-dimensional model. At this stage it is unclear what differences would arise. FE models could be re-run to be more representative of the exact system that has been measured experimentally, however the agreement in general is very good, and it is not considered worthwhile to pursue such details. Consideration is however given to a more specialised three-dimensional case, which is discussed in Section 5.4.

From all the experimental data points, only 0.1% had a signal attenuation that was less than -

30.0 dB. Practically this implies that the likelihood of encountering a defect that would attenuate the signal amplitude this severely is rare. Furthermore, the statistical nature of this problem means that encountering a crack with such a high signal attenuation across the entire crack surface is an even less likely event.

## 5.2 Oblique incidence backscatter

The presence of defect roughness will result in the attenuation of back-scattered ultrasonic signals for the normal incidence case. For oblique incidence, the backscattering from rough surfaces is still characterised by the total, coherent and diffuse signals; however, the same attenuation characteristics are not observed.

Conventionally, for NDE applications in the power generation industry, defect roughness is thought to attenuate scattered signals with respect to the equivalent smooth surface, even for oblique incidence. However, this is not necessarily the case, since the rough surface will always have a diffuse component scattered across multiple scattering angles, which is not apparent for smooth surfaces. Figure 5.2.1 shows an oblique incidence wave scattering from a rough surface where the back-scattered signal is being measured back along the path of propagation of the incident wave.

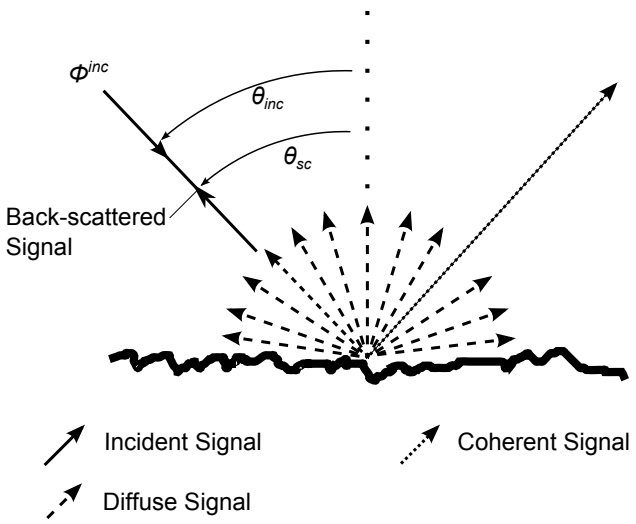


Figure 5.2.1: Figure to show oblique incidence wave scattering from a rough surface. The scattered signal consists of diffuse and coherent fields. The back-scattered signal lies back along the path of propagation.

For oblique incidence the combined effect of the coherent and diffuse scattering signals is difficult to assess quantitatively using analytical methods; therefore a numerical approach must be applied.

This approach is capable of deducing the total scattered field in any desired direction for any incident angle. Furthermore, as with the case of normal incidence, a statistical distribution of results can be obtained to provide the mean signal amplitude from multiple realisations of rough defects from the same statistical class.

Here we consider the effects of defect roughness on the total scattered field for the specific case of backscatter, that is the field that is scattered back along the path of the incident wave. This case has practical importance for pulse-echo inspections using a single element transducer. We consider this case for a range of oblique angles of incidence. In this case an incident shear wave is used, with all spatial dimensions expressed in terms of the incident wavelength. To provide some understanding for the effect of increasing defect roughness for angular performance, these simulations are compiled for two different classes of roughness, $\sigma = 0.063\lambda_{inc}$ and $\sigma = 0.200\lambda_{inc}$. The amplitude of the total field is then compared to the smooth defect case. Comparisons will be made for defects that are of a finite size or that can be considered to be infinite in extent. The significance of this relates to scenarios where the extent of the defect is either greater than or less than the extent of the incident beam, or the inspection of surfaces at oblique angles of incidence.

### 5.2.1 Infinite defect extent

The oblique incidence case for an infinite defect cannot be simulated using the Unit Cell model that was deployed for the normal incidence study. Therefore, in order to satisfy the requirement for a Gaussian representation of the surface roughness, the extent of the defect must be significantly larger than the wavelength of the incident wave. In this case the term 'infinite defect' therefore applies to scenarios where the incident beam has no interaction with the tips of the defect.

To achieve this, the FE model represents a relatively large spatial domain. Furthermore, performing multiple realisations, across multiple angles of incidence, for multiple class of defect roughness, dramatically increases the number of computations required to extract a statistically significant result. For these reasons, the FE model had to be adapted slightly through the use of a domain linking algorithm as shown in Figure 5.2.2 [82].

This allows for the FE model to only consider the area immediately surrounding the defect. An algorithm based on Greens' functions is used, linking the wave potentials around the FE domain to any desired location in the far-field, in this case a position that is back along the propagation path of the incident wave. All other model variables remain consistent with the normal incident case.

The displacements and stresses for the scattered response are recorded by a monitoring box, which are then passed to the domain linking algorithm. Here, defect roughness remains fixed whilst the angle of incidence is varied from $-60^o$ to $60^o$ in $10^o$ increments. This range is limited because greater values of defect tilt drastically increase the size of the FE model. Multiple realisations of the same defect

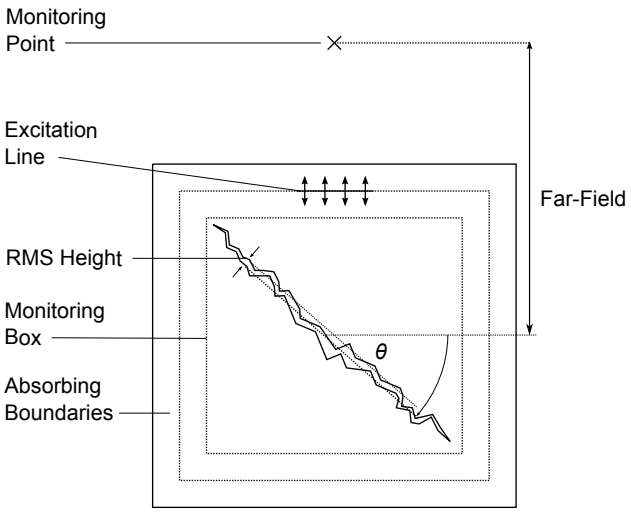


Figure 5.2.2: FE model with significantly reduced spatial domain for an incident shear wave interacting with a rough defect at oblique incidence where the extent of the defect is greater than the incident beam.

roughness are considered to calculate the mean total field across all angles of incidence. The results are compared to the response from a smooth defect at normal incidence, see Figure 5.2.3.

For smooth defects, increasing the misorientation of the defect results in a reduction of the magnitude of the total ultrasonic signal that is measured back along the path of propagation. The maximum signal is observed at a misorientation of $0^o$, which relates to the normal incidence case. The reduction observed is due to the fact that the specularly reflected signal no longer lies along the path of the incident wave. For smooth defects the signal amplitude drops off rapidly, indicating that small degrees of misorientation will hinder the detection of defects. The amplitude of the back-scattered signal returning from the defect, although low, is not measured to be zero. This is due to some component of the specularly reflected signal resulting in an indication back-along the path of propagation.

For defects with roughness of $\sigma = 0.063\lambda_{inc}$, at $0^o$ there is an observed reduction in the mean amplitude of the total field, which is consistent with what has been measured in Figure 5.1.6. As the misorientation increases, the mean amplitude of the total field is again reduced, however, the reduction in signal amplitude is less than what is observed for the smooth case. This is due to an increase in the diffuse scattered field, which is a dominant component of the total scattered field measured back along the path of the incident wave.

As defect roughness is increased further still, as is seen for $\sigma = 0.200\lambda_{inc}$, the same trends are observed. Again at $0^o$ there is a observed reduction in the mean amplitude of the total field and as the misorientation increases, the amplitude of the total field is again reduced. But in this case, the

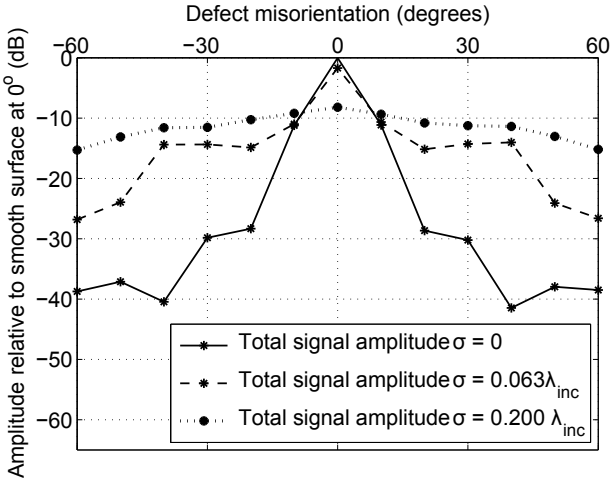


Figure 5.2.3: The mean total reflected signal amplitude as a function of defect misorientation for an incident shear wave. The scattered response for two classes of defect roughness ($\sigma = 0.063\lambda_{inc}$ and $\sigma = 0.200\lambda_{inc}$) is plotted and normalised against the normal incidence case for a smooth defect.

increase in roughness results in an increase in the diffuse component of the scattered field and therefore a higher amplitude signal than for the smooth and $\sigma = 0.063\lambda_{inc}$ cases.

### 5.2.2 Finite defect extent

The oblique incidence case for a finite sized defect can also be calculated using a domain linking algorithm [82]. This is applicable to instances where the extent of the incident beam can be considered to be greater than the extent of the defect. Here, the tip diffracted signals will contribute to the total scattered signal that is observed in the back-scattered direction. For particularly small defects with high degrees of misorientation, the tip diffracted signal will become the dominant component of the detection mechanism. Figure 5.2.4 shows the FE model used to calculate the response. The length of the excitation line is significantly greater than the extent of the defect, such that any interaction with the defect tips is recorded by the monitoring box.

The displacements and stresses for the scattered response are recorded by the monitoring box, which are then passed to the domain linking algorithm. The total field is calculated at a position in the far-field. Here, defect roughness remains fixed whilst the angle of incidence is varied from $-90^o$ to $90^o$ in $10^o$ increments. Multiple realisations of the same defect roughness are considered to calculate the mean total field across all angles of incidence. To provide some understanding for the effect of increasing defect roughness for angular performance, these simulations are compiled for two different

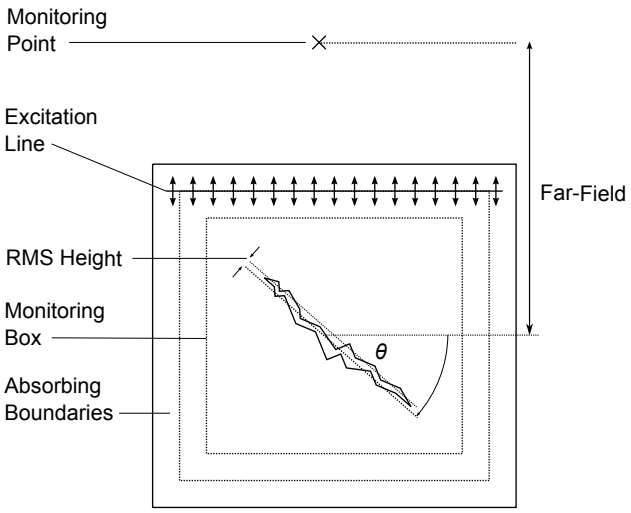


Figure 5.2.4: FE model with significantly reduced spatial domain for an incident shear wave interacting with a rough defect at oblique incidence where the beam spread is greater than the extent of the defect.

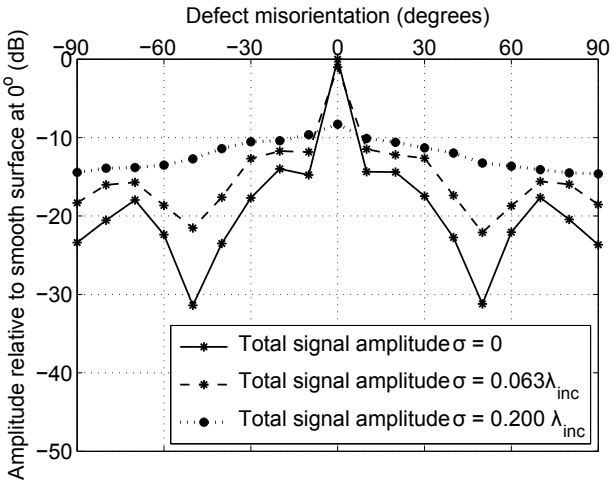


Figure 5.2.5: Magnitude of the total back-reflected signal for an incident shear wave interacting with a rough defect at oblique incidence where the beam spread is greater than the extent of the defect; the magnitude is expressed as attenuation with respect to the reflection from a smooth crack at normal incidence.

classes of roughness, $\sigma = 0.063\lambda_{inc}$ and $\sigma = 0.200\lambda_{inc}$. The results are compared to the response from a smooth defect, see Figure 5.2.5.

For smooth defects, increasing the misorientation of the defect results in a reduction of the magnitude of the total ultrasonic signal that is measured back at the transducer. However, the inclusion of tip diffracted signals contributes to the total field, affecting the overall amplitude when compared to the infinite defect extent case. The contribution of tip diffracted signals to the total field is not a constant across all angles of misorientation; the scattered field is a function of incident angle, scattering angle and wave mode. Predictions can be made using GTD, however a more important factor is the superposition of signals from the top and bottom tips [24]. As the size of the defect approaches the wavelength of the incident wave, diffracted signals from the top and bottom tips will superpose. This interference can be either constructive or destructive and is responsible for the fluctuations in the total field observed with increasing defect misorientation, as illustrated in Figure 5.2.6.

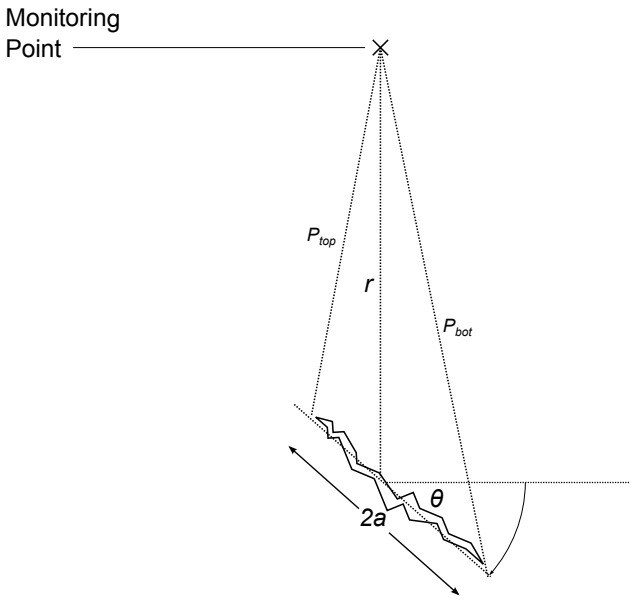


Figure 5.2.6: Figure to show superposition of top and bottom tip diffracted signals.

For a defect at depth $r$, with misorientation $\theta$ about the horizontal, and length $2a$; the path lengths from the top and bottom tips, $P_{top}$ and $P_{bot}$, can be calculated by:

$$P_{top} = \left(r^2 + a^2 - 2ra\cos(90 - \theta)\right)^{\frac{1}{2}} \tag{5.2.1}$$

$$P_{bot} = \left(r^2 + a^2 - 2ra\cos(90 + \theta)\right)^{\frac{1}{2}} \tag{5.2.2}$$

When the differences between the path lengths is equal to an integer number of wavelengths destructive interference will occur. Similarly, if the difference should be equal to an integer number of half wavelengths, constructive interference will occur (it is also necessary to account for the natural change in phase that occurs between the top and bottom tips). This is expressed by Equation 5.2.3, where $n$ is an integer.

$$\frac{n\lambda_{inc}}{2} = |P_{bot} - P_{top}| \tag{5.2.3}$$

If $n$ is even, destructive interference will occur and the signal amplitude will be reduced. If $n$ is odd constructive interference will occur and the signal amplitude will be increased.

As defect roughness is increased, the same general characteristics are observed. Defect roughness attenuates the ultrasonic signal for the normal incidence case and although the signal is attenuated for increasing levels of defect misorientation, the attenuation is not as severe as for the smooth defect case. Again this can be attributed to an increase in the diffuse field, which dominates the total measured field as roughness increases. The addition of tip diffracted signals also contributes to the total ultrasonic signal in the same manner, resulting in a slight change to the signal amplitudes when compared to defects which are greater in extent.

The increase in defect roughness has also nullified the superposition of top and bottom tip diffracted signals. For the smooth defect case, the tip diffracted signals are entirely coherent and will superpose in a manner that is consistent with GTD. For defects with increasing roughness, the tip diffracted signal will contain coherent and diffuse components. The coherent components will still behave in the same manner, however their contribution to the total field is reduced. The diffuse field components from the tips are incoherent, reducing the occurrence of instances where destructive super-positioning is taking place. This effect can be observed at defect misorientations approaching $\pm 50^o$. Here the increase in defect roughness has removed the effects of destructive super-positioning, affecting the signal amplitude in this range.

## 5.3 Influence of roughness on tip diffraction

For the purposes of sizing and defect characterisation, one such detection mechanism relies upon the diffraction of ultrasound from defect tips and edges. A review of detection methods using pulse-echo ultrasonics is given by Doyle and Scala [124], however, the difficulties associated with achieving accurate sizing led to the development of the commonly used ToFD technique [125, 126].

Due to the complexities of scattering behaviour, the nature of the diffracted signals from defect tips is a function of the defect geometry, inspection frequency and the incident and scattering angles. Therefore, when designing an ultrasonic NDE inspection, it is important to have an understanding

of the complete scattering scenario such that the optimal configuration for defect detection can be employed. This can be achieved through the adaptation of viable analytical modelling techniques such as GTD, which is discussed thoroughly in Section 2.2.3.

Despite successful application, GTD does not account for defect roughness. As a result the effects of multiple wave scattering, fully elastic mode conversion and surface shadowing are not considered. Ultimately, this impedes the ability of the technique to differentiate between the scattering signals that originate from different features of the defect, and therefore, increases the uncertainty in accurately sizing and characterising the defect. Furthermore, defect roughness will result in potential attenuation of tip diffracted signals. If these fall below background noise levels then features of the defect may become undetectable. Improving the understanding of tip diffracted signals from rough defects will help to remove any uncertainty associated with this phenomenon.

FE models are used to calculate the elastic scattering from two-dimensional smooth and rough defects tips across all incident and scattering angles. Results from FE models for smooth crack tips are compared with GTD predictions in order to establish confidence in the numerical model. Following this, the approach is extended towards multiple realisations of rough defect tips which are defined by the same statistical class of roughness.

### 5.3.1 Comparison between Geometrical Theory of Diffraction and Finite Elements

It has been demonstrated that FE is a well validated method for calculating ultrasonic scattering in general, and it is therefore expected that this would be true for tip diffracted signals as well. To confirm this point, a comparison is made between GTD and FE for calculating tip diffraction from a smooth defect. GTD has a thorough history of validation in this regime and agreement with FE for the smooth case will increase confidence for future use of these tools when applied to calculating the influence of roughness on tip diffracted signals.

A two-dimensional FE model is used to calculate the magnitude of the reflected compression and shear wave modes scattered across an angular range from a smooth crack tip, that results from a compression wave, incident across an angular range. The results from the FE model will be compared with Equation 2.2.17 and Equation 2.2.18 (which have been introduced in Section 2.2.3), and the spatial domain of the FE model is shown in Figure 5.3.1.

A stress-free boundary defines the tip of the defect with the remainder of the crack embedded within absorbing boundaries. The model is comprised of a free mesh of triangular elements, as described in Section 4.1, where nodal separation is used to define the opening of the crack. The opening of the crack can be considered to be sufficiently narrow such that it is of negligible extent. This approximation is not expected to result in any discrepancy. Due to the symmetry of this model, the incident angle is varied from $27^o$ to $179^o$ in increments of $2^o$. The presence of the defect itself means that it is not

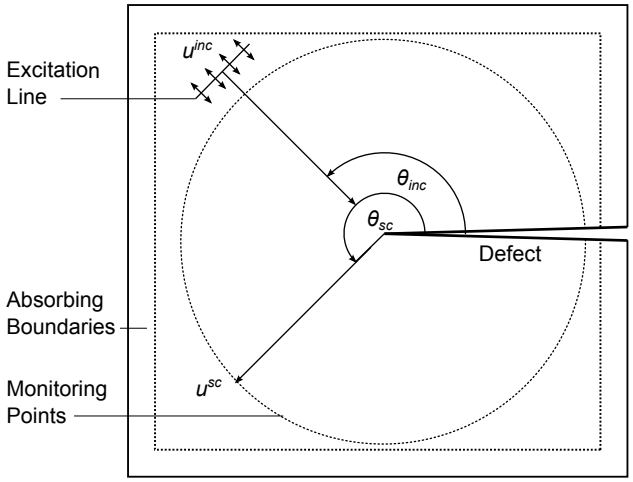


Figure 5.3.1: Incident compression wave on a crack tip across angular range, $\theta_{inc}$, where the compression and shear wave modes are monitored across scattering angle $\theta_{sc}$.

possible to consider incident angles that are less than $27^o$ without maintaining the excitation line.

The model is configured to produce non-dimensional results, such that all scalar quantities can be expressed as a function of the incident wavelength. Forcing along the nodes of the excitation line represents the generation of a plane compression wave incidence on the defect tip. An excitation frequency of 1 Hz is used in a material in which the bulk velocities are 2 and 1 units for compression and shear waves respectively and the mesh is discretised at 20 nodes per incident wavelength. Forcing along the nodes of the excitation line, which has a length of 2.5 units, represents the generation of a plane wave incidence on the defect tip.

The signal is monitored at nodes around a circular arc from $1^o$ to $360^o$ in $1^o$ increments. The monitoring nodes are at a sufficient range to differentiate between the compression and shear wave modes scattering from the tip, but not so far as to unnecessarily increase the size of the spatial domain. From these simulations, scattering matrices showing the magnitude of the scattered compression and shear wave modes from a crack tip are extracted. This is achieved by recording the nodal displacements of the monitoring nodes in the direction that is normal to the circular arc and taking the maximum displacement observed at this location. This is performed for all incident and scattering angles and compared against those values obtained from GTD, shown in Figure 5.3.2 and Figure 5.3.3 respectively.

Figures 5.3.2 and Figure 5.3.3 show very good agreement between GTD and FE simulations for calculating the scattering from a smooth defect tip. The same trends are observed in both data sets, remaining consistent for the amplitude of the scattered signals. A lack of data is observed from the FE simulations for incident angles below $27^o$ and above $333^o$, since these simulations could not be

a)

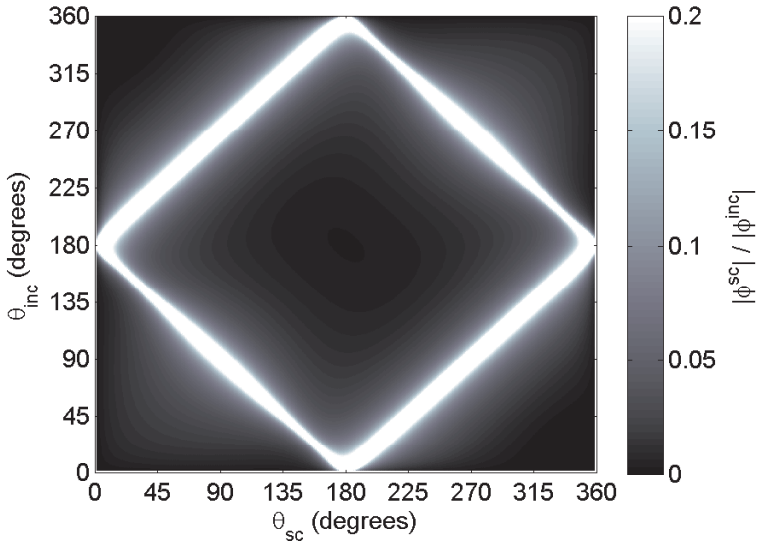


b)

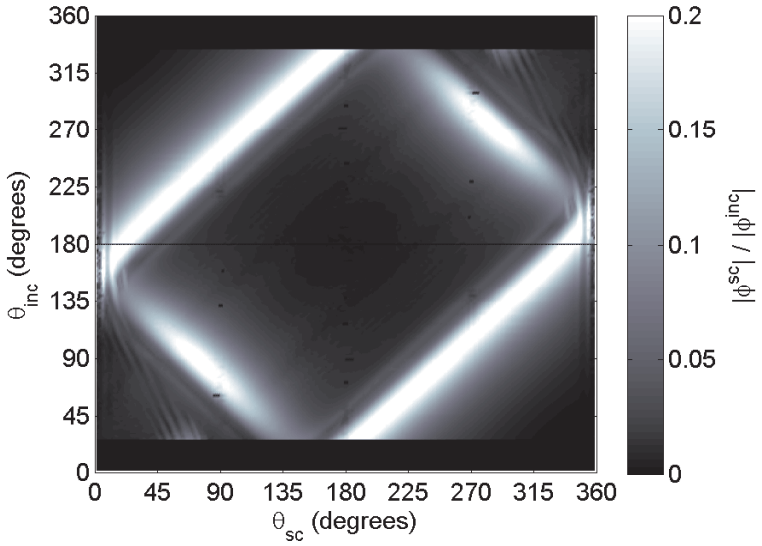


Figure 5.3.2: Scattering matrices showing the magnitude of the scattered compression wave from a smooth defect tip due to an incident compression wave for a) GTD and b) FE simulations.

a)

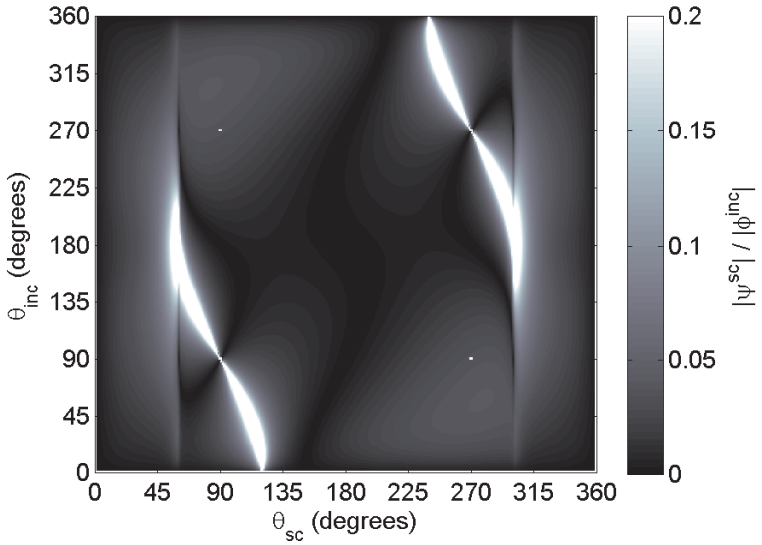


b)

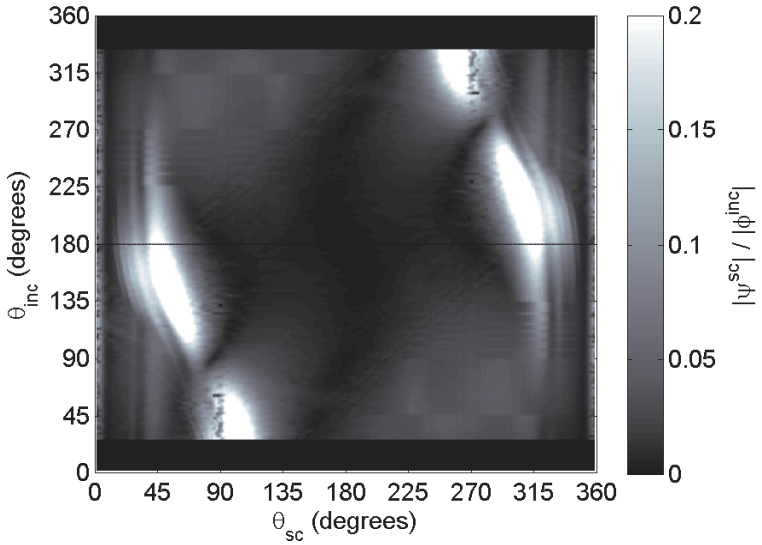


Figure 5.3.3: Scattering matrices showing the magnitude of the scattered shear wave from a smooth defect tip due to an incident compression wave for a) GTD and b) FE simulations.

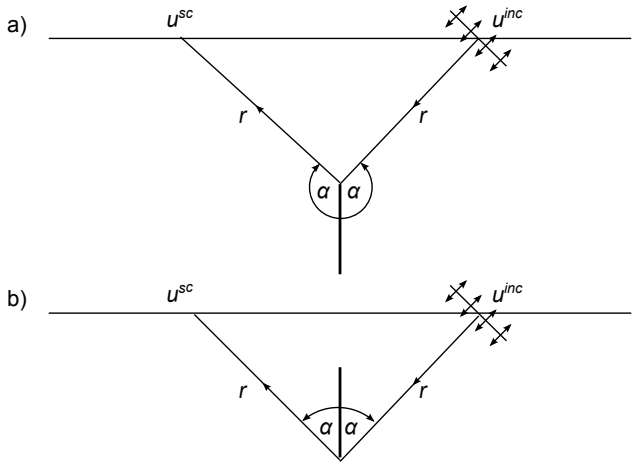


Figure 5.3.4: Figure to show the special case where the magnitude of the incident angle equals the magnitude of the scattered angle, $\alpha$ for a) top tip diffraction and b) bottom tip diffraction.

calculated due to the width and implementation of the excitation line.

Discrepancies can be observed between the two simulations. The GTD data visually appears to be sharper, meaning that changes in signal amplitude between adjacent incident and scattering angles are more clearly defined. This is not apparent in the FE data, where the gradient in the scattered signal shows signs of small fluctuations. This can be attributed to the fact that the GTD solution is a pure analytical expression, where a monochromatic infinite plane wave is directly incident on the defect tip. In the FE simulations, an approximation to the analytical model is made by introducing a tone burst signal, which is generated using a finite excitation line. It can be argued however, that the FE simulations are perhaps more representative of a real inspection, revealing information about the scattering solution that is not possible from GTD alone.

Comparisons can also be made for a special application of GTD for ToFD set out by Ogilvy and Temple [24]. Here, the response is monitored at a location corresponding to the special case where the magnitude of the incident angle equals the magnitude of the scattered angle, which is directly applicable to ToFD for the scattering from top and bottom defect tips, illustrated in Figure 5.3.4.

Incident angles where $\alpha$ is less than $90^o$ correspond to bottom tip diffraction, and when greater than $90^o$ correspond to top tip diffraction. The expression derived by Ogilvy and Temple [24], provides a solution at the tip of the defect. Because of the nature of the solution, certain scattering angles have asymptotic solutions. This can be corrected for by including range dependence $r$, which accounts for the attenuation of the signal as it propagates away from the defect tip. For the two-dimensional solution considered here, range dependence is included in the solution by dividing Equation 2.2.17 and Equation 2.2.18 by the distance to the receiving transducer, $r$.

a)

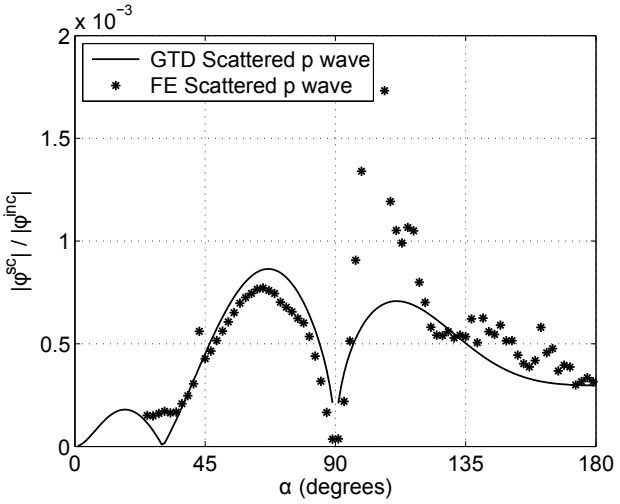


b)

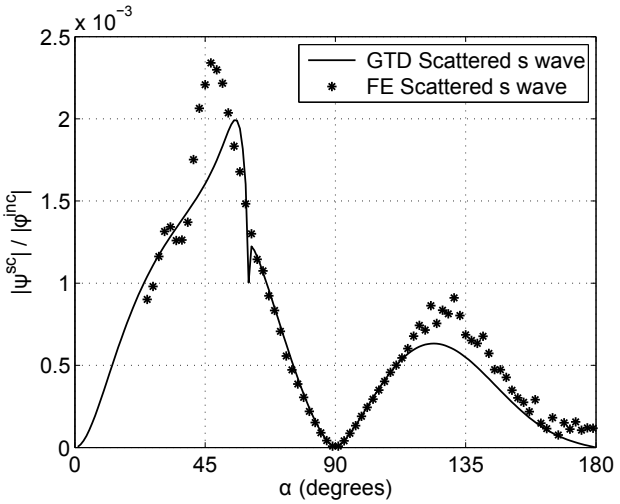


Figure 5.3.5: Comparison between GTD and FE for the magnitude of scattered signal from a smooth defect tip due to an incident compression wave at incident and scattered angle $\alpha$ for a) scattered compression wave and b) mode converted scattered shear wave.

The FE model results can also account for the range dependence by taking the solution at the monitoring points, and using this to calculate the solution of the scattered field at the defect tip. Once the solution at the defect tip is known, this can be used to find the scattered field at location $r$, as in Equation 2.2.17 and Equation 2.2.18. Figure 5.3.5 shows a comparison between GTD and FE for the special case where the magnitude of the incident angle equals the magnitude of the scattered angle for a scenario applicable to ToFD.

Figure 5.3.5 shows very good agreement between GTD and FE for the scattering from a smooth defect tip. For the scattered compression wave shown in Figure 5.3.5a), differences between the two data sets are observed, however, these discrepancies can be attributed to the differences associated with the pure analytical solution and implementation of this system into a numerical model, as previously discussed.

From the cases considered here, comparisons between the FE models with GTD solutions have verified that FE offers a means to accurately calculate the scattering from smooth defect tips. This provides confidence going forward for the use of numerical methods to calculate elastic wave scattering from rough defect tips and to quantify what effect defect roughness has on tip diffracted signals.

### 5.3.2 FE model for rough tip scattering

Having established that FE models are capable of calculating wave scattering from smooth defect tips, it is now necessary to quantify the effects of defect roughness on the scattering signals. The same FE model that was used to calculate the response from a smooth tip for an incident compression wave can be used, however an adaptation has to be made to include defect roughness which is defined by the rms height, as illustrated in Figure 5.3.6.

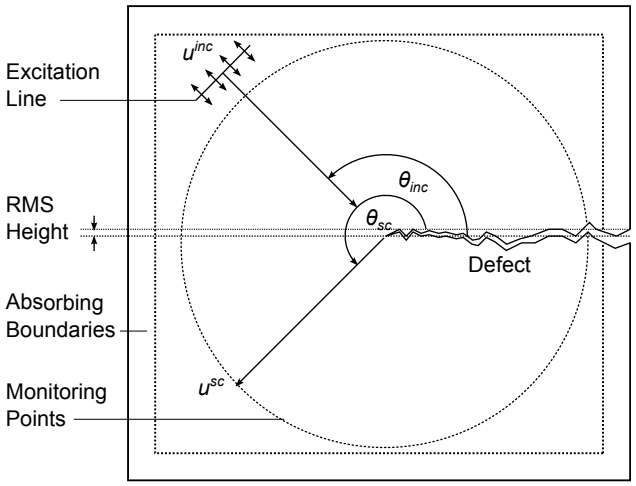


Figure 5.3.6: Incident compression wave on a rough crack tip across angular range $\theta_{inc}$, where the compression and shear wave modes are monitored across scattering angle $\theta_{sc}$.

Due to the statistical nature of rough defects multiple realisations of each class of defect roughness must be considered using a Monte-Carlo based approach. However, in this instance the results are needed also for a range of incident angle. To consider both a varying incident angle and varying classes of defect roughness across a suitable number of surface realisations would drastically increase

the number of simulations that must be considered. Therefore, in this study, defect roughness will remain fixed at a value that is within a typical range for ultrasonic NDE inspections of $\sigma = 0.100\lambda_{inc}$. The model described here is for the two-dimensional case and therefore does not consider the influence of defect roughness in or out of the plane. The roughness of the defect tips in these instances can therefore be considered to be rutted or corrugated.

Considering multiple angles of incidence must also be controlled. It is unrealistic to run a simulation at $1^o$ increments, therefore, the incident angle is varied from $39^o$ to $179^o$ in increments of $10^o$. The minimum incident angle considered here is greater than for the smooth defect case, this is because the rms height of the defect impedes upon the position where an unperturbed excitation line can be placed.

The signal is monitored along nodes across a circular arc from $1^o$ to $360^o$ in $1^o$ increments. The monitoring nodes are at a sufficient range to differentiate between the compression and shear wave modes scattering from the defect tip, but not so far as to unnecessarily increase the size of the spatial domain. The amplitude of the scattered signal is then averaged for every surface realisation considered, at every incident angle. Using an empirical cumulative distribution function, 95.4% confidence bands ($2\sigma$) can be placed about the mean total amplitude of the scattered signal [117]. The results from the Monte-Carlo study from a rough surface are compared against the GTD solution from a smooth surface and are shown in Figure 5.3.7 for the scattered compression wave and Figure 5.3.8 for the mode converted, scattered shear wave.

The results shown in Figure 5.3.7 and Figure 5.3.8 are normalised against the magnitude of the incident compression wave. Each figure shows the scattered field across $360^o$ scattering angle, relative to the plane of the defect, where the defect tip lies in the centre of each plot. The radial distance of the scattered field away from the centre of the plot corresponds to the amplitude at that scattering angle. All plots can be directly compared, and show the $\frac{|\phi^{sc}|}{|\phi^{inc}|} = 0.2$ or $\frac{|\psi^{sc}|}{|\phi^{inc}|} = 0.2$ line as a point of reference. For every plot, the direction of the incident beam is shown, putting the nature of the scattered field into context.

The number of realisations required to obtain the mean total scattered field has not been consistent with previous studies in this chapter. From the convergence study carried out for the normal incident case (shown in Figure 5.1.5), an estimate can be obtain which is of the order of one-hundred simulations. However, this is applicable to the coherent scattered field, lying in a single scattering direction, and upon examination of the results at this stage, it was felt that further simulations were required. The difference in the nature of the mean scattered signal across an angular range possesses local fluctuations in the amplitude of the scattered field. It would be expected that after a suitable number of realisations had been considered, that these local fluctuations would eventually diminish. The number of realisations at each scattering angle was therefore increased to five-hundred. Local fluctuations in the amplitude of the scattering signal with the scattering angle can still be observed, however these

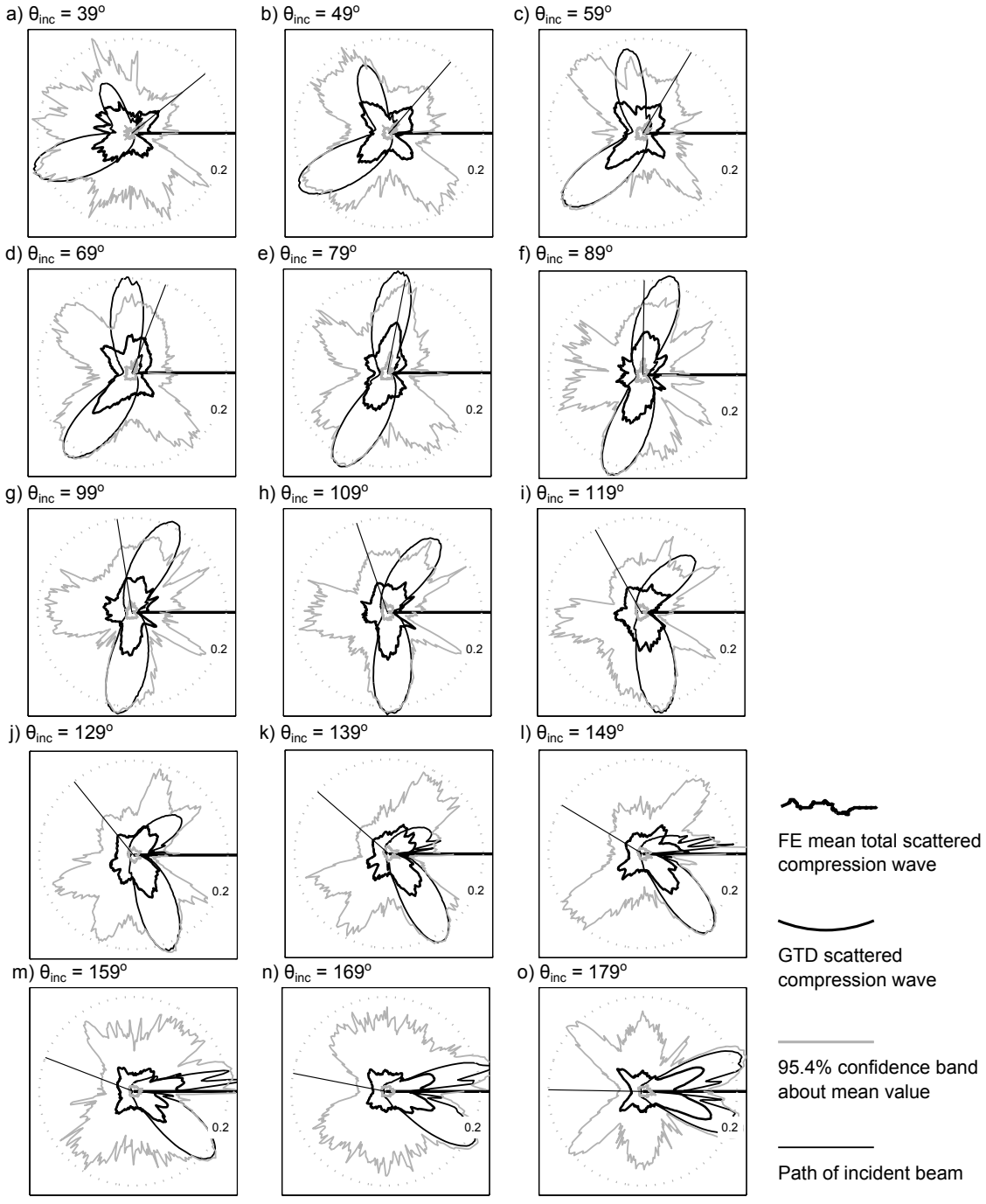


Figure 5.3.7: Polar plots showing the mean scattered compression wave from five hundred realisations from a rough defect tip along with the 95.4% confidence spread, compared to the scattered compression wave obtained from GTD for a smooth defect tip, due to an incident compression wave at angles $39^o$ to $179^o$ in $10^o$ increments shown in a) to o).

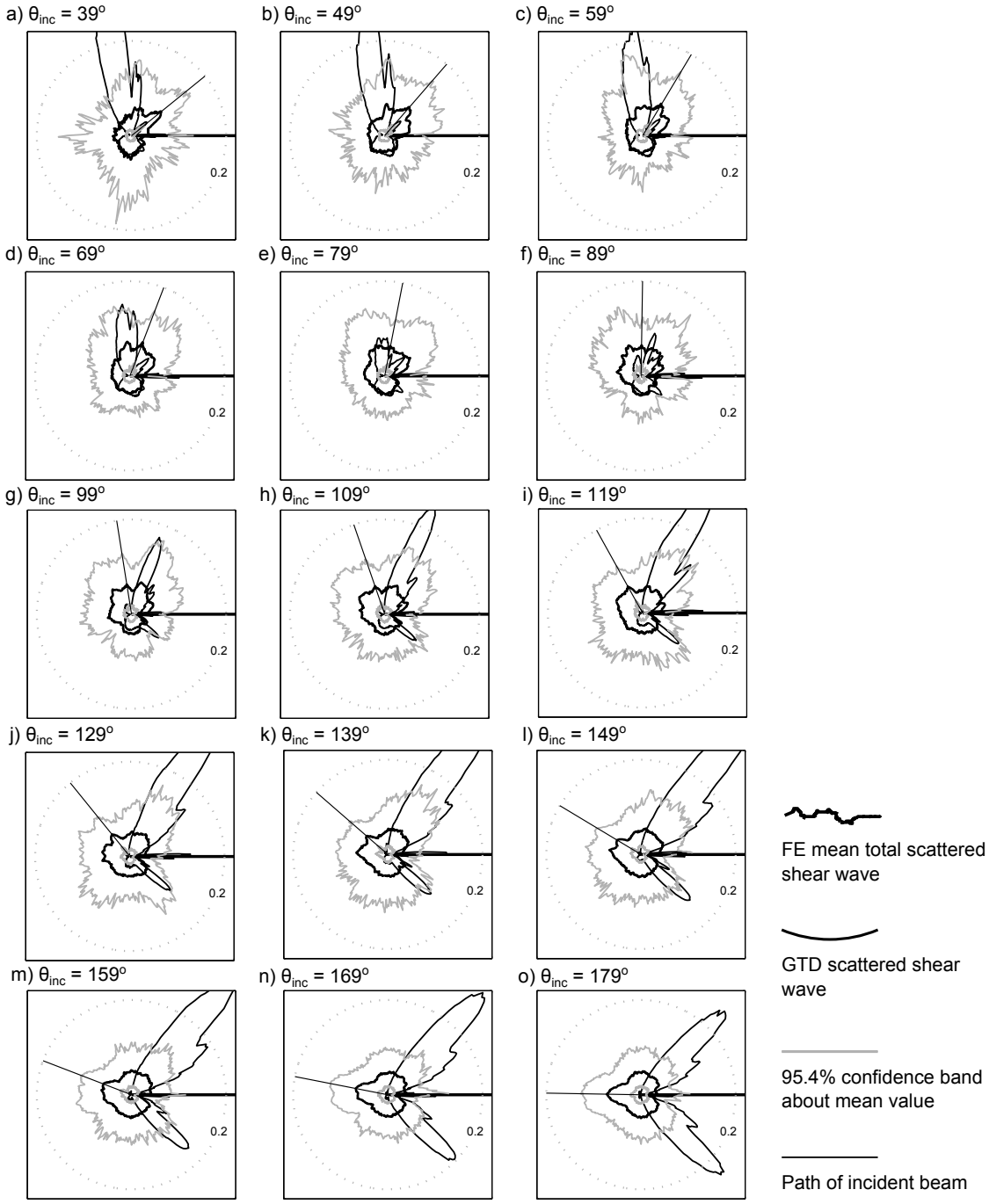


Figure 5.3.8: Polar plots showing the mean scattered shear wave from five hundred realisations from a rough defect tip along with the 95.4% confidence spread, compared to the scattered shear wave obtained from GTD for a smooth defect tip, due to an incident compression wave at angles $39^o$ to $179^o$ in $10^o$ increments shown in a) to o).

have now been minimised. A further increase in the number of realisations considered would have diminishing returns on the improvement of the scattering signal, and are therefore not considered.

From the scattered compression wave plots, trends can be observed in the nature of the scattered field. The field that is scattered in the specular direction from the rough crack tip is attenuated in comparison to the smooth defect case. This observation remains consistent with studies in previous sections where the scattering from the crack face was calculated. This level of attenuation is also consistent in the through transmission direction.

The second observation is that the signal that returns back along the path of propagation (in cases where the back-scattered direction and specular direction are not aligned, e.g. excluding Figure 5.3.7 e) f) g)) has an increased average amplitude compared to the smooth defect case. Furthermore, this increase in average amplitude is also apparent in scattering directions that lie in the direction that is $360^o - \theta_{inc}$. This has significance for ToFD inspections, and corresponds to the special case where the magnitude of the incident angle equals the magnitude of the scattered angle, $\alpha$, as shown in Figure 5.3.4.

To summarise these observations, defect roughness will influence tip diffracted signals. The mean total scattered field from a rough defect tip, due to an incident compression wave, in the directions that lie in the specular and through transmission directions, will be attenuated. However, signals lying away from these directions, especially those in the back-scattered and $360^o - \theta_{inc}$ directions can have increased amplitude when compared to the smooth defect case. The phenomena discussed however, only applies to a mean scattered signal from multiple realisations. The scattering signal from a single defect may not be representative of the mean, which has been discussed here. By examining the confidence bands, the uncertainty in the magnitude of the scattered field across all scattering angles can be appreciated.

For the mode converted shear wave signals shown in Figure 5.3.8, the general trend is more straight forward. Again the signals that scatter in the specular direction are attenuated. The through transmission signals are also attenuated, especially for incident angles greater than $90^o$. Across all other scattering angles, the average amplitude of the mode converted shear wave seems consistent, with only small fluctuations apparent due to the change in scattering angle or incident angle. Therefore, for scattering angles that do not lie in the specular or through transmission directions, the scattered shear wave signals have increased average amplitude when compared to the smooth defect case.

Similar to the smooth defect tip, scattering matrices showing the magnitude of the mean scattered compression and mode converted shear wave modes from a rough defect tip due to an incident compression wave are calculated, see Figure 5.3.9.

Comparisons of Figure 5.3.9 can be made against the scattering matrices obtained from GTD and FE simulations for the smooth defect case (Figure 5.3.2 and Figure 5.3.3). Because the incident angles considered for the rough defect tip are in $10^o$ increments, an interpolation function is used to populate

a)

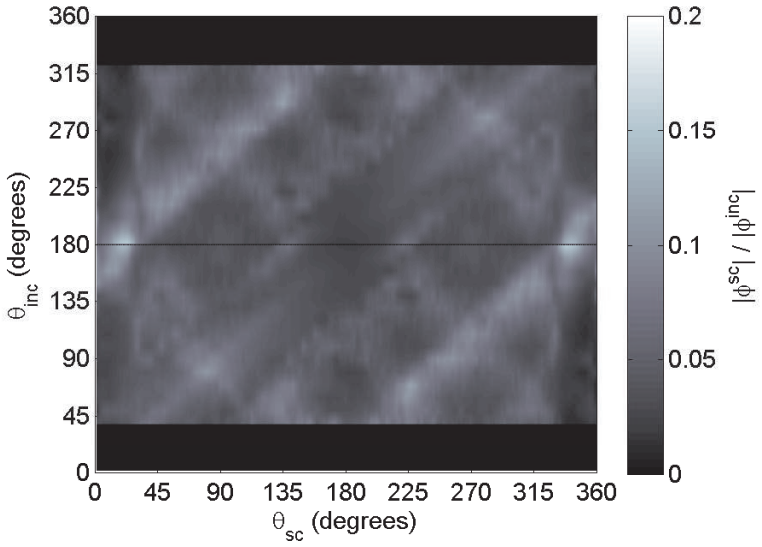


b)

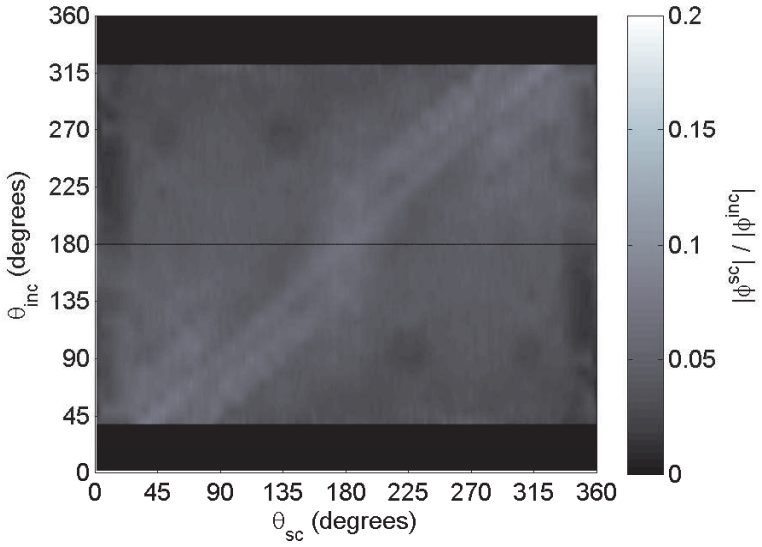


Figure 5.3.9: Scattering matrices showing the mean total scattered signal of the a) scattered compression wave and b) scattered shear wave, from a defect tip with roughness $\sigma = 0.100\lambda_{inc}$ due to an incident compression wave.

the response for incident angles that have not been directly calculated.

The scattering matrices confirm and summarise the points highlighted from the evaluation of the polar plots. The mean total scattered field from a rough crack tip will be attenuated in the specular and through transmission directions. However, the average scattering across all other scattering angles has increased, especially in the $360^o - \theta_{inc}$ direction, which has implications for ToFD inspections. The mode converted shear wave in also attenuated in the specularly reflected directions, however, in this instance the average scattering across all other scattering angles has higher amplitude than the smooth defect case, and is of a more uniform nature, with little deviation in the amplitude of the signal due to changes in the incident or scattering angles.

The effects of further increases in defect roughness have not been considered, however it is possible to postulate results by carrying forward conclusions made from the investigation of scattering from the defect face. It is likely that the mean levels of attenuation observed in the specular and through transmission directions would be further attenuated, and that there would be an increase in the magnitude of the uncertainty about the mean value. However, this trend would plateau, and subsequent further increases in defect roughness would result in little difference in the nature of the scattered signal.

The influence of an incident shear wave has not be considered, although the study presented here for the longitudinal work could easily be reported for the shear case. Throughout this investigation, the influence on roughness on signal scattering has been calculated as a function of the incident wavelength, irrespective of the wave mode. Extending this investigation to incident shear waves should therefore reveal the same overall trends when compared to GTD, however, the magnitude and scattering angles will deviate in comparison to the incident compression wave, due to the complexities of mode conversion.

The study made here has only considered the two-dimensional case, where defect roughness only varies in one dimension. Extending this problem to the three-dimensional case, where defect roughness will vary in and out of the plane, could result in a different set of conclusions. However, it is expected that the general mechanism observed here, where specular and through transmission directions are attenuated and scattering across all other scattering angles has increased, should still be apparent.

### 5.3.3 Influence of roughness on Time of Flight Diffraction

Previously, comparisons have been made between GTD and FE for the smooth defect tip scattering. Further comparisons have been made for the special case where the magnitude of the incident angle equals the magnitude of the scattered angle for a setup applicable to ToFD. Having now considered the scattering from multiple realisations from a rough defect tip, the ToFD case can be revisited, this time to consider the mean total scattered field and the uncertainty about this value.

Figure 5.3.10a) and Figure 5.3.10b) show the magnitude of the scattered compression and shear wave

a)

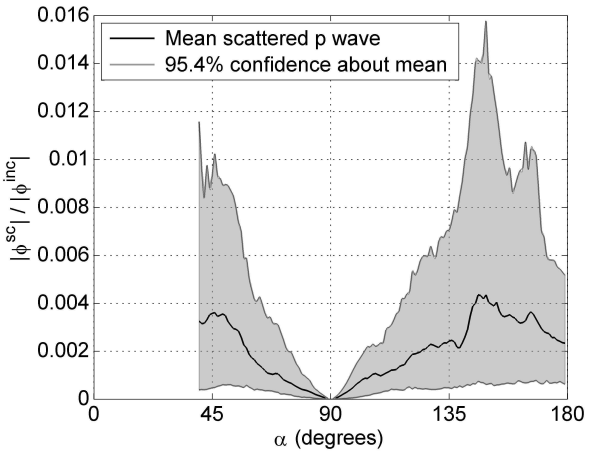


b)

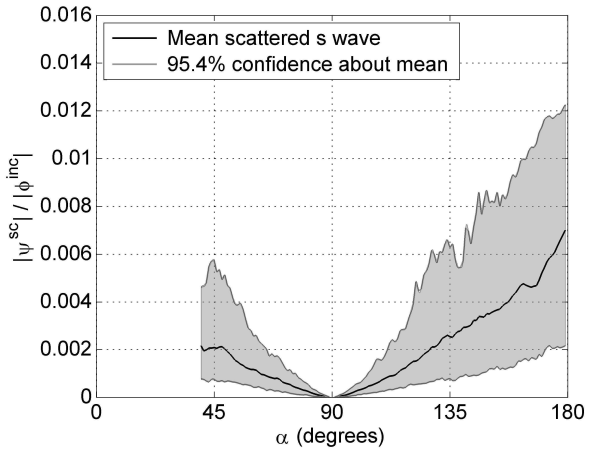


Figure 5.3.10: FE simulations to calculate the magnitude of the mean scattered signal and confidence bands from a defect tip with roughness $\sigma = 0.100\lambda_{inc}$, due to an incident compression wave at incident and scattered angle $\alpha$ for a) scattered compression wave and b) scattered shear wave.

modes due to an incident compression wave scattering from a rough crack tip.

Incident angles where $\alpha$ is less than $90^o$ correspond to bottom tip diffraction, and when greater than $90^o$ correspond to top tip diffraction. The scattering amplitudes can be directly compared to those shown in Figure 5.3.5a) and Figure 5.3.5b) for the smooth defect case (so as not to over complicate Figure 5.3.10, the results from the smooth defect case are not shown, however, the scales can be directly compared).

When the angle $\alpha$ is within the range $75^o$ to $105^o$, the mean scattered compression wave from a

rough tip is attenuated in comparison to the smooth defect case. Outside of this range, the mean scattered compression wave has an amplitude that is significantly higher than the smooth defect case. The uncertainty associated with these values is also a function of the scattering angle. Increasing or decreasing the value of $\alpha$ from $90^o$ causes an increase in the uncertainty about the mean value. For the top tip response, the greatest uncertainty is observed at $145^o$, after which the uncertainty decreases. A similar response is observed for the bottom tip response, however the limitations of the FE model have meant that values below $39^o$ have not been considered.

The mode converted shear wave does not follow the same trends as the scattered compression wave. For cases where $\alpha$ is less than $90^o$, the mean total scattered shear wave has equal magnitude to the smooth defect cases, although the uncertainty in this value decreases as $\alpha$ approaches $90^o$. However, when $\alpha$ is greater than $90^o$, the magnitude of the scattered shear wave is greater than the smooth defect case. Again, the uncertainty in this value increases as $\alpha$ increases beyond $90^o$, but unlike the scattered compression wave, the uncertainty continues to increase though to $180^o$.

The influence of roughness on tip diffracted signals does have an impact on ToFD inspections. However, in these cases, detection is primarily based on identifying changes in phase variation from tips of the defect and not necessarily the amplitude of the scattered field. The significance of these findings is to reduce the uncertainty that is introduced by defect roughness, for example, where tip diffracted signals may fall below the noise threshold.

When using incident compression waves, for the case considered here, where $\alpha$ is within the range $75^o$ to $105^o$, tip diffracted signals are attenuated in comparison to the smooth defect case. However, outside of this range, the mean total scattered signal is increased. Therefore, outside of the $75^o$ to $105^o$ range, defect roughness should not attenuate tip diffracted signal amplitudes, and will in fact, increase the detectability of the tips.

## 5.4 Three-dimensional rough surfaces

So far, the FE models have only considered two-dimensional cases. This has allowed like-for-like comparisons to be made with well established analytical methods that have formed the basis for technical justifications within the UK power generation industry. However, the FE models are not limited to a two-dimensional approximation, and with the inclusion of spatially efficient absorbing boundary methods and domain linking algorithms, the ultrasonic response can be considered for the three-dimensional case.

In this final study a more applied inspection setup is considered. The FE model is still used to calculate the ultrasonic response from multiple realisations of rough surfaces, however in this instance a finite embedded defect is examined, as shown in Figure 5.4.1.

The defect has surface roughness of $\sigma$ =200 µm, planar dimensions of 3 mm × 3 mm and a depth of

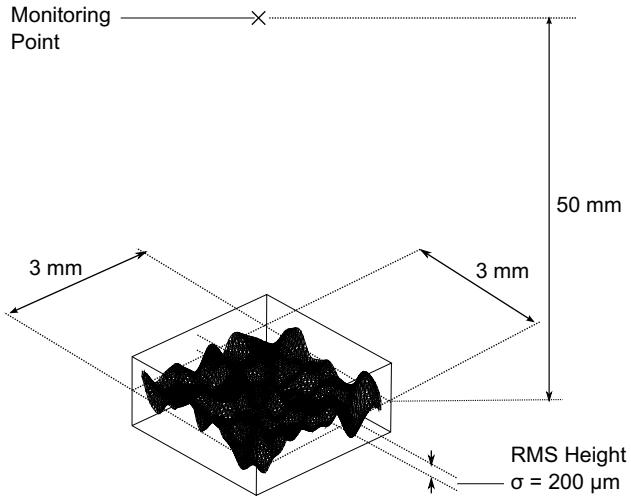


Figure 5.4.1: Embedded three-dimensional planar rough defect used to calculate the attention in ultrasonic response.

50 mm, each of these dimensions remains fixed. The defect is defined using a free mesh of tetrahedral elements of size 50 μm, to which a structured mesh of tetrahedral elements is appended that contains monitoring nodes and absorbing boundaries (not shown in Figure 5.4.1). A normal incident compression wave is used to excite the FE domain, and a domain linking algorithm is used to calculate the response back along the path of propagation, corresponding to a defect at a depth of 50 mm.

Previously, defect roughness has been expressed as a function of the incident wavelength. The effect of increasing roughness had been examined by calculating the ultrasonic response from defects with increasing roughness at a fixed frequency inspection. In this instance, increasing defect roughness will present a challenge for standard meshing algorithms in commercial FE solvers. Furthermore, the dimensions of the defect considered here are consistent with typical defect values that may arise for an applied inspection, and should remain fixed. Therefore, to assess the effects of varying defect roughness, the inspection frequency is varied from 2 MHz to 8 MHz in 1 MHz increments, thereby changing the defect roughness when expressed as a function of the incident wavelength. The response from the rough defects will be analysed in the same manner as the two-dimensional case using a Monte-Carlo method. Multiple realisation of rough defects will be considered for each inspection frequency and from these models, the attenuation due to defect roughness (expressed as a function of the incident wavelength) can be calculated.

For the three-dimensional case, it is not possible to apply Monte-Carlo analysis with as many realisations as were used for the two-dimensional models. Despite the improvements made to significantly reduce the size of the computation burden, the consideration of hundreds of surface realisations to ob-

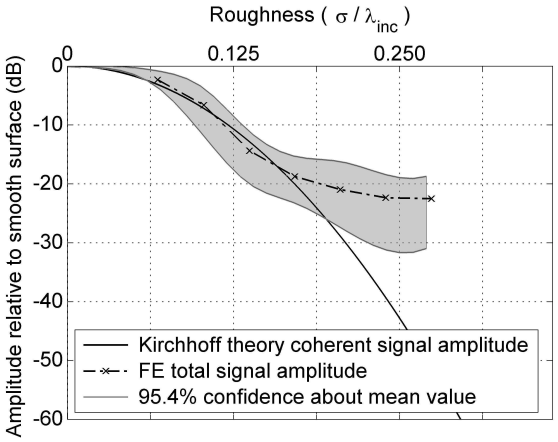


Figure 5.4.2: Reduction in signal amplitude for the mean total reflected signal from three-dimensional rough defects with increasing roughness expressed as a function of the incident wavelength. The total reflected signal is plotted with the 95.4% spread (or $2\sigma$ confidence) about the mean value.

tain a statistically significant result is not feasible. Instead, twenty-five surface realisations are used at each inspection frequency. Since only the total back-scattered signal is of interest here, this is deemed a sufficient number to provide a fair estimate for the mean signal attenuation and spread about this value whilst maintaining a computational run time that is acceptable.

The effects of changing the inspection frequency will alter the number of nodes per wavelength of each respective model. Higher frequency inspections will be simulated using a lower number of nodes per wavelength than lower frequency inspections. As a result, there will be an associated increase in the errors of propagation velocities, as discussed in Section 4.1. It is therefore important to normalise each simulation correctly. The responses are compared to that obtained from the smooth defect cases, at that inspection frequency. This removes any variation this variable may have on the results. Furthermore, the range of inspection frequencies considered is such that the lowest number of nodes per wavelength considered is 14.6. This is within a range that ensures a good FE result as discussed by Drozdz [115].

The results for the mean signal attenuation from a three-dimensional rough defect expressed as a function of increasing roughness, are given by Figure 5.4.2.

The results are normalised against the smooth defect case and compared against the attenuation of the coherent signal amplitude provided by Kirchhoff theory (Equation 2.5.7), since this has formed the basis for calculating signal attenuation in the UK nuclear power generation industry.

The same overall trends are present between the two-dimensional results (Figure 5.1.6 and Figure 5.1.8) and three-dimensional results. Increasing defect roughness attenuates the ultrasonic response

from the surface. For low levels of roughness there is very good agreement between the prediction for the coherent signal amplitude provided by Kirchhoff theory and the mean total signal amplitude calculated using FE. However, as defect roughness increases beyond $\sigma = 0.170\lambda_{inc}$, the mean total scattered signal begins to plateau to a value of approximately -20 dB, and the coherent signal becomes overly pessimistic.

The confidence bands that are associated with the mean total signal amplitude demonstrate the deviation about this value. For low levels of roughness the spread is relatively narrow, however, for increasing levels of roughness the divergence increases. It should however be noted, that only twenty-five surface realisations are considered for each inspection frequency, thereby reducing the confidence in this result.

An important difference is noticed between the two and three-dimensional cases. In two-dimensions the plateau in the signal amplitude begins at $\sigma = 0.125\lambda_{inc}$ and tends to a value of approximately -12 dB, therefore, the reduction in signal amplitude is more severe for the three-dimensional case. This is an undesirable finding since it has previously been assumed that the two-dimensional approximation would render a viable solution.

The cause for this discrepancy will result from any of the differences in the two models, the most obvious being the additional dimension to defect surface roughness. It is possible that the extra dimension in roughness could result in a further loss in signal in the three-dimensional case, that maybe roughly twice that in two-dimensional case because the defect is now rough in two dimensions rather than just one. It is also important to note that here a finite sized defect is considered meaning that the addition of edge diffraction events could be contributing to the scattered field in some previously unrealised manner.

A likely explanation could result from differences in how signal amplitude varies away from the defect in the two and three-dimensional cases. As has already been discussed, the total scattered signal consists of a coherent signal (scattered in the specular or mirror like direction) and a diffuse scattered signal (scattered across all scattering angles). For the two-dimensional case the diffuse signal amplitude is radiated in a circular manner, and as result, will have a amplitude that reduces as $\sqrt{\frac{1}{r}}$, where $r$ is the range from the defect to any point of observation. However, for the three-dimensional case the diffuse signal amplitude is radiated in a spherical manner and will reduce as $\frac{1}{r}$. Therefore, the amplitude of the diffuse scattered field at a given point $r$ will be attenuated more for the three-dimensional case than the two dimensional case. Since the total scattered field consists of a diffuse component, this will therefore exhibit the same behaviour.

The reasons that this is only thought to apply to the diffuse component of the scattered signal and not the coherent component, is because the coherent field lies in a single scattering direction only and is therefore not affected by differences exhibited by two and three-dimensional cases. Unfortunately, due to the limited number of surface realisations considered, it is not possible to make an accurate

measurement for the coherent signal amplitude, making it difficult to confirm this conclusion.

Comparisons can also be made between these results and those shown in Figure 5.1.13, where the two-dimensional Monte-Carlo study is compared to experimental data points (Section 5.1.4.2). The experimental data shows the attenuation in signal amplitude from a three-dimensional rough surface. It is noted that overall the agreement is very good, however, a number of the experimental data points lie below the two-dimensional predictions. This is consistent with the observations made here, however the drop in the three-dimensional signal is more significant than the modest difference observed in Figure 5.1.13.

Three-dimensional surfaces appear to attenuate signal amplitudes more than two dimensional surfaces, however, the FE results appear to be slightly more pessimistic, especially when considering the spread in the data. The significance of comparing three-dimensional experimental results from a surface, to three-dimensional modelled results from a finite sized defect, is also called into question. This introduces an area where more investigation is needed in order to fully understand what parameters are influencing these results.

## 5.5 Conclusions

Defects which possess rough surfaces greatly affect ultrasonic wave scattering behaviour, usually reducing the magnitude of reflected signals. Understanding and accurately predicting the influence of roughness on signal amplitudes is crucial, especially in the NDE for the inspection of safety-critical components. Kirchhoff theory has been the tool of choice for industrial applications modelling elastodynamic scattering problems from complex geometrical scatterers; however, it has been widely recognised that this approach often over estimates signal attenuation, especially for high levels of roughness. A numerical method, such as a FE model, does not have the same limitations as an analytical technique and offers the potential to calculate a fully representative elastic solution to the scattering from rough surfaces.

FE models have been used to calculate the elastic scattering from multiple realisations of defects within a statistical class of roughness for normal and oblique incidence. Results from the FE models were compared with Kirchhoff theory predictions and experimental measurements in order to establish confidence in the new approach.

At low roughness excellent agreement was observed, whilst higher values confirmed the pessimism of Kirchhoff theory. Furthermore, the mean total signal amplitude was calculated, which is more representative of the information obtained during an NDE inspection, as opposed to the consideration of the coherent scattered component alone. The reductions in the total signal amplitude due to increasing roughness have been found to be significantly less than indicated by the coherent single.

The validity of the FE model has been assessed by comparing the predicted attenuation in signal

amplitude due to roughness, to that measured on experimental samples. Good agreement between the FE and experimental data was demonstrated. The 95.4% spread (or $2\sigma$ confidence) from the FE model has been shown to be narrower than the spread measured experimentally, however, the mean attenuation in the total field amplitude is consistent with the experimental data points.

The numerical model was extended to consider the response for oblique incidence cases. It has been shown that as defect roughness increases the total scattered field reflected in the direction that is back along the path of the incident signal is increased when compared to the smooth defect case. The scenarios considered have also assessed the contribution of tip diffracted signals from finite sized defects, which add a significant contribution to the total measured field.

The influence of roughness on tip diffracted signals has also been calculated. The cases considered the effects of scattering from a rough defect tip, calculated using a Monte-Carlo FE method, and compared the findings to the scattering from a smooth defect tip, calculated using GTD. The FE model was validated by making like-for-like comparisons with GTD within a well established valid range. For cases where a compression wave is incident on a rough defect tip, the mean total scattered field will be attenuated in the specular and through transmission directions. However, the average scattering across all other angles has increased, especially in the $360^o - \theta_{inc}$ direction, which has implications for ToFD inspections. The mode converted shear wave is also attenuated in the specularly reflected directions, however, in this instance the average scattering across all other angles has higher amplitude than in the smooth defect case, and is of a more uniform nature, with little deviation in the amplitude of the signal due to changes in the incident or scattering angles. The results from this study however have only been calculated for the incident compression wave case using a two-dimensional approximation. Furthermore, the scattering from a single defect tip will have a varied response governed by the size of the confidence bands and may not be representative of the mean scattered signal calculated, which is also influenced by the class of defect roughness.

Finally, the FE models are applied to the three-dimensional case for a finite embedded planar rough defect. This final study draws upon all aspect of the thesis, and demonstrates a clear example of modelling of the ultrasonic response from rough defects using efficient FE techniques. The attenuation due to defect roughness for the three-dimensional case shows the same overall trends as the two-dimensional simulations. However, it is noted that for the case considered here, the attenuation of the mean total signal plateaus at a value of approximately -20 dB which is less than the two-dimensional prediction of -12 dB. Despite this, the three-dimensional estimate still lies significantly above the previously used estimate, which was provided by the coherent signal component of Kirchhoff theory.

The results from this study present a means to reliably calculate the ultrasonic response from rough defect types, which is of direct benefit for ultrasonic NDE inspections in the nuclear power generation industry. The analysis provides a robust basis for a less sensitive, yet safe, threshold for inspection of rough defects in safety critical components.

# 6 Conclusions

This thesis has researched and developed the use of efficient FE modelling techniques for calculating the ultrasonic response from rough defects for NDE applications specific to the nuclear power generation industry.

One of the fundamental principles of regulation and operation within the UK nuclear power generation industry is a robust safety culture where the highest levels of quality assurance are applied to safety critical components. This principle places a requirement on NDE to deploy reliable and accurate inspections to ensure the structural integrity of the plant.

To achieve this goal, modelling techniques can be used to aid in the design and justification of ultrasonic NDE inspections on safety critical components. Currently, analytical modelling techniques are used, however, for more complex defect geometries, conventional analytical methods can be imprecise and are no longer suitable for calculating the nature of ultrasonic responses.

As a result, an overly conservative approach has been taken, whereby scattered ultrasonic signals from rough defects are assumed to be severely attenuated. This approach ensures that the sensitivity of a deployed inspection is at a suitable level to identify all potential flaws within a component. However, as a result the inspection becomes overly conservative, potentially oversizing or mis-classifying insignificant flaws as being hazardous.

The application of numerical modelling tools can significantly reduce the level of uncertainty that was previously associated with this problem, owed to the use of analytical methods. Numerical modelling tools do not fall victim to the same fundamental assumptions as conventional analytical methods, and provide a far more accurate solution to ultrasonic scattering from rough surfaces. This provides a means for a less conservative, yet safe, approach for calculating the ultrasonic response from rough defect types, allowing for increased confidence in the design and justification of ultrasonic NDE inspections.

## 6.1 Summary of thesis

The thesis begins by establishing the motivation for this research task, outlining the need to be able to accurately size and characterise potential flaws within safety critical components. The importance of this problem is emphasised for applications in the UK nuclear power generation industry, where a reliable and accurate inspection capability is paramount.

A detailed description of the theoretical background is given in the second chapter. This introduces the fundamental principles of ultrasonic wave propagation and recommends key texts that cover the subject in its entirety. Following this a review of conventional analytical methods for calculating the ultrasonic response from smooth defect geometries is given, with specific application to ultrasonic NDE inspection problems. Suitable numerical modelling techniques are then introduced and discussed. A number of techniques are assessed against the requirements of this project, including suitability as an industrially viable solution. The literature review extends to consider previous investigations towards calculating the ultrasonic response from rough surfaces. This has served an important purpose, firstly helping to identify the limitations of current analytical methods being applied to this task, and secondly, ensuring that the manner in which the findings of this investigation are presented remain consistent with the work of previous authors. Following a review of the literature, the FE method was identified as being the most suitable technique.

A key driver for this research has been to ensure successful transfer of this technology into industry. Therefore, efficient FE methods have been developed that are capable of delivering results in an industrial context. To achieve this goal, FE models must be able to perform accurate simulations within a significantly reduced spatial domain. This allows for computational resource to be allocated to a highly accurate representation of the defect or feature of interest. This has been achieved in two parts.

The first are discussed in Chapter 3 absorbing boundary methods which are used to simulate infinite elastic space. A number of methods are available, but again the suitability of each of these methods must be assessed in the context of the bespoke requirements of this project. Despite recent advances by many researchers in this field, significant further progress has been made as part of the work of this thesis: a new absorbing boundary technique has been developed called the SRM, which provides a high performing solution within a much reduced spatial domain, and this can be easily implemented into commercial FE codes. The performance of the SRM is compared to other viable methods, for applications specific to those of this project. An optimisation algorithm has been used that calculates the necessary input parameters to achieve a high performing absorbing boundary, this is of significant importance when designing three-dimensional FE models.

The second aspect to reducing the size of FE spatial domains, involves the application of a domain linking algorithm; this is discussed in Chapter 4. Using this technique, the FE model need only consider the area immediately surrounding the defect or feature of interest. The scattered ultrasonic signal is monitored around the edge of this domain, and then propagated to a desired point in space using an analytical Greens' function. The method is validated by performing like-for-like comparisons with the more conventional Full FE models, increasing confidence in the use of this technique. A beam computation tool is added to the FE model, which allows for the excitation of the FE domain to be representative of the ultrasonic field generated by a single crystal transducer. Experimental validation

is performed against standard calibration targets used in NDE, with the modelled results showing very good agreement with experimental data.

The next chapter, Chapter 5, applies the FE modelling techniques previously discussed to calculate the ultrasonic response from rough defects. Firstly, comparisons are made against a specific extension of Kirchhoff theory that has formed the basis for calculating the ultrasonic response from rough defects for applications in the UK power generation industry. An important distinction is made between the coherent, diffuse and total scattered signals. Here, the total scattered signal is identified as being the one of significance, since this is consistent with observations made during a practical NDE inspection. To remain consistent with the work of previous authors, a statistical approach is taken where each rough surface is defined by its surface rms height. This allows for a Monte-Carlo method to be applied where the ultrasonic response from multiple realisations of rough surfaces is calculated.

Good agreement is observed between FE and Kirchhoff theory at low levels of roughness where both techniques are known to give accurate solutions. However, at higher levels of roughness, the pessimism of Kirchhoff theory is confirmed, with the FE model providing a more accurate means to calculate signal attenuation. Comparisons of the FE modelled results are made with experimental samples and in all cases considered good agreement has been observed. Any discrepancies have been attributed to the differences that arise between a two-dimensional model and three-dimensional experimental data.

The investigation also considers oblique incident configurations applicable to pulse-echo inspections of misorientated defects, where the scattered signal from the defect lies back along the path of propagation. In this instance the influence of roughness on misorientated defects can result in an increase in the average magnitude of back-scattered signal when compared to the smooth defect case. This is due to a diffuse scattered signal that is present across all scattering angles for rough surfaces.

The influence of roughness on tip diffracted signals is also investigated. Comparisons between FE simulations and GTD have been made for the smooth defect case, establishing confidence in the FE approach. Again, a Monte-Carlo method is used, where multiple realisations of defect roughness are considered across multiple incident and scattering angles. The findings are consistent with the previous work in the chapter. Defect roughness attenuates signals in the specular and through transmission directions, however an increase in the diffuse field across all remaining scattering angles results in an increase in the average scattered signal in comparison to the smooth defect case. The importance of this result is illustrated in applications using ToFD, suggesting that, on average, defect roughness will increase (as opposed to decrease) the magnitude of the average scattered signal back towards the receiving transducer.

The chapter concludes by considering the response from a three-dimensional embedded rough defect. In this case the defect geometry remained fixed and the inspection frequency was varied to assess the influence of roughness as a function of the incident wavelength on the reflected signals. The attenuation due to defect roughness for the three-dimensional case showed the same overall trends

as the two-dimensional simulations. However, it was noticed that the attenuation of the mean total signal plateaus at a value which is less than that for the two-dimensional predictions. Despite this, the three-dimensional estimate is still significantly above the previously used estimate that was provided by the coherent signal component of Kirchhoff theory.

The concepts that have been outlined within this thesis have been successfully transfered from academia into industry. The modelling capability has been thoroughly documented for use within in Rolls-Royce and supplied with validation evidence, worked examples and an associated user guide. Furthermore, the discussions made in Chapter 5 that make reference to the use of total scattered signals over the more commonly used coherent scattered signal, has provided a new basis from which the influence of roughness can be considered. Previously, industry has taken great benefit from the approach taken by researchers such as Ogilvy, where increasingly complex scattering phenomenon are condensed into usable, simplistic attenuation curves. The work of this thesis remained consistent with the work of previous authors, and presented findings in a similar manner. By achieving this, it is hoped that the work presented here will form a new basis for setting less conservative, yet safe, reporting thresholds for ultrasonic inspections.

## 6.2 Future work

The use of numerical methods to solve ultrasonic scattering problems has long been established within the academic community and has undergone thorough and extensive research. The recent advances made by academia in reducing the computational burden that is associated with these numerical approaches, has now meant that these tools are viable for use in a rigorous industrial context. As a result, this project opens many avenues for future research.

From an industrial perspective, having identified a means to calculate the ultrasonic response from embedded planar rough defects, it would be highly desirable to extend this capability to other defect types. These could include increasingly more complex defect geometries or the inclusion of local component geometry into the scattering solution.

Extensions can be made to the domain linking algorithm presented in this thesis. Currently, a relatively simple beam computation tool is coupled to the FE domain, and the experimental validation demonstrated that this was a viable and accurate approach. However, if a more complex transducer configuration is desired, then this model would need to be extended to include the complete elastic solution from the transducer. The transducer response could also be calculated numerically be re-introducing a FE source domain. This would provide a highly accurate calculation for the nature of the incident field, however, this would be at the expense of increased computation.

This thesis demonstrated that the use of absorbing layers is the most viable solution to implementing absorbing boundaries into commercial FE codes for this project. This lead to the development of

the SRM absorbing boundary, which when combined with an optimisation function, could reduce the extension made to the spatial domain to as little as $\frac{\lambda_{inc}}{4}$. This solution, despite being highly successful, is far from the perfect situation of complete absorption in zero space. This will remain the ultimate goal and further progress towards this can perhaps be achieved by manipulating the FE solver through the selection of idealised material properties. Alternative solutions postulated by the author to further reduce the absorbing layer thicknesses would be to implement scatterers embedded within the absorbing boundaries themselves, or perhaps boundary conditions that result in destructive interference of backscattered waves. A final idea (although how this would be implemented is unclear) would be to simulate some form of 'potential well' or 'passive boundary' where incident ultrasonic waves are not attenuated, but simply trapped such they do not propagate back into the region of interest.

Ultimately, it is hoped that this thesis will support future work in the continued development of numerical methods to solve ultrasonic wave scattering problems for ultrasonic NDE applications.

## 6.3 Concluding remarks

This project has brought together three areas of research to allow numerical calculations to be made on the attenuation due to defect roughness. Each of these subject areas remains a field of study within its own right, and will perhaps influence other areas of research. Absorbing boundary methods are an essential tool for simulating infinite elastic space. This study has revealed that there are as many ways to solving this problem as there are applications. Modellers can be confident that a solution to simulating silent boundaries, even for bespoke requirements, is likely to be obtainable. Extensions can be made to well established methods, as has been the case in this thesis, or optimisation functions can be applied, tailoring the solution as necessary. Improvements can still be made to this subject area. Frequency domain solutions offer a perfect solution to this problem, completely cancelling out reflections from model boundaries with no-extension to the spatial domain of the FE model. A means to achieve this in the time-domain has yet to be realised, with these methods still balancing a compromise between performance and undesired increase in model size. It may be that this trade-off will be ever present, however improving the level of compromise will be a highly desirable result.

The efficient FE methods developed here are specific to ultrasonic NDE inspection problems. Although applications could be easily extended to other time-domain FE simulations, this project represents a significant advance in making efficient FE modelling techniques a viable tool for industrial ultrasonic NDE applications. Computational resource remains the greatest challenge to overcome. The advances made in domain linking algorithms allow this capability to be possible on an industrial scale. Due to the relative youth of this capability, there are a number of avenues available for further investigation. For example, it is highly desirable for an extension to be made towards defects that

include local component geometry. This would allow numerical modelling for inner-surface breaking defects to be calculated, which is highly desirable for the power generation industry.

Calculating the ultrasonic response from rough defects is essential for designing reliable and dependable inspections for safety critical components. This project has made advances in taking those calculations from an analytical environment into a numerical one. When like-for-like comparisons have been made with analytical methods, excellent agreement has been observed between the two techniques. The needs for accurate simulations of the complex cases go beyond the validity of the analytical methods, the numerical methods have provided a consistent and reliable results. The ability to model complex defect geometry is now available, allowing natural extensions to be made to this project, perhaps considering features that are characteristic of more specific forms of cracking. This project has focused on the viability of numerical models to replace well established analytical techniques, with more emphasis placed on two-dimensional models. Therefore, further work can also be made in extending the findings of this project towards three-dimensional cases or more specific inspection tasks.

To conclude, FE modelling techniques allow for a highly accurate and reliable means to calculate the ultrasonic response from rough defect types, offering solutions that extend beyond those available from current analytical methods. The application of these techniques reduces the conservatism that is currently associated with the inspection of complex defect types and provides a robust basis for a less sensitive, yet safe, inspection, reducing the likelihood of false-calls and therefore reducing any unnecessary expenditure for the inspection of safety critical components.

# 7 Bibliography


[1] "ASME Boiler and Pressure Vessel Code, Section III, Division I, Rules for construction of nuclear plant components, Division 1 - Subsection NB, Class 1 Components," *Am. Soc. Mech. Eng.*, 2013.

[2] "ASME Boiler and Pressure Vessel Code, Section XI, Rules for Inservice Inspection of Nuclear Power Plant Components," *Am. Soc. Mech. Eng.*, 2013.

[3] C. D. Bell, C. T. Watson, J. Howson, and A. E. Walker, "Safety classification informed structural integrity assessment of nuclear plant components," *Proceedings of the ASME 2010 pressure vessels & piping division/K-PVP Conference PVP 2010.*

[4] B. A. Auld, *Acoustic fields and waves in solids*, vol. 1-2. Krieger Publishing Company Inc., 1973.

[5] J. D. Achenbach, *Wave propagation in elastic solids.* North-Holland Pub. Co./American Elsevier, Amsterdam/New York, 1973.

[6] J. Krautkramer and H. Krautkramer, *Ultrasonic testing of materials.* Springer-Verlag, Berlin, Heidelberg, 1977.

[7] J. L. Rose, *Ultrasonic Waves in Solid Media.* University of Cambridge, 1999.

[8] W. Schmerr, *Fundamentals of ultrasonic NDE - A modelling approach.* Plenum Press, New York, 1998.

[9] J. A. Ogilvy, *Theory of wave scattering from random rough surfaces.* Institute of Physics Publishing, 1991.

[10] I. N. Ermolov, "The reflection of ultrasonic waves from targets of simple geometry," *Non-Destructive Testing*, vol. 5, no. 2, pp. 87–91, 1972.

[11] J. D. Achenbach, L. Adler, D. K. Lewis, and H. McMaken, "Diffraction of ultrasonic waves by penny-shaped cracks in metals: Theory and experiment," *J. Acoust. Soc. Am.*, vol. 66, no. 6, pp. 1848–1856, 1979.

[12] R. K. Chapman, "Ultrasonic scattering from smooth flat cracks: an elastodynamic Kirchhoff diffraction theory," *CEGB report, North Western Region NDT Application Centre/SSD/84/0059/R*, 1984.

[13] R. K. Chapman, "A system model for the ultrasonic inspection of smooth planar cracks," *J. Nondestruct. Eval.*, vol. 9, no. 2-3, pp. 197–210, 1990.

[14] A. L. Lopez-Sanchez, Kim, Hak-Joon, Schmerr, L. W., Jr., and A. Sedov, "Measurement models and scattering models for predicting the ultrasonic pulse-echo response from side-drilled holes," *J. Nondestruct. Eval.*, vol. 24, no. 3, pp. 83–96, 2005.

[15] J. A. Ogilvy, "An estimate of the accuracy of the Kirchhoff approximation in acoustic wave scattering from rough surfaces," *J. Phys. D: Appl. Phys.*, vol. 19, no. 11, pp. 2085–2113, 1986.

[16] J. A. Ogilvy, "Theoretical comparison of ultrasonic signal amplitudes from smooth and rough defects," *NDT Int.*, vol. 19, no. 6, pp. 371–385, 1986.

[17] J. A. Ogilvy, "Model for the ultrasonic inspection of rough defects," *Ultrasonics*, vol. 27, no. 2, pp. 69–79, 1989.

[18] J. Zhang, B. W. Drinkwater, and P. D. Wilcox, "Longitudinal wave scattering from rough crack-like defects," *IEEE Trans. Ultrason. Ferroelectr. Freq. Contr.*, vol. 58, no. 10, pp. 2171–2180, 2011.

[19] F. G. Bass and I. M. Fuks, *Wave scattering from statistically rough surfaces.* Pergamon Press, Oxford, 1979.

[20] J. B. Keller, "Diffraction by an Aperture," *J. Appl. Phys.*, vol. 28, no. 4, pp. 426–444, 1957.

[21] J. B. Keller, "Geometrical Theory of Diffraction," *J. Optical Soc. Am.*, vol. 52, no. 2, pp. 116–130, 1962.

[22] J. B. Keller and F. C. Karal, "Geometrical theory of elastic surface-wave excitation and propagation," *J. Acoust. Soc. Am.*, vol. 36, no. 1, pp. 32–40, 1964.

[23] J. D. Achenbach, A. K. Gautesen, and H. McMaken, *Ray methods for waves in elastic solids: with applications to scattering by cracks.* Monographs and studies in mathematics, Pitman Advanced Pub. Program, 1982.

[24] J. A. Ogilvy and J. A. G. Temple, "Diffraction of elastic waves by cracks: application to time-of-flight inspection," *Ultrasonics*, vol. 21, no. 6, pp. 259–269, 1983.

[25] R. K. Chapman, "An integrated model of ultrasonic ndt and its practical application," *Mathematical Modeling in Non-Destructive Testing*, pp. 209–232, 1988.

[26] M. Born and E. Wolf, *Principles of Optics.* Pergamon Press, 1965.

[27] J. E. Gubernatis, E. Domany, and J. A. Krumhansl, "Formal aspects of the theory of the scattering of ultrasound by flaws in elastic materials," *J. of Applied Physics*, vol. 48, no. 7, pp. 2804–2811, 1977.

[28] J. E. Gubernatis, E. Domany, J. A. Krumhansl, and M. Huberman, "The born approximation in the theory of the scattering of elastic waves by flaws," *J. of Applied Physics*, vol. 48, no. 7, pp. 2812–2819, 1977.

[29] R. B. Thompson, "Quantitative Ultrasonic Nondestructive Evaluation Methods," *J. of Applied Mechanics*, vol. 50, pp. 1191–1201, 1983.

[30] I. Yalda, F. J. Margetan, and R. B. Thompson, "Predicting ultrasonic grain noise in polycrystals: A Monte Carlo model," *J. Acoust. Soc. Am.*, vol. 99, no. 6, pp. 3445–3455, 1996.

[31] O. Nowers, D. J. Duxbury, and B. W. Drinkwater, "Accurate modelling of anisotropic effects in austenitic stainless steel welds," in *Rev. Prog. QNDE*, vol. 1581 of *AIP Conference Proceedings*, pp. 985–991, 2014.

[32] K. J. Bathe, "Finite Element procedures in engineering analysis," *Prentice-Hall Inc., New York*, 1982.

[33] C. A. Brebbia, "The boundary element method for engineers," *Pentech Press, London*, 1978.

[34] G. D. Smith, *Numerical solution of partial differential equations: finite difference methods.* Oxford University Press, 1985.

[35] R. Eymard, T. Gallouét, and R. Herbin, *The finite volume method.* P.G. Ciarlet, J.L. Lions (Eds.), Handbook of Numerical Analysis.

[36] J. D. Achenbach, "Mathematical modeling for quantitative ultrasonics," *Nondestructive Testing and Evaluation*, vol. 8-9, no. 1-6, pp. 363–377, 1992.

[37] L. Andersen, S. R. K. Nielsen, and S. Krenk, "Numerical methods for analysis of structure and ground vibration from moving loads," *Computers and structures*, vol. 85, pp. 43–58, 2007.

[38] S. Wang, S. Huang, and W. Zhao, "Simulation of Lamb wave's interactions with transverse internal defects in an elastic plate," *Ultrasonics*, vol. 51, pp. 432–440, 2011.

[39] G. Green, "An essay on the application of mathematical analysis to the theories of electricity and magnetism," *Mathematical Papers of George Green*, pp. 1–115, 1970.

[40] A. H.-D., Cheng and D. T. Cheng, "Heritage and early history of the boundary element method," *Engineering Analysis with Boundary Elements*, vol. 29, no. 3, pp. 268–302, 2005.

[41] A. S. Ferguson and G. Stroink, "Factors affecting the accuracy of the boundary element method in the forward problem. I. Calculating surface potentials," *Biomedical Engineering, IEEE Transactions*, vol. 44, no. 11, pp. 1139–1155, 1997.

[42] L. J. Bond, "Methods for the computer modelling of ultrasonic waves in solids," *Research techniques in Non-Destructive Testing*, vol. 6, pp. 107–150, 1982.

[43] A. H. Harker, "Numerical modelling of the scattering of elastic waves in plates," *J. Nondestruct. Eval.*, vol. 4, no. 2, pp. 89–106, 1984.

[44] K. Harumi, F. Suzuki, and Y. Satô, "Computer simulation of nearfield for elastic wave in a solid half-space," *J. Acoust. Soc. Am.*, vol. 53, no. 2, pp. 660–664, 1973.

[45] N. Saffari and L. J. Bond, "Mode-conversion phenomena at surface breaking cracks for defect characterisation," *IEEE Ultrasonic Symp.*, pp. 960–964, 1983.

[46] J. A. G. Temple, "Modelling the propagation and scattering of elastic waves in inhomogeneous anisotropic media," *J. Phys. D: Appl. Phys.*, vol. 21, no. 6, pp. 859–874, 1988.

[47] R. J. Blake, *Numerical models for Rayleigh wave scattering from surface features.* PhD thesis, Electronic and Electrical Engineering, University of London, 1988.

[48] B. Lombard and J. Piraux, "Modeling 1-D elastic P-waves in a fractured rock with hyperbolic jump conditions," *J. Comp. and Appl. Math.*, vol. 204, pp. 292–305, 2007.

[49] Minhhuy Le, Jinyi Lee, Jongwoo Jun, Jungmin Kim, Sangman Moh, and Kisu Shin, "Hall sensor array based validation of estimation of crack size in metals using magnetic dipole models," *NDT&E Int.*, vol. 53, pp. 18–25, 2013.

[50] A. Cheriet, M. Feliachi, and S. M. Mimoune, "3D movement simulation technique in FVM method application to eddy current non destructive testing," *The Int. J. for Computation and Mathematics in Electrical and Electronic Engineering*, vol. 28, no. 1, pp. 77–84, 2009.

[51] J. H. Park, M. Y. Choi, and W. T. Kim, "Infrared thermography and modeling to the concrete deck with internal defects as a non-destructive testing," *Advances in Non-Destructive Evaluation*, vol. 270-273, pp. 938–943, 2004.

[52] V. Bolborici, F. P. Dawson, and M. C. Pugh, "Modeling of composite piezoelectric structures with the finite volume method," *IEEE Trans. Ultrason. Ferroelectr. Freq. Contr.*, vol. 59, no. 1, pp. 156–162, 2012.

[53] C. T. Hsiao, X. Lu, and G. Chahine, "Three-dimensional modeling of the dynamics of therapeutic ultrasound contrast agents," *Ultrasound in medicine and biology*, vol. 36, no. 12, pp. 2065–2079, 2010.

[54] C. Vanhille, C. Conde, and C. Campos-Pozuelo, "Finite-difference and finite-volume methods for nonlinear standing ultrasonic waves in fluid media," *Ultrasonics*, vol. 42, no. 1-9, pp. 315–318, 2004.

[55] A, Lhémery, P. Calmon, S. Chatillon, and N. Gengembre, "Modeling of ultrasonic fields radiated by contact transducer in a component of irregular surface," *Ultrasonics*, vol. 40, pp. 231–236, 2002.

[56] C. E. Baumann and J. T. Oden, "A discontinuous hp finite element method for convection-diffusion problems," *Computer Methods in Applied Mechanics and Engineering*, vol. 175, no. 3-4, pp. 311–341, 1999.

[57] G. A. O. Davies, *Virtual work in structural analysis.* Wiley-Blackwell, 1982.

[58] I. M. Smith and D. V. Griffiths, *Programming the Finite Element Method.* John Wiley and Sons, Ltd, ed.4, 2004.

[59] B. J. Mac Donald, *Practical Stress Analysis with Finite Elements.* Glasnevin Publishing, 2007.

[60] J. Fish and T. Belytschko, *A first course in finite elements.* John Wiley and Sons Ltd., 2007.

[61] N. Rebelo, J. C. Nagtegaal, L. M. Taylor, and R. Passmann, "Comparison of implicit and explicit finite element methods in the simulation of metal forming processes," *Numerical methods in industrial forming processes*, pp. 99–108, 1992.

[62] J. S. Sun, K. H. Lee, and H. P. Lee, "Comparison of implicit and explicit finite element methods for dynamic problems," *J. of Materials Processing Technology*, vol. 105, no. 1-2, pp. 110–118, 2000.

[63] W. D. Smith, "Application of finite element analysis to body wave propagation problems," *Geophys. J. R. Astron. Soc.*, vol. 42, no. 2, pp. 747–768, 1975.

[64] R. Ludwig and W. Lord, "A finite-element formulation for the study of ultrasonic NDT systems," *IEEE Trans. Ultrason. Ferroelectr. Freq. Contr.*, vol. 35, no. 6, pp. 809–820, 1988.

[65] R. Courant, K. Friedrichs, and H. Lewy, "On the partial difference equations of mathematical physics," *IBM Journal of Research and Development 11*, vol. 2, pp. 215–234, 1967.

[66] M. Frehner, S. M. Schmalholz, E. H. Saenger, and H. Steeb, "Comparison of finite difference and finite element methods for simulating two-dimensional scattering of elastic waves," *Phys. Earth Planet. Inter.*, vol. 171, no. 1-4, pp. 112–121, 2008.

[67] J. A. Ogilvy, "Wave scattering from rough surfaces," *Rep. Prog. Phys.*, vol. 50, no. 12, pp. 1553–1608, 1987.

[68] M. S. Longuet-Higgins, "Statistical properties of an isotropic random surface," *Phil. Trans. R. Soc. Lond. A*, vol. 250, no. 975, pp. 157–174, 1957.

[69] J. A. Greenwood, "A unified theory of surface roughness," *Proc. R. Soc. Lond. A*, vol. 393, no. 1804, pp. 133–157, 1984.

[70] F. Gilbert and L. Knopoff, "Seismic scattering from topographic irregularities," *J. Geophys. Res.*, vol. 65, no. 10, pp. 3437–3444, 1960.

[71] J. A. Hudson, R. F. Humphryes, I. M. Mason, and V. K. Kembhavi, "The scattering of longitudinal elastic waves at a rough free surface," *J. Phys. D: Appl Phys.*, vol. 6, no. 18, pp. 2174–2186, 1973.

[72] C. Eckart, "The scattering of sound from the sea surface," *J. Acoust. Soc. Am.*, vol. 25, no. 3, pp. 566–570, 1953.

[73] B. E. Parkins, "Omnidirectional scattering of acoustic waves by rough, imperfectly reflecting surfaces," *J. Acoust. Soc. Am.*, vol. 41, no. 1, pp. 126–134, 1967.

[74] M. L. Boyd and R. L. Deavenport, "Forward and specular scattering from a rough surface: Theory and experiment," *J. Acoust. Soc. Am.*, vol. 53, no. 3, pp. 791–801, 1973.

[75] S. F. Burch, N. Collett, R. K. Chapman, and M. W. Toft, "Experimental validation of the TRANGLE and related NDT codes for modelling the ultrasonic inspection of rough cracks," *Insight*, vol. 46, no. 2, pp. 74–76, 2004.

[76] Lord Rayleigh, *The Theory of Sound*, vol. 2. London: Macmillan, 1st ed., 1878.

[77] P. Rajagopal and M. J. S. Lowe, "Scattering of the fundamental shear horizontal guided wave by a part-thickness crack in an isotropic plate.," *J. Acoust. Soc. Am.*, vol. 124, no. 5, pp. 2895–2904, 2008.

[78] L. Moreau, A. Velichko, and P. D. Wilcox, "Accurate finite element modelling of guided wave scattering from irregular defects," *NDT&E Int.*, vol. 45, no. 1, pp. 46–54, 2012.

[79] P. D. Wilcox and A. Velichko, "Efficient frequency-domain finite element modeling of two-dimensional elastodynamic scattering," *J. Acoust. Soc. Am.*, vol. 127, no. 1, pp. 155–165, 2010.

[80] S. Mahaut, N. Leymarie, C. Poidevin, T. Fouquet, and O. Dupond, "Study of complex ultrasonic NDT cases using hybrid simulation method and experimental validations," *Insight*, vol. 53, no. 12, pp. 664–667, 2011.

[81] A. Velichko and P. D. Wilcox, "Efficient finite element modeling of elastodynamic scattering with non-reflecting boundary conditions," *AIP Conference Proceedings*, vol. 1430, no. 1, pp. 142–149, 2012.

[82] P. Rajagopal, E. A. Skelton, W. Choi, M. J. S. Lowe, and R. V. Craster, "A generic Hybrid model for bulk elastodynamics, with application to ultrasonic Nondestructive Evaluation," *IEEE Trans. Ultrason. Ferroelectr. Freq. Contr.*, vol. 59, no. 6, pp. 1239–1252, 2012.

[83] D. Placko and K. Kundu, *DPSM for modeling engineering problems.* New Jersey: John Wiley and Sons, Inc., 2007.

[84] F. B. Cegla, A. J. C. Jarvis, and J. O. Davies, "High temperature ultrasonic crack monitoring using SH waves," *NDT&E Int.*, vol. 44, no. 8, pp. 669–679, 2011.

[85] F. B. Cegla and A. J. C. Jarvis, "Modeling the effect of roughness on ultrasonic scattering in 2D and 3D," vol. 1581, pp. 595–601, 2014.

[86] P. Bettess, *Infinite Elements.* Penshaw Press, 1992.

[87] D. Givoli and J. B. Keller, "Non-reflecting boundary conditions for elastic waves," *Wave Motion*, vol. 12, no. 3, pp. 261–279, 1990.

[88] J. P. Berenger, "A perfectly matched layer for the absorption of electromagnetic waves," *J. Comp. Phys.*, vol. 114, no. 2, pp. 185–200, 1994.

[89] M. Israeli and S. A. Orszag, "Approximation of radiation boundary conditions," *J. Comp. Phys.*, vol. 41, no. 1, pp. 115–135, 1981.

[90] J. F. Semblat, L. Lenti, and A. Gandomzadeh, "A simple multi-directional absorbing layer method to simulate elastic wave propagation in unbounded domains," *Int. J. for Numerical Methods in Engineering*, vol. 85, no. 12, pp. 1543–1563, 2011.

[91] J. R. Pettit, A. Walker, P. Cawley, and M. J. S. Lowe, "A Stiffness Reduction Method for efficient absorption of waves at boundaries for use in commercial Finite Element codes," *Ultrasonics*, vol. 54, no. 7, pp. 1868–1879, 2014.

[92] P. Rajagopal, M. Drozdz, E. A. Skelton, M. J. S. Lowe, and R. V. Craster, "On the use of absorbing layers to simulate the propagation of elastic waves in unbounded isotropic media using commercially available finite element packages," *NDT&E Int.*, vol. 51, pp. 30–40, 2012.

[93] J. R. Pettit, A. Walker, and M. J. S. Lowe, "A stiffness reduction method for efficient modelling of waves in unbound media using commercially available finite elements packages," in *Rev. Prog. QNDE*, vol. 1581 of *AIP Conference Proceedings*, pp. 579–586, 2014.

[94] J. R. Pettit, A. Walker, and M. J. S. Lowe, "An optimised stiffness reduction method for simulating infinite elastic space using commercial Finite Element codes," *J. Phys: Conference Series, in press*, 2015.

[95] J. Lysmer and R. L. Kuhlemeyer, "Finite dynamic model for infinite media," *J. Engineering Mechanics Division*, vol. 95, no. 4, pp. 859–878, 1969.

[96] G. Kouroussis, O. Verlinden, and C. Conti, "Finite-dynamic model for infinite media: corrected solution of viscous boundary efficiency," *J. Engineering Mechanics*, vol. 137, no. 7, pp. 509–511, 2011.

[97] G. R. Liu and S. S. Quek Jerry, "A non-reflecting boundary for analyzing wave propagation using the finite element method," *Finite Elements in Analysis and Design*, vol. 39, no. 5-6, pp. 403–417, 2003.

[98] B. Engquist and A. Majda, "Radiation boundary conditions for acoustic and elastic wave calculations," *Communications on Pure and Applied Mathematics*, vol. 32, no. 3, pp. 313–357, 1979.

[99] A. Bayliss and E. Turkel, "Radiation boundary conditions for wave-like equations," *Communications on Pure and Applied Mathematics*, vol. 33, no. 6, pp. 707–725, 1980.

[100] J. M. Carcione, "Boundary conditions for wave propagation problems," *Finite Elements in Analysis and Design*, vol. 16, no. 3-4, pp. 317–327, 1994.

[101] D. Givoli, "High-order local non-reflecting boundary conditions: a review," *Wave Motion*, vol. 39, no. 4, pp. 319–326, 2004.

[102] Q. Qi and T. L. Geers, "Evaluation of the perfectly matched layer for computational acoustics," *J. Comput. Phys.*, vol. 139, no. 1, pp. 166–183, 1998.

[103] E. Bécache, Bonnet-Ben Dhia A.-S., and G. Legendre, "Perfectly matched layers for the convected Helmholtz equation," *SIAM J. Numer. Anal.*, vol. 42, no. 1, pp. 409–433, 2004.

[104] I. Singer and E. Turkel, "A perfectly matched layer for the Helmholtz equation in a semi-infinite strip," *J. Comput. Phys.*, vol. 201, no. 2, pp. 439–465, 2004.

[105] F. D. Hastings, J. B. Schneider, and S. L. Broschat, "Application of the perfectly matched layer (PML) absorbing boundary condition to elastic wave propagation," *J. Acoust. Soc. Am.*, vol. 100, no. 5, pp. 3061–3069, 1996.

[106] F. Collino and C. Tsogka, "Application of the perfectly matched absorbing layer model to the linear elastodynamic problem in anisotropic heterogeneous media," *Geophysics*, vol. 66, no. 7, pp. 294–307, 2001.

[107] D. Komatitsch and J. Tromp, "A perfectly matched layer absorbing boundary condition for the second-order seismic wave equation," *Geophysical J. Int.*, vol. 154, no. 1, pp. 146–153, 2003.

[108] U. Basu and A. K. Chopra, "Perfectly matched layers for transient elastodynamics of unbounded domains," *Int. J. Numer. Meth. Eng.*, vol. 59, no. 8, pp. 1039–1074, 2004.

[109] E. A. Skelton, S. D. M. Adams, and R. V. Craster, "Guided elastic waves and perfectly matched layers," *Wave Motion*, vol. 44, no. 7-8, pp. 573–592, 2007.

[110] M. Castaings, C. Bacon, B. Hosten, and M. V. Predoi, "Finite element predictions for the dynamic response of thermo-viscoelastic material structures," *J. Acoust. Soc. Am.*, vol. 115, no. 3, pp. 1125–1133, 2004.

[111] M. Castaings and C. Bacon, "Finite element modeling of torsional wave modes along pipes with absorbing materials," *J. Acoust. Soc. Am.*, vol. 119, no. 6, pp. 3741–3751, 2006.

[112] W. Ke, M. Castaings, and C. Bacon, "3D finite element simulations of an air-coupled ultrasonic NDT system," *NDT&E Int.*, vol. 42, no. 6, pp. 524–533, 2009.

[113] ABAQUS v 6.9, http://abaqus.cc.ic.ac.uk/v6.9/, Version Abaqus 6.9.1, 2006.

[114] M. J. S. Lowe, "Matrix techniques for modeling ultrasonic waves in multilayered media," *IEEE Trans. Ultrason. Ferroelectr. Freq. Contr.*, vol. 42, no. 4, pp. 525–542, 1995.

[115] M. Drozdz, *Efficient Finite Element Modelling of Ultrasound Waves in Elastic Media.* PhD thesis, Imperial College of Science and Technology and Medicine, 2008.

[116] J. A. Ogilvy, "Computer simulation of acoustic wave scattering from rough surfaces," *J. Phys. D: Appl. Phys.*, vol. 21, pp. 260–277, 1988.

[117] MATLAB R2007a, The MathWorks Inc., United Kingdom, 2012.

[118] W. Choi, E. A. Skelton, J. R. Pettit, M. J. S. Lowe, and R. V. Craster, "A generic hybrid model: Three-dimensional bulk elastodynamics in non-destructive evaluation," *in review.*

[119] W. Choi, E. Skelton, M. J. S. Lowe, and R. Craster, "Unit cell finite element modelling of ultrasonic scattering from periodic surfaces," in *Rev. Prog. QNDE*, vol. 1511 of *AIP Conference Proceedings*, pp. 83–90, 2013.

[120] J. M. Coffey and R. K. Chapman, "Application of elastic scattering theory for smooth flat cracks to the quantitative prediction of ultrasonic defect detection and sizing," *Nucl. Energy*, vol. 22, no. 5, pp. 319–333, 1983.

[121] J. R. Pettit, A. Walker, and M. J. S. Lowe, "Improved detection of rough defects for ultrasonic NDE inspections based on finite element modeling of elastic wave scattering," in *Rev. Prog. QNDE*, vol. 1581 of *AIP Conference Proceedings*, pp. 521–528, 2014.

[122] J. R. Pettit, A. Walker, and M. J. S. Lowe, "Improved Detection of Rough Defects for Ultrasonic Non-Destructive Evaluation Inspections Based on Finite Element Modelling of Elastic Wave Scattering," *IEEE Trans. Ultrason. Ferroelectr. Freq. Contr., in review.*

[123] J. R. Pettit, A. Walker, and M. J. S. Lowe, "Modelling NDE pulse-echo inspection of misorientated planar rough defects using an elastic Finite Element method," in *Rev. Prog. QNDE, in review*, AIP Conference Proceedings, 2015.

[124] P. A. Doyle and C. M. Scala, "Crack depth measurements by ultrasonics: a review," *Ultrasonics*, vol. 16, no. 4, pp. 164–170, 1978.

[125] M. G. Silk, "Sizing crack-like defects by ultrasonic means," *Research Techniques in Nondestructive Testing, Ed. R.S. Sharpe. Academic Press Vol. 3, Ch. 2*, 1977.

[126] J. P. Charlesworth and J. A. G. Temple, *Engineering Applications of Ultrasonic Time-of-Flight Diffraction.* Research studies press Ltd., 1989.

[127] O. Nowers and J. R. Pettit, "Willkommen im Kernkraftwerk Leibstadt," *Nuclear Future*, vol. 10, no. 3, pp. 36–37, 2014.

# 8 List of Publications

1. J. R. Pettit, A. Walker, P. Cawley, and M. J. S. Lowe, A Stiffness Reduction Method for efficient absorption of waves at boundaries for use in commercial Finite Element codes, Ultrasonics, vol. 54, no. 7, pp. 1868-1879, 2014. [91]

2. J. R. Pettit, A. Walker, and M. J. S. Lowe, Improved detection of rough defects for ultrasonic NDE inspections based on finite element modeling of elastic wave scattering, in Rev. Prog. QNDE, vol. 1581 of AIP Conference Proceedings, pp. 521-528, 2014. [121]

3. J. R. Pettit, A. Walker, and M. J. S. Lowe, A stiffness reduction method for efficient modelling of waves in unbound media using commercially available finite elements packages, in Rev. Prog. QNDE, vol. 1581 of AIP Conference Proceedings, pp. 579-586, 2014. [93]

4. O. Nowers and J. R. Pettit, Willkommen im Kernkraftwerk Leibstadt, Nuclear Future, vol. 10, no. 3, pp. 36-37, 2014. [127]

5. J. R. Pettit, A. Walker, and M. J. S. Lowe, Modelling NDE pulse-echo inspection of misorientated planar rough defects using an elastic Finite Element method, in Rev. Prog. QNDE, in review, AIP Conference Proceedings, 2015. [123]

6. J. R. Pettit, A. Walker, and M. J. S. Lowe, An optimised stiffness reduction method for simulating infinite elastic space using commercial Finite Element codes, J. Phys: Conference Series, in press, 2015. [94]

7. J. R. Pettit, A. Walker, and M. J. S. Lowe, Improved Detection of Rough Defects for Ultrasonic Non-Destructive Evaluation Inspections Based on Finite Element Modelling of Elastic Wave Scattering, IEEE Trans. Ultrason. Ferroelectr. Freq. Contr., in review. [122]

8. W. Choi, E. A. Skelton, J. R. Pettit, M. J. S. Lowe, and Craster. R. V., A generic hybrid model: Three-dimensional bulk elastodynamics in non-destructive evaluation, in review. [118]

# 9 Appendices

## 9.1 Appendix 1: Permission documents

From: Copyright Clearance Center <rightslink@marketing.copyright.com>
Date: 16 June 2014 08:28:32 GMT+01:00
To: <james.pettit06@imperial.ac.uk>
Subject: Thank you for your RightsLink / Elsevier transaction
Reply-To: Copyright Clearance Center <reply-fe6410767365077c7411-14153369_HTML-1088066290-114453-56758@info.copyright.com>

To view this email as a web page, go here.

**Do Not Reply Directly to This Email**

To ensure that you continue to receive our emails,
please add rightslink@marketing.copyright.com to your address book.

### Thank You For Your Order!

Dear Mr. James Pettit,

Thank you for placing your order through Copyright Clearance Center's RightsLink service. Elsevier has partnered with RightsLink to license its content. This notice is a confirmation that your order was successful.

Your order details and publisher terms and conditions are available by clicking the link below:
http://s100.copyright.com/CustomerAdmin/PLF.jsp?ref=114daf98-0cd7-49f3-9fb2-3354c2a5cd54

**Order Details**
Licensee: James Pettit
License Date: Jun 16, 2014
License Number: 3410650590141
Publication: Ultrasonics
Title: A Stiffness Reduction Method for efficient absorption of waves at boundaries for use in commercial Finite Element codes
Type Of Use: reuse in a thesis/dissertation
Total: 0.00 GBP

To access your account, please visit https://myaccount.copyright.com.

Please note: Online payments are charged immediately after order confirmation; invoices are issued daily and are payable immediately upon receipt.

To ensure that we are continuously improving our services, please take a moment to complete our customer satisfaction survey.

**B.1:v4.2**

**+1-877-622-5543 / Tel: +1-978-646-2777**

This email was sent to: **jrp06@ic.ac.uk**

Please visit Copyright Clearance Center for more information.

This email was sent by Copyright Clearance Center
222 Rosewood Drive Danvers, MA 01923 USA

To view the privacy policy, please go here.

**ELSEVIER LICENSE**
**TERMS AND CONDITIONS**

Sep 28, 2014

This is a License Agreement between James Pettit ("You") and Elsevier ("Elsevier") provided by Copyright Clearance Center ("CCC"). The license consists of your order details, the terms and conditions provided by Elsevier, and the payment terms and conditions.

**All payments must be made in full to CCC. For payment instructions, please see information listed at the bottom of this form.**

| | |
|---|---|
| Supplier | Elsevier Limited<br>The Boulevard,Langford Lane<br>Kidlington,Oxford,OX5 1GB,UK |
| Registered Company Number | 1982084 |
| Customer name | James Pettit |
| Customer address | 55 Panama Circle<br>Derby, DE24 1AE |
| License number | 3410650590141 |
| License date | Jun 16, 2014 |
| Licensed content publisher | Elsevier |
| Licensed content publication | Ultrasonics |
| Licensed content title | A Stiffness Reduction Method for efficient absorption of waves at boundaries for use in commercial Finite Element codes |
| Licensed content author | J.R. Pettit,A. Walker,P. Cawley,M.J.S. Lowe |
| Licensed content date | 12 December 2013 |
| Licensed content volume number | None |
| Licensed content issue number | None |
| Number of pages | 1 |
| Start Page | 0 |
| End Page | 0 |
| Type of Use | reuse in a thesis/dissertation |
| Portion | figures/tables/illustrations |
| Number of figures/tables/illustrations | All |
| Actual number of figures/tables/illustrations | 50 |
| Format | electronic |
| Are you the author of this | Yes |

| | |
|---|---|
| Elsevier article? | |
| Will you be translating? | No |
| Title of your thesis/dissertation | Modelling the ultrasonic response from rough defects using efficient finite element modelling techniques |
| Expected completion date | Oct 2014 |
| Estimated size (number of pages) | 200 |
| Elsevier VAT number | GB 494 6272 12 |
| Permissions price | 0.00 GBP |
| VAT/Local Sales Tax | 0.00 GBP / 0.00 GBP |
| Total | 0.00 GBP |
| Terms and Conditions | |

## INTRODUCTION

1. The publisher for this copyrighted material is Elsevier. By clicking "accept" in connection with completing this licensing transaction, you agree that the following terms and conditions apply to this transaction (along with the Billing and Payment terms and conditions established by Copyright Clearance Center, Inc. ("CCC"), at the time that you opened your Rightslink account and that are available at any time at http://myaccount.copyright.com).

## GENERAL TERMS

2. Elsevier hereby grants you permission to reproduce the aforementioned material subject to the terms and conditions indicated.

3. Acknowledgement: If any part of the material to be used (for example, figures) has appeared in our publication with credit or acknowledgement to another source, permission must also be sought from that source. If such permission is not obtained then that material may not be included in your publication/copies. Suitable acknowledgement to the source must be made, either as a footnote or in a reference list at the end of your publication, as follows:

"Reprinted from Publication title, Vol /edition number, Author(s), Title of article / title of chapter, Pages No., Copyright (Year), with permission from Elsevier [OR APPLICABLE SOCIETY COPYRIGHT OWNER]." Also Lancet special credit - "Reprinted from The Lancet, Vol. number, Author(s), Title of article, Pages No., Copyright (Year), with permission from Elsevier."

4. Reproduction of this material is confined to the purpose and/or media for which permission is hereby given.

5. Altering/Modifying Material: Not Permitted. However figures and illustrations may be altered/adapted minimally to serve your work. Any other abbreviations, additions, deletions and/or any other alterations shall be made only with prior written authorization of Elsevier Ltd. (Please contact Elsevier at permissions@elsevier.com)

6. If the permission fee for the requested use of our material is waived in this instance,

please be advised that your future requests for Elsevier materials may attract a fee.

7. Reservation of Rights: Publisher reserves all rights not specifically granted in the combination of (i) the license details provided by you and accepted in the course of this licensing transaction, (ii) these terms and conditions and (iii) CCC's Billing and Payment terms and conditions.

8. License Contingent Upon Payment: While you may exercise the rights licensed immediately upon issuance of the license at the end of the licensing process for the transaction, provided that you have disclosed complete and accurate details of your proposed use, no license is finally effective unless and until full payment is received from you (either by publisher or by CCC) as provided in CCC's Billing and Payment terms and conditions. If full payment is not received on a timely basis, then any license preliminarily granted shall be deemed automatically revoked and shall be void as if never granted. Further, in the event that you breach any of these terms and conditions or any of CCC's Billing and Payment terms and conditions, the license is automatically revoked and shall be void as if never granted. Use of materials as described in a revoked license, as well as any use of the materials beyond the scope of an unrevoked license, may constitute copyright infringement and publisher reserves the right to take any and all action to protect its copyright in the materials.

9. Warranties: Publisher makes no representations or warranties with respect to the licensed material.

10. Indemnity: You hereby indemnify and agree to hold harmless publisher and CCC, and their respective officers, directors, employees and agents, from and against any and all claims arising out of your use of the licensed material other than as specifically authorized pursuant to this license.

11. No Transfer of License: This license is personal to you and may not be sublicensed, assigned, or transferred by you to any other person without publisher's written permission.

12. No Amendment Except in Writing: This license may not be amended except in a writing signed by both parties (or, in the case of publisher, by CCC on publisher's behalf).

13. Objection to Contrary Terms: Publisher hereby objects to any terms contained in any purchase order, acknowledgment, check endorsement or other writing prepared by you, which terms are inconsistent with these terms and conditions or CCC's Billing and Payment terms and conditions. These terms and conditions, together with CCC's Billing and Payment terms and conditions (which are incorporated herein), comprise the entire agreement between you and publisher (and CCC) concerning this licensing transaction. In the event of any conflict between your obligations established by these terms and conditions and those established by CCC's Billing and Payment terms and conditions, these terms and conditions shall control.

14. Revocation: Elsevier or Copyright Clearance Center may deny the permissions described in this License at their sole discretion, for any reason or no reason, with a full refund payable to you. Notice of such denial will be made using the contact information provided by you. Failure to receive such notice will not alter or invalidate the denial. In no event will Elsevier or Copyright Clearance Center be responsible or liable for any costs, expenses or damage incurred by you as a result of a denial of your permission request, other than a refund of the

amount(s) paid by you to Elsevier and/or Copyright Clearance Center for denied permissions.

**LIMITED LICENSE**

The following terms and conditions apply only to specific license types:

15. **Translation**: This permission is granted for non-exclusive world **English** rights only unless your license was granted for translation rights. If you licensed translation rights you may only translate this content into the languages you requested. A professional translator must perform all translations and reproduce the content word for word preserving the integrity of the article. If this license is to re-use 1 or 2 figures then permission is granted for non-exclusive world rights in all languages.

16. **Posting licensed content on any Website**: The following terms and conditions apply as follows: Licensing material from an Elsevier journal: All content posted to the web site must maintain the copyright information line on the bottom of each image; A hyper-text must be included to the Homepage of the journal from which you are licensing at http://www.sciencedirect.com/science/journal/xxxxx or the Elsevier homepage for books at http://www.elsevier.com; Central Storage: This license does not include permission for a scanned version of the material to be stored in a central repository such as that provided by Heron/XanEdu.

Licensing material from an Elsevier book: A hyper-text link must be included to the Elsevier homepage at http://www.elsevier.com . All content posted to the web site must maintain the copyright information line on the bottom of each image.

**Posting licensed content on Electronic reserve**: In addition to the above the following clauses are applicable: The web site must be password-protected and made available only to bona fide students registered on a relevant course. This permission is granted for 1 year only. You may obtain a new license for future website posting.

**For journal authors:** the following clauses are applicable in addition to the above: Permission granted is limited to the author accepted manuscript version* of your paper.

***Accepted Author Manuscript (AAM) Definition:** An accepted author manuscript (AAM) is the author's version of the manuscript of an article that has been accepted for publication and which may include any author-incorporated changes suggested through the processes of submission processing, peer review, and editor-author communications. AAMs do not include other publisher value-added contributions such as copy-editing, formatting, technical enhancements and (if relevant) pagination.

You are not allowed to download and post the published journal article (whether PDF or HTML, proof or final version), nor may you scan the printed edition to create an electronic version. A hyper-text must be included to the Homepage of the journal from which you are licensing at http://www.sciencedirect.com/science/journal/xxxxx. As part of our normal production process, you will receive an e-mail notice when your article appears on Elsevier's online service ScienceDirect (www.sciencedirect.com). That e-mail will include the article's Digital Object Identifier (DOI). This number provides the electronic link to the published article and should be included in the posting of your personal version. We ask that you wait until you receive this e-mail and have the DOI to do any posting.

**Posting to a repository:** Authors may post their AAM immediately to their employer's institutional repository for internal use only and may make their manuscript publically available after the journal-specific embargo period has ended.

Please also refer to Elsevier's Article Posting Policy for further information.

18. **For book authors** the following clauses are applicable in addition to the above: Authors are permitted to place a brief summary of their work online only.. You are not allowed to download and post the published electronic version of your chapter, nor may you scan the printed edition to create an electronic version. **Posting to a repository:** Authors are permitted to post a summary of their chapter only in their institution's repository.

20. **Thesis/Dissertation**: If your license is for use in a thesis/dissertation your thesis may be submitted to your institution in either print or electronic form. Should your thesis be published commercially, please reapply for permission. These requirements include permission for the Library and Archives of Canada to supply single copies, on demand, of the complete thesis and include permission for UMI to supply single copies, on demand, of the complete thesis. Should your thesis be published commercially, please reapply for permission.

## Elsevier Open Access Terms and Conditions

Elsevier publishes Open Access articles in both its Open Access journals and via its Open Access articles option in subscription journals.

Authors publishing in an Open Access journal or who choose to make their article Open Access in an Elsevier subscription journal select one of the following Creative Commons user licenses, which define how a reader may reuse their work: Creative Commons Attribution License (CC BY), Creative Commons Attribution – Non Commercial - ShareAlike (CC BY NC SA) and Creative Commons Attribution – Non Commercial – No Derivatives (CC BY NC ND)

**Terms & Conditions applicable to all Elsevier Open Access articles:**

Any reuse of the article must not represent the author as endorsing the adaptation of the article nor should the article be modified in such a way as to damage the author's honour or reputation.

The author(s) must be appropriately credited.

If any part of the material to be used (for example, figures) has appeared in our publication with credit or acknowledgement to another source it is the responsibility of the user to ensure their reuse complies with the terms and conditions determined by the rights holder.

**Additional Terms & Conditions applicable to each Creative Commons user license:**

**CC BY:** You may distribute and copy the article, create extracts, abstracts, and other revised versions, adaptations or derivative works of or from an article (such as a translation), to include in a collective work (such as an anthology), to text or data mine the article, including for commercial purposes without permission from Elsevier

**CC BY NC SA:** For non-commercial purposes you may distribute and copy the article, create extracts, abstracts and other revised versions, adaptations or derivative works of or from an article (such as a translation), to include in a collective work (such as an anthology), to text and data mine the article and license new adaptations or creations under identical terms without permission from Elsevier

**CC BY NC ND:** For non-commercial purposes you may distribute and copy the article and include it in a collective work (such as an anthology), provided you do not alter or modify the article, without permission from Elsevier

Any commercial reuse of Open Access articles published with a CC BY NC SA or CC BY NC ND license requires permission from Elsevier and will be subject to a fee.

Commercial reuse includes:

- Promotional purposes (advertising or marketing)
- Commercial exploitation ( e.g. a product for sale or loan)
- Systematic distribution (for a fee or free of charge)

Please refer to Elsevier's Open Access Policy for further information.

21. **Other Conditions**:

v1.6

**Questions? customercare@copyright.com or +1-855-239-3415 (toll free in the US) or +1-978-646-2777.**

**Gratis licenses (referencing $0 in the Total field) are free. Please retain this printable license for your reference. No payment is required.**

## AIP PUBLISHING LLC LICENSE
## TERMS AND CONDITIONS

Sep 29, 2014

**All payments must be made in full to CCC. For payment instructions, please see information listed at the bottom of this form.**

| | |
|---|---|
| License Number | 3478060041501 |
| Order Date | Sep 29, 2014 |
| Publisher | AIP Publishing LLC |
| Publication | AIP Conference Proceedings |
| Article Title | Improved detection of rough defects for ultrasonic NDE inspections based on finite element modeling of elastic wave scattering |
| Author | J. R. Pettit,A. Walker,M. J. S. Lowe |
| Online Publication Date | Feb 18, 2014 |
| Volume number | 1581 |
| Issue number | 1 |
| Type of Use | Thesis/Dissertation |
| Requestor type | Author (original article) |
| Format | Electronic |
| Portion | Figure/Table |
| Number of figures/tables | 10 |
| Title of your thesis / dissertation | Modelling the ultrasonic response from rough defects using efficient finite element modelling techniques |
| Expected completion date | Oct 2014 |
| Estimated size (number of pages) | 200 |
| Total | 0.00 USD |

Terms and Conditions

AIP Publishing LLC -- Terms and Conditions: Permissions Uses

AIP Publishing LLC ("AIPP"") hereby grants to you the non-exclusive right and license to use and/or distribute the Material according to the use specified in your order, on a one-time basis, for the specified term, with a maximum distribution equal to the number that you have ordered. Any links or other content accompanying the Material are not the subject of this license.

1. You agree to include the following copyright and permission notice with the reproduction of the Material:"Reprinted with permission from [FULL CITATION]. Copyright [PUBLICATION YEAR], AIP Publishing LLC." For an article, the copyright and permission notice must be printed on the first page of the article or book chapter. For photographs, covers, or tables, the copyright and permission notice may appear with the Material, in a footnote, or in the reference list.
2. If you have licensed reuse of a figure, photograph, cover, or table, it is your responsibility to ensure that the material is original to AIPP and does not contain the copyright of another entity, and that the copyright notice of the figure, photograph, cover, or table does not indicate that it was reprinted by AIPP, with permission, from another source. Under no circumstances does AIPP, purport or intend to grant permission to reuse material to which it does not hold copyright.
3. You may not alter or modify the Material in any manner. You may translate the Material into another language only if you have licensed translation rights. You may not use the

Material for promotional purposes. AIPP reserves all rights not specifically granted herein.

4. The foregoing license shall not take effect unless and until AIPP or its agent, Copyright Clearance Center, receives the Payment in accordance with Copyright Clearance Center Billing and Payment Terms and Conditions, which are incorporated herein by reference.
5. AIPP or the Copyright Clearance Center may, within two business days of granting this license, revoke the license for any reason whatsoever, with a full refund payable to you. Should you violate the terms of this license at any time, AIPP, AIP Publishing LLC, or Copyright Clearance Center may revoke the license with no refund to you. Notice of such revocation will be made using the contact information provided by you. Failure to receive such notice will not nullify the revocation.
6. AIPP makes no representations or warranties with respect to the Material. You agree to indemnify and hold harmless AIPP, AIP Publishing LLC, and their officers, directors, employees or agents from and against any and all claims arising out of your use of the Material other than as specifically authorized herein.
7. The permission granted herein is personal to you and is not transferable or assignable without the prior written permission of AIPP. This license may not be amended except in a writing signed by the party to be charged.
8. If purchase orders, acknowledgments or check endorsements are issued on any forms containing terms and conditions which are inconsistent with these provisions, such inconsistent terms and conditions shall be of no force and effect. This document, including the CCC Billing and Payment Terms and Conditions, shall be the entire agreement between the parties relating to the subject matter hereof.

This Agreement shall be governed by and construed in accordance with the laws of the State of New York. Both parties hereby submit to the jurisdiction of the courts of New York County for purposes of resolving any disputes that may arise hereunder.

**Questions? customercare@copyright.com or +1-855-239-3415 (toll free in the US) or +1-978-646-2777.**

**Gratis licenses (referencing $0 in the Total field) are free. Please retain this printable license for your reference. No payment is required.**

# AIP PUBLISHING LLC LICENSE TERMS AND CONDITIONS

Sep 29, 2014

**All payments must be made in full to CCC. For payment instructions, please see information listed at the bottom of this form.**

| | |
|---|---|
| License Number | 3478060254467 |
| Order Date | Sep 29, 2014 |
| Publisher | AIP Publishing LLC |
| Publication | AIP Conference Proceedings |
| Article Title | A stiffness reduction method for efficient modelling of waves in unbound media using commercially available finite elements packages |
| Author | J. R. Pettit,A. Walker,M. J. S. Lowe |
| Online Publication Date | Feb 18, 2014 |
| Volume number | 1581 |
| Issue number | 1 |
| Type of Use | Thesis/Dissertation |
| Requestor type | Author (original article) |
| Format | Electronic |
| Portion | Figure/Table |
| Number of figures/tables | 10 |
| Title of your thesis / dissertation | Modelling the ultrasonic response from rough defects using efficient finite element modelling techniques |
| Expected completion date | Oct 2014 |
| Estimated size (number of pages) | 200 |
| Total | 0.00 USD |

Terms and Conditions

AIP Publishing LLC -- Terms and Conditions: Permissions Uses

AIP Publishing LLC ("AIPP"") hereby grants to you the non-exclusive right and license to use and/or distribute the Material according to the use specified in your order, on a one-time basis, for the specified term, with a maximum distribution equal to the number that you have ordered. Any links or other content accompanying the Material are not the subject of this license.

1. You agree to include the following copyright and permission notice with the reproduction of the Material:"Reprinted with permission from [FULL CITATION]. Copyright [PUBLICATION YEAR], AIP Publishing LLC." For an article, the copyright and permission notice must be printed on the first page of the article or book chapter. For photographs, covers, or tables, the copyright and permission notice may appear with the Material, in a footnote, or in the reference list.
2. If you have licensed reuse of a figure, photograph, cover, or table, it is your responsibility to ensure that the material is original to AIPP and does not contain the copyright of another entity, and that the copyright notice of the figure, photograph, cover, or table does not indicate that it was reprinted by AIPP, with permission, from another source. Under no circumstances does AIPP, purport or intend to grant permission to reuse material to which it does not hold copyright.
3. You may not alter or modify the Material in any manner. You may translate the Material

into another language only if you have licensed translation rights. You may not use the Material for promotional purposes. AIPP reserves all rights not specifically granted herein.

4. The foregoing license shall not take effect unless and until AIPP or its agent, Copyright Clearance Center, receives the Payment in accordance with Copyright Clearance Center Billing and Payment Terms and Conditions, which are incorporated herein by reference.
5. AIPP or the Copyright Clearance Center may, within two business days of granting this license, revoke the license for any reason whatsoever, with a full refund payable to you. Should you violate the terms of this license at any time, AIPP, AIP Publishing LLC, or Copyright Clearance Center may revoke the license with no refund to you. Notice of such revocation will be made using the contact information provided by you. Failure to receive such notice will not nullify the revocation.
6. AIPP makes no representations or warranties with respect to the Material. You agree to indemnify and hold harmless AIPP, AIP Publishing LLC, and their officers, directors, employees or agents from and against any and all claims arising out of your use of the Material other than as specifically authorized herein.
7. The permission granted herein is personal to you and is not transferable or assignable without the prior written permission of AIPP. This license may not be amended except in a writing signed by the party to be charged.
8. If purchase orders, acknowledgments or check endorsements are issued on any forms containing terms and conditions which are inconsistent with these provisions, such inconsistent terms and conditions shall be of no force and effect. This document, including the CCC Billing and Payment Terms and Conditions, shall be the entire agreement between the parties relating to the subject matter hereof.

This Agreement shall be governed by and construed in accordance with the laws of the State of New York. Both parties hereby submit to the jurisdiction of the courts of New York County for purposes of resolving any disputes that may arise hereunder.

**Questions? customercare@copyright.com or +1-855-239-3415 (toll free in the US) or +1-978-646-2777.**

**Gratis licenses (referencing $0 in the Total field) are free. Please retain this printable license for your reference. No payment is required.**